Dissertation

Study of High-Q Nanomechanical Silicon Nitride Resonators

submitted for the degree of
Doctor of Technical Sciences (Dr. techn.)

Institute of Sensor and Actuator Systems
Technische Universität Wien

Author:
Pedram Sadeghi (01651819)

Supervisor:
Prof. Dr. Silvan Schmid

Vienna, 2021

Abstract

The growing interest in the field of nanomechanical resonators stems from their potential use as high performance sensors of a variety of physical quantities by means of detecting the resonance frequency shift. With the recent advancements in nanofabrication techniques as well as an abundance of new materials, sensors optimized for the detection of mass, force, and temperature with unprecedented responsivities are within reach. Central to many reported nanomechanical sensor investigations has been to maximize the mechanical quality factor Q, which directly results in an enhanced force sensitivity. Concurrently, high-Q resonators present an opportunity to unite the quantum regime with real-world applications by allowing quantum phenomena to be observed at room temperature, which is a topic of the so-called cavity optomechanics research field. As such, methods employed to reliable enhance the Q are in high demand in several fields employing nanomechanical resonators.

In order to properly use high-Q resonators, both as sensors as well as building blocks in optomechanics, an in-depth analysis of their properties needs to be made. The most important questions to answer would be, what are the fundamental limits to the dissipation of mechanical resonators, and what sources of fluctuations determine the maximum sensitivities? This thesis aims to partly answer the above questions using high-stress silicon nitride nanomechanical resonators. Such resonators present a nanomechanical system capable of room temperature Qs approaching 1 billion due to the dissipation dilution effect. The presented results follow a linear pattern, first focusing on methods used to enhance the mechanical Q, then discussing fundamental limits to the frequency stability, and finally presenting a possible application of high-Q resonators as thermal sensors.

Two approaches to Q-enhancement are presented, one focusing on the optimization of the dissipation dilution effect and the other on reducing intrinsic losses. The former works by widening the clamping of nanomechanical string resonators, which is numerically shown to reduce the curvature at the string clamping, thus potentially circumventing one of the limiting mechanisms of stressed resonators. Through a systematic investigation of strings with different orientations relative to the surrounding substrate, only marginal Q-enhancements result from the method, attributed to the increased material bending resulting from the clamp-widening. Finite element method simulations corroborate all the presented measurements,

thus offering a path to further optimization of the resonator design.

For nanomechanical resonators, with increasingly large surface-to-volume ratios, surface friction becomes the dominant intrinsic loss mechanism. In the second Q-enhancement approach, an effort is made to reduce the surface friction by means of high-temperature annealing of resonators in an ultrahigh vacuum environment. This procedure is performed on a variety of stressed resonator geometries, resulting in a clear Q-enhancement regardless of the geometry. Increases in the intrinsic Q approaching an order of magnitude are observed, which is shown to be directly related to reduced surface losses. The annealing treatment is shown to be reproducible and nondestructive, only marginally influencing the mechanical properties of the resonator. Given that this approach can be applied to current state-of-the-art high-Q resonators in literature, these results present an important step forward in the pursuit of room-temperature quantum experiments.

Moving on to the second part of the thesis concerning applying high-Q resonators as sensors, a detailed investigation into the frequency fluctuations of such resonators is presented. Nanomechanical string resonators are employed as the system under consideration and the frequency stability is characterized using the Allan deviation, both in open-loop and closed-loop tracking configurations. For open-loop tracking, it is shown how the Allan deviation is divided into a regime limited by thermomechanical noise and another limited by the background noise of the detection. Despite the latter noise source potentially lower in level than the thermomechanical noise, the frequency stability is shown to always be limited fundamentally by thermomechanical noise with a response time defined by intrinsic properties of the resonator. Closed-loop tracking is shown to offer a response faster than the intrinsic limit at the expense of increased noise. Additionally, when employing optical detection schemes, the laser power fluctuations are shown to be a potentially limiting factor in the frequency stability. Measurements are supported by theory-based calculations of the Allan deviation, showing great agreement, allowing the design of future sensors with optimized frequency stability.

The final part of the thesis demonstrates how localized defect modes of low-stress phononic crystal (PnC) membranes can be utilized as thermal sensors. Here, the thermal response is quantified through laser heating of the membrane center, which shifts the frequency through the photothermal effect. Owing to the perforation of the membranes and the increased overlap between the defect modes and the temperature field resulting from the laser heat source, the thermal responsivity of PnC membranes is shown to be potentially an order of magnitude greater than that of uniform membranes of equal size. Even larger thermal response is reported through geometrical stress reduction, achieved by fabricating a PnC membrane inside a nanomechanical trampoline. Lastly, defect mode and bandgap tuning through laser heating are presented, demonstrating how the defect mode can be thermally detuned enough to completely exit the phononic bandgap. These results serve as a basis upon which further opti-

mization of resonator design can be made, paving the way for a new class of thermal sensors with unparalleled thermal response.

Zusammenfassung

Das wachsende Interesse am Bereich der nanomechanischen Resonatoren stammt von ihren potenziellen Anwendungen als hoch-sensitive Sensoren für eine Vielzahl physikalischer Größen, durch die Messung der Resonanzfrequenzverschiebung. Durch die steten Fortschritte von Nanofabrikationstechniken, sowie einer Fülle neuer Materialien sind Sensoren für die Messung von Masse, Kraft und Temperatur mit bisher unerreichten Empfindlichkeiten, in Reichweite. Im Mittelpunkt vieler Untersuchungen von nanomechanischen Sensoren steht die Maximierung des mechanischen Gütefaktors Q, der direkt zu einer erhöhten Kraftempfindlichkeit führt. Gleichzeitig bieten Hoch-Q Resonatoren die Möglichkeit, das Quantenregime mit realen Anwendungen zu vereinen, indem sie die Beobachtung von Quantenphänomenen bei Raumtemperatur ermöglichen; ein Thema der sogenannten Kavitäten-Optomechanik. Darum sind Methoden zur zuverlässigen Erhöhung von Q in unterschiedlichsten Bereichen, in denen nanomechanische Resonatoren eingesetzt werden, sehr gefragt.

Um Hoch-Q Resonatoren sowohl als Sensoren, sowie als Bausteine in der Optomechanik richtig einzusetzen, ist eine gründliche Analyse ihrer Eigenschaften notwendig. Die wichtigsten Fragen, die es zu beantworten gilt, sind: Wo liegen die fundamentalen Grenzen der Dissipations Verlusten und welche Fluktuations Quellen bestimmen die maximalen Empfindlichkeit? Diese Arbeit zielt darauf ab, die oben genannten Fragen zu beantworten, indem nanomechanische Resonatoren aus high-stress (mechanisch stark gespanntem) Siliziumnitrid untersucht werden. Diese nanomechanischen Systeme können, aufgrund des Dissipationsverdünnungseffekts, Qs von fast 1 Milliarde bei Raumtemperatur erreichen. Die präsentierten Ergebnisse zeigen systematisch, welche Methoden zur Erhöhung des mechanischen Qs es gibt, wo die grundlegenden Grenzen der Frequenzstabilität liegen und welches Potential Hoch-Q Resonatoren als thermische Sensoren bieten.

Zunächst werden zwei Ansätze zur Erhöhung von Q vorgestellt. Der eine konzentriert sich auf die Optimierung des Dissipationsverdünnungseffekts, der andere auf die Reduzierung der intrinsischen Dämpfung. Ersterer basiert auf einer Verbreiterung der Einspannung von nanomechanischen String-Resonatoren, wobei numerisch gezeigt wird, dass die Krümmung an der Grenze String-Substrat reduziert und somit einer der limitierenden Faktoren von stark gespannten Resonatoren potenziell umgangen wird. Durch eine systematische Untersuchung

von Strings mit unterschiedlichen Orientierungen und Krümmungsradien relativ zu dem umgebenden Substrat, ergeben sich jedoch nur marginale Q-Erhöhungen. Die Limitierung ist auf die erhöhte, biegunsfähige Materialmenge durch die Klemmverbreiterung zurückzuführen. Simulationen mit der Finite-Elemente-Methode bestätigen die Experimente und zeigen dadurch einen einfachen Weg zur Optimierung des Resonator-Designs.

Bei nanomechanischen Resonatoren wird bei immer größeren Oberflächen-zu-Volumen-Verhältnissen die Oberflächenreibung zum dominierenden intrinsischen Dämpfungsmechanismus. Im zweiten Ansatz zur Q-Erhöhung wird versucht, die Oberflächenreibung durch Ausheizen der Resonatoren in einer Ultrahochvakuum-Umgebung, zu reduzieren. Dieses Verfahren wird an unterschiedlichen Resonatorgeometrien durchgeführt. Unabhängig von der Geometrie führt diese Methode immer zu einer deutlichen Q-Erhöhung. Es werden Steigerungen des intrinsischen Gütefaktors um eine Größenordnung beobachtet, die in direktem Zusammenhang mit einer reduzierten Oberflächendämpfung stehen. Es wurde gezeigt, dass die Glühbehandlung reproduzierbar und zerstörungsfrei ist und die mechanischen Eigenschaften des Resonators nur vernachlässigbar beeinflusst. In Anbetracht der Tatsache, dass diese Methode auf alle in der Literatur zu findenden Hoch-Q Resonatoren angewandt werden kann, stellen diese Ergebnisse einen wichtigen Fortschritt bei der Realisierung von Quantenexperimenten bei Raumtemperatur dar.

Im zweiten Teil dieser Doktorarbeit, der sich mit der Anwendung von Hoch-Q Resonatoren als Sensoren beschäftigt, wird eine detaillierte Untersuchung der Frequenzschwankungen vorgestellt. Als betrachtetes System werden nanomechanische String-Resonatoren eingesetzt und die Frequenzstabilität wird mit Hilfe der Allan-Deviation, sowohl in offenen, als auch in geschlossenen Regelschleifen Konfigurationen, charakterisiert. Für die offene Regelschleife wird gezeigt, wie die Allan-Deviation in einen durch thermomechanisches Rauschen begrenzten Bereich und einen, durch das Hintergrundrauschen der Detektion begrenzten unterteilt wird. Da die letztgenannte Rauschquelle potenziell ein niedrigeres Level als das thermomechanische Rauschen aufweist, wird gezeigt, dass die Frequenzstabilität grundsätzlich immer durch das thermomechanische Rauschen begrenzt wird, wobei die Reaktionszeit durch die intrinsischen Eigenschaften des Resonators definiert ist. Weiters wird gezeigt, dass die Reaktionszeit bei Verwendung einer geschlossene Regelschleife, schneller ist als durch die intrinsische Grenze vorgegeben, allerdings auf Kosten eines erhöhten Rauschens. Außerdem wurde gefunden, dass bei der Verwendung von optischen Detektionsmethoden die Fluktuationen der Laserleistung ein potentiell begrenzender Faktor für die Frequenzstabilität sind. Die Messungen werden durch theoretische Berechnungen der Allan-Deviation unterstützt und zeigen eine sehr gute Übereinstimmung, was das Design zukünftiger Sensoren mit optimierter Frequenzstabilität ermöglicht.

Der letzte Teil der Arbeit demonstriert, wie lokalisierte Defekt-Moden von low-stress

phononischen Kristallmembranen (PnC) als thermische Sensoren genutzt werden können. Hier wird die thermische Antwort durch Lasererwärmung der Membranmitte quantifiziert, die durch den photothermischen Effekt die Resonanzfrequenz verschiebt. Aufgrund der Perforation der Membranen und der erhöhten Überlappung zwischen den Defekt-Moden und dem Temperaturfeld, das aus der Laserwärmequelle resultiert, zeigt sich, dass die thermische Empfindlichkeit von PnC-Membranen potenziell um eine Größeordnung größer ist, als die von vergleichbaren Membranen. Eine noch größere thermische Antwort wird durch eine geometrische Spannungsreduktion erreicht, die durch die Implementierung einer PnC-Membran in ein nanomechanisches Trampolin erzielt wird. Schließlich wird die relative Verschiebung von Defekt-Mode und Bandlücke durch Lasererwärmung präsentiert. Es wird gezeigt, wie die Defekt-Mode thermisch so weit verschoben werden kann, dass sie die phononische Bandlücke vollständig verlässt. Diese Ergebnisse dienen als Grundlage für die weitere Optimierung des Resonatordesigns und ebnen den Weg für eine neue Klasse von thermischen Sensoren mit noch nicht da gewesenen Sensitivitäten.

Contribution to Original Knowledge

The research conducted during this PhD project represents a small, but important step forward in the field of nanomechanical resonators. Various original contributions to the knowledge in this field could be made, the most significant of which include:

- Investigation of widening the clamping of nanomechanical string resonators as a method of enhancing the dissipation dilution effect and thus the quality factor. For the first time, the influence of the resonator orientation relative to the substrate is presented, which is revealed to be essential in achieving quality factor enhancement. The limitation of this method is also shown, resulting only in slight enhancements even in the optimum configuration, which contributes to the solving of a puzzle in the stressed nanomechanical resonators field.

- Significant enhancement of the quality factor through reduction of surface friction. This was achieved by means of annealing nanomechanical resonators in an ultrahigh vacuum, conducted on both uniform resonators and soft-clamped phononic crystal membranes, with enhancements approaching an order of magnitude through annealing alone achievable. The influence of annealing on the tensile stress was also investigated, which provides further understanding of the origin of the quality factor enhancement. These findings contribute to perhaps the final step necessary for increasing the quality factor to values allowing room-temperature quantum optomechanics.

- Systematic investigation into the frequency fluctuations of high quality factor string resonators, representing a regime where the resolution bandwidth is significantly greater than the resonance linewidth. The different sources of noise present in such systems are measured and their contribution to the frequency stability revealed, which includes a fundamental limitation to optical detection schemes set by the power stability of the probe laser. Frequency tracking is performed in both open-loop and closed-loop configurations, which shows the unavoidable trade-off between high speed and low noise. All of the measured data are corroborated by a theory-based model, meaning these findings serve as a platform for the design of future resonators with optimal sensor performance.

- Application of low-stress phononic crystal membranes as thermal sensors, investigated through laser heating of the membranes and measuring the photothermal detuning. It is shown how the perforation of such resonators, combined with the larger overlap between the defect mode shape and the laser heating induced temperature field, results in an enhanced thermal response compared to uniform membrane resonators of equal size. It is also shown how the stress can be lowered by engineering a phononic crystal into a nanomechanical trampoline, which further enhances the thermal responsivity. This phononic crystal trampoline design adds knowledge to the stress engineering field and can be used as a template for future thermal sensor designs as well.

List of Publications

I. N. Luhmann, A. Jachimowicz, J. Schalko, **P. Sadeghi**, M. Sauer, A. Foelske-Schmitz, & S. Schmid, "Effect of oxygen plasma on nanomechanical silicon nitride resonators," Applied Physics Letters **111**, 063103 (2017).

II. **P. Sadeghi**, M. Tanzer, S. L. Christensen, & S. Schmid, "Influence of clamp-widening on the quality factor of nanomechanical silicon nitride resonators," Journal of Applied Physics **126**, 165108 (2019).

III. N. Cazier, **P. Sadeghi**, M.-H. Chien, M. M. Shawrav, & S. Schmid, "Spectrally broadband electro-optic modulation with nanoelectromechanical string resonators," Optics Express **28**, 12294-12301 (2020).

IV. M.-H. Chien, J. Steurer, **P. Sadeghi**, N. Cazier, & S. Schmid, "Nanoelectromechanical position-sensitive detector with picometer resolution," ACS Photonics **7**, 2197-2203 (2020).

V. M. Piller, **P. Sadeghi**, R. G. West, N. Luhmann, P. Martini, O. Hansen, & S. Schmid, "Thermal radiation dominated heat transfer in nanomechanical silicon drum resonators," Applied Physics Letters **117**, 034101 (2020).

VI. **P. Sadeghi**, M. Tanzer, N. Luhmann, M. Piller, M.-H. Chien, & S. Schmid, "Thermal transport and frequency response of localized modes on low-stress nanomechanical silicon nitride drums featuring a phononic-band-gap structure," Physical Review Applied **14**, 024068 (2020).

VII. **P. Sadeghi**, A. Demir, L. G. Villanueva, H. Kähler, & S. Schmid, "Frequency fluctuations in nanomechanical silicon nitride string resonators," Physical Review B **102**, 214106 (2020).

VIII. **P. Sadeghi**, M. Tanzer, N. Luhmann, Y. Tsaturyan, A. Schliesser, & S. Schmid, "Reduction of intrinsic friction at room temperature in high-Q nanomechanical silicon nitride resonators," Manuscript in preparation.

Acknowledgements

After a journey lasting more than four years, I realize how many people have contributed positively to my work during this time, though I cannot possibly hope to properly thank everyone here. Nonetheless, I will attempt to mention as many people here, without whom I could not have finished my doctorate.

First and foremost, I would like to thank my supervisor and mentor Professor **Silvan Schmid**, with whom I made acquaintance during my MSc in Denmark. I approached him while looking for a topic for my MSc thesis and his enthusiastic and optimistic attitude immediately sold me on his research ideas. Later on, while I was still an MSc student, he offered me an opportunity to join him in his new Micro- and Nanosensors (MNS) group in the Institute of Sensor and Actuator Systems (ISAS) at the TU Wien, which I gladly accepted. During my time working for **Silvan**, he has always been an excellent supervisor, always willing to provide support and answer any question that I may have had (and there were quite a few). If not for **Silvan's** offer, I might never have lived in Austria and therefore never gotten to understand the beauty of this country and would also never have made several new beautiful friendships. Thank you a lot for all you have done for me in these last few years!

Moving on, I would like to thank several people in the MNS group. First of all, I should mention **Miao-Hsuan Chien** and **Niklas Luhmann**, both of whom, along with me, were among the first members of the MNS group in 2016 and whom I ended up working alongside for most of my PhD. As such, we were responsible for setting up the MNS labs in the early stages, an exhausting task made fun because of these guys. Not only could I always rely on them for support at work, but they were also equally fun to hang out with outside of work. An additional thanks to **Markus Piller**, **Hendrik Kähler**, and **Robert West**, who were always available for help and discussing peculiar data, which is a common theme in our line of work. At the later stages of my PhD, **Paolo Martini** and **Kostas Kanellopulos** joined, with whom I, unfortunately, did not have a lot of time to get to know, but nonetheless left a good impact on me by being both fun and helpful colleagues.

I would like to give special thanks to **Manuel Tanzer**, who became my MSc student halfway into my project. At a time of great personal stress and frustration, he joined my project and immediately made a positive impact. He worked incredibly hard to fabricate sam-

ples for me in the cleanroom, with his samples leading to some of the best results presented in my thesis, while additionally providing measurements and simulations to support my results. Furthermore, he became a great friend, always available for any kind of discussion and joining me for many TU Wien student parties. Overall, as good of a student as a person could hope for.

In addition to the MNS group, I would also like to thank several members of the Microsystems Technology (MST) group at ISAS. Despite us being in different groups, most of these guys were always there, when I needed their help, from supporting me with measurements in the labs to having beers on the rooftop after work. The ones deserving of a special mention are **Florian Patocka**, **Jonas Hafner**, **Christopher Zellner**, **Fabian Triendl**, **Claudio Berger**, **Ali Hajian**, **André Gesing**, **Gernot Fleckl**, and **Davide Disnan**, thank you for being great colleagues as well as friends. Another thanks go out to Professor **Ulrich Schmid**, for his hard work not only being the head of the MST group, but also the entire ISAS institute.

Any sort of lab requires dedicated technical staff in order to function properly. Therefore, I would like to thank **Johannes Schalko** for managing our sample fabrication and characterization labs, which are essential to the work of all members of ISAS. An additional thanks to **Michael Buchholz**, **Patrick Meyer** and **Sophia Ewert**, who work hard every day to support a huge amount of PhD students simultaneously, while also being fun people to hang out with outside of work. I would also like to extend my gratitude to **Ewald Pirker**, who could produce pretty much any desired mechanical component in record time.

Naturally, there would be no sense of order at our institute if not for the great secretaries doing wonderful work to support the disordered scientists. I am therefore very thankful to **Martina Nuhsbaumer**, **Martina Bittner**, **Sabine Fuchs**, and **Andreas Astleitner**.

Lastly, I would like to thank all my friends and family members outside of work, who were there for me in the occasionally stressful times of a PhD. A very special mention of my parents has to be made. Without their endless support, I would not be where I am today and therefore, I thank you from the bottom of my heart for being there for me!

Contents

List of Figures

List of Tables

1 Introduction

Resulting from the technological revolution of the previous century, the amount of scientific discoveries has increased rapidly [1]. From these scientific advances, a new field of research named *nanotechnology* has emerged [2]. As the name would suggest, nanotechnology deals with research conducted at length scales on the order of nanometers, i.e. one-billionth of a meter. Typically, however, the transition between micro- (10^{-6} meters) and nanotechnology is set by having one dimension smaller than 100 nanometers. On such small scales, the properties of materials can differ significantly from the physical and chemical laws describing the macroscale, with quantum mechanical effects often coming into play [3]. Many well-established subfields of nanotechnology, spanning the fields of physics, chemistry, and biology, have emerged, with prime examples being nanomedicine [4], nanoelectronics [5], nanophotonics [6], and, central to this thesis, nanomechanics [7]. A great deal of progress in all of these fields is owed to the continuous development of micro- and nanofabrication techniques, allowing reliable and reproducible manufacturing of increasingly small structures [8].

The origin of nanomechanics can be traced back to the microelectronics field, where the incorporation of mechanical elements into microscale devices has led to the well-established field of *microelectromechanical systems* (MEMS) [9]. One of the main drives behind MEMS is their application as sensors, where changes to the environment of the mechanical element result in a shift of the mechanical resonance frequency [10]. Logically, by reducing the device scale even further, the field of *nanoelectromechanical systems* (NEMS) has emerged [11]. The mechanical element in NEMS, from this point on called a (nano)mechanical resonator, can be of any given shape, with common geometries including cantilevers [12], bridges [13], and drums [14]. The properties of nanomechanical resonators resemble their macro- and microscale counterparts, but, owing to the smaller dimensions, the resonance frequencies of mechanical modes will be higher, while their effective masses are significantly smaller [15]. The implications of these benefits are a faster sensor response and increased responsivity

towards external stimuli [16], which has lead to such accomplishments as yoctogram mass sensitivity [17] and attonewton force sensitivity [18].

An additional parameter of great importance to the study of nanomechanical resonators is the *mechanical quality factor* Q, which quantifies the energy decay rate per cycle of vibration [19]. Maximizing the Q results in a reduction of the phase noise [20] and intrinsic force noise [21], while enhancing the force responsivity of resonant sensors based on the vibrational amplitude [16]. Besides the potential benefits of increased Q for sensing applications, a great deal of effort towards enhancing Q has been made in the field of quantum cavity optomechanics [22, 23]. The primary focus of this field is to study the coupling of light to the motion of mechanical resonators. What makes this field particularly interesting is the possibility of exploring the quantum regime of mechanical devices, with, among others, ground-state cooling [24, 25], entanglement [26, 27], and mechanical mode squeezing [28, 29] already experimentally demonstrated. Nonetheless, such observations have thus far been limited to cryogenic temperatures, owing to the very few coherent oscillations possible at room temperature before a thermal phonon enters the system and causes decoherence [23, 30]. The point at which room temperature quantum mechanics should be achievable is determined by the product of the Q and the resonance frequency f_r, with a theoretically required limit of $Q \times f_r > 6 \times 10^{12}$ Hz. This explains the attention given towards nanomechanical resonators since they allow the potential combination of high Q, as well as high f_r owing to the reduced size.

Despite the benefits of high-Q nanomechanical resonators, a general observation is a reduction in Q with decreasing resonator dimensions [31, 32]. This can be more clearly visualized by inspecting Figure 1.1, which plots Qs of a variety of different mechanical resonators found in the literature as a function of the resonator volume V [33]. An overall $Q \propto V^{1/3}$ trend can be observed, which has been attributed to increased surface friction resulting from the larger surface-to-volume ratio. However, a notable exception to this trend can also be discerned from this plot, namely the case of high-stress resonators. Indeed, recent investigations have shown remarkably large room temperature Qs of resonators under tensile stress [34–36], which is owed to the stress-induced dissipation dilution effect [37, 38]. By maximizing this effect, room temperature Qs approaching one billion for megahertz devices have been reported [39, 40], resulting in a $Q \times f_r$ products exceeding 10^{15} Hz. Evidently, research is now pushing closer to the limit where room temperature quantum experiments are feasible.

Even though the Qs of stressed resonators already far exceed the expectations for such dimensions and frequencies, the dissipation dilution effect is independent of the above-mentioned surface friction. In fact, it has been shown that stressed resonators remain surface loss limited, indicating that a ceiling in terms of Q is yet to be reached [48]. This is exactly where the research presented in this thesis comes into play. On the one hand, the thesis aims to further enhance the Qs of stressed silicon nitride (SiN) resonators, which is the most well-

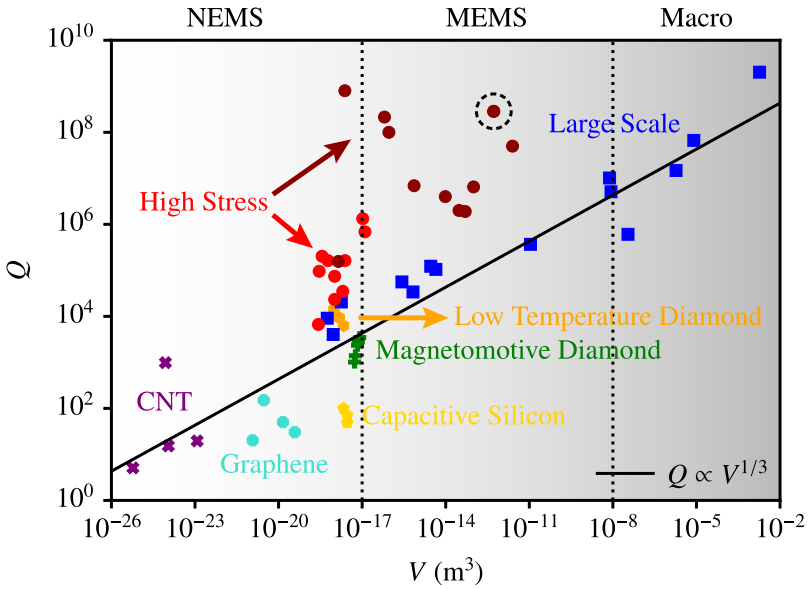

Figure 1.1: Dependence of the mechanical quality factor Q on the resonator volume V. Various types of mechanical resonators are included in the plot, spanning a size range from nanomechanical to macroscopic devices. The style of the figure as well as most of the data points are taken from Figure 2 in [33], while additional values for the Qs of strings [37, 38], membranes [41–45], trampolines [46], and soft-clamped resonators [39, 40] have been added (dark red data points). Some of the added points were taken from Figure 1.5 in [47]. The circled data point represents the largest measured Q shown in this thesis. NEMS: Nanoelectromechanical systems, MEMS: Microelectromechanical systems, CNT: Carbon nanotube.

studied nanomechanical system displaying the dissipation dilution effect. The main approach to enhancing the Q will be by reducing the surface friction, with the goal of reaching unprecedentedly large room temperature Qs. On the other hand, it was explicitly stated above that one of the main motivations behind NEMS is their application as sensors. In particular, despite the benefits of high Qs mentioned above, very few investigations into the frequency fluctuations of high-Q resonators exist. Therefore, the application of SiN resonators as resonant sensors is addressed in this thesis, both by investigating the fundamental limitations to their frequency stability and by demonstrating superior thermal sensing ability.

1.1 Thesis Outline

As already mentioned, the main focus of this thesis is to study various properties of high-Q nanomechanical SiN resonators to achieve both unrivaled room temperature Qs as well as excellent thermal responsivities for quantum optomechanics and thermal sensing applications,

respectively. In that sense, the results of the thesis can be divided into two main parts:

(i) The first part of the presented results is primarily concerned with maximizing the mechanical quality factor of stressed SiN resonators. In the first approach, the clamping of nanomechanical string resonators is widened with the purpose of minimizing the bending at the clamping, which is the limiting factor in the dissipation dilution effect. The second approach focuses on reducing surface friction by annealing resonators in an ultrahigh vacuum. Here, the main goal is to not only study the possible Q-enhancements, but also achieving record Qs at room temperature by combining the reduced surface friction with state-of-the-art stressed SiN resonator designs.

(ii) Provide an understanding of the fundamental limits to the frequency stability of high-Q SiN resonators as well as displaying their possible use as thermal sensors. The frequency fluctuations are investigated by means of SiN string resonators, where the influence of various experimentally controllable parameters are shown, as well as providing a theory-based model capable of predicting the frequency stability limits. Thermal sensing is demonstrated using phononic crystal membranes, where the displacement field of soft-clamped defect modes combined with the membrane perforation promises potentially enhanced thermal responsivities compared to uniform resonators.

Keeping the above-mentioned goals in mind, the subsequent chapters of the thesis are structured as follows:

Chapter 2: Fundamental theory of mechanical resonators is provided, attempting to narrow down the focus to the case of stressed resonators. Theoretical models describing different properties of resonators are shown and discussed, including bending vibrations of one-dimensional and two-dimensional mechanical systems, different extrinsic and intrinsic dissipation mechanisms, heat transfer mechanisms, and fundamental noise processes.

Chapter 3: A detailed introduction to the different methodologies required for the acquisition of the presented results is given, which includes a fabrication process flow for suspended resonators, optical analysis of the vibrational properties using laser-Doppler vibrometry, ultrahigh vacuum systems capable of integration with optical transduction schemes, and finite element method simulations of the various mechanical properties.

Chapter 4: The influence of clamp-widening on the quality factors of nanomechanical string resonators is explored in this chapter. A comparative study is made between strings oriented diagonally and perpendicularly with respect to the supporting silicon frame. It is shown how only marginal Q-enhancements are possible using this approach, with the experimental results

supported by numerical simulations throughout the chapter.

Chapter 5: An experimental investigation into the surface friction loss mechanism in stressed resonators is given. By annealing samples in an ultrahigh vacuum environment, results in support of reduced surface friction are given for both strings, membranes, and phononic crystal membranes. Through the latter geometry, room temperature Qs on the order of 10^8 are measured, rivaling the current state-of-the-art Qs previously demonstrated.

Chapter 6: Limits to the frequency stability of high-Q nanomechanical string resonators are presented here. Such resonators are characterized by resonance linewidths significantly smaller than the measurement bandwidth, which leads to the detection noise of the transduction system being discernible in the resonator noise. In addition, it is shown how laser power fluctuations pose a fundamental limitation to the frequency stability, when employing optical detection schemes. Theory-based models corroborate most of the measurements, thereby presenting a tool for the prediction of frequency fluctuations in mechanical resonators.

Chapter 7: The application of low-stress phononic crystal membranes as thermal sensors is demonstrated. Resulting from the soft clamping effect, the localized modes on such membranes display a greater overlap to the temperature field of a central point source. As a result of this overlap, and the reduced effective thermal conductivity resulting from the membrane perforation, thermal responsivities an order of magnitude greater than uniform membranes of equal size are possible. Additional enhancement in the thermal responsivity is demonstrated using geometrical stress reduction.

2

Theoretical Background of Mechanical Resonators

In this chapter, fundamental models describing the vibrational properties of nanomechanical resonators are presented, with a particular emphasis on resonators under tensile stress. The first part of the chapter deals with the modeling of mechanical vibrations, introducing the driven damped vibration model, followed by a derivation discussion of the equations of motion for both string and membrane resonators. Focus then shifts toward discussing the various dissipation mechanisms influencing the mechanical quality factor, both extrinsic and intrinsic to the resonator. Thereafter, heat transfer mechanisms and theoretical models of the thermal responsivity in strings and membranes are introduced. Finally, frequency noise in nanomechanical systems is discussed, focusing on thermomechanical noise, before moving into describing the Allan deviation. The notation used for physical quantities and variables is similar to that used in [16].

2.1 Modeling of Mechanical Vibrations

This section will provide an introduction to analytical models describing the vibrations of mechanical systems. The focus will initially be on the modeling of driven damped vibrations, which introduces some general concepts essential to the remainder of the theory. Afterwards, theoretical models of the bending vibrations of one-dimensional and two-dimensional stressed resonators are presented.

2.1.1 Driven Damped Vibration

By definition, a vibration is described as the periodic oscillation of a given elastic body about its equilibrium position [49]. The vibration can, for example, be initiated by an external force and restoring forces then pull the structure back towards equilibrium. The frequency at which this vibration naturally occurs in a lossless structure is called the *eigenfrequency* [16]. At the eigenfrequency, the kinetic energy of the mechanical vibration equals the potential energy stored in the deformation of the elastic body. For continuum mechanical structures, more than one natural frequency exists, corresponding to individual *eigenmodes*. In a lossless mechanical structure, no energy would be lost during the oscillation and the system would endlessly oscillate at the eigenfrequency at a constant amplitude as a result. However, real mechanical structures exhibit dissipation, translating into a loss of energy during oscillation and decay of the vibrational amplitude. When dissipation is present, the term eigenmode is replaced by *resonance* and the frequency at which the damped vibration has its largest amplitude is called the *resonance frequency*. The specific case of a *driven damped vibration* is derived and discussed in this section, since this model gives an introduction to many physical quantities that will be used extensively throughout the thesis, and also discusses how they are related to one another. Dissipation is here introduced as a quantity in the model, while the different dissipation mechanisms will be explained in Section 2.2. The derivation presented here is based predominantly on Section 1.2.1.3 in [16].

In order to model driven damped vibrations analytically, a lumped-element model is employed, where the mechanical structure is modeled as a one-dimensional resonator composed of an ideal (massless) linear spring, a linear damping element, and a mass, as sketched in Figure 2.1(a). Nonlinear vibrations will not be considered here. The change in the length of a linear spring is proportional to the applied force, thus serving to model the resonator displacement. Dissipative forces are assumed to be proportional to the velocity of the vibration and modeled using a dashpot. Given that the support, to which the spring is attached, is assumed to be immovable, motion is only allowed along a single direction, hence it being classified as a single degree of freedom system. Based on these assumptions of the lumped-element model, one can derive the equation of motion by means of force balancing [50]

$$m\ddot{z}(t) + c\dot{z}(t) + kz(t) = F(t), \tag{2.1}$$

where m is the total mass, c the damping coefficient, k the spring constant, and $z(t)$ the time-dependent displacement response resulting from the driving force $F(t)$. Before moving into the driven damped response, a number of properties have to be defined. Assuming a free vibration, i.e. the case of $F(t) = 0$, one can derive the mechanical eigenfrequency ω_0 of

a lossless mechanical system, also called an oscillator, and the damping ratio ζ, which are defined as

$$\omega_0 = \sqrt{\frac{k}{m}} \tag{2.2}$$

$$\zeta = \frac{c}{2\sqrt{km}}. \tag{2.3}$$

In order to derive the driven damped response of the mechanical system, a sinusoidal driving force $F(t) = F_0 \cos(\omega t)$ is assumed, where F_0 is the amplitude and ω the frequency of the drive. With this force in mind, the stationary solution to Equation (2.1) is

$$z(t) = z_0 e^{i\omega t}, \tag{2.4}$$

with z_0 being the vibrational amplitude. By inserting Equation (2.4) into Equation (2.1), one arrives at the following expression for the amplitude

$$z_0 = \frac{F_0/m}{\left(\omega_0^2 - \omega^2\right) + 2i\zeta\omega_0\omega}. \tag{2.5}$$

This amplitude can then be converted from complex to polar form with the magnitude

$$|z_0| = \frac{F_0/m}{\sqrt{\left(\omega_0^2 - \omega^2\right)^2 + 4\zeta^2\omega_0^2\omega^2}}, \tag{2.6}$$

and the phase lag with respect to the drive

$$\phi = \arg(z_0) = \arctan\left(\frac{2\zeta\omega_0\omega}{\omega^2 - \omega_0^2}\right). \tag{2.7}$$

The real specific solution to the equation of motion then becomes

$$z(t) = z_0 \cos(\omega t - \phi) = \frac{F_0/m}{\sqrt{\left(\omega_0^2 - \omega^2\right)^2 + 4\zeta^2\omega_0^2\omega^2}} \cos\left(\omega t - \arctan\left(\frac{2\zeta\omega_0\omega}{\omega^2 - \omega_0^2}\right)\right). \tag{2.8}$$

Rewriting Equations (2.6) and (2.7) as functions of relative frequency ω/ω_0, one arrives at

$$|z_0| = \frac{F_0/k}{\sqrt{\left(1 - (\omega/\omega_0)^2\right)^2 + 4\zeta^2(\omega/\omega_0)^2}} \tag{2.9}$$

$$\phi = \arctan\left(\frac{2\zeta(\omega/\omega_0)}{(\omega/\omega_0)^2 - 1}\right). \tag{2.10}$$

The coefficient F_0/k in the numerator of Equation (2.9) represents the quasi-static displace-

ment amplitude, which the system would experience at very low frequencies. As such, normalizing Equation (2.9) to the static displacement results in the *dynamic magnification factor*

$$\delta z_0 = \frac{1}{\sqrt{\left(1-(\omega/\omega_0)^2\right)^2 + 4\zeta^2\,(\omega/\omega_0)^2}}. \tag{2.11}$$

Equations (2.11) and (2.10) have been plotted in Figures 2.1(b) and 2.1(c), respectively, for increasing values of ζ. Inspecting the driven amplitude response, a maximum is observed around $\omega/\omega_0 = 1$, i.e. with a driving frequency near the eigenfrequency ω_0. The frequency at which the maximum amplitude occurs is called the resonance frequency ω_r and is given as

$$\omega_r = \omega_0\sqrt{1-2\zeta^2}. \tag{2.12}$$

It can be observed that when the damping ratio $\zeta \ll 1$, the resonance frequency will be nearly equal to the eigenfrequency, $\omega_r \approx \omega_0$, hence why the two terms are often used interchangeably for systems with low damping. Inserting Equation (2.12) into Equation (2.10) gives the phase lag at resonance

$$\phi_r = \arctan\left(\frac{\sqrt{1-2\zeta^2}}{\zeta}\right), \tag{2.13}$$

which, for $\zeta \ll 1$, gives $\phi_r \approx \pi/2 = 90°$.

At lower frequencies, the dynamic magnification $\delta z_0 = 1$, meaning a vibrational amplitude equal to the static deflection $z_0 = F_0/k$. For slight damping, the vibrational amplitude can be observed to increase beyond the static deflection in Figure 2.1(b), with the amplitude increasing for lower damping. By inserting Equation (2.12) into Equation (2.9), the amplitude at resonance can be shown to be

$$z_0\big|_{\omega=\omega_r} = \frac{F_0}{k}\frac{1}{2\zeta\sqrt{1-\zeta^2}} = \frac{F_0}{k}Q. \tag{2.14}$$

The amount of amplitude amplification at resonance is therefore given by the so-called *quality factor* Q of the resonance, which, for $\zeta \ll 1$, reduces to

$$Q \approx \frac{1}{2\zeta}. \tag{2.15}$$

This factor not only describes the amplitude amplification, it also determines the sharpness of the resonance peak [51]. In terms of the phase, the slope of the phase response at resonance (Equation (2.10)) can be seen to become steeper for lower damping. For very slight damping,

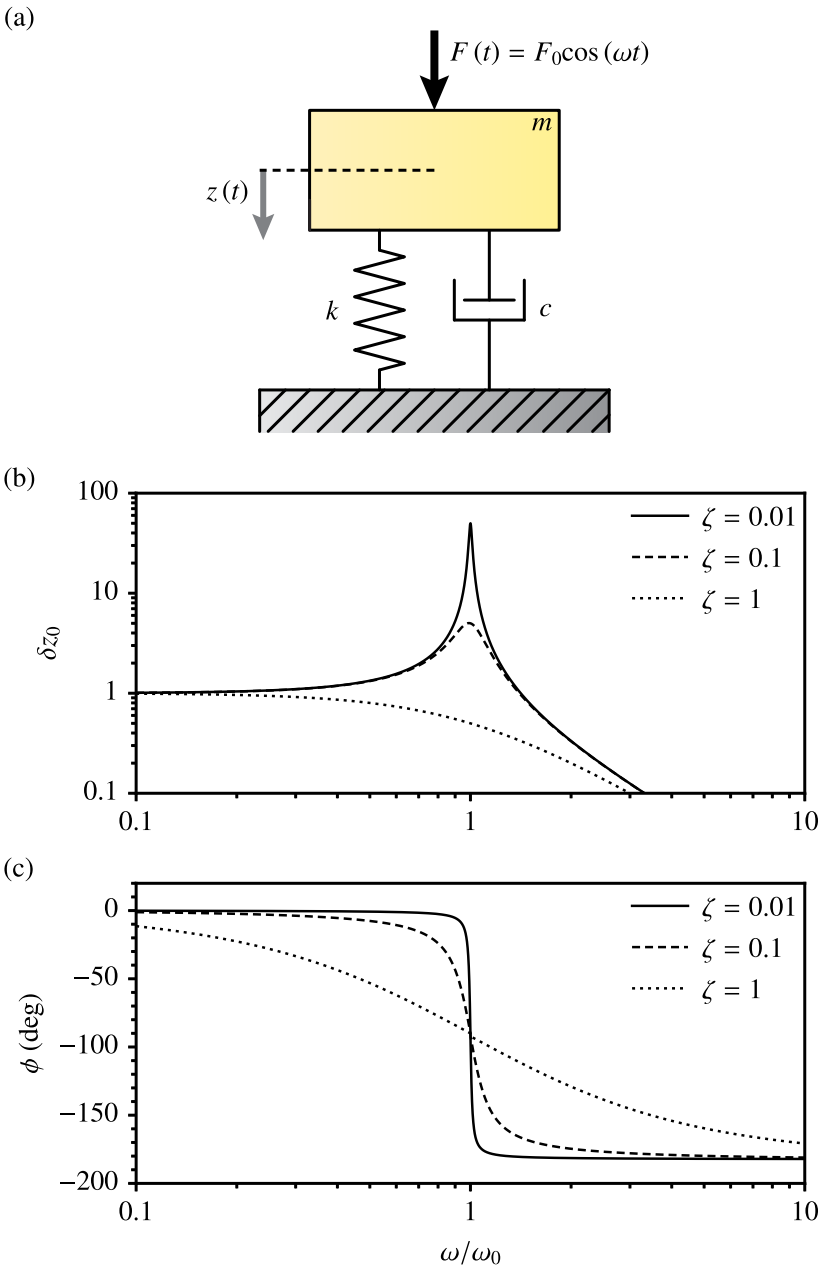

Figure 2.1: Driven damped vibration of a lumped-element model resonator. (a) Schematic of a damped one-dimensional resonator driven by a sinusoidal force $F(t) = F_0\cos(\omega t)$, where ω is the driving frequency, resulting in a displacement $z(t)$. The resonator is characterized by its mass m, spring constant k, and damping coefficient c. (b) Amplitude response of linear resonator according to Equation (2.11) for increasing damping ratios ζ. The x-axis shows ω normalized to the mechanical eigenfrequency ω_0. (c) Phase response of a linear resonator calculated using Equation (2.10) for increasing ζ. Figure is inspired by Figure 1.18 in [16].

where $\omega_r \approx \omega_0$, the slope at resonance becomes

$$\left.\frac{\partial\phi}{\partial\omega}\right|_{\omega=\omega_0} = \frac{1}{\zeta\omega_0} \approx \frac{2Q}{\omega_0}. \tag{2.16}$$

Since the quality factor is directly related to the amount of damping in a given resonance, it is physically defined as the ratio of the total energy in the system W to the energy lost during one cycle of vibration ΔW according to

$$Q = 2\pi\frac{W}{\Delta W}. \tag{2.17}$$

As mentioned in the beginning of this section, the energy of a mechanical structure constantly commutes between kinetic and potential energy, meaning that the total energy of the system can be defined as both the maximum kinetic energy and the maximum elastic energy stored in the spring. Here, the former is employed for the derivation, and, assuming a displacement at resonance $z(t) = z_0\cos(\omega_r t)$, the total energy can be written as

$$W = \frac{1}{2}m\dot{z}^2 = \frac{1}{2}mz_0^2\omega_r^2. \tag{2.18}$$

Given that the displacement is periodic in time, then so must the total energy as well. The energy lost during one cycle of vibration must therefore be equal to the work done by the dissipative force $F_d = -c\dot{z}$ over one cycle

$$\Delta W = -\int_0^{2\pi/\omega_r} F_d\dot{z}dt = \int_0^{2\pi/\omega_r} c\dot{z}^2dt = \pi cz_0^2\omega_r^2. \tag{2.19}$$

Inserting Equations (2.18) and (2.19) into (2.17), one arrives at

$$Q = 2\pi\frac{W}{\Delta W} = \frac{m\omega_r}{c}. \tag{2.20}$$

Using the fundamental definitions of the damping ratio and resonance frequency given in Equations (2.3) and (2.12), respectively, one finally arrives at

$$Q = \frac{\sqrt{1-2\zeta^2}}{2\zeta}, \tag{2.21}$$

which reduces to Equation (2.15) for $\zeta \ll 1$, meaning that the amplitude amplification factor and energy-based definitions are equivalent for slight damping. Different sources of dissipation will be discussed in Section 2.2, while methods employed to determine Q experimentally are discussed in Section 3.2.4.

2.1.2 Free Bending Vibration of Strings

Having established some general properties of resonators in the previous section, it is time to move the focus towards specific mechanical geometries. In this section, the bending modes of mechanical strings will be derived and discussed, following the approach of Section 1.1.1 in [16]. The analytical models presented here are derived using *Euler-Bernoulli beam theory*, which are a set of models developed in the eighteenth century to calculate the bending characteristics of beams. A beam is defined as a very long and narrow mechanical structure, and its properties can be modelled accurately assuming rotational inertia and shear deformation can be neglected [9]. The most common cases are beams with rectangular and circular cross-sections, with the latter not considered here. A rectangular beam is characterized by its length L, width w, and thickness h. Beams fixed at both ends are called *doubly clamped beams* or *bridges*, and a string is a special case of a doubly clamped beam under tensile stress σ, with an illustration given in Figure 2.2(a). A substrate has been included in the schematic as well, but this only serves to illustrate actual samples, and the models presented do not take any substrate into account.

The equation of motion of a string is similar to that of a doubly clamped beam, but with an added tensile force term $N = \sigma A$, where $A = wh$ is the cross-sectional area of the beam. Only out-of-plane vibrations of the string are discussed here. Assuming a linear elastic material, small deflections $u(x,t)$, and no damping, the equation of motion of a string can be written as

$$\rho A \frac{\partial^2 u(x,t)}{\partial t^2} + E I_y \frac{\partial^4 u(x,t)}{\partial x^4} - N \frac{\partial^2 u(x,t)}{\partial x^2} = 0. \tag{2.22}$$

Here, ρ is the mass density, E the Young's modulus, and I_y the geometrical moment of inertia with respect to the y-axis, which, for a beam of rectangular cross-section, is defined as

$$I_y = \frac{Ah^2}{12}. \tag{2.23}$$

In the case of simply supported beam, i.e. one that allows rotation of the clamping points, the solution to Equation (2.22) is a superposition of the string eigenmodes, and through separation of variables, can be divided into a position-dependent and a time-dependent term

$$u(x,t) = \sum_{n=1}^{\infty} \psi_n(x) \cos(\omega_n t), \tag{2.24}$$

where n is the modal number and ω_n is the eigenfrequency of the nth mode. The mathematical function $\psi_n(x)$ is called the *mode shape function* of the beam, which models the deformation of the string. Given the simply supported beam assumption, the boundary conditions of a

string are

$$\psi_n(0) = \psi_n(L) = \frac{\partial^2}{\partial x^2}\psi_n(0) = \frac{\partial^2}{\partial x^2}\psi_n(L) = 0. \tag{2.25}$$

The mode shape is assumed to sinusoidal with wavenumber β_n

$$\psi_n(x) = \psi_{0,n}\sin(\beta_n x), \tag{2.26}$$

which can be inserted into Equation (2.22), yielding the eigenfrequency

$$\omega_n = \beta_n^2 \sqrt{\frac{EI_y}{\rho A}} \sqrt{1 + \frac{\sigma A}{EI_y \beta_n^2}}. \tag{2.27}$$

A wavenumber that satisfies the boundary condition given in Equation (2.25) is

$$\beta_n = \frac{n\pi}{L}, \tag{2.28}$$

which one can insert into Equation (2.27) to identify two extremes. In the first case

$$\frac{\sigma A}{EI_y}\left(\frac{L}{n\pi}\right)^2 \ll 1, \tag{2.29}$$

which leads to the eigenfrequency reducing to that of an unstressed doubly clamped beam [16]. In the opposite extreme

$$\frac{\sigma A}{EI_y}\left(\frac{L}{n\pi}\right)^2 \gg 1, \tag{2.30}$$

the flexural rigidity can be neglected and the eigenfrequency reduces to

$$\omega_n = \frac{n\pi}{L}\sqrt{\frac{\sigma}{\rho}}, \tag{2.31}$$

which is the eigenfrequency equation of a string. In experiments, when discussing the eigenfrequency of a string, the temporal frequency is used instead of the angular frequency, in which case Equation (2.31) becomes

$$f_n = \frac{\omega_n}{2\pi} = \frac{n}{2L}\sqrt{\frac{\sigma}{\rho}}. \tag{2.32}$$

Assuming that the condition given in Equation (2.30) is fullfilled, the eigenfrequency of a string can be accurately calculated using Equation (2.31). However, real strings are clamped at the ends, which adds a non-negligible flexural rigidity that alters the mode shape from the

purely sinusoidal assumption used above. In order to find the real mode shape of a string, Equation (2.27) is rearranged to

$$\beta_n^4 + \frac{\sigma A}{EI_y}\beta_n^2 - \omega_n^2 \frac{\rho A}{EI_y} = 0, \tag{2.33}$$

which can be solved to yield four values of β_n. Through some derivation, two positive solutions can be found, the first of which turns out to be the wavenumber of a perfect string given in Equation (2.28), from here on out labeled β_σ, while the other solution is

$$\beta_n = \beta_E = \sqrt{\frac{\sigma A}{EI_y}}, \tag{2.34}$$

which is related to the flexural rigidity of the string. Using these two wavenumbers, a general solution to the mode shape function can be written as

$$\psi_n(x) = a_n \cos(\beta_\sigma x) + b_n \sin(\beta_\sigma x) + c_n \cosh(\beta_E x) + d_n \sinh(\beta_E x), \tag{2.35}$$

where a_n, b_n, c_n, and d_n are coefficients specific to each boundary condition. Using the boundary conditions of a doubly clamped bridge

$$\psi_n(0) = \psi_n(L) = \frac{\partial}{\partial x}\psi_n(0) = \frac{\partial}{\partial x}\psi_n(L) = 0, \tag{2.36}$$

the coefficients in Equation (2.35) can be found, in the end leading to a simplified expression for the mode shape function of a string

$$\psi_n(x) = \left(\sin(\beta_\sigma x) - \frac{\beta_\sigma}{\beta_E}\left[\cos(\beta_\sigma x) - e^{-\beta_E x}\right]\right). \tag{2.37}$$

This mode shape has been plotted in Figure 2.2(b) for the first 3 bending modes of a string. From the equation, the mode shape function can be seen to consist of a sinusoidal term representing the string-like motion, and an exponential edge-correction term coming from β_E. The length scale at which this correction is relevant is called the decay length and is given as

$$L_c = \frac{1}{\beta_E} = \sqrt{\frac{EI_y}{\sigma A}}. \tag{2.38}$$

Not only does the edge-shape term impact the mode shape function, it turns out to influence the quality factor of stressed resonators significantly, as will be discussed in Section 2.2.4.

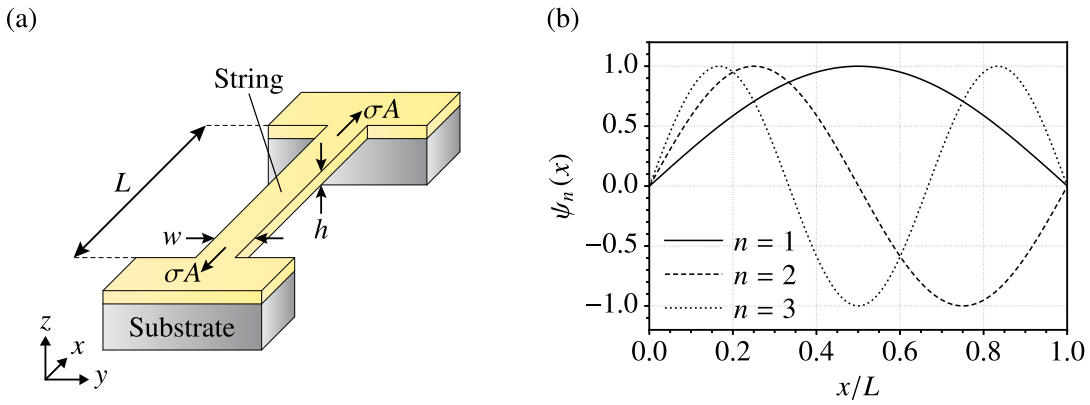

Figure 2.2: Mechanical vibrations of a string resonator. (a) Illustration of a string resonator on a substrate, showing how the length L, width w, and thickness h of the string are defined. The string is subjected to a pulling force $N = \sigma A$, where σ is the tensile stress and $A = wh$ the cross-sectional area. (b) Analytical calculations of the mode shape of the first three bending modes of a string resonator according to Equation (2.37).

2.1.3 Free Bending Vibration of Membranes

The two-dimensional equivalents to bridges and strings are called plates and membranes (also called drums), respectively. In the case of a plate, the flexural rigidity of the structure dictates its mechanical properties, while for a membrane, the tensile stress is the dominating factor. Only membranes will be given further attention here, specifically the case of rectangular membranes. The derivation given here is based predominantly on Section 1.1.3 in [16]. Assuming once again a linear elastic material, the equation of motion of a rectangular membrane is given by the two-dimensional wave equation [52, 53]

$$\sigma \nabla^2 u - \rho \frac{\partial^2 u}{\partial t^2} = 0, \tag{2.39}$$

which can be solved, assuming the membrane is simply supported, by separation into temporal and spatial terms. For any specific mode, the solution can be written as

$$u_{nj}(x, y, t) = \psi_{nj}(x, y) \cos\left(\omega_{nj} t\right), \tag{2.40}$$

with a sinusoidal mode shape function given as

$$\psi_{nj}(x, y) = u_{0,nj} \sin\left(\frac{n\pi x}{L_x}\right) \sin\left(\frac{j\pi y}{L_y}\right). \tag{2.41}$$

Here, n and j are the modal numbers, L_x and L_y are the side lengths of the membrane in the x- and y-directions, respectively, and ω_{nj} the eigenfrequency of mode (n, j). Inserting

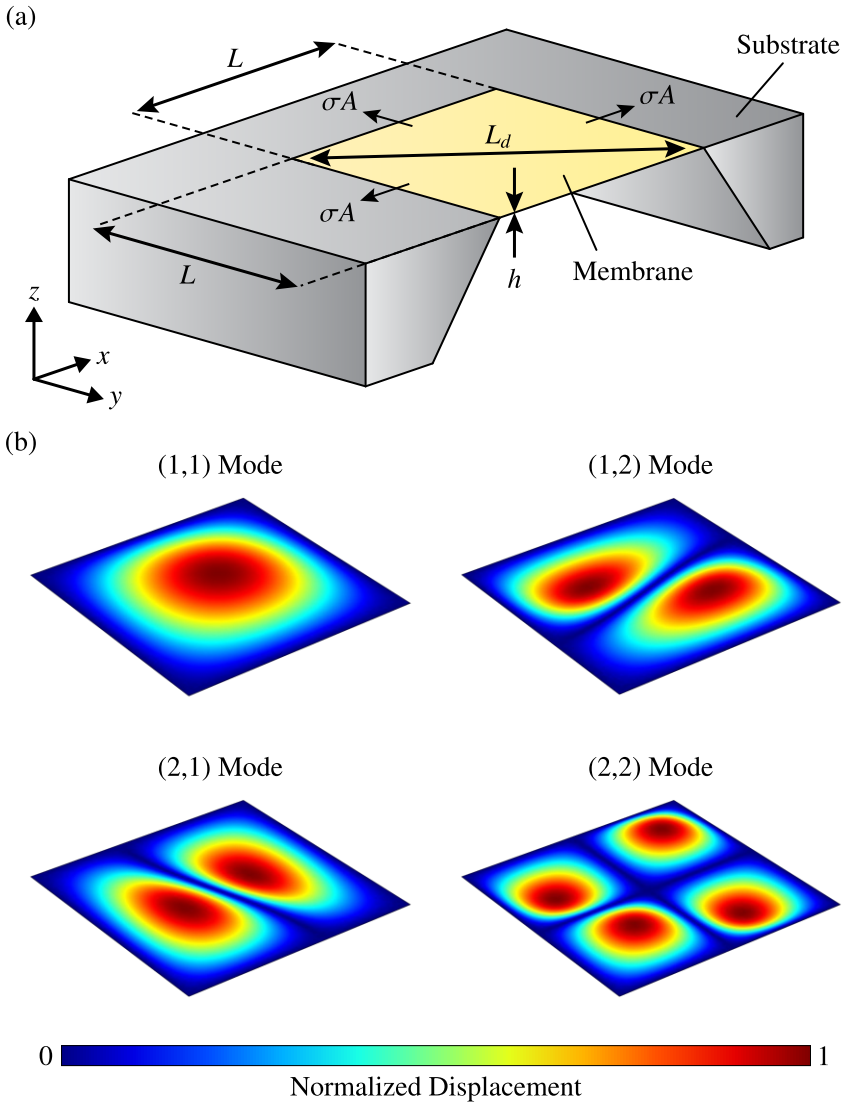

Figure 2.3: Mechanical modes of square membrane resonators. (a) Illustration of a square membrane on a substrate, highlighting the definitions of side length L, thickness h, and diagonal length L_d. (b) Finite element method simulated mode shape of the (1,1), (1,2), (2,1), and (2,2) bending modes of a square membrane.

Equation (2.40) into Equation (2.39) gives the eigenfrequency of a membrane

$$\omega_{nj} = \sqrt{\frac{\sigma}{\rho}} \sqrt{\left(\frac{n\pi}{L_x}\right)^2 + \left(\frac{j\pi}{L_y}\right)^2}, \tag{2.42}$$

which, assuming a square membrane where $L_x = L_y = L$, reduces to

$$\omega_{nj} = \frac{\pi\sqrt{n^2 + j^2}}{L}\sqrt{\frac{\sigma}{\rho}}. \tag{2.43}$$

Further converting this expression to temporal frequencies results in

$$f_{nj} = \frac{\omega_{nj}}{2\pi} = \frac{\sqrt{n^2 + j^2}}{2L}\sqrt{\frac{\sigma}{\rho}}. \tag{2.44}$$

Figure 2.3(a) displays a schematic of a square membrane on a substrate. While the mode shapes of membranes can be approximated analytically, finite element method (FEM) simulations provide a more accurate representation of the actual mode shape and is therefore used here instead [16]. FEM simulations of the (1,1), (1,2), (2,1), and (2,2) bending modes of a square membrane are shown in Figure 2.3(b). How these simulations are performed will be described in Section 3.4.1.

2.2 Dissipation Mechanisms of Nanomechanical Resonators

In Section 2.1.1, the quality factor was introduced, shown to directly increase both the maximum displacement and sharpness of the amplitude response of a resonator. Physically, it is defined as the total energy of a mechanical system divided by the energy lost during one cycle of vibration. This section serves to introduce the different dissipation mechanisms causing the energy loss. In general, multiple mechanisms can cause dissipation of energy for a system at the same time, each loss mechanism characterized by its own Q [19]. The most prominent sources of dissipation for the resonators investigated here include *gas damping* (Q_{gas}), *radiation loss* (Q_{rad}), and *intrinsic loss* (Q_{int}), and the total mechanical quality factor can be found by adding each dissipation mechanism according to [16]

$$\frac{1}{Q} = \frac{1}{Q_{\text{gas}}} + \frac{1}{Q_{\text{rad}}} + \frac{1}{Q_{\text{int}}}. \tag{2.45}$$

Additional sources of loss also exist, such as *electrical charge damping* [54] and *Eddy current losses* [55, 56], both of which are of no relevance to the resonators studied here and therefore not given any further attention.

2.2.1 Gas Damping

This section deals with the energy loss resulting from the interaction of a mechanical resonator with a surrounding gas, which is conveniently labeled gas damping. It belongs to a class of loss mechanisms called *medium interaction losses*, which includes both liquid and gas damping. The effect of immersing a resonator in a liquid, including the dependency on the viscosity of the liquid, has been theoretically modeled, mainly for cantilever beams employed for atomic force microscopy [57–60]. Since no measurements presented here were performed on resonators immersed in liquids, focus will be on gas damping exclusively.

The influence of gas damping depends not only on the pressure of the gas surrounding the resonator but also on the geometry and frequency of the resonator itself [61–64]. When discussing analytical models that describe gas damping, it is important to note the different regimes existing depending on the pressure of the surrounding gas. Two overall regimes emerge, which are called the *ballistic regime* and *fluidic regime*. A common quantity used to separate the two regimes is called the *Knudsen number*, Kn, which is the ratio of the mean free path of the surrounding gas λ_f to the characteristic length scale of the resonator L_r [62, 65, 66]

$$Kn = \frac{\lambda_f}{L_r}. \tag{2.46}$$

As an example, for a string resonator, L_r can be set equal to both the length, width, or thickness of the string, though the size transverse to the direction of motion is most often chosen [65]. However, in the case of squeeze-film damping, which will be discussed further below, L_r would refer to the gap between the resonator and the nearby surface. The mean free path can be written as

$$\lambda_f = \frac{k_\mathrm{B} T}{\sqrt{2}\pi d_\mathrm{gas}^2} \frac{1}{p}, \tag{2.47}$$

where k_B is the Boltzmann constant, T is the temperature, d_gas is the diameter of the gas particles, and p is the pressure. If the mean free path of the gas molecules is shorter than the characteristic length of the resonator, meaning $Kn < 1$, then the system is said to be in the fluidic regime, while in the opposite case, where $Kn > 1$, the system is in the ballistic regime. The fluidic regime typically occurs at larger pressures, where the air can be modelled as a viscous fluid. Given that nearly all results presented in this thesis were performed at low vacuum pressures, meaning at pressures far below the fluidic regime, only models describing the ballistic regime are provided below.

In the ballistic regime, the fluidic assumption breaks down and interaction with individual

gas molecules has to be modeled. The energy loss in this regime occurs due to momentum transfer between the surrounding gas and the resonator. Depending on the direction of gas particles relative to the motion of the resonator, energy will either be transferred to or taken from the resonator. Since more particles collide with the frontside of the resonator than the backside, an overall energy loss will occur. With this in mind, two different scenarios exist, namely an isolated resonator in vacuum, which is limited by *drag-force damping* [67], and a resonator in close proximity to an underlying substrate, which is limited by *squeeze-film damping* [68]. For a resonator limited by drag-force (df) damping, the Q can be defined as [67]

$$Q_{\text{gas,df}} = \frac{\rho h \omega_0}{4} \sqrt{\frac{\pi}{2}} \sqrt{\frac{R_{\text{gas}} T}{M_m}} \frac{1}{p}, \tag{2.48}$$

with ω_0 being the eigenfrequency of the mode, R_{gas} the universal molar gas constant, and M_{m} the molar mass of the gas. Though Equation (2.48) was derived for an isolated plate in vacuum, it has been shown to be valid for flexible beams as well [69]. In the case of squeeze-film (sf) damping, a theoretical expression for the quality factor of plates exists as well and is given as [68]

$$\begin{aligned} Q_{\text{gas,sf}} &= 16\pi \frac{d_0}{L_p} Q_{\text{gas,df}} \\ &= (2\pi)^{3/2} \rho h \omega_0 \frac{d_0}{L_p} \sqrt{\frac{R_{\text{gas}} T}{M_m}} \frac{1}{p}. \end{aligned} \tag{2.49}$$

Here, d_0 is the distance between the resonator and the substrate, and L_p is the peripheral length of the resonator. Both of these models predict a linear dependence of Q on the gas pressure. In reality, where multiple damping mechanisms coexist simultaneously, the p-dependence is less straightforward, as shown in Figure 2.4. Measured Qs of a nanomechanical string resonator made of the photoresist SU-8 are shown, with the data taken from [63]. The pressure at which $Kn = 1$ has been marked on the plot as well. As the pressure is reduced, the expected linear behavior is observed down to $p \sim 1$ mbar. At lower pressures, a plateau is reached, which shows a transition to a regime where intrinsic losses dominate. Given that both Equations (2.48) and (2.49) were derived for the case of plates, a string resonator can be modeled by defining a fit parameter c_1, and then fitting the data with a function of the type

$$Q^{-1} = Q_{\text{int}}^{-1} + c_1 p, \tag{2.50}$$

with such a fit included in Figure 2.4. The fit can be observed to describe the data accurately at lower pressures but starts to deviate for $Kn < 1$, at which point the assumptions of the ballistic regime break down.

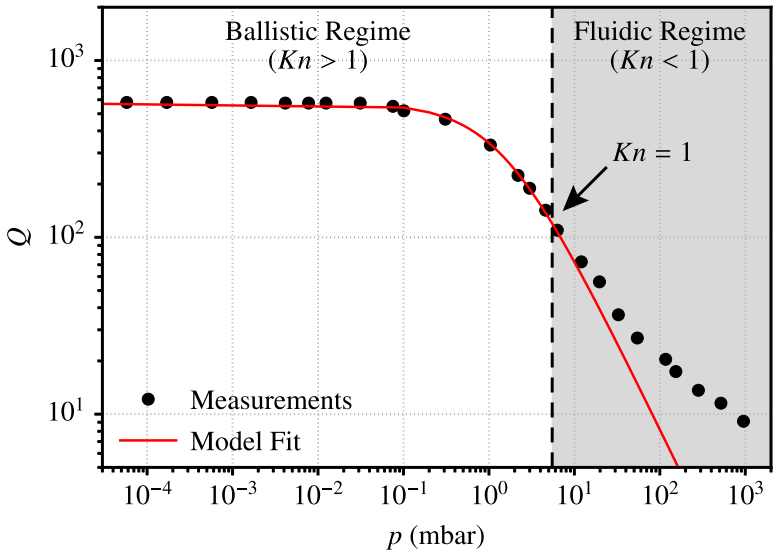

Figure 2.4: Measured quality factors versus pressure for a nanomechanical SU-8 string resonator along with a fit to Equation (2.50). The vertical dashed line indicates the pressure at which the Knudsen number $Kn = 1$. Figure adapted from Figure 2.4 in [16] and based on data taken from [63].

2.2.2 Radiation Loss

During vibration of a mechanical resonator, energy can be lost through phonons tunneling out of the resonator and into the substrate, which is typically labeled acoustic radiation loss or clamping loss in the literature [33]. The amount of energy loss is highly dependent on the mechanical mode as well as the mounting conditions of the chip during measurements [38, 42, 44]. Given this dependency on the chip mounting, existing analytical models typically only serve as approximations rather than accurate estimates of the quality factor. Nonetheless, presenting some of these models can increase the understanding of radiation losses. This section is based predominantly on Section 4.2 in [33].

Analytical models describing radiation losses have been developed for a variety of mechanical geometries [16]. A general proportionality factor for elastic wave transmission from a beam into a support structure can be written as [70]

$$Q_{\mathrm{rad}}^{-1} \propto \frac{v_g}{L\omega}\mathcal{T}_n, \tag{2.51}$$

with the group velocity of sound v_g and energy transmission coefficient $\mathcal{T}_n$ from the nth mode of a beam into the support. For the specific case of singly clamped beams, or cantilevers,

analytical models for the fundamental out-of-plane mode have been derived. Defining a finite base thickness h_b, assumed to be of the same material as the cantilever and significantly thinner than the propagating elastic waves, radiation loss can be expressed as [71]

$$Q_{\text{rad}}^{-1} = \gamma_{\text{thin}} \frac{w}{L} \left(\frac{h}{h_b} \right)^2 . \tag{2.52}$$

Here, γ_{thin} is a unitless factor weakly dependent on Poisson's ratio ν. For example, for $\nu = 0.3$, a $\gamma = 0.95$ can be calculated. Here, it is important to note the $Q_{\text{rad}} \propto L/w$ relation, which is a general observation made for the out-of-plane modes of both cantilevers, as well as doubly clamped beams [70, 72]. For in-plane modes, a $(w/L)^3$ relation has been shown [70, 73]. In the opposite regime, where the base is significantly thicker than the propagating elastic waves, radiation loss for a cantilever is given as [71]

$$Q_{\text{rad}}^{-1} \approx \gamma_{\text{thick}} \frac{w}{L} \left(\frac{h}{L} \right)^4 , \tag{2.53}$$

with γ_{thick} another unitless factor dependent on Poisson's ratio (for $\nu = 0.3$, $\gamma_{\text{thick}} = 0.31$). The equations presented here would suggest that radiation losses in beams can be minimized by working with very long and slender beams and by using very thick substrates.

In the case of stressed resonators, analytical models have been developed as well. The theoretical framework for high-stress membranes was initially developed by Wilson-Rae *et al.*, showing a harmonic frequency dependence [74]. For certain modes, it was shown how destructive interference of waves could lead to a suppression of radiation losses. Based on the general expression for the radiation loss limited Q developed by Wilson-Rae *et al* [74]., Villanueva *et al.* then showed the asymptotic limit for a square membrane, which is given as [48]

$$Q_{rad} \approx 1.5 \alpha_{\text{fit}} \frac{\rho_s}{\rho_r} \eta^3 \frac{n^2 j^2}{(n^2 + j^2)^{3/2}} \frac{L}{h}, \tag{2.54}$$

where ρ_r and ρ_s are the mass densities of the resonator and substrate material, respectively, and α_{fit} is a fitting parameter accounting for substrate imperfections, which, assuming a semi-infinite substrate, should be unity ($\alpha_{\text{fit}} = 1$). The factor η corresponds to the acoustic mismatch (phase velocity ratio) between a semi-infinite substrate and the resonator, and is approximately given as

$$\eta \approx \sqrt{\frac{E_s \rho_r}{\sigma \rho_s}}. \tag{2.55}$$

An inverse relation to the tensile stress can be observed, meaning that low-stress structures actually suffer less from radiation losses. Furthermore, Equation (2.54) shows how radiation loss is suppressed for harmonic modes ($n = j$) and that Q_{rad} increases for higher-order modes. These observations are of great importance to the results discussed in Chapter 5.

Various methods have been developed to suppress radiation losses, the most simple of which being to change the chip mounting conditions [38, 42, 44]. Additionally, embedding the mechanical resonators inside phononic crystals has been a successfully employed method to suppress radiation losses [75, 76]. By designing phononic crystals with bandgaps matching the eigenfrequency of the investigated mode, the tunneling of phonons into the substrate is prohibited and the Q therefore increased. Alternatively, the phononic crystal can be engineered directly into the resonator, which has additional benefits for the Q, as will be discussed further in Section 2.2.4.3 [39, 77].

2.2.3 Intrinsic Loss

The previous two sections dealt with so-called extrinsic losses, i.e. resulting from environmental conditions of the resonator. Now, attention is turned toward the intrinsic losses, which concerns loss mechanisms internal to the resonator. Given that a number of different internal loss mechanisms exist [16, 19, 32, 33], the section will only describe losses that are of relevance to the work presented in this thesis. The focus will be on dissipation occurring due to the irreversible motion of atoms during vibration, which is named *friction losses*. This loss mechanism is first described analytically using the *standard linear solid model*, also known as the Zener model [78, 79]. Afterwards, it is shown how the intrinsic quality factor is limited by surface friction in thin resonators. The derivation and associated discussion presented here is based mainly on [21] and [33].

2.2.3.1 Standard Linear Solid Model

In order to model the internal friction, the resonator is assumed to be anelastic, i.e. a viscous solid that fully recovers its initial state after deformation. An assumption of this model is that the dissipation is linear and independent of the vibrational amplitude. The model further assumes that the deformation induced stress σ and strain ϵ are not perfectly in phase, but have a phase lag relative to one another resulting from mechanical relaxation. One can then add this relaxation to Hooke's law, which is now written as [21]

$$\sigma = E\epsilon \rightarrow \sigma + \tau_\sigma \dot{\sigma} = E_{\mathrm{r}} \left(\epsilon + \tau_\epsilon \dot{\epsilon}\right), \tag{2.56}$$

where E_r is the *relaxed Young's modulus*, while τ_σ and τ_ϵ are the relaxation times of the stress and strain, respectively. Assuming a harmonic stress and strain variations, these can be written as

$$\sigma = \sigma_0 e^{i\omega t} \tag{2.57}$$

$$\epsilon = \epsilon_0 e^{i\omega t}, \tag{2.58}$$

with ω being the frequency of vibration. Inserting these expression for the stress and strain into Equation (2.56), it turns out that the Young's modulus will be complex and frequency dependent

$$E = E_r \frac{1 + i\omega\tau_\epsilon}{1 + i\omega\tau_\sigma}. \tag{2.59}$$

Based on this equation, two frequency extremes can be identified. For this purpose, the mean relaxation time $\overline{\tau} = \sqrt{\tau_\sigma \tau_\epsilon}$ is defined. At low frequencies, $\omega\overline{\tau} \ll 1$, and the Young's modulus is equal to the relaxed modulus, $E = E_r$. At high frequencies, $\omega\overline{\tau} \gg 1$, resulting in the so-called *unrelaxed Young's modulus* $E = E_u = E_r(\tau_\epsilon/\tau_\sigma)$. In between these extremes is a regime, where the Young's modulus is complex and can be written as

$$E = E_{\text{eff}}\left(1 + \frac{i\omega\overline{\tau}}{1 + \omega^2\overline{\tau}^2}\Delta\right), \tag{2.60}$$

with $\Delta = (E_u - E_r) / \sqrt{E_u E_r}$ being the fractional modulus difference. The real and imaginary parts of the Young's modulus in Equation (2.60) can be shown to be

$$E_{\text{real}} = E_{\text{eff}} = E_r \frac{1 + \omega^2\overline{\tau}^2}{1 + \omega^2\tau_\sigma^2} \tag{2.61}$$

$$E_{\text{imag}} = E_r \frac{\omega\overline{\tau}}{1 + \omega^2\tau_\sigma^2}\Delta. \tag{2.62}$$

In order to define an internal friction quality factor, the physical definition provided in Equation (2.17) is revisited. The energy dissipated per cycle of vibration can be calculated based on rewriting the stress and strain expressions in Equations (2.57) and (2.58), respectively, resulting in

$$\Delta W = \oint_0^{2\pi/\omega} \Re(\sigma)\,\Re(\dot{\epsilon})\,dt = \pi\epsilon_0^2 E_{\text{imag}}, \tag{2.63}$$

where the $\mathfrak{R}$-labels denote the real part of the function. Similarly, the maximum strain energy is given by integrating over a quarter of a cycle

$$W = \oint_0^{\pi/2\omega} \mathfrak{R}(\sigma)\,\mathfrak{R}(\dot{\epsilon})\,dt = \frac{1}{2}\epsilon_0^2 E_{\text{real}}. \tag{2.64}$$

The friction loss can then be calculated to be

$$Q^{-1}_{\text{friction}} = \frac{\Delta W}{2\pi W} = \frac{E_{\text{imag}}}{E_{\text{real}}} = \frac{\omega\bar{\tau}}{1+\omega^2\bar{\tau}^2}\Delta. \tag{2.65}$$

Hence, Δ quantifies the magnitude of the dissipation, while the $\omega\bar{\tau}/\left(1+\omega^2\bar{\tau}^2\right)$ term determines the dynamics of the dissipation mechanism. As a function of frequency, Q^{-1}_{friction} would display a peak, called a Debye peak, around $\omega\bar{\tau} = 1$, in which case $Q^{-1}_{\text{friction}} = 1/2\Delta$. Friction losses can be further interpreted by studying the frequency extremes. For very low frequencies, $\omega\bar{\tau} \ll 1$, the system remains in equilibrium and little energy is dissipated. In the high frequency regime, $\omega\tau \gg 1$, the system has no time to relax and little energy is again dissipated. Only when the frequency matches the internal relation rate, where $\omega\bar{\tau} = 1$, does the system display significant dissipation [80].

2.2.3.2 Surface Friction

In Figure 1.1, it was shown how the quality factors generally deteriorate with reducing resonator dimensions. The reason behind this trend is the increased surface-to-volume ratio of smaller resonators, in which case losses on the resonator surface dominate the quality factor over the bulk losses. This loss mechanism is called *surface friction* and has been shown to be the limiting loss mechanism of a variety of nanomechanical resonator geometries and materials [48, 81]. Dissipation on the surface can occur for a number of reasons, including defects and impurities [48], adsorbates [82], free dangling bonds [83], surface roughness [32, 84], or surface oxidation [85, 86].

A theoretical description of surface friction exists for the case of cantilever resonators [81, 82]. In order to model surface friction, one can assume a complex surface Young's modulus $E_{\text{surf}} = E_{\text{surf,real}} + iE_{\text{surf,imag}}$, in a sense characterizing losses on the surface in the form of a surface layer with a Young's modulus E_{surf} and a thickness δ_{surf}. The energy lost per cycle can then be written as

$$\Delta W = \pi \int_V E_{\text{surf,imag}}\epsilon_m^2(\mathbf{r})\,dV, \tag{2.66}$$

where the volume integration is performed on the surface layers assumed to be on all sides of the cantilever. For a cantilever of rectangular cross section vibrating sinusoidally, the strain is

given according to

$$\epsilon_m(\mathbf{r}) = \frac{2z}{h}\epsilon_{\max}(x), \tag{2.67}$$

with $\epsilon_{\max}(x)$ being the maximum strain, which occurs along the top surface of the cantilever, while x and z indicate the position along the length and thickness of the cantilever, respectively. If δ_{surf} is much smaller than the dimensions of the cantilever, then Equation (2.66) can be written as a sum of surface integrals, resulting in

$$\Delta W = 2\pi\delta_{\text{surf}}E_{\text{surf,imag}}\left(w + \frac{h}{3}\right)\int_0^L \epsilon_{\max}^2(x)\,dx. \tag{2.68}$$

Given the assumption that dimensional parameters are far greater than the surface layer thickness, the stored energy is assumed to be the total elastic energy stored in the volume of the cantilever, which is given as

$$W = \frac{1}{6}whE_{\text{vol,real}}\int_0^L \epsilon_{\max}^2(x)\,dx, \tag{2.69}$$

where $E_{\text{vol,real}}$ is the real part of the bulk Young's modulus. The quality factor resulting from surface friction is then found to be

$$Q_{\text{surf}} = 2\pi\frac{W}{\Delta W} = \frac{wh}{2\delta_{\text{surf}}(3w+h)}\frac{E_{\text{vol,real}}}{E_{\text{surf,imag}}}. \tag{2.70}$$

For a wide cantilever, where $h \ll w$, Q_{surf} becomes proportional to the resonator thickness

$$Q_{\text{surf}} = \frac{1}{6\delta_{\text{surf}}}\frac{E_{\text{vol,real}}}{E_{\text{surf,imag}}}h. \tag{2.71}$$

Despite evidence of surface loss being a limiting source of dissipation for nanomechanical resonators, the exact contribution from the different sources of surface friction are not known. As such, no analytical model currently exists, which can predict the value of the loss Young's modulus $E_{\text{surf,imag}}$. Nonetheless, the specific case of surface friction of silicon nitride resonators has been investigated in more detail by Villanueva *et al.* [48]. The authors examined published intrinsic Qs of SiN resonators, in conjunction with resonators fabricated by the authors themselves. For both sets of Q_{int}-data, the linear dependence on resonator thickness predicted from Equation (2.71) could be shown in the thin resonator limit, while saturating to a limit set by bulk losses for thicker resonators. In this way, an approximate model for Q_{int} was found by fitting the measured data with the following function

$$Q_{\text{int}}^{-1} = Q_{\text{surf}}^{-1} + Q_{\text{vol}}^{-1}, \tag{2.72}$$

where Q_{vol}^{-1} quantifies the bulk/volume losses, which most likely arise from internal friction discussed in Section 2.2.3.1. From the fit, a $Q_{\text{vol}} \approx 28000 \pm 2000$ could be extracted, while the Q resulting from surface friction was given by $Q_{\text{surf}} = \beta h$, with the factor $\beta = (6 \pm 4) \times 10^{10}$ m^{-1}. The uncertainty in β was estimated through variations in dimensions and tensile stress from sample to sample. Equation (2.72) has been plotted in Figure 2.5, along with the limits of Q_{int} set by Q_{vol} and Q_{surf}. Additionally, the grey-shaded region displays the uncertainty in Q_{int} based on the uncertainty in Q_{surf}. It can be observed how surface losses completely dominate the intrinsic losses for very thin resonators.

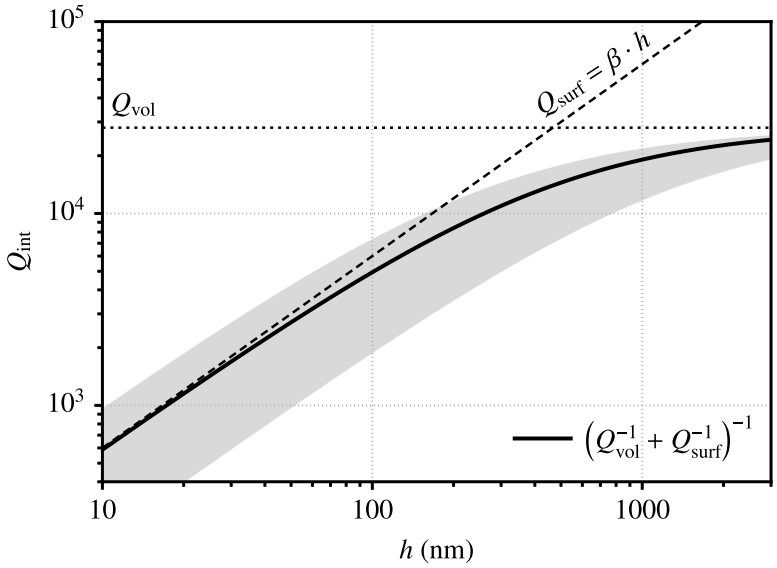

Figure 2.5: Intrinsic quality factor in the surface loss limited regime. Theoretical calculations of $Q_{\text{int}} = \left(Q_{\text{vol}}^{-1} + Q_{\text{surf}}^{-1}\right)^{-1}$ versus resonator thickness are shown, along with calculations of the limits set by Q_{surf} and Q_{vol}. The grey-shaded region indicates the uncertainty of Q_{int}, which arises from the uncertainty in Q_{surf}. Figure is inspired by Figure 2(b) in [48].

2.2.4 Dissipation Dilution

The derivation and discussion presented here are based mainly on Section 2.3.2 in [16]. Now that the dominant extrinsic and intrinsic loss mechanisms relevant for the resonators studied here have been presented, it is time to discuss a physical phenomenon occurring in stressed nanomechanical resonators. Already in Chapter 1, it was shown how stressed resonators deviate from the expected trend of reduced Q for smaller resonator dimensions. The effect responsible for this observation is named *dissipation dilution*. Only recently did this effect

begin to receive a significant amount of attention in the nanomechanical resonators field [34], but the effect was already studied in pendulums used for gravitational wave interferometers by Saulson *et al.* in the 90s [87–89]. The authors showed how the Q of such pendulums was much larger than their intrinsic loss limits, with the Q increased by the ratio between the energy stored in the gravitational field and the flexing of the wire. By adding more energy to the system through the gravitational field, without affecting the intrinsic losses of the pendulums, the Q could be enhanced. How this effect was related to the tension added to the wire holding the pendulum, resulting from the pendulum mass, was also established analytically by González and Saulson [88]. Given that the gravitational field works as a lossless potential, adding energy to the system without influencing its dissipation, the effect was given the name dissipation dilution.

In the same period as the investigations performed by the Saulson group, Berry *et al.* made findings in support of dissipation dilution in thin silicon and polymer membranes [90]. Based on these observations, Berry developed an analytical model describing tensioned strings [91, 92], where the lossless potential is represented by a static tensile stress instead of the gravitational force employed by the Saulson group. However, while Berry's theory took nonlinear damping into account, it did not include the local bending at the string clamping (discussed further below) and was therefore incomplete compared to the full model developed by the Saulson group [88]. Nonetheless, both of these groups laid the foundation for dissipation dilution, which is now being actively employed in the pursuit of ultrahigh-Q mechanical resonators.

The introduction of the dissipation dilution effect to the nanomechanical resonators field occurred in 2006 after Verbridge *et al.* observed inexplicably large Qs in stressed string resonators [34]. It was shown how the Q was increased for increased tension [35], and Qs greater than one million were observed at room temperature both for nanomechanical strings [36] and membranes [41]. These observations were later related to the dissipation dilution effect by Schmid *et al.* in 2008 [63], again showing how the increased energy stored in the tension diluted the intrinsic losses of the resonators. By now, the theoretical framework for dissipation dilution developed by Saulson *et al.* and Berry *et al.* has been successfully employed to describe the behaviour of nanomechanical string resonators by both Untereithmeier *et al.* [37] and Schmid *et al.* [38], while that of membranes was developed by Yu *et al.* [43]. A generalized dissipation dilution theory has also recently been provided by Fedorov *et al.* [93].

In order to understand how the dissipation dilution effect comes about, one has to revisit the fundamental definition of the quality factor given in Equation (2.17). During vibration of a mechanical resonator, energy is stored in the bending W_{bend} and the elongation of resonator W_{elong}, while energy is also dissipated due to bending ΔW_{bend} and elongation ΔW_{elong} as well.

In the case of stressed resonators, energy will additionally be stored in the tension, which is labeled W_{tensile}. This can be interpreted as the stored elastic energy required to vibrate the string against the tensile force, acting as the lossless potential equivalent to the gravitational field for the pendulums [88]. With these energies in mind, one can rewrite Equation (2.17) into [16]

$$Q = 2\pi \frac{W_{\text{tensile}} + W_{\text{bend}} + W_{\text{elong}}}{\Delta W_{\text{bend}} + \Delta W_{\text{elong}}}. \tag{2.73}$$

In order to quantify the dissipation dilution effect, one first assumes the mechanical behavior to be dominated by the tensile stress. Then, by equating the dissipation resulting from bending and elongation of the resonator and setting them both equal to the intrinsic losses, Equation (2.73) can be written as

$$Q \approx \alpha_{\text{dd}} Q_{\text{int}}, \tag{2.74}$$

where α_{dd} is called the *dissipation dilution factor*

$$\alpha_{\text{dd}} = \left[\frac{W_{\text{bend}}}{W_{\text{tensile}}} + \frac{W_{\text{elong}}}{W_{\text{tensile}}} \right]^{-1}. \tag{2.75}$$

For $\alpha_{\text{dd}} \gg 1$, as is expected for high-stress strings and membranes [16], the stress can be observed to dilute the intrinsic losses and therefore enhance the quality factor. In the following, expressions for the dissipation dilution factor will be derived for both strings and membranes, which can be shown to depend on physical parameters of the resonator. Afterwards, the soft clamping effect is introduced and discussed, which represents the dissipation dilution effect at its optimum.

2.2.4.1 Strings

In order to derive the dissipation dilution effect for strings, one can employ the displacement function $u(x) = u_0 \psi_n(x)$ combined with the mode shape function provided in Equation (2.37). Keeping this in mind, the energy stored in the tension is given as

$$\begin{aligned} W_{\text{tensile}} &= \frac{1}{2}\sigma A \int_0^L \left(\frac{\partial u}{\partial x} \right)^2 dx \\ &\approx \frac{1}{4} u_0^2 \sigma A L \beta_\sigma^2, \end{aligned} \tag{2.76}$$

with β_σ the wavenumber given in Equation (2.28). As such, the exponential edge-correction term appears to have negligible effect on the tensile energy. The energy stored in the string

bending can be calculated as

$$\begin{aligned} W_{\text{bend}} &= \frac{1}{2} EI_y \int_0^L \left(\frac{\partial^2 u}{\partial x^2}\right)^2 dx \\ &\approx \underbrace{\frac{1}{4} u_0^2 EI_y \beta_\sigma^4 L}_{\text{sine shape}} + \underbrace{\frac{1}{2} u_0^2 EI_y \beta_\sigma^2 \beta_E}_{\text{edge shape}}, \end{aligned} \tag{2.77}$$

with the wavenumber β_E coming from the flexural rigidity of the string (see Equation (2.34)). In a similar fashion, the energy stored in the elongation can be approximated as

$$\begin{aligned} W_{\text{elong}} &= \frac{1}{8} EA \int_0^L \left(\frac{\partial u}{\partial x}\right)^4 dx \\ &\approx \frac{3}{64} u_0^4 EAL \beta_\sigma^4. \end{aligned} \tag{2.78}$$

While the elongation term can once again be approximated by a term coming from the sinusoidal motion of the string, the bending consists not only of such a sine term, but also of a second term coming from the bending at the string clamping. By inserting the energies approximated in Equations (2.76), (2.77), and (2.78) into the Equation (2.75), one arrives at

$$\alpha_{\text{dd,string}} = \left[\underbrace{\left(\frac{\beta_\sigma}{\beta_E}\right)^2 + \frac{2}{\beta_E L}}_{\text{bending}} + \underbrace{\frac{9}{4}\left(\frac{u_0}{h}\right)^2 \left(\frac{\beta_\sigma}{\beta_E}\right)^2}_{\text{elongation}} \right]^{-1}. \tag{2.79}$$

The bending energy terms can be seen to be independent of the vibrational amplitude u_0, while a dependency can be seen for the elongation term. Even though this observation indicates that the dissipation dilution effect depends on the vibrational amplitude, it is only of concern for very thin resonators, where the amplitude is comparable to the resonator thickness, or when actuating a vibration at very large amplitudes. When working with resonators having $h \gg u_0$ and remaining in the linear vibration regime, both conditions applying to the investigations presented in this thesis, one can dismiss the elongation term in Equation (2.79). Further assuming a rectangular cross-section, where I_y is defined according to Equation (2.23), the dissipation dilution factor of a string becomes

$$\alpha_{\text{dd,str}} = \left[\underbrace{\frac{(n\pi)^2}{12} \frac{E}{\sigma} \left(\frac{h}{L}\right)^2}_{\text{sine shape}} + \underbrace{\frac{1}{\sqrt{3}} \sqrt{\frac{E}{\sigma}} \frac{h}{L}}_{\text{edge shape}} \right]^{-1}, \tag{2.80}$$

which, by inserting this factor into Equation (2.74), results in the following quality factor for strings

$$Q_{\text{str}} = \alpha_{\text{dd,str}} Q_{\text{int}} = \left[\frac{(n\pi)^2}{12} \frac{E}{\sigma} \left(\frac{h}{L} \right)^2 + \frac{1}{\sqrt{3}} \sqrt{\frac{E}{\sigma}} \frac{h}{L} \right]^{-1} Q_{\text{int}}. \tag{2.81}$$

This expression is similar to that derived for pendulums by González and Saulson [88]. Inspecting the equation, it is clear that the edge shape term is the limiting factor to the dissipation dilution effect for resonators with $h \ll L$ [37, 38]. The bending at the clamping creates strain, which increases the dissipation, the origin of which can be traced back to the friction losses mentioned in Section 2.2.3. This is more clearly understood by studying Figure 2.6. A schematic plot of the fundamental mode displacement is given in Figure 2.6(a), both for the case of the actual mode shape calculated using Equation (2.37) and a purely sinusoidal mode shape. Close to the clamping region, the two mode shapes deviate significantly, which highlights the importance of the edge shape term in the calculation of Q. The huge amount of bending near the clamping can be visualized more clearly by plotting the curvature of the displacement functions $\partial^2 u/\partial x^2$, which is shown in Figure 2.6(b). A sine-shaped displacement would predict zero bending near the clamping, while the actual mode shape shows a huge increase in bending for $x < L_c$, with L_c defined in Equation (2.38). Interestingly, this indicates that the Q of millimeter-sized strings is determined by a region less than 1 micrometer in size.

Higher-order modes generally display a reduced dissipation dilution effect due to the increased amount of antinodes. Nonetheless, for long strings, this reduction is still small and the sinusoidal term only really plays a large role for higher-order modes of short strings. The intrinsic losses, quantified by Q_{int} in Equation (2.81), have been shown to originate mainly from surface friction for resonators with thicknesses on the order of nanometers [48]. As such, one can insert Equation (2.72) into Equation (2.81) in order to fully predict the Qs of nanomechanical string resonators.

2.2.4.2 Membranes

The derivation of the dissipation dilution factor of membranes is done in a similar fashion to that of strings, namely by first calculating the different energies of the system and then inserting those expressions into Equation (2.75). One only has to take into account that the integrations now have to performed along both side lengths of the membrane. Without going into details of the derivation, assuming small vibrational amplitudes, the dissipation dilution

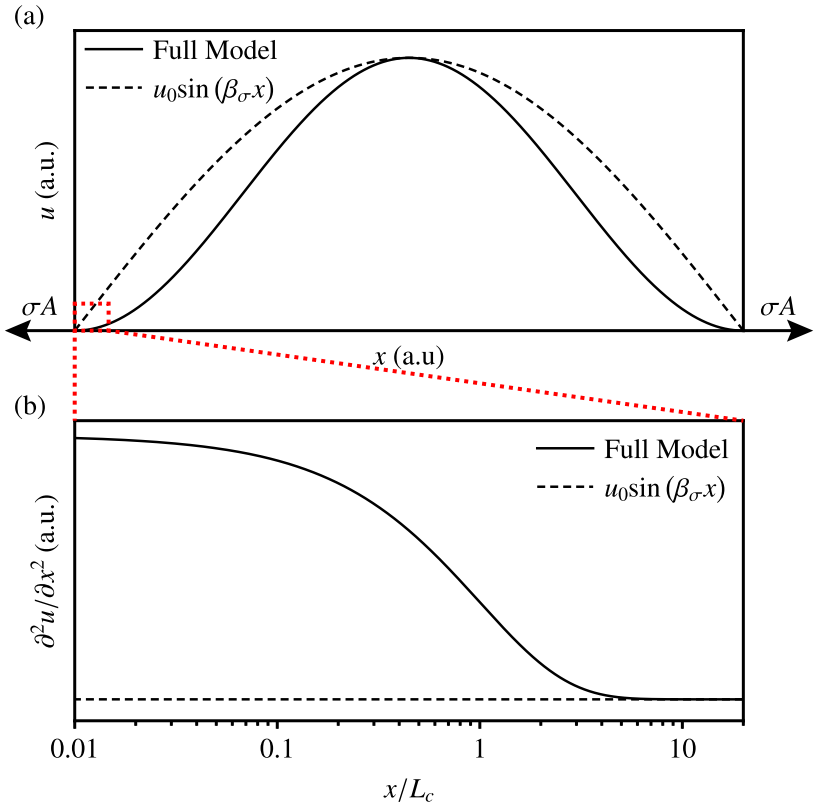

Figure 2.6: Limitations to the quality factor resulting from the dissipation dilution effect in strings. (a) Schematic comparison between the out-of-plane displacement function along the length of a string based on the full string model including the edge-correction term and that of a purely sinusoidal mode shape. The difference between the two cases has been exaggerated for clarity. (b) Calculated curvature for the two displacement functions near the clamping region of a string, with the position given in units of the decay length L_c defined in Equation (2.38).

factor of a rectangular membrane is given as

$$\alpha_{\mathrm{dd,mem}} \approx \left[\underbrace{\frac{D_P}{\sigma h}\pi^2 \left(\left(\frac{n}{L_x}\right)^2 + \left(\frac{j}{L_y}\right)^2 \right)}_{\text{sine shape}} + \underbrace{2\sqrt{\frac{D_P}{\sigma h}} \frac{L_y \left(\frac{n}{L_x}\right)^2 + L_x \left(\frac{j}{L_y}\right)^2}{L_x L_y \left(\left(\frac{n}{L_x}\right)^2 + \left(\frac{j}{L_y}\right)^2 \right)}}_{\text{edge shape}} \right]^{-1}, \tag{2.82}$$

with the flexural rigidity of a plate defined as

$$D_P = \frac{Eh^3}{12\,(1-\nu^2)}. \tag{2.83}$$

Assuming a square membrane ($L_x = L_y = L$) and zero transversal strain ($\nu = 0$), Equation (2.82) can be further simplified to

$$\alpha_{\mathrm{dd,mem}} \approx \left[\underbrace{\frac{\left(n^2+j^2\right)\pi^2}{12}\frac{E}{\sigma}\left(\frac{h}{L}\right)^2}_{\text{sine shape}} + \underbrace{\frac{1}{\sqrt{3}}\sqrt{\frac{E}{\sigma}}\frac{h}{L}}_{\text{edge shape}}\right]^{-1}, \tag{2.84}$$

which evidently is very similar to the expression for a string given in Equation (2.80).

2.2.4.3 Soft Clamping

As should be clear at this point, the limiting factor of the dissipation dilution effect for both strings and membranes is the large bending at the resonator clamping. For this reason, effort has been made recently to reduce this effect and thus enhance the dissipation dilution factor. In Section 2.2.2, it was briefly mentioned how phononic crystals (PnCs) could be engineered into a resonator in order to minimize radiation losses. While this method indeed produces the desired isolation of the resonator, it adds an additional benefit to the quality factor, which was first shown by Tsaturyan *et al.* [39]. The authors showed how, due to the phononic crystal pattern surrounding the investigated mechanical mode, the displacement would exponentially decay into the phononic crystal until reaching the outer rim of the membrane. In this way, the large bending associated with a sharp edge was shown to be reduced significantly and the Qs enhanced as a result. Given this smooth decay of the displacement, the effect was labeled *soft clamping*.

Soft clamping can occur in two dimensions by periodically engineering holes in a membrane [39] or in one dimension by a periodic altering of the width of a string [77]. The first is the approach employed in this thesis and will therefore be visualized now. An optical micrograph of a fabricated PnC membrane sample of the same design used by Tsaturyan *et al.* is shown in Figure 2.7. The PnC is formed by a hexagonal arrangement of the holes, with details of the design given in Section 3.4.3. At the center of the membrane, holes are displaced and removed, forming a defect in the center of the membrane. Mechanical modes with frequencies located inside the phononic bandgap will be localized to this defect and in this way display the soft clamping effect. The inset of Figure 2.7 shows a FEM simulation of the fundamental defect mode shape, highlighting its confinement to the central defect while decaying inside the PnC.

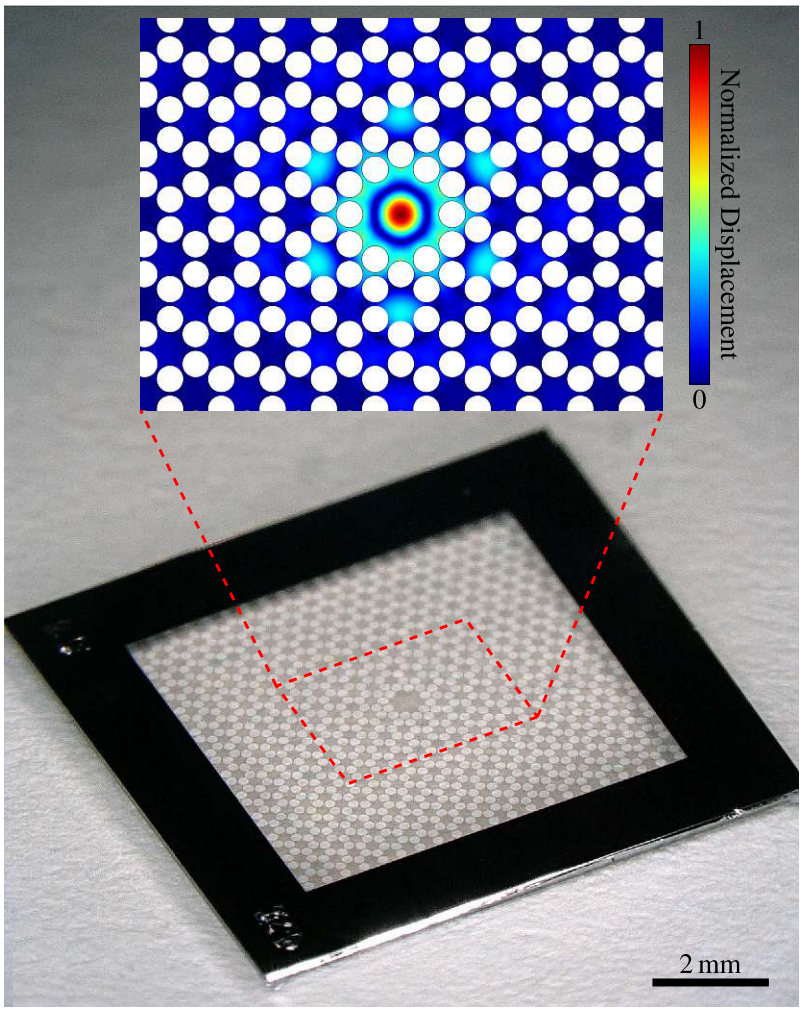

Figure 2.7: Localized modes in phononic crystal membranes. The figure shows an optical micrograph of an as-fabricated PnC membrane chip with a lattice constant $a = 340$ µm and lateral size $L \approx 7$ mm. The inset shows a finite element method simulation of the displacement pattern of the fundamental defect mode.

Further understanding of the soft clamping effect can be acquired by inspecting the displacement along the length of the membrane, with a simulated displacement pattern given in Figure 2.8(a). It can be observed how the displacement decays exponentially through the PnC, highlighted by means of exponential function fits of the displacement peaks. Given that the curvature serves to convey the amount of bending in a given structure, Figure 2.8(b) plots the normalized curvature along the length of a PnC membrane. For comparison, the curvature of a uniform membrane of equal frequency has been plotted as well. Evidently, the curvature is reduced substantially through the soft clamping effect, which results in an enhanced

dissipation dilution effect.

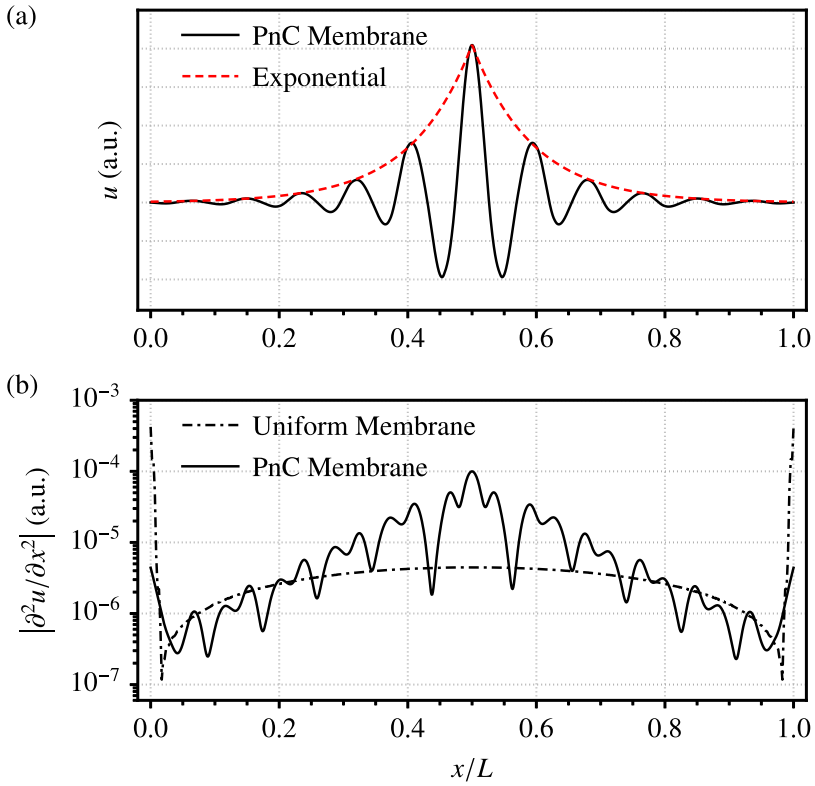

Figure 2.8: Soft clamping effect in localized defect modes of phononic crystal membranes. (a) Finite element method simulation of the displacement along the length of a PnC membrane. Exponential fits to the peaks of the displacement have been shown as well for clarity. (b) Simulated absolute curvature along the length of a PnC membrane and uniform square membrane of equal eigenfrequency. The line plots of the PnC displacement and curvature are polynomial fits to the simulated values for clarity.

In order to quantify the degree of Q-enhancement achieved through the soft clamping method, one can assume the edge shape term to be completely eliminated from the dissipation dilution factor. For square membranes, Equation (2.84) can be written as

$$\alpha_{\text{dd,mem-sc}} \approx \frac{12}{(n^2+j^2)\pi^2}\frac{\sigma}{E}\left(\frac{L}{h}\right)^2, \tag{2.85}$$

which is now limited only by the sinusoidal bending of the membrane. The ratio of Equations (2.85) to (2.84) would predict a potential two orders of magnitude Q-enhancement through soft clamping. This estimate is roughly in agreement with the observations made by Tsaturyan *et al.* [39]. A similar conclusion can be made for strings using the one-dimensional dissipation dilution factor (see Equation (2.80)). Even larger enhancements have

been achieved by strain engineering of softly clamped string resonators, where the investigated mode displayed stress values several factors larger than that of the as-deposited resonator material [40]. Using this approach, Qs greater than 800 million have been measured at room temperature, which remains a record in the nanomechanical resonators field.

2.3 Heat Transfer

One of the most promising applications of nanomechanical resonators is as thermal sensors [16]. The principle of detection for such sensors is a shift of the resonance frequency as the temperature changes, which is caused either by the temperature dependence of the Young's modulus $E(T)$ [94] or, for resonators under tension, a temperature-dependent tensile stress $\sigma(T)$ [95]. This section will only focus on introducing the latter case, as strained resonators are the focus of this thesis.

The response of resonators to temperature changes can be further divided into that resulting from ambient temperature changes and local heating of the resonator. Local heating, such as that achieved employing lasers, is at the heart of the application of strained resonators as photothermal sensors, where the absorption of radiation causes a local reduction of the stress and therefore a frequency detuning, as will be discussed further in Chapter 7 [96–101]. Given that all measurements presented here were conducted using lasers, only the local heating case will be introduced in this section.

When nanomechanical resonators are heated locally at the resonator center, the dominant mechanisms responsible for heat transfer are conduction and radiation, as illustrated in Figure 2.9. Analytical models exist for the cases of pure conduction-based transfer, while radiation needs to be evaluated numerically. Heat transfer in both strings and membranes will be discussed separately, which is of particular relevance to the results shown in Chapter 6 and Chapter 7, respectively. For both resonator geometries, the discussion is divided into a conduction and a radiation part in order to evaluate the influence of mechanisms separately. The concept of thermal responsivity is introduced here, which is an essential quantity for evaluating thermal sensor performance. It should be mentioned that convection is another source of heat transfer as well, which can dominate the thermal response at higher vacuum pressures [102]. However, since most measured data shown here was acquired at a high vacuum, convection will not be given any further attention.

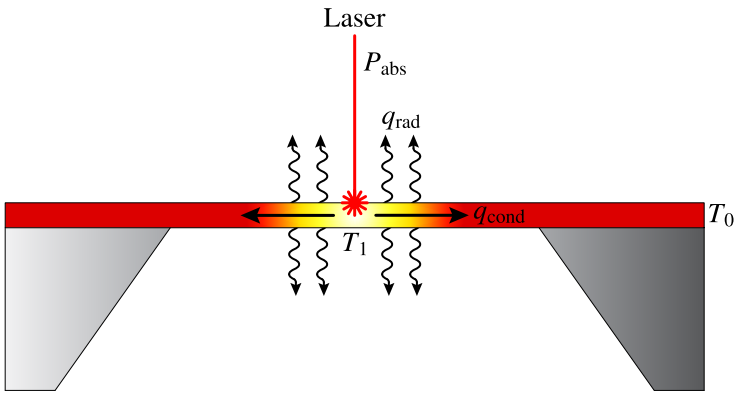

Figure 2.9: Heat transfer mechanisms in nanomechanical resonators for a central pointlike source such as a laser. An amount of light power P_{abs} is absorbed at the resonator center and the resulting heat can dissipate through thermal conduction q_{cond} and radiation q_{rad}. The temperatures at the center and frame of the resonator are T_1 and T_0, respectively, with the relation $T_1 > T_0$.

2.3.1 Strings

In the case of heat transfer dominated by conduction, analytical models have been developed for string resonators [97, 98]. These will be presented initially, before numerically examining the influence of radiative heat transfer.

2.3.1.1 Thermal Conduction

The derivation and notation shown in this section follows the supporting information of Yamada *et al.* [97]. In order to derive the thermal responsivity of strings for a local heat source, a power P_{abs} is assumed to be absorbed at the string center. A quasi one-dimensional situation is considered, where the temperature is assumed to be uniform across the cross-section of the string, while flowing out along the string length into the frame, which is fixed at a temperature T_0. The heat flux density $\mathbf{J}_q$ is governed by Fourier's law, which states that

$$\mathbf{J}_q = -\kappa \nabla T, \tag{2.86}$$

where κ is the thermal conductivity and ∇T the temperature gradient, with the negative sign indicating heat flow in the direction of decreasing temperature. The heat continuity equation gives the temporal and spatial evolution of the temperature according to

$$\begin{aligned} \rho c_p \frac{\partial T}{\partial t} &= -\nabla \cdot \mathbf{J}_q + q \\ &= \kappa \nabla^2 T + q \end{aligned} \tag{2.87}$$

with c_p being the specific heat capacity and q the heat dissipated per unit volume. Considering only the steady state situation, where $\nabla \cdot \mathbf{J}_q = 0$, except at the string center ($x = L/2$), a linear temperature distribution results, assuming the thermal conductivity to be constant along the string

$$T(x) = \begin{cases} T_0 + 2(T_1 - T_0)\, x/L, & \text{for } 0 \le x \le L/2 \\ T_0 + 2(T_1 - T_0)(L - x)/L, & \text{for } L/2 \le x \le L \end{cases} \tag{2.88}$$

Here, $T_1 = T(x = L/2)$ is the temperature at the center of the string. According to the heat continuity equation, the absorbed power at $x = L/2$ must equal the sum of heat fluxes in the remainder of the string

$$P_{\text{abs}} = A\kappa(T_1 - T_0)\left(\frac{1}{L/2} + \frac{1}{L - L/2}\right) = \frac{4A\kappa}{L}(T_1 - T_0), \tag{2.89}$$

with $A = wh$ being the cross-sectional area of a rectangular string. From Equation (2.88), it can be seen that the average temperature change along the length of the string is half the difference between T_1 and T_0. By isolating the temperature difference in Equation (2.89), the average temperature change can be written as

$$\Delta T = \frac{T_1 - T_0}{2} = \frac{P_{\text{abs}} L}{8A\kappa}. \tag{2.90}$$

With the power-dependent temperature field derived, the temperature-induced stress change can be calculated. The in-plane thermoelastic strain of the string is governed by

$$\epsilon(T) = \epsilon_0 - \alpha\Delta T, \tag{2.91}$$

where ϵ_0 is the built-in strain prior to heating, and α is the coefficient of thermal expansion of the string. Assuming the string can be described as a linear elastic material, the stress and strain are related via Hooke's law

$$\sigma(T) = E\epsilon(T) = E\epsilon_0 - \alpha E\Delta T = E\epsilon_0\left(1 - \frac{\alpha}{\epsilon_0}\Delta T\right) = \sigma_0\left(1 - \frac{\alpha E}{\sigma_0}\Delta T\right), \tag{2.92}$$

with $\sigma_0 = E\epsilon_0$ being the initial tensile stress. Inserting Equation (2.92) into Equation (2.31), the eigenfrequency of a string becomes

$$\omega_n(P_{\text{abs}}) = \frac{n\pi}{L}\sqrt{\frac{\sigma(T)}{\rho}} = \frac{n\pi}{L}\sqrt{\frac{\sigma_0}{\rho}}\sqrt{1 - \frac{\alpha E}{\sigma_0}\Delta T} = \omega_{n,0}\sqrt{1 - \frac{\alpha E}{\sigma_0 \kappa}\frac{P_{\text{abs}} L}{8A}}. \tag{2.93}$$

Here, $\omega_{n,0}$ is the eigenfrequency for no absorbed power, i.e. Equation (2.31). For small stress changes, Equation (2.93) can be approximated by a Taylor series approximation

$$\omega_n\left(P_{\text{abs}}\right) \approx \omega_{n,0}\left(1 - \frac{1}{16}\frac{\alpha E}{\sigma_0 \kappa}\frac{L}{A}P_{\text{abs}}\right). \tag{2.94}$$

Having established how the frequency is related to the absorbed power, it is time to introduce the concept of thermal responsivity, which is an essential parameter used to describe thermal sensor performance. In general, responsivity refers to the slope of the sensor output as a function of the measured input parameter [16]. In the case of nanomechanical thermal sensors, the thermal responsivity typically refers to the change in the resonance frequency as the temperature is changed. For local heating of a string resonator, the thermal responsivity is found by taking the derivative of Equation (2.94)

$$\mathscr{R} = \frac{\partial \omega_n\left(P_{\text{abs}}\right)}{\partial P_{\text{abs}}} = -\frac{1}{16}\frac{\alpha E}{\sigma_0 \kappa}\frac{L}{A}\omega_{n,0}, \tag{2.95}$$

and, in the case of relative frequency changes, the relative thermal responsivity $\delta\mathscr{R}$ is defined as

$$\delta\mathscr{R} = \frac{\mathscr{R}}{\omega_{n,0}} = -\frac{1}{16}\frac{\alpha E}{\sigma_0 \kappa}\frac{L}{A}. \tag{2.96}$$

Based on Equation (2.96), it is clear that long and narrow strings provide the largest temperature response. A large coefficient of thermal expansion and a low thermal conductivity also enhances the responsivity, which can be understood intuitively. Furthermore, the responsivity can be seen to be inversely proportional to the tensile stress, which has led to efforts focused on engineering reduced stress in nanomechanical resonators [86, 101]. It should also be noted that the derived thermal responsivity assumes an absorbance $\mathcal{A} = 1$, i.e. 100% light absorption, which is of course not the case in real experiments. However, one can account for this difference by dividing equation Equation (2.96) by a suitable correction factor.

2.3.1.2 Thermal Radiation

In the previous section, the response of a string to a local heat source was derived based on heat transferring solely through conduction. This analytical model has been successfully employed for describing the response of strings used for photothermal spectroscopy [97, 98]. Nonetheless, recent investigations into nanomechanical membranes have shown a significant contribution from radiative heat transfer [103, 104]. The influence of thermal radiation on the response of strings has thus far not been reported. However, observations in support of radiative heat transfer are made in Section 6.3 and the effect is therefore described in this

section. Given that no analytical models taking thermal radiation into account exist, FEM simulations are employed in this section.

Details of the simulation setup will be given in Section 3.4.4. Briefly, a pointlike heat source is focused on the string center, while the rim of string is set to $T_0 = 293.15$ K. In order to account for radiative heat transfer, the model includes radiation from the bottom and top string surface, with the radiative heat flux density given as

$$\mathbf{J}_q = \epsilon_\lambda \sigma_{\mathrm{SB}} \left(T_0^4 - T^4\right), \tag{2.97}$$

where σ_{SB} is the Stefan-Boltzmann constant [105]. The simulated influence of increasing ϵ_λ on the thermal response of a nanomechanical string resonator is shown in Figure 2.10. As a first test, the effect on the temperature profile along the length of the string is demonstrated, as can be seen in Figure 2.10(a). Temperature profiles are acquired for an absorbed power $P_{\mathrm{abs}} = 0.1$ µW and for emissivities from $\epsilon_\lambda = 0.0$ up to $\epsilon_\lambda = 0.4$. For $\epsilon_\lambda = 0.0$, the temperature displays a linear distribution in agreement with Equation (2.88). As the emissivity is increased, the distribution becomes increasingly exponential, while the maximum temperature in the string center decreases. These simulations thus show a reduced temperature response for a given absorbed power, when thermal radiation is included.

The reduction of the thermal response can also be shown by inspecting the absorbed power dependence of the resonance frequency shift, which is displayed in Figure 2.10(b). As the surface emissivity is increased, the frequency detuning for a given P_{abs} decreases, i.e. the thermal responsivity is reduced. In addition, the relationship between f_n and P_{abs} changes for increasing ϵ_λ. For $\epsilon_\lambda = 0.0$, f_n shifts approximately linearly with P_{abs}, as expected from Equation (2.94). At larger values of P_{abs}, the Taylor approximation breaks down due to the thermal stress approaching the intrinsic stress value, in which case the full model given in Equation (2.93) has to be used to describe the shift. When the emissivity increases, the power dependence becomes exponential, which is more clearly observable in Figure 2.10(c). The shift of f_n is plotted for even larger P_{abs}-values, and an exponential relation can be discerned. A similar frequency detuning is observed experimentally, as will be shown in Section 6.3.

2.3.2 Membranes

Heat transfer in nanomechanical membrane resonators has also received a decent amount of attention in recent years [100, 103, 104]. Similar to the case of strings, an analytical model describing the heat transfer in the conduction-dominated regime has been developed, which will be discussed first. The influence of radiative heat transfer is once again demonstrated numerically.

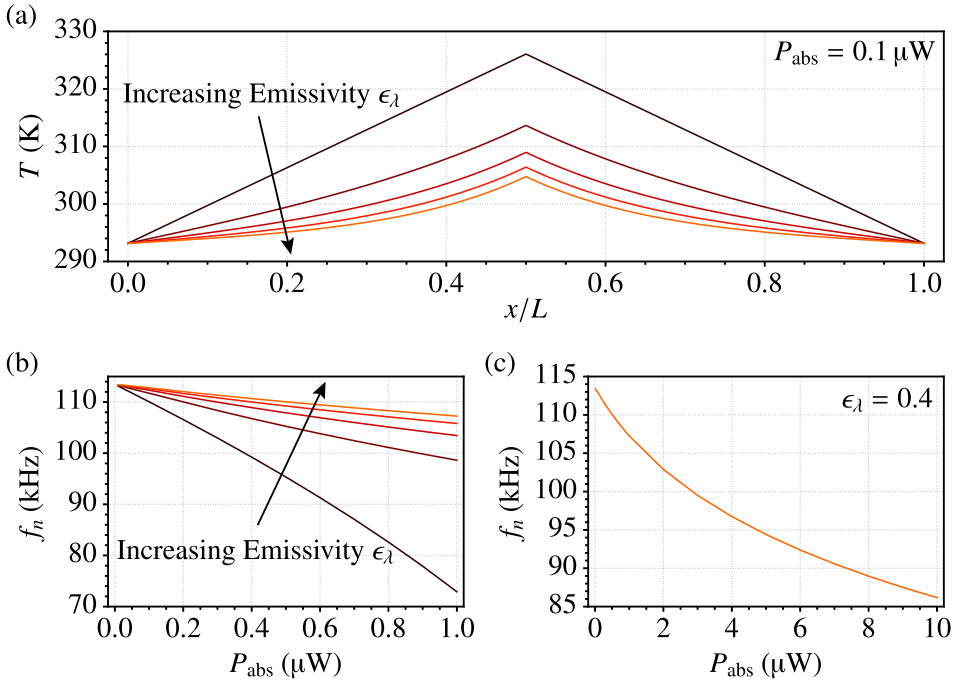

Figure 2.10: Influence of radiative heat transfer on the thermal response of strings. (a) Finite element method simulations of the temperature field along the length of a string resonator for surface emissivities of 0.0, 0.1, 0.2, 0.3, and 0.4. (b) Simulated eigenfrequency shift of the string versus absorbed power for the same values of ϵ_λ as in (a). (c) Power-dependency of the frequency shift for $\epsilon_\lambda = 0.4$ for larger values of P_{abs}. Parameters of the simulated string are $L = 1$ mm, $w = 5$ µm, $h = 50$ nm, $E = 250$ GPa, $\nu = 0.23$, $\rho = 3000$ kg/m^3, $\sigma_{film} = 200$ MPa, $\alpha = 2.2 \times 10^{-6}$ K^{-1}, $\kappa = 3$ W/(m·K), and $c_p = 700$ J/(kg·K).

2.3.2.1 Thermal Conduction

This section is based on the analytical model provided in the supporting information of Kurek *et al.* [100]. The complexity of the math used to derive this model is significantly larger than that of strings and many steps will therefore not be included here. A circular membrane is assumed in the derivation of the mode, which has been shown to provide a good description of square membranes as well [106]. Given the circular geometry, polar coordinates are used for the derivation. The radius of the membrane and the central heat source are labeled a and b, respectively. Description of the temperature evolution is made according to Equation (2.87), as was the case for strings. The heat dissipated per unit volume can be described according to

$$q(r) = \frac{P_{abs}}{\pi b^2 h} \times H(b - r), \tag{2.98}$$

where $H(r)$ is the Heaviside step function. Exploiting the rotational symmetry of the problem, such that $T = T(r)$ and $T(a) = 0$, Equation (2.87) can be written as

$$\kappa \frac{1}{r}\frac{\partial}{\partial r}\left(r\frac{\partial T}{\partial r}\right) = -\frac{P_{\text{abs}}}{\pi b^2 h} \times H(b-r). \tag{2.99}$$

The solution for $r > b$ can be found to be

$$T(r) = -\frac{P_{\text{abs}}}{2\pi\kappa h}\ln\left(\frac{r}{a}\right). \tag{2.100}$$

Assuming no stress in the direction of the membrane thickness ($\sigma_z = 0$), and therefore also no shear stress, one can find the in-plane thermal stress using a force balance condition on a volume element, which requires the following stress-strain temperature relations

$$\epsilon_x = \frac{1}{E}\left(\sigma_x - \nu\sigma_y\right) + \alpha T(r) \tag{2.101}$$

$$\epsilon_y = \frac{1}{E}\left(\sigma_y - \nu\sigma_x\right) + \alpha T(r), \tag{2.102}$$

with ν being Poisson's ratio. At this point, a number of steps will be skipped, but the final stress distribution is found by solving the in-plane displacement problem arising from the thermal expansion of the membrane. The thermal stress generated from the central heat source can be written in polar coordinates as

$$\sigma_r = -\alpha E\left(\frac{1}{r^2}\int_0^r rT(r)\,dr + \frac{1+\nu}{1-\nu}\frac{1}{a^2}\int_0^a rT(r)\,dr\right). \tag{2.103}$$

If one now assumes $b = 0$, i.e. a point source, then the temperature profile is described according to Equation (2.100) and the stress beomces

$$\sigma_r = -\frac{\alpha E P_{\text{abs}}}{4\pi\kappa h}\left(\frac{1}{1-\nu} - \ln\left(\frac{r}{a}\right)\right). \tag{2.104}$$

With the radial stress distribution at hand, the eigenfrequency can be found by solving the equation of motion for the heated membrane

$$\frac{1}{r}\frac{\partial}{\partial r}\left((\sigma_0 + \sigma_r)\, r\frac{\partial u(r,t)}{\partial r}\right) - \rho\frac{\partial^2 u(r,t)}{\partial t^2} = 0, \tag{2.105}$$

where σ_0 is the stress prior to heating. In the case of zero thermal stress, the exact solution for the angular frequency of the fundamental mode is known and is given as [107]

$$\omega_{nj,0} = \frac{2.404}{a}\sqrt{\frac{\sigma_0}{\rho}}. \tag{2.106}$$

In order to get the eigenfrequency from Equation (2.105), an approximate solution can be found according to Rayleigh's method, from which the relative frequency shift of the fundamental mode for a heated circular membrane becomes

$$\delta\omega = \frac{\omega - \omega_{nj,0}}{\omega_{nj,0}} = -\frac{\alpha E P_{\text{abs}}}{8\pi\kappa h\sigma_0}\left(\frac{2-\nu}{1-\nu} - 0.642\right), \tag{2.107}$$

which then gives the relative responsivity equation for a membrane

$$\delta\mathscr{R} = \frac{\delta\omega}{P_{\text{abs}}} = -\frac{\alpha E}{8\pi\kappa h\sigma_0}\left(\frac{2-\nu}{1-\nu} - 0.642\right). \tag{2.108}$$

Evidently, assuming conduction dominated heat transfer, $\delta\mathscr{R}$ turns out to be independent on the lateral dimensions of the membrane. Other than that, the dependence on material parameters is similar to that of strings (see Equation (2.96)).

2.3.2.2 Thermal Radiation

For square membranes, the effect of radiative heat transfer has been investigated both theoretically and experimentally [103, 104]. Importantly, these results have shown a pronounced dependence on the lateral size of the membrane, contrary to the expectation based on Equation (2.108). This length-dependence can be demonstrated using FEM simulations, as shown in Figure 2.11. A square membrane heated using a pointlike source is simulated, and surface emissivity is added as a variable in the same way as for strings in Section 2.3.1.2. The simulated temperature distribution along the diagonal length L_d of the membrane can be seen in Figure 2.11(a) for various values of ϵ_λ. A clear reduction of the maximum temperature for increasing ϵ_λ can be observed, as would be expected from radiative heat transfer. This cooling of the membrane for larger emissivities results in a reduced thermal responsivity, which is shown in Figure 2.11(b). Simulations of the relative responsivity versus lateral size for the fundamental mode of a square membrane are shown for increasing ϵ_λ-values. For zero emissivity, the analytical model given in Equation (2.108) is plotted, which predicts a constant $\delta\mathscr{R}$ versus membrane size. The effect of a non-zero emissivity is a decrease of $\delta\mathscr{R}$ for increasing L, which becomes more pronounced as ϵ_λ is increased.

2.4 Noise in Nanomechanical Systems

One of the main reasons behind the increased research into nanomechanical resonators is the increased responsivities to physical quantities [16]. The most common way of employing resonant sensors is to detect shifts of the resonance frequency as the detection principle. As

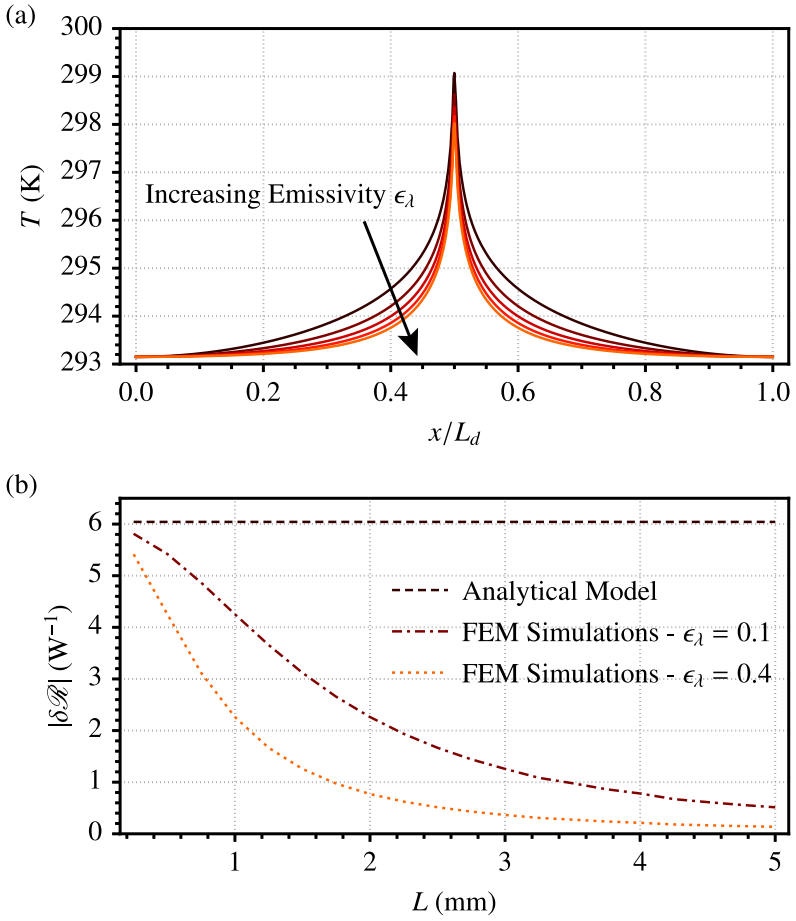

Figure 2.11: Influence of radiative heat transfer on the thermal response of membranes. (a) Finite element method simulations of the temperature distribution along the diagonal length of a square membrane for an absorbed power $P_{\text{abs}} = 0.1$ µW and surface emissivities of 0.0, 0.1, 0.2, 0.3, and 0.4. Dimensional parameters of the membrane are $L = 1$ mm and $h = 50$ nm. (b) Simulated relative responsivities $\delta\mathscr{R}$ versus lateral size L of a square membrane with $h = 50$ nm for increasing ϵ_λ. The case of $\epsilon_\lambda = 0.0$ is represented using a calculation of $\delta\mathscr{R}$ according to Equation (2.108). All $\delta\mathscr{R}$-values have been divided by a factor of 200 corresponding to 0.5% absorption [101]. Material parameters used for the simulations in both (a) and (b) are $E = 250$ GPa, $\nu = 0.23$, $\rho = 3000$ kg/m^3, $\sigma_{\text{film}} = 200$ MPa, $\alpha = 2.2 \times 10^{-6}$ K^{-1}, $\kappa = 3$ W/(m·K), and $c_{\text{p}} = 700$ J/(kg·K).

such, any unwanted process resulting in frequency fluctuations acts as a source of noise in the detection. A natural consequence of the large responsivities of nanomechanical resonators is an increased susceptibility towards microscopic noise processes, including thermomechanical noise [108], adsorption-desorption noise [109], defect motion [21], surface diffusion [110], and damping fluctuations [111]. Most of the noise sources listed above are predictions based

on theory and only a few experimental demonstrations of said limits have been published [112]. The most fundamental intrinsic limit is the thermomechanical noise, which arises from a coupling between the resonator and a thermal bath of randomly distributed phonons [113–115]. As such, this section will briefly present an analytical model of thermomechanical noise. The second part of the section will introduce the Allan variance, which can be employed to quantify the frequency fluctuations of a resonator.

2.4.1 Thermomechanical Noise

This section is based on derivation and discussion provided in [116]. Thermomechanical noise can be modelled assuming a lumped-element resonator, which was discussed in Section 2.1.1. Based on the equipartition theorem [117], a mechanical system in thermal equilibrium has an average total energy equal to $k_B T$, which, using the elastic energy, gives the following relation assuming a lumped-element model

$$\frac{1}{2}k_B T = \frac{1}{2}k_{\text{eff}}\left\langle z_{\text{th}}^2(t)\right\rangle = \frac{1}{2}m_{\text{eff}}\omega_0^2\left\langle z_{\text{th}}^2(t)\right\rangle, \tag{2.109}$$

where k_{eff} and m_{eff} are the effective spring constant and mass, respectively, while $\left\langle z_{\text{th}}^2(t)\right\rangle$ is the mean thermomechanical displacement. Effective parameters are used to model the dynamics of resonators according to those of a harmonic oscillator, depending on both the resonator geometry and mechanical mode [16]. Isolating $\left\langle z_{\text{th}}^2(t)\right\rangle$ in Equation (2.109) results in

$$\left\langle z_{\text{th}}^2(t)\right\rangle = \frac{k_B T}{m_{\text{eff}}\omega_0^2}. \tag{2.110}$$

Typically, the thermomechanical noise is quantified in the frequency domain by measuring the undriven vibrational signal of a resonator around the resonance frequency. Squaring this signal and dividing by the resolution bandwidth employed to measure the noise, results in a noise magnitude quantity called the (one-sided) *power spectral density* (PSD) $S_{zz}(\omega)$. The mean thermomechanical displacement can be expressed in terms of its PSD as

$$\left\langle z_{\text{th}}^2(t)\right\rangle = \frac{1}{2\pi}\int_0^\infty S_{zz}(\omega)\,d\omega. \tag{2.111}$$

Recalling the equation of motion of a lumped-element resonator provided in Equation (2.1), the force $F(t)$ generated by random thermal noise is flat with respect to frequency. Defining a thermal force noise S_{FF}^{th} and through some derivation, the thermomechanical displacement

can be written as

$$\begin{aligned}\left\langle z_{\text{th}}^2(t)\right\rangle &= \frac{S_{FF}^{\text{th}}}{2\pi m_{\text{eff}}^2}\int_0^\infty \frac{d\omega}{\left(\omega^2-\omega_0^2\right)^2+(\omega\omega_0/Q)^2} \\ &= \frac{S_{FF}^{\text{th}}Q}{4\omega_0^3 m_{\text{eff}}^2}.\end{aligned} \tag{2.112}$$

Combining this result with Equation (2.110) results in the following formula for the thermal force noise

$$S_{FF}^{\text{th}} = \frac{4k_{\text{B}}T\omega_0 m_{\text{eff}}}{Q}, \tag{2.113}$$

which can be used to express the PSD resulting from thermomechanical noise of a resonator [113]

$$S_{zz}(\omega) = \frac{4k_{\text{B}}T\omega_0}{m_{\text{eff}}Q\left[\left(\omega^2-\omega_0^2\right)^2+(\omega\omega_0/Q)^2\right]}. \tag{2.114}$$

In the temporal frequency regime, this expression is given as

$$S_{zz}(f) = \frac{k_{\text{B}}Tf_0}{2\pi^3 m_{\text{eff}}Q\left[\left(f^2-f_0^2\right)^2+(ff_0/Q)^2\right]}. \tag{2.115}$$

The magnitude of the noise at the peak of the function can be shown to be

$$S_{zz}(f)\big|_{f=f_0} = \frac{k_{\text{B}}TQ}{2\pi^3 m_{\text{eff}}f_0^3}. \tag{2.116}$$

It should be noted that the noise peak is proportional to the Q, but the thermal white noise in Equation (2.113) is inversely proportional to the Q. As such, higher Q lowers the overall noise but increases the peak noise [16].

2.4.2 Allan Variance

In addition to knowledge of the resonator noise, it is crucial to have a tool with which the amount of frequency fluctuations can be quantified. For the determination of the frequency fluctuations of a resonator, one first has to record its frequency for a given amount of time. Then, the most straightforward approach to quantifying the frequency stability would be to extract the variance of the measurement, which is the average of the squared differences from the mean [118]. However, the classical variance does not allow one to clearly distinguish different noise sources present in a system. Furthermore, in the presence of unwanted phe-

nomena such as thermal drifting of the frequency, the classical variance will not converge and therefore overestimates the frequency stability limit.

Due to the limitations of the classical variance, an alternative variance was developed. Instead of just measuring how much the frequency varies over time, one can also determine how much the classical variance itself varies over time. More specifically, one can estimate how much the frequency changes from one sample interval of the frequency to the next and then vary this sampling time over the duration of the measurement. The resulting variance is called the *Allan variance*, named after its inventor David. W. Allan [119–121]. In its most general form, the Allan variance can be written as

$$\sigma_{\mathrm{A}}^2(\tau) = \frac{1}{2(M-1)} \sum_{i=1}^{M-1} (y_{i+1} - y_i)^2 , \tag{2.117}$$

where M is the number of samples of the measured quantity $y_{i+1}...y_i$, each measurement averaged over an integration, or sampling, time τ. The Allan variance circumvents the issues associated with the classical variance in that it will converge for most commonly encountered types of noise and allows the type and level of different noise sources to be inferred [120]. In addition to the fundamental definition of the Allan variance, the so-called overlapping Allan variance exists as well, where different samples of y_i are allowed to overlap. In this way, all possible combinations of the measured data set are utilized for the computation of the Allan variance, improving the confidence of the calculated frequency stability at the expense of increased computational time [122, 123]. The overlapped Allan variance is defined as

$$\sigma_{\mathrm{A}}^2(\tau) = \frac{1}{2m_s^2(M-2m_s+1)} \sum_{j=1}^{M-2m_s+1} \left[\sum_{i=j}^{j+m_s-1} (y_{i+m_s} - y_i) \right]^2 , \tag{2.118}$$

where m_s is the amount of overlapped samples out of the original non-overlapped sample. Both of these equations are general and can be used for the measurement of any given quantity y_i. In the case of frequency stability measurements, the Allan variance is typically computed using fractional frequencies, in which case one can write

$$y_i = \frac{f_{0,i} - f_0}{f_0}, \tag{2.119}$$

where f_0 is the nominal value of the eigenfrequency.

For most published frequency stability data, the *Allan deviation* is reported, since the values of the Allan variance are squared and therefore harder to interpret. The Allan deviation is simply the square root of the Allan variance, $\sigma_{\mathrm{A}}(\tau) = \sqrt{\sigma_{\mathrm{A}}^2(\tau)}$, be it the non-overlapping or the overlapping Allan variance. In this thesis, all presented measurements of the Allan

deviation are of the overlapping class. A plot of a typical Allan deviation curve is given in Figure 2.12, which shows the contribution from various noise processes. When limited by white noise, σ_A converges for increasing values of τ with a slope proportional to $\tau^{-1/2}$. Flicker noise, also known as $1/f$ noise, is flat for all integration times, meaning no improvement in stability for increased averaging. Thermal drift manifests itself through an increase in σ_A at large integration times with a slope proportional to τ.

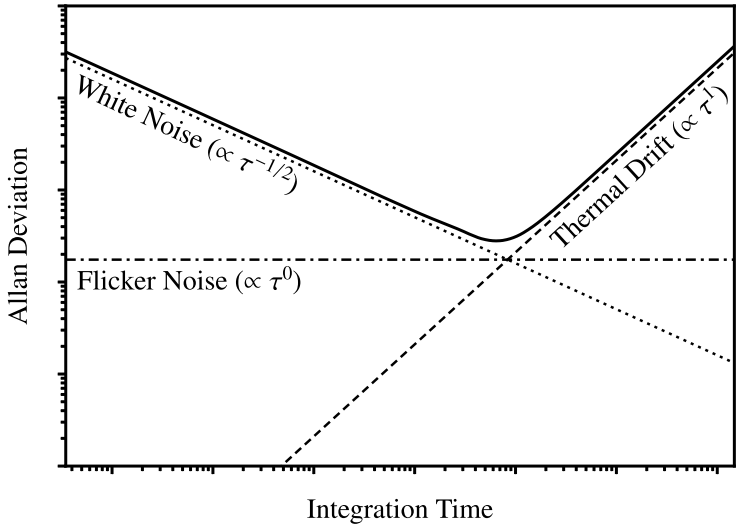

Figure 2.12: Frequency stability analysis using the Allan deviation. The plot shows how a typical Allan deviation measurement appears, highlighting typically observable noise processes in such a measurement. In the white noise limited regime, the Allan deviation converges for increasing integration times with a slope proportional to $\tau^{-1/2}$, while thermal drift causes it to diverge at larger integration times proportional to τ. Flicker, or $1/f$, noise gives a flat contribution for all integration times ($\propto \tau^0$). Figure inspired by Figure 5.11 in [16].

It is also possible to compute the Allan variance through knowledge of the noise spectrum of a resonance. In the frequency domain, the Allan variance can be expressed in terms of the (two-sided) PSD S_y according to [124]

$$\sigma_A^2(\tau) = \frac{4}{\pi\tau^2}\int_{-\infty}^{\infty}\frac{[\sin(\omega\tau/2)]^4}{\omega^2}S_y(\omega)\,d\omega, \tag{2.120}$$

or equivalently in the temporal frequency domain as

$$\sigma_A^2(\tau) = \frac{2}{\pi^2\tau^2}\int_{-\infty}^{\infty}\frac{[\sin(\pi\tau f)]^4}{f^2}S_y(f)\,df \tag{2.121}$$

The Allan deviation is then again calculated by taking the square root of the Allan variance. In

order to accurately model measured Allan deviations based on Equations (2.120) or (2.121), characteristics of the demodulation scheme used to detect the resonance frequency need to be incorporated into S_y [125, 126]. Computed Allan deviation curves based on Equation (2.121) are shown alongside measurements throughout Chapter 6.

3

Experimental and Computational Methods

A discussion of all the main experimental and computational methods employed in this thesis is provided in this chapter. The first part gives an overall explanation of the cleanroom fabrication process used to manufacture the nanomechanical resonators. Focus then moves towards the laser-Doppler vibrometry setup employed for the vibrational analysis of the samples, including a description of how various physical quantities are measured experimentally. A section is then dedicated to introducing the ultrahigh vacuum setup, focusing both on presenting the different components of the setup as well as discussing how experiments are conducted inside the ultrahigh vacuum. The final part of the chapter gives a thorough explanation of the finite element method simulations of the mechanical properties of the resonators.

3.1 Fabrication

An essential part of the progress made in the field of nanomechanical systems has been the development of nanofabrication processes capable of reliable and reproducible manufacturing of functioning samples. The samples employed in this thesis were fabricated at different times and with differing fabrication process flows, rendering a detailed description of each individual process cumbersome. However, since all samples consist of silicon nitride (SiN) resonators on silicon (Si) substrates, this means that certain crucial steps are needed for the fabrication of all the investigated samples. An overall fabrication process flow is therefore given in this section, with illustrations of the different steps shown in Figure 3.1. The presented process flow only considers the fabrication of bare mechanical resonators without any metals deposited on top.

The first step of the fabrication process flow is to grow the material used for the resonators (Figure 3.1(a)). SiN is the material of choice for all investigated samples since this is the most well-studied nanomechanical system displaying the dissipation dilution effect [34, 36–

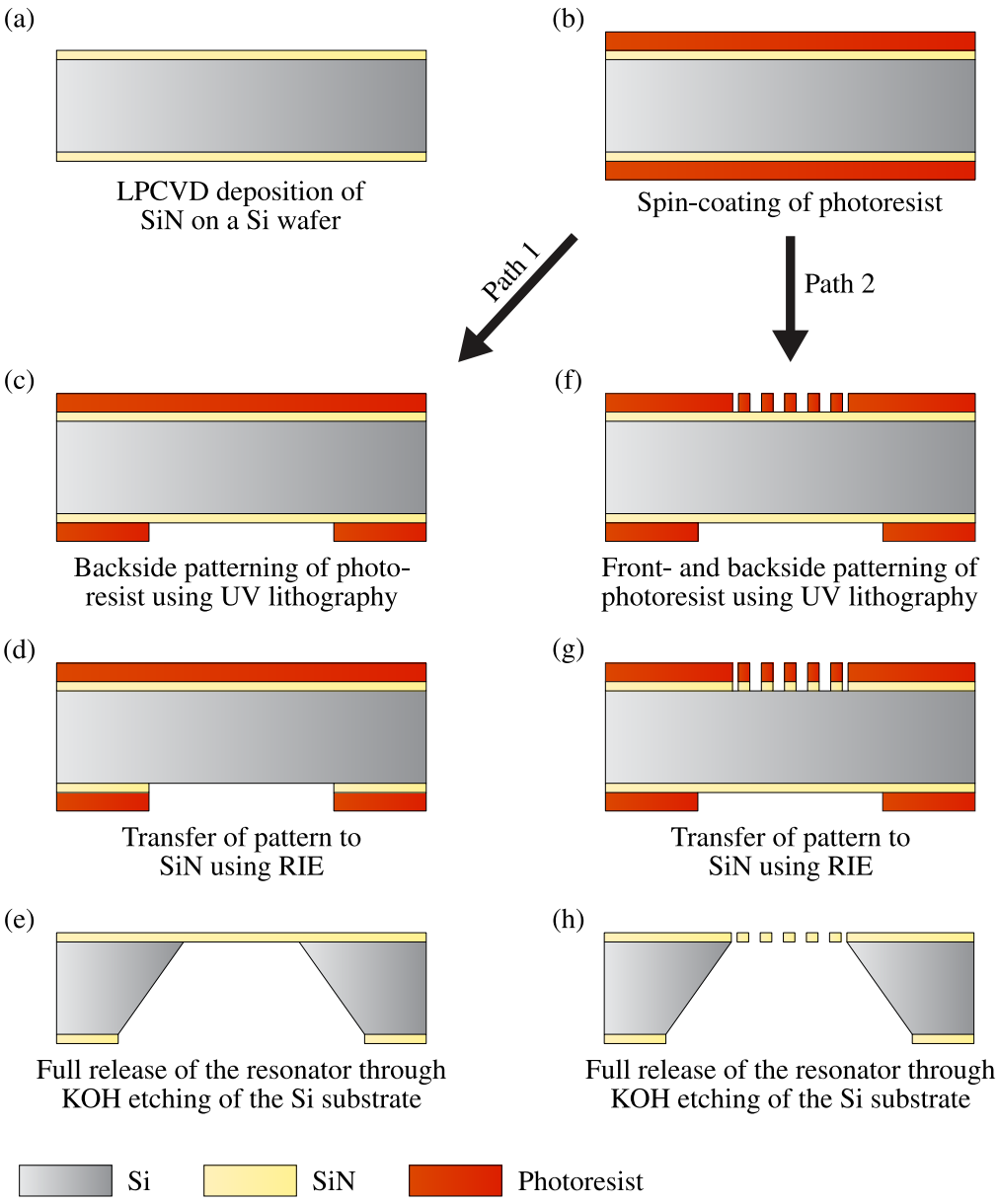

Figure 3.1: Overall process flow for the fabrication of nanomechanical silicon nitride resonators. Path 1 describes the fabrication of uniform membrane resonators, which only includes backside patterning, while Path 2 displays the fabrication of resonators such as strings and phononic crystal membranes, which require a frontside patterning step as well.

38]. Growth of SiN on Si substrates is achieved by means of low pressure chemical vapor deposition (LPCVD) [127]. The gases used for the LPCVD growth of SiN typically consist of a mixture of dichlorosilane (SiH_2Cl_2) or silane (SiH_4), serving as the source of silicon, and ammonia (NH_3), which is the source of nitrogen. As-grown SiN films have been shown to

possess a large residual tensile stress σ_{film} [128], consisting of a compressive thermal stress part, arising from the mismatch between the coefficients of thermal expansion of SiN and Si, and a tensile intrinsic (growth) stress [129–131]. The origin of the intrinsic stress is not entirely understood but is postulated to arise due to coalescence of separate clusters or islands of SiN, forming grain boundaries, during film growth [132, 133]. The exact value of the final film stress is dependent on the ratio of the employed gases used for the growth process. Stoichiometric SiN, with the chemical formula Si_3N_4, typically displays large tensile stress values of around 1 GPa. This value can then be lowered by increasing the Si content of the SiN, forming so-called silicon-rich SiN [128, 134–136]. LPCVD can either be done in-house in local cleanroom facilities, but Si wafers with as-grown SiN on top can also be commercially ordered [137].

In order to define the resonators in the SiN film, a photolithography step is required. For this purpose, patterns used for a dedicated photomask have to be drawn, which can be achieved using various layout editors such as *CleWin* [138]. The photomasks themselves are transparent glass plates, where the desired pattern is incorporated into a thin absorbing chromium film deposited on the plate, such that light only passes through regions not containing chromium. Depending on the type of resonator to be fabricated, one or more photomasks are needed both for front- and backside patterning. The photomasks can be manufactured commercially by various companies, with examples of dedicated companies being *Delta Mask* [139] and *Rose Fotomasken* [140].

Before commencing the photolithography step, a thin film of photoresist is spun on the wafers using spin-coating (Figure 3.1(b)), followed by a short bake of the wafer with resist on top. The photoresist is typically spun on both sides of the wafer, in order to protect the unexposed side during the various fabrication steps. At this point, two paths to the fabrication of nanomechanical resonators can be taken, depending on whether a frontside patterning step is needed. For the fabrication of uniform membranes, labeled Path 1 in Figure 3.1, the photoresist on the backside of the wafer is exposed to ultraviolet (UV) light and then developed, which, in the case of positive photoresists, refers to the removal of the photoresist in the exposed regions (Figure 3.1(c)). The photoresist pattern is then transferred to the SiN using reactive ion etching (RIE), using the unexposed photoresist as a shadow mask (Figure 3.1(d)). SiN is typically dry-etched using tetrafluoromethane (CF_4), often with the addition of oxygen (O_2), which suppresses the formation of a fluorocarbon layer on the SiN surface during etching and thus allowing a constant nitride etch rate [141, 142].

After the dry etching step, the photoresist is stripped off the wafer using suitable removers depending on the choice of photoresist. Then, the next step is to release the resonators by etching through the parts of the substrate exposed after dry etching of the SiN. In the case of Si substrates, this is done through an anisotropic potassium hydroxide (KOH) wet etching

step, with the KOH heated up to a temperature of 80 °C (Figure 3.1(e)). KOH is the etchant of choice due to its selectivity towards the crystal orientation of the Si, with KOH having a much larger etch rate for the ⟨100⟩ direction compared to the ⟨110⟩ and ⟨111⟩ directions [143]. Furthermore, the etch rate of LPCVD-grown SiN in KOH is nearly zero, making it the ideal etchant for resonators based on SiN [144]. The etching of Si using KOH results in a trapezoidal ditch with slopes at an angle of 54.7°. As the final step of the fabrication process, the wafers are washed in water and diced into separate chips. An additional cleaning step of the wafers using a piranha solution, which is a mixture of sulfuric acid (H_2SO_4) and hydrogen peroxide (H_2O_2), can be added to remove organic residues [145].

Path 2 follows the same procedure as Path 1, but additionally patterns the frontside of the wafer as well. This process flow is necessary for the fabrication of, among others, strings [146], trampolines [46], and phononic crystal membranes [39]. After the wafer backside dry etching step (see Figure 3.1(d)) and subsequent removal of the photoresist, another layer of photoresist is spun on the wafer and the photoresist on the wafer frontside patterned using UV lithography (Figure 3.1(f)). Similar to what was done for the backside, the pattern is transferred to the SiN on the frontside using a dry etching step (Figure 3.1(g)). Release of the resonators can then be done through KOH etching from the backside alone, or by exposing both the front- and backside of the wafer to the KOH (Figure 3.1(h)). Afterwards, the wafers are washed and then diced into individual chips, thus concluding the fabrication process.

As a final note, it should be mentioned that the fabrication process flow described above is very general and certain additional steps might be included for the successful fabrication of samples. In particular, the fragility of nanomechanical resonators typically demands a more delicate release process than simply dipping the wafers into KOH. Plasma-enhanced chemical vapor deposition (PECVD) SiN may be added as a protective layer on the frontside of the wafer to protect the released structures during the fabrication process. Furthermore, a sacrificial wet oxide (WOx) layer can be added between the Si and SiN, which can increase the final sample yield [102]. A number of excellent PhD theses exist, which explain the fabrication of various nanomechanical resonators in far greater detail [47, 147, 148].

3.2 Vibrational Analysis

In order to characterize the vibrational properties of nanomechanical resonators, it is essential to have a reliable and flexible transduction scheme, both for the detection and actuation of mechanical vibrations. Various transduction techniques have been developed for the accurate measurement of resonators, including optical [149], capacitive [150], inductive [151, 152], dielectric [153, 154], and piezoelectric [155, 156]. As will be discussed in the following,

optical detection is employed exclusively for the measurements presented in this thesis. The first part discusses the principle behind the optical detection scheme, including describing the measurement setup used for many of the displayed results. Then, an introduction to principles of optical actuation is given, including a comparison of the different available methods. The remaining sections describe the experimental methods employed to measure various physical properties central to the results shown in this thesis, including the frequency stability, quality factor, and thermal responsivity.

3.2.1 Optical Detection

External optical transduction techniques, i.e. no chip integration, are among the most utilized for nanomechanical resonators due to the high sample flexibility and having little influence on sample properties. In this project, lasers were employed both for the actuation and detection of mechanical vibrations, with the latter being central to all presented results. This section will serve to introduce the principle behind the laser-Doppler vibrometry method used for the vibrational analysis of samples, before explaining how this method can be implemented in practice by providing a description of the employed optical measurement setup.

3.2.1.1 Laser-Doppler Vibrometry

A laser-Doppler vibrometer, or vibrometer for short, is a type of Michelson interferometer, which relies on the superposition of two monochromatic and coherent light sources, such as lasers [16]. Figure 3.2 presents a schematic of a vibrometer setup of the type employed here. A laser beam is split into a reference beam and an object beam using a beamsplitter (BS1). The object beam passes through a second beamsplitter (BS2) before hitting the vibrating sample and the reflected light directed towards a photodetector using BS2. As a result of the sample vibration, a Doppler frequency shift, $f_D(t)$, is induced in the object beam [157]:

$$f_D(t) = \frac{2\dot{u}(t)}{\lambda}, \tag{3.1}$$

where $\dot{u}(t)$ is the time-dependent sample velocity and λ the wavelength of the laser. The object beam is then recombined with the reference beam using a third beamsplitter (BS3) and the merged beams are sent to a photodetector. Given that the optical path of the reference beam remains unchanged, the recombination of the two beams results in an interferometric pattern with a frequency directly proportional to the sample velocity. To detect the direction of the vibration, an acousto-optic modulator, or Bragg cell, is used to generate a known frequency shift to the reference beam. The interference signal of the two beams is then converted to an

electrical signal using the photodetector, which is then transformed into a measured displacement using decoders in the vibrometer controller.

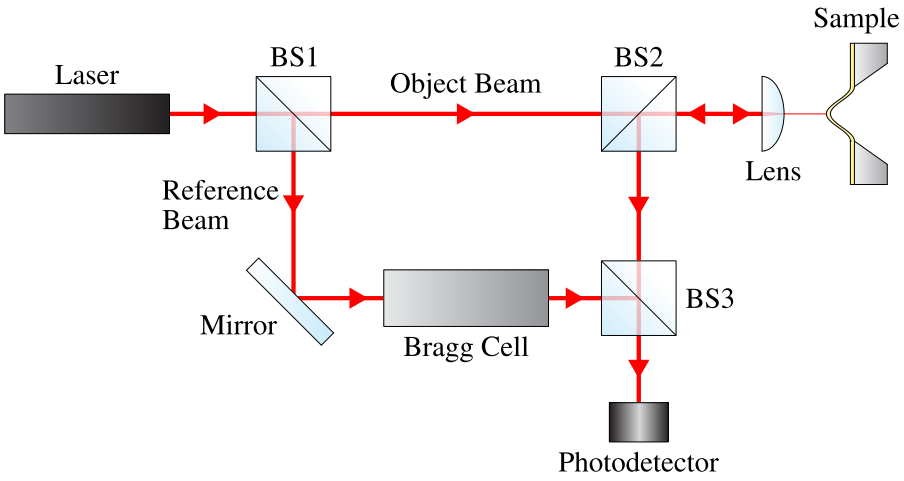

Figure 3.2: Schematic of the components used in a standard laser-Doppler vibrometer. A laser beam is split into an object and a reference beam, with the former interacting with a vibrating sample and causing it to gain a Doppler frequency shift. The two beams are recombined and the optical path difference between results in an interference pattern detected using a photodetector. A Bragg cell generates a known frequency shift in the reference beam, which is used to detect the direction of the sample vibration.

3.2.1.2 Vibrometer Setup

Implementation of an interferometric detection scheme for the measurement and imaging of mechanical vibrations can be done in a number of ways. Barg *et al.* provide an excellent overview of how custom interferometer setups can be built in any lab by combining the necessary optical and electrical components [149]. For this project, however, a commercial laser-Doppler vibrometer is employed (MSA-500 from Polytec GmbH) and a sketch of the standard configuration of the measurement setup used here is given in Figure 3.3. This section serves to give an overview of the various components of this setup.

The coherent source of the vibrometer is a helium-neon (HeNe) laser with a center wavelength $\lambda = 633$ nm, which is coupled to the vibrometer microscope using an optical fiber. Control of the laser position on the sample is achieved by means of piezo scanners and mirrors inside the vibrometer microscope. An internal liquid-crystal (LCD) display of the vibrometer is placed in the optical path and used to vary the output power of the laser, which can be used to control the signal-to-noise ratio of the measurement. The amount of laser power P on the samples can vary from $P \sim 1$ µW up to $P > 200$ µW. Typically, the output power is slightly

lower immediately after turning on the laser, and the laser is therefore left to stabilize for some time before commencing measurements. The laser is focused onto samples using objective lenses (Plan Apochromat Objectives from Mitutoyo Corporation) of varying magnifications.

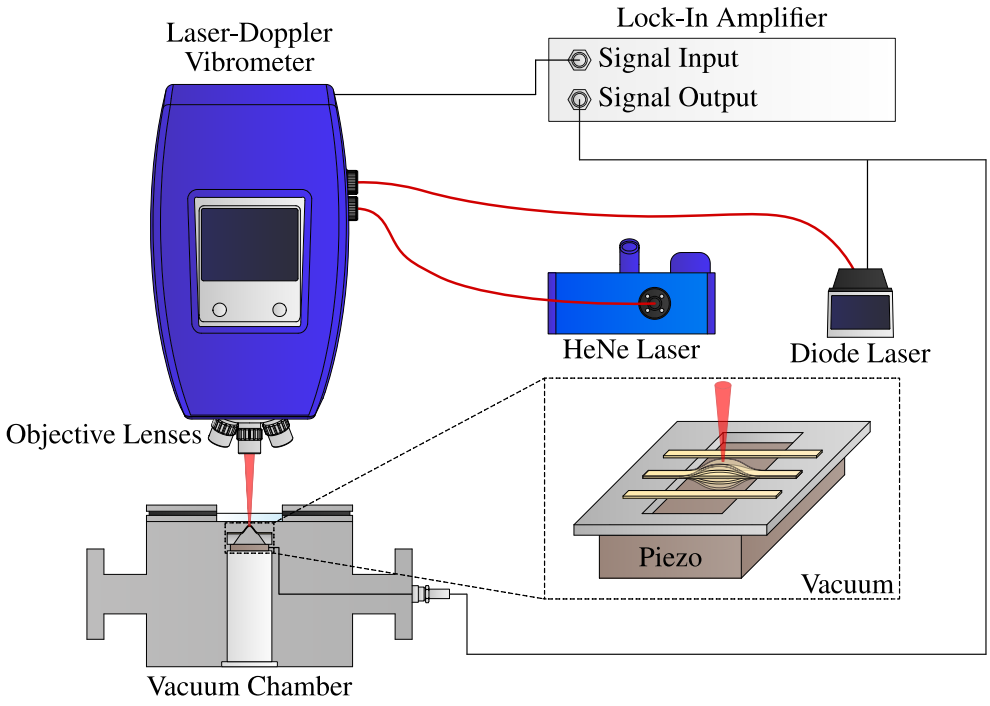

Figure 3.3: Interferometric setup used for the vibrational analysis of mechanical resonators. Mechanical vibrations are detected using a laser-Doppler vibrometer, with a helium-neon laser acting as the coherent light source. The laser is focused onto the samples using objective lenses of variable magnification. Samples are placed inside a vacuum chamber capable of reaching pressures $p < 10^{-6}$ mbar. Actuation of mechanical vibrations is achieved either by utilizing an amplitude-modulated diode laser or a piezo. The signal of the vibrometer is fed into a lock-in amplifier for further analysis.

For most measurements, the investigated samples are placed inside a dedicated vacuum chamber, in order to minimize gas damping [62] as well as the thermal conductivity of air [158], which is of relevance when measuring the quality factor and the thermal responsivity, respectively. The vacuum chamber is made of aluminium and cylindrical in shape, with an anti-reflection coated borosilicate (BK7) optical viewport at its center for the optical transduction of samples. For the evacuation of the chamber, a dedicated pumpstand (HiCube 80 Eco from Pfeiffer Vacuum GmbH) is employed, which consists of a diaphragm pump (MVP 015-2 DC from Pfeiffer Vacuum GmbH) and a turbopump (HiPace 80 from Pfeiffer Vacuum GmbH), serving as the roughing and high vacuum pump, respectively. Using this vacuum chamber and pumpstand, pressures $p < 10^{-6}$ mbar can be reached. Measured samples are

placed on a dedicated pillar post inside the chamber, which has a surface large enough to allow multiple samples to be measured simultaneously. To move from one sample to another, the entire chamber is moved for the alignment of the desired sample with the vibrometer.

Mechanical vibrations are actuated in one of two ways: Optically or piezoelectrically. Optical actuation, which will be discussed further in the next section, is achieved by amplitude modulation of a fiber-pigtailed laser diode (LPS-635-FC from Thorlabs GmbH) with a center wavelength $\lambda = 638$ nm. The diode laser is mounted to a dedicated controller (CLD1010LP from Thorlabs GmbH), allowing control of the output power and the diode temperature during operation. Integration of the diode laser with the measurement setup is done by coupling its fiber to the vibrometer microscope so that it follows the same optical path as the HeNe laser. The position of the diode laser on the measured samples can be controlled via the internal optics of the vibrometer microscope. Piezoelectric actuation is done by placing samples on top of piezoelectric plates, or piezos (NAC2003 from CTS Corporation or a custom-sized plate of piezo ceramic type PIC252 from PI Ceramic GmbH). The piezos are therefore also placed inside the vacuum chamber and connected to signal generators using an electrical feedthrough of the chamber.

The analog signal of the vibrometer is fed into a lock-in amplifier (HF2LI from Zurich Instruments), where additional analysis of the samples can be conducted, with the standard measurements being explained in the following sections. Whenever the lock-in amplifier is employed, the signal output of the lock-in is connected to either the diode laser or the piezo for sample actuation.

3.2.2 Optical Actuation

As mentioned in the previous section, mechanical vibrations can be optically actuated by amplitude-modulation of a laser. Two different physical principles are typically responsible for the actuation: Radiation pressure force or the thermoelastic effect through photothermal heating. Depending on the type of sample or the mechanical mode to be actuated, one method may be more appropriate, while both can be used interchangeably sometimes. Both types of optical actuation will now be described separately.

3.2.2.1 Radiation Pressure

Radiation pressure actuation relies on the fact that photons carry a momentum $p_{\text{phot}} = h/\lambda$, where h is the Planck constant and λ the wavelength, as predicted by James Clerk Maxwell in the nineteenth century [159]. This momentum can be transferred to an object upon reflection/absorption of the photon. Considering a flux of photons instead of a single one, the

resulting applied radiation pressure force F_{rad} on the object for normal incidence is given by [160, 161]:

$$F_{\text{rad}} = \frac{(2\mathcal{R} + \mathcal{A})\, P}{c}. \tag{3.2}$$

Here, $\mathcal{R}$ and $\mathcal{A}$ are the reflection and absorption coefficients of the object, respectively, P the total incident power, and c the vacuum speed of light. As can be seen from Equation 3.2, calculation of the applied force requires precise knowledge of the optical properties of the actuated material, which typically depend on the wavelength of the light. Since the laser applies a force directly on the sample, it should be placed on anti-nodes of resonances for optimum actuation.

3.2.2.2 Thermoelastic

Thermoelastic actuation is based on local heating of a mechanical resonator, resulting in a non-uniform expansion of the material and thus the generation of thermal stresses, which leads to a bending of the resonator. Modulation of the heating temperature results in an active actuation of the resonator [162, 163]. This can be achieved optically by means of photothermal heating employing an amplitude-modulated laser. While it is possible to thermoelastically actuate resonances through local heating of a single-layer material, optimal actuation is achieved through heating of multilayer structures [164]. The difference in coefficients of linear thermal expansion of two different materials causes a much larger deflection than for a single-layer material [165]. Since nanomechanical resonators typically are released on top of a substrate of a different material, thermoelastic actuation is still feasible for single-layer materials by heating at the anchor of the resonator.

3.2.2.3 Comparative Study of Optical Actuation Methods

A comparison between the two optical actuation methods is provided here based on an experimental study of a mechanical resonator. For this study, a SiN cantilever of the type employed by Larsen *et al.* is used [166]. An illustration of the two actuation configurations is given in Figure 3.4(a). Radiation pressure actuation is realized by focusing the diode laser beam on the tip of the cantilever, while thermoelastic actuation is achieved by focusing the laser on the cantilever anchoring. The vibrometer laser is focused on the tip of the cantilever, where the displacement is at its largest [16]. For each actuation method, the first 10 bending modes of the cantilever are measured and the maximum out-of-plane displacement z_{max} extracted, with a comparison of z_{max} versus frequency given in Figure 3.4(b). Measurements for the fundamental bending mode are excluded from this plot since the resonance frequency was lo-

cated near that of the turbopump (~ 1500 Hz), which rendered visualization of the cantilever resonance difficult. Both the laser power and the modulation depth provided by the signal generator were kept fixed for all measurements.

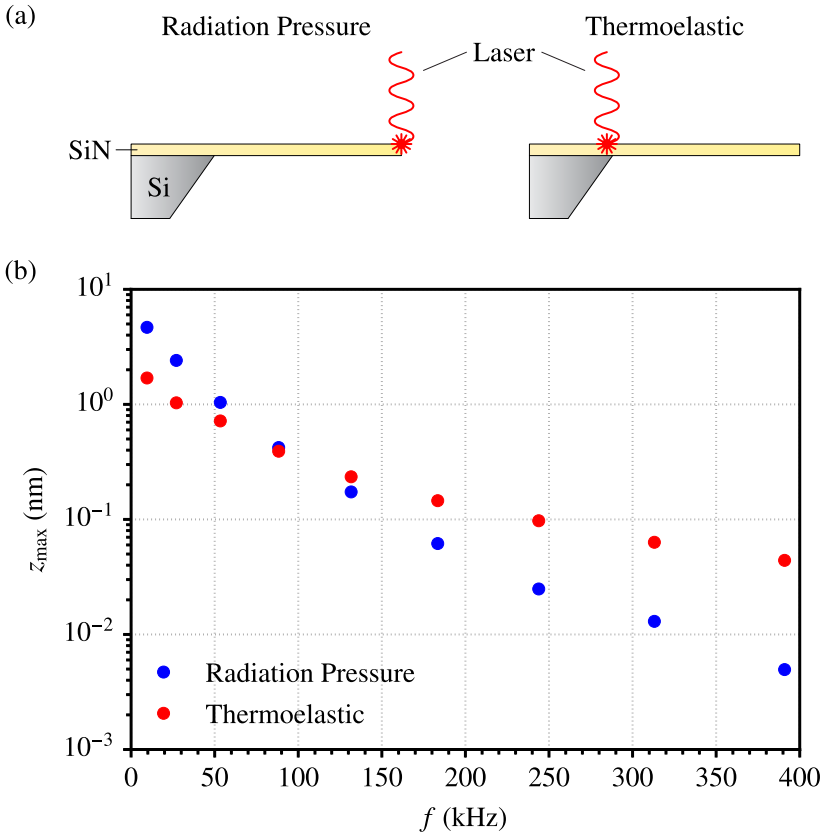

Figure 3.4: Comparison of optical actuation methods using a micromechanical cantilever. (a) Illustrations of the amplitude-modulated laser position for actuation based on radiation pressure force and the thermoelastic effect through photothermal heating. (b) Maximum out-of-plane displacement versus frequency for the first 10 bending modes of the investigated cantilever, excluding the fundamental bending mode, acquired via radiation pressure and thermoelastic actuation. Dimensional parameters for the investigated cantilever were $L = 715$ µm, $w = 100$ µm, and $h = 500$ nm.

Evidently, the maximum actuated displacement decreases with increasing frequency regardless of the actuation method, which is expected due to the increased stiffness of higher-order modes [16]. From the comparative study, it can be observed that radiation pressure appears to provide stronger actuation for lower-frequency modes, while the thermoelastic effect becomes stronger for higher frequencies. Intuitively, one would expect the thermoelastic actuation to roll off sooner due to thermal relaxation times on the order of milliseconds (as shown in Chapter 6). Nonetheless, for a given drive signal, a consistently larger displacement

for higher-order modes was measured, when employing thermoelastic actuation. This could simply be a result of the rather low actuation laser powers, with nominal output powers for the diode laser of $P \sim 100$ μW. If larger powers were available, one would perhaps observe a better performance of the radiation pressure method for higher frequency modes as well.

3.2.3 Frequency Tracking

Focus now shifts towards the different physical properties investigated using the measurement setup described above. First of all, a discussion of methods used to track the mechanical resonance frequency is provided. Here, frequency tracking refers to the continuous monitoring of the frequency over time. Given that most sensors based on nanomechanical resonators employ frequency shifts as the principle of detection, developing accurate and reliable tracking schemes is a necessity of the resonant sensors research field. This section aims to introduce the frequency tracking schemes employed in this thesis, focusing on elucidating the different tracking configurations used, which is of particular relevance to the results shown in Chapter 6.

3.2.3.1 Tracking Configurations

For all presented results, the lock-in amplifier of the interferometric setup (see Figure 3.3) serves as the frequency tracking platform. The use of laser-Doppler vibrometry as the detection scheme removes the need for any sort of additional amplification, as the signal-to-noise ratio available via the vibrometer proves to be more than enough to accurately track the frequency. As such, the analog signal of the vibrometer is sent directly into the lock-in amplifier, where frequency tracking can be performed.

Frequencies can be tracked in either an *open-loop* or a *closed-loop* configuration, as outlined in Figure 3.5. Additionally, *self-sustained oscillator* schemes also exist and have been successfully employed for the frequency tracking of nanomechanical resonators [167–169]. However, this configuration was not utilized in this work and is therefore not given any further consideration here. Interested readers are referred to theoretical investigations into frequency stability limits of nanomechanical resonators, where comparisons between all tracking configurations are given [125, 126].

As the name would suggest, open-loop tracking concerns the case, where the frequency is tracked without implementation of any feedback. In this configuration, which is illustrated in Figure 3.5(a), the resonator is driven using a signal generator at a frequency close to resonance [126]. The corresponding driven signal from the resonator (measurement signal) along with that of the signal generator (reference signal) is demodulated. As such, any events causing

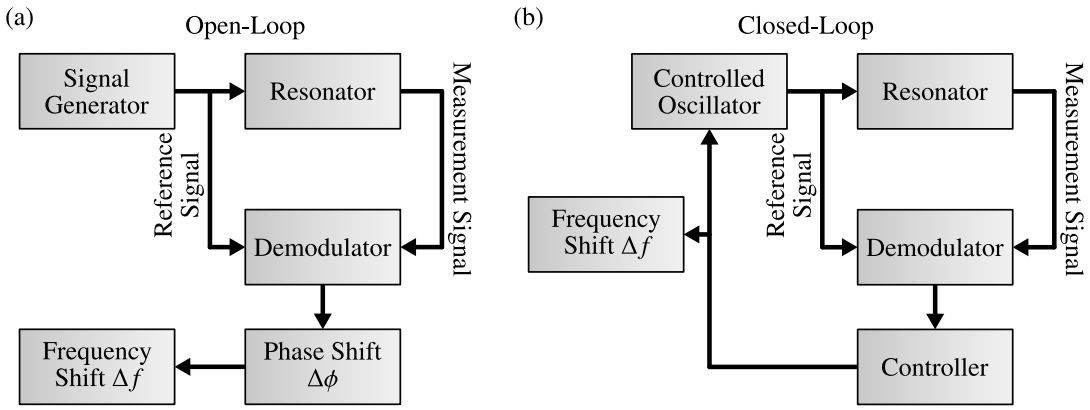

Figure 3.5: Schematics describing the frequency tracking configurations used in this project. (a) Open-loop, or feedback-free, tracking scheme. (b) Closed-loop, or phase-locked loop, tracking scheme. Figures (a) and (b) are adapted from Figures 1 and 2 in [126], respectively.

frequency shifts of the resonator will result in a phase shift $\Delta\phi$ between the reference and measurement signals, which the demodulator detects. If the amplitude and phase response of the resonator are known, the phase shift can be converted back to the frequency shift Δf caused by any frequency changing event. The biggest disadvantage of this method is unwanted thermal drifts of the resonance frequency during measurements, potentially shifting the frequency far away from that of the drive signal and into the flat phase regime (see Figure 2.1(c)) [170]. Furthermore, the bandwidth of the detection is limited by the response time of the resonator, as will be a major topic in Chapter 6. On the other hand, the intrinsic limitations of the technique make it ideal for fundamental investigations into frequency fluctuations of nanomechanical resonators [112].

In order to circumvent the issues presented above for the open-loop configuration, closed-loop schemes have been developed, with a general schematic given in Figure 3.5(b) [126]. Similar to the open-loop case, the driven signal of the resonator along with the reference signal is sent to a demodulator. However, the phase difference between the two signals is sent to a controller, typically a proportional-integral-derivative (PID) controller, which actively adjusts the drive signal frequency to stay at resonance, thus forming a negative feedback control loop, also called a *phase-locked loop* (PLL). In this way, this configuration overcomes the thermal drift problem of open-loop tracking, which has made it an ideal method for characterizing nanomechanical resonant sensors in literature [17, 171–174]. The fundamental speed limits set by the intrinsic response of the resonator can also be overcome at the expense of more noise, which will be discussed further in Chapter 6.

3.2.3.2 Frequency Stability Measurements

With the tracking schemes established in the previous section, a description of the method used to determine the frequency stability of investigated resonators is given here. This method was used for the acquisition of all the frequency stability results displayed in Chapter 6. The lock-in amplifier of the interferometric setup is used for such analysis, which is equipped with a PLL, thus enabling both open-loop and closed-loop measurements.

The steps required for the analysis of the frequency stability are presented in Figure 3.6. These measurements were conducted on a ceramic resonator (PBRC-2.00BR from Kyocera Corporation), which provides an excellent platform for optimizing the parameters of the lock-in amplifier, due to their known frequencies and not requiring a vacuum for measurements. In order to commence any tracking of the resonance frequency, the amplitude and phase response of the resonance under investigation needs to be accurately measured, with measurements for the quartz resonator given in Figure 3.6(a). From this plot, the resonance frequency f_r can be deduced, in addition to the phase lag at resonance ϕ_r. The quality factor is determined before such measurements (as will be discussed in Section 3.2.4), since the value of the low-pass filter has to be at least a factor of 2 smaller than the resonance linewidth Γ to ensure that the response is accurately resolved.

Depending on whether open-loop or closed-loop tracking is to be performed, two directions can be taken from here. For open-loop measurements, the frequency of the signal generator in the lock-in amplifier is set to f_r and the phase shift with respect to the drive recorded for a minimum duration of 1 minute. Then, using the measured phase response, the phase shift is converted to a frequency shift, as will be explained in Section 6.2. An exemplary 5-minute open-loop recording of f_r for the ceramic resonator is shown in Figure 3.6(b). The low-pass filter bandwidth and sampling rate of the demodulator were set to 3598 Hz and 28784 Sa/s, respectively. These values were chosen to withhold a 1:8 ratio between the filter bandwidth and sampling rate, which was recommended by the lock-in amplifier manufacturer. The order of the low-pass filter was found to have no influence on the measured frequency stabilities and therefore always set to 1.

When performing closed-loop tracking, both f_r and ϕ_r are given as parameters in the PLL controller of the lock-in amplifier. The bandwidth of the PLL phase detector has to be set and is normally set to the same value as that of the demodulator. Parameters of the PID controller are set automatically using a built-in PID advisor of the PLL. Only the bandwidth of the loop, also called *target bandwidth*, and the advise mode have to be set manually. The effect of this target bandwidth is a topic discussed in Section 6.6, while the advise mode is mostly set to PI mode (D = 0). For better tracking, the PLL has a built-in device under test (DUT) model for resonators, where one can set measured values of f_r and Q as parameters. Once all parameters

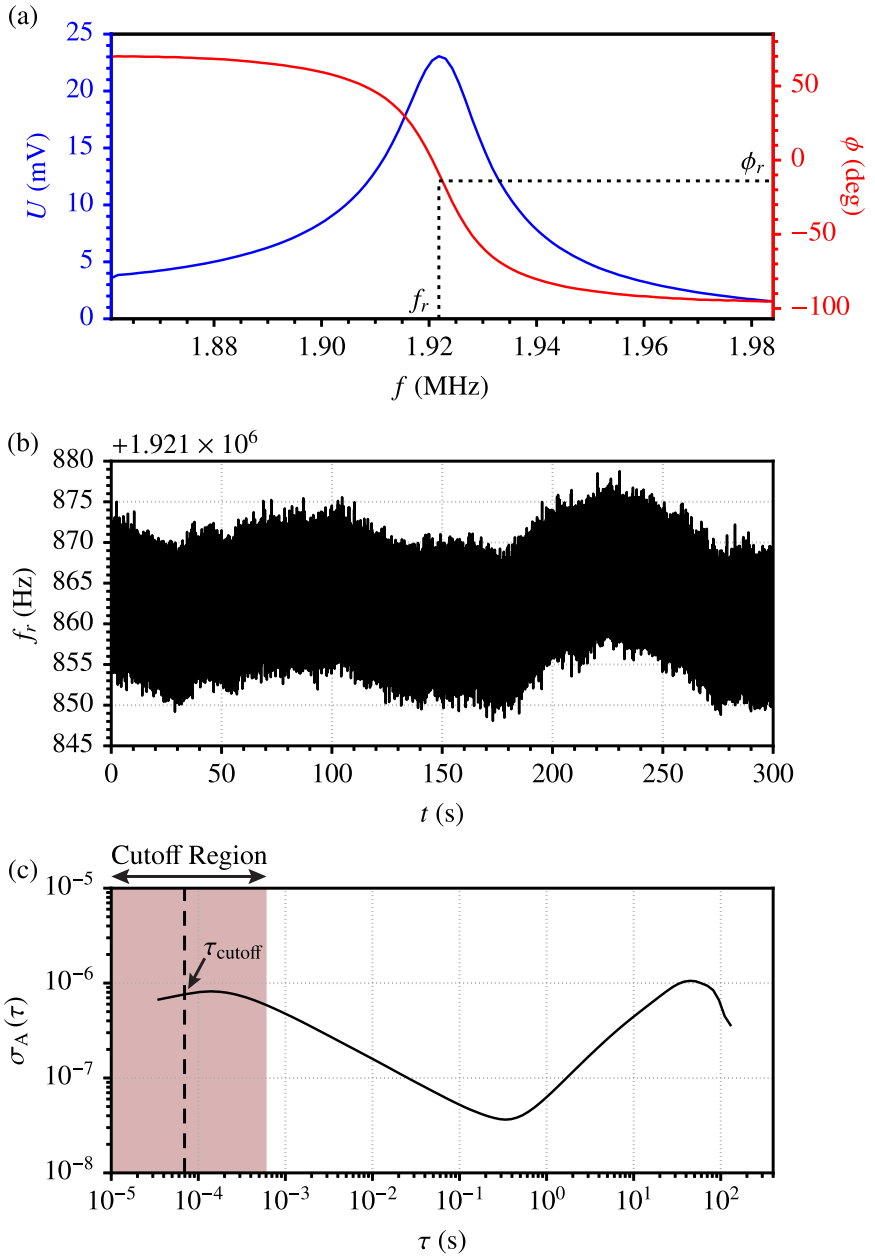

Figure 3.6: Demonstration of the measurement method for the determination of frequency stability using a ceramic resonator. (a) Measured amplitude and phase response of the resonator, from which the resonance frequency f_r and phase lag ϕ_r are extracted. (b) 5-minute open-loop recording of the resonance frequency. (c) Allan deviation of the data shown in (b). The integration time corresponding to the cutoff from the low-pass filter τ_{cutoff} has been highlighted in the plot. Reported Allan deviations in Chapter 6 leave the entire "cutoff region" out of plots, in order to only show the parts originating from the sample itself.

are set, the advisor sets the values of the controller, and tracking of f_r can commence.

After frequency tracking data have been acquired, the frequency stability is evaluated using the Allan deviation (see Section 2.4.2). The Allan deviation of the recording shown in Figure 3.6(b) is shown in Figure 3.6(c). A publicly available graphical user interface dedicated to the calculation of the Allan deviation using MATLAB was utilized for the analysis of all stability measurements presented here [175]. The integration time at which the low-pass filter has its cutoff is labeled τ_{cutoff}. Normally, the decrease in Allan deviation at low τ resulting from the low-pass filtering begins for τ-values slight larger than the τ_{cutoff}. To ensure that the reported Allan deviations only display features arising from the resonator response, parts of the Allan deviation within the so-called "cutoff region" (red-shaded area in Figure 3.6(c)) are neglected from all such plots shown in Chapter 6.

3.2.4 Quality Factor Measurements

Quality factors of mechanical resonators are typically deduced in one of two different ways, namely by means of the *bandwidth method* or by performing so-called *ringdown measurements*. The former is based on the definition of Q in electrical resonant circuits [9, 176]

$$Q = \frac{\omega_r}{\Gamma} = \frac{1 - 2\zeta^2}{2\zeta}, \tag{3.3}$$

with the resonance linewidth Γ defined as the width of the amplitude response at $1/\sqrt{2}$ of the peak amplitude, also called the full width at half maximum (FWHM). For slight damping ($\zeta \ll 1$), the definition of Q in Equation (3.3) is equivalent to the physical definition given in Equation (2.17), which is the only regime in which the bandwidth method is valid. Fitting measured amplitude responses with a Lorentzian function allows the extraction of Γ [16]. Then, Q can be calculated by dividing the resonance frequency with the linewidth according to Equation (3.3).

For high-Q resonators, where linewidths on the order of mHz are readily available, the bandwidth method requires incredibly slow frequency sweeps as well as a large number of data points in order to properly resolve the resonance linewidth. In cases where thermal drifts are present, which can occur from variations of the temperature in the measurement laboratory as well as, in the case of optical detection, power fluctuations of the readout laser (see Section 6.3), it becomes increasingly difficult to employ the bandwidth method. As such, the ringdown method is almost exclusively employed for the measurement of the Qs reported in this thesis.

When the drive signal responsible for actuating a resonator is abruptly switched off, dis-

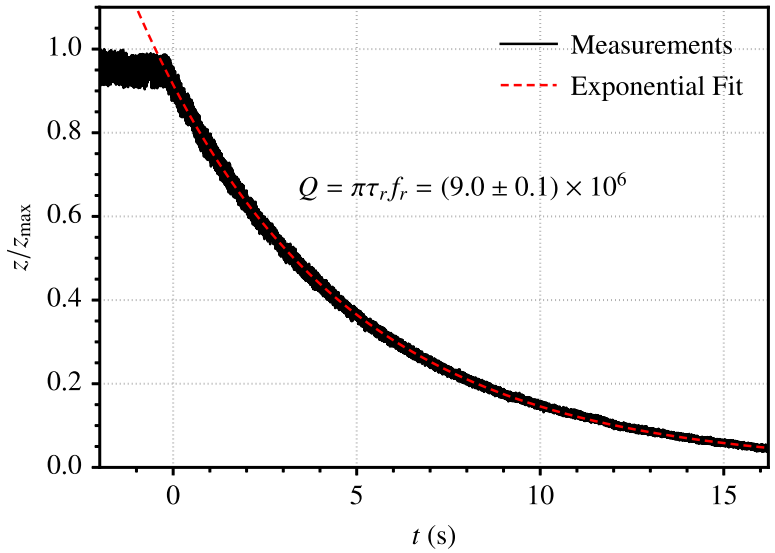

Figure 3.7: Decay of the normalized resonance amplitude over time upon switching off the drive signal at time $t = 0$ s, along with an exponential fit to the data, showing how the ringdown method works. From the time constant τ_r of the exponential and the resonance frequency f_r the quality factor can be calculated using the relation $Q = \pi\tau_r f_r$. The presented measurement is for the (3,3) mode of a uniform square membrane with $L = 1$ mm, $h = 50$ nm, and $\sigma = 166$ MPa.

sipation causes the amplitude to exponentially decay over time [16]. The time constant of the amplitude decay is directly proportional to the Q of the resonance, and measurement of this amplitude decay is the basis of the ringdown method. Evidently, a requirement of applying this method is the accurate recording of the amplitude over time. In this project, this is achieved using the lock-in amplifier. As a first step, both the amplitude and phase response of the resonance in question are measured. The extracted values of f_r and ϕ_r are used to lock the resonance in a closed-loop configuration, allowing the tracking of the amplitude over time. Once the amplitude is properly tracked, the drive signal is switched off abruptly and the exponential decay recorded. An exemplary ringdown measurement is shown in Figure 3.7 for the (3,3) mode of a square membrane. The time constant τ_r of the decay is extracted by fitting an exponential function of the type:

$$z(t) = z_0 e^{-t/\tau_r}. \tag{3.4}$$

Using this value of τ_r and the recorded f_r, the Q can be calculated using the following relation:

$$Q = \pi \tau_r f_r. \tag{3.5}$$

Reported uncertainties in Q are based on at least 5 recordings of the same decay, which accounts for fluctuations in the amplitude over time. Despite the occasional presence of thermal drifts, the uncertainty in the measurements of f_r is minimal and therefore not included in the calculation of the Q-uncertainty.

3.2.5 Thermal Responsivity Measurements

In this thesis, the thermal response of nanomechanical resonators is quantified using the relative thermal responsivity $\delta\mathscr{R}$ [16]. This quantity can be determined experimentally in a straightforward way, which will be described in this section. In simple terms, as already discussed in Section 2.3, $\delta\mathscr{R}$ quantifies the relative frequency shift per change in the resonator temperature. For nearly all the results shown here, relative responsivity is considered for the case of laser heating in the center of the resonators, meaning the temperature change arises from the photothermal effect. Experimentally, photothermal detuning of the resonance frequency can be measured by closed-loop tracking of the frequency and then vary the laser power. While this method provides the most accurate measurement of f_r at any given time, the main drawbacks are long acquisition times, since the resonance has to be locked for every sample and mechanical mode, and inability stay locked to the mode due to thermal drifts.

Instead of involving any frequency tracking scheme, the detuning is evaluated by measuring the Brownian motion spectrum for varying laser powers, as shown in Figure 3.8(a) for the (1,1) mode of a uniform square membrane. For any given laser power P, the center frequency of the Brownian motion peak is extracted and used to calculate $\delta\mathscr{R}$. A plot of the relative frequency shift corresponding to the measurements shown in Figure 3.8(a) is given in Figure 3.8(b) as a function of P. The frequencies can be observed to display a linear dependence on P and the slope of the shift is the relative responsivity. Since $\delta\mathscr{R}$ is a negative quantity, the absolute value is reported for the investigations shown in later chapters.

3.3 Ultrahigh Vacuum Setup

One of the main goals of this project is the reduction of surface friction, which is the main topic of Chapter 5. In order to properly clean and characterize surfaces of materials, an ultrahigh vacuum (UHV) environment is required [177]. The exact pressure at which UHV

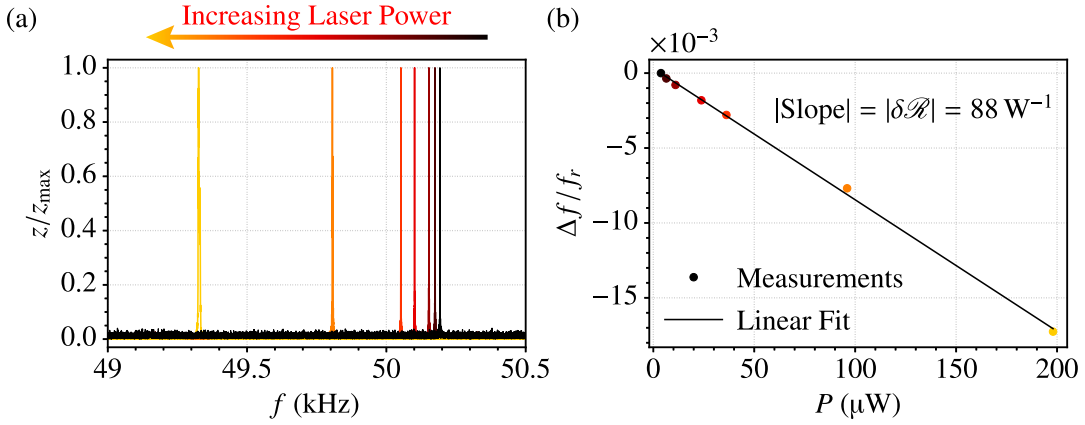

Figure 3.8: Experimental measurements of the relative thermal responsivity. (a) Brownian motion spectra of the (1,1) mode of a uniform square membrane for increasing laser powers focused on the membrane center. (b) Relative frequency shift versus laser power extracted from the Brownian motion peaks shown in (a). A linear fit to the data points is given as well, with the slope of the fit corresponding to the relative thermal responsivity. Parameters for the membrane in question are $L = 1$ mm, $h = 50$ nm, and $\sigma = 15$ MPa.

is achieved varies slightly in literature, but pressures $p \leq 10^{-9}$ mbar is generally considered UHV [178]. As such, an ultrahigh vacuum setup was built for this project, a drawing of which can be seen in Figure 3.9. Individual components of the setup will be discussed in the following section.

3.3.1 Setup Components

The ultrahigh vacuum chamber was designed and manufactured by PREVAC sp. z o.o. It is a cylindrical stainless steel (SS304) chamber with a diameter of 256 mm not including the vacuum flanges. Its vacuum connections are built entirely of ConFlat (CF) flanges, which consist of a knife-edge machined into the flanges flat surface [179]. The seal mechanism works by placing a soft metal gasket between the knife-edges of a pair of flanges and then uniformly tightening a set of bolts on the outer edges of flanges. As these bolts are tightened, the knife-edge cuts into the metal gasket, with the deformed metal now filling manufacturing defects in the flange, and a leak-tight seal is therefore achieved. To minimize the risk of leaks, annealed copper gaskets were used in this project, since the annealing results in even softer copper.

The main chamber is pumped down from atmospheric pressure using a rotary vane pump (Duo 3 M from Pfeiffer Vacuum GmbH), which functions as the roughing pump, and a turbopump (HiPace 80 from Pfeiffer Vacuum GmbH), serving at the high vacuum pump. For

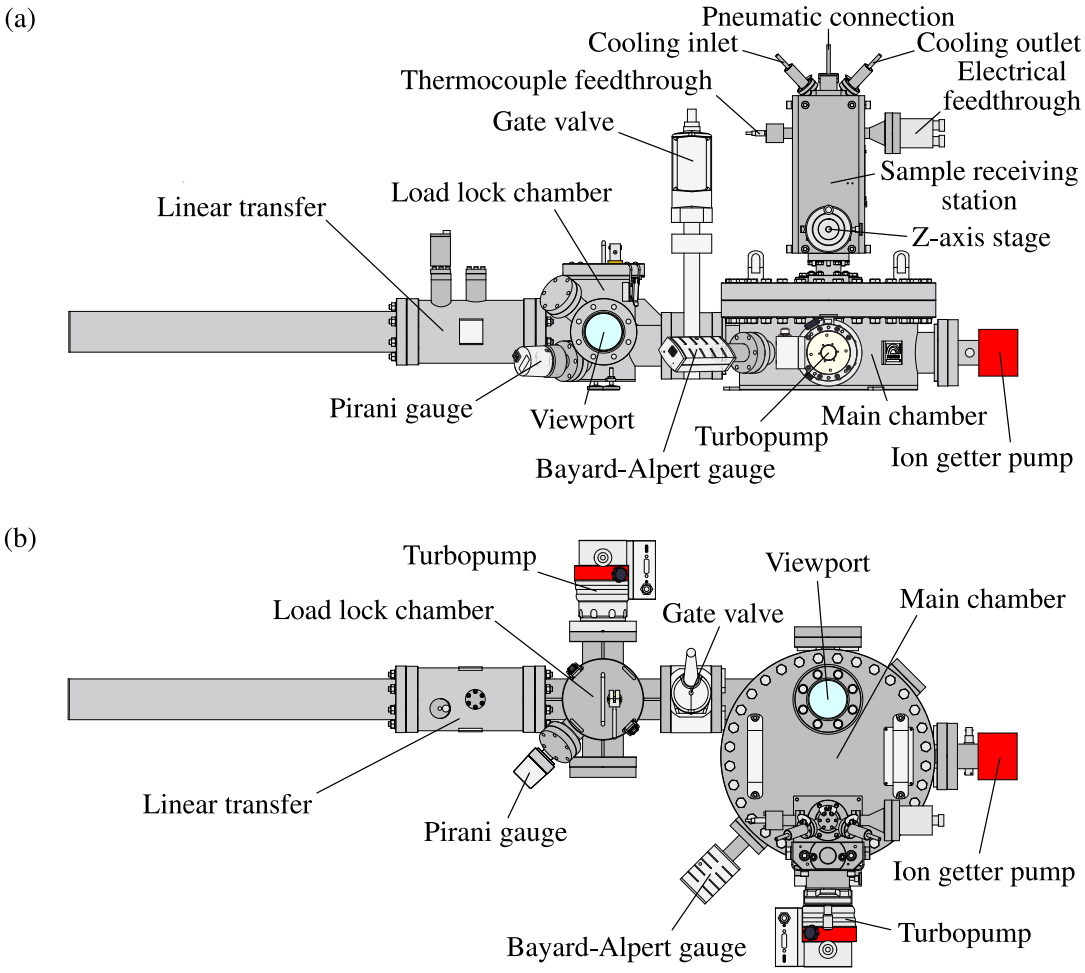

Figure 3.9: Drawing of the ultrahigh vacuum setup employed in this project, including a side view (a) and top view (b) projection of the setup. The main vacuum chamber is pumped down using both a turbopump and an ion getter pump, in conjunction with a bakeout of the chamber body using heating tape (not shown in the sketch). Vacuum pressure is measured using a Bayard-Alpert gauge. Samples loaded into the chamber are attached to the sample receiving station. Resistive heating of samples is achieved using the electrical feedthrough of the receiving station, while the cooling inlet/outlet allows both air cooling and liquid nitrogen cooling. The temperature of the sample holder is monitored using a thermocouple. A pneumatic connection enables exchange between sample heating and cooling utilizing compressed air. Samples are loaded into the UHV by means of a load lock chamber, separated from the main chamber using a gate valve. The load lock is pumped using a turbopump and its pressure measured using a Pirani gauge. A linear transfer mechanism is employed to move samples from the load lock and into the main chamber.

pressures $p \leq 10^{-7}$ mbar, an additional ion getter pump (NEXTorr D500-5 from SAES Getter S.p.A.) is used to further reduce the pressure. The vacuum pressure is monitored using

a Bayard-Alpert gauge (PBR 260 from Pfeiffer Vacuum GmbH), which can accurately measure pressures down to $p = 5 \times 10^{-10}$ mbar. An additional rough estimate of the pressure for values as low as $p = 1 \times 10^{-10}$ mbar can be made using the current readout of the ion getter pump. The exact process employed to achieve an ultrahigh vacuum, which includes a bakeout step, is explained in the next section.

Before loading samples into the UHV chamber, they are secured to a sample holder specifically designed for heating and cooling (PTS 1000 RES/C-K from PREVAC sp. z o.o.). The PTS sample holder allows heating of samples to temperatures up to 1000 °C and cooling down to −170 °C. Samples are loaded into the chamber by placing the sample holder on a sample receiving station. The receiving station can be seen sticking out of the main chamber body in Figure 3.9(a). It is equipped with a manual z-axis manipulator, which is used to move the sample holder from transferring position to measuring position. By measuring position, it is meant that the sample is located directly below the anti-reflection coated fused silica viewport positioned on top of the chamber, which allows optical transduction of the samples. This viewport can be seen in Figure 3.9(b).

A pneumatic valve is employed to move the sample holder between heating and cooling operation using compressed air. When samples need to be exchanged, the valve can be set to transfer mode, which means closing for the compressed air supply. Heating of the sample holder is achieved using resistive heating. High voltage cables used for resistive heating are connected to the sample holder using the electrical feedthrough of the sample receiving station. Cooling is achieved employing a sapphire sphere located below the sample holder. The cooling process can be accelerated using compressed air, while liquid nitrogen allows for cooling down to the aforementioned limit of $T = -170$ °C. Sample holder temperature is constantly monitored using a thermocouple (type K).

To avoid venting the main chamber every time a sample has to be exchanged, a load lock chamber (designed by PREVAC sp. z o.o.) is used for sample loading. This chamber has a dedicated mounting station for the PTS sample holder. After placing the sample inside the load lock chamber, the load lock is pumped down by means of a membrane pump (MVP 015-2 from Pfeiffer Vacuum GmbH) and a secondary turbopump (HiPace 80 from Pfeiffer Vacuum GmbH) to pressures $p \sim 10^{-7}$ mbar, monitored using a Pirani gauge (PKR 251 from Pfeiffer Vacuum GmbH). Once the base pressure has been reached, a gate valve (series 10.8, number 10836-E01/08 from VAT Vakuumventile AG) separating the load lock and the main chamber is opened, so that samples can be transported inside the UHV. A linear transfer mechanism is responsible for loading the sample holder into the main chamber, consisting of an arm that can lock onto the sample holder and a rotary feedthrough located outside the chamber, which can be used to manually move the transferring arm. In order to accept samples, the sample receiving station of the main chamber is moved down during the transfer process to be aligned

in height with the load lock arm height. A viewport located on a side flange of the load lock allows monitoring of the sample holder and transferring arm positions during transfer.

3.3.2 Chamber Evacuation Process

In this section, a detailed description of the process with which the UHV system is evacuated down to pressures $p \sim 10^{-10}$ mbar is provided. As mentioned in the previous section, a rotary vane pump is used as the roughing pump, enabling a rough vacuum pressure $p \sim 10^{-3}$ mbar, which reduces the load on the turbopump. The rotary vane pump is connected in series with the turbopump. Typically, the rotary vane pump is allowed to operate alone until $p < 1 \times 10^{-2}$ mbar, upon which the turbopump is turned on, which further reduces the pressure to $p < 1 \times 10^{-7}$ mbar within 1 day of operation. This initial pump down can be sped up by venting the chamber with nitrogen instead of air.

If one were to rely entirely on vacuum pumps, the vacuum pressure typically approaches a limiting value in the $\sim 10^{-8}$ mbar range, below which the pressure decreases at a significantly slower rate. The reason for this is the adsorption of water, in addition to other less significant rest gases, to the chamber walls, with the vapor pressure of the water limiting the final pressure of the vacuum [178]. While this water slowly desorbs and gets pumped out over time, this process is incredibly slow and might even take years. To accelerate this desorption process, a chamber bakeout is performed. In simple terms, a bakeout is the systematic heating of the entire vacuum system to temperatures above 100 °C for a given amount of time, typically on the order of days. Bakeout of a UHV system can be accomplished in a number of different ways, including the use of heating tapes, jackets, tens, or even placing the entire system inside a dedicated oven [179].

For this UHV system, heating tapes (metal braided type MB from Hemi Heating AB) are employed for the bakeout process, since these allow more flexibility in the case additional components are added to the system. The tapes are wrapped around all surfaces of the chamber, including flanges and the sample receiving station. In the later stages of the project, the whole UHV system was placed on pillar supports, allowing the heating tape to be wrapped around the bottom of the chamber as well and therefore a more efficient bakeout. The different tapes are connected in series using a daisy chain cable set (DCCF-4 from Hemi Heating AB), and the cable set is connected to a temperature controller (HTC 5500 LT from Hemi Heating AB). This controller has a built-in PID controller, which can be used to manage the temperature setpoint, as well as the duration of the temperature ramp-up. The temperature controller is equipped with a thermocouple (type K), which monitors the temperature and uses this measured value to actively adjust the PID controller settings.

While the heating tapes are capable of temperatures up to 400 °C, the temperature setpoint is restricted here by the 120 °C limit of the turbopump. To circumvent this limit, the controller thermocouple is placed on the turbopump flange and the temperature setpoint fixed at 110 °C to ensure a low enough temperature on the turbopump. Nonetheless, despite the temperature setpoint, the turbopump is cooled additionally using a water chiller (WRK 508-40 from Lahntechnik GmbH) during annealing. For the remainder of the system, temperatures as large as 180 °C are possible, which is constantly monitored using a steak thermometer. In order to thermally insulate the system and distribute the heat evenly across all components, the entire UHV system is wrapped in aluminium foil (ALU-FOLIE-500-25 from Vakuum Komponenten & Messtechnik GmbH) [180]. Overall, the chamber is left to bakeout for at least 2 days in this configuration, ensuring that most water has desorbed from the chamber walls.

Once the system has been baked for a while, the heating is switched off and the system allowed to slowly cool down. Typically, this bakeout process alone results in pressures of 5×10^{-10} mbar to 1×10^{-9} mbar after the chamber has cooled down to room temperature, depending on the duration of the bakeout. To further reduce the pressure to $p \leq 1 \times 10^{-10}$ mbar, an ion getter pump is utilized. As the name would suggest, this pump consists of both a sputter ion pump and a non-evaporable getter (NEG) pump, both working on different principles [181]. The getter material of the NEG pump has to be activated before it can begin to pump [182, 183]. Here, activation refers to heating it to 550 °C for 1 hour, removing all gas molecules adsorbed in the material as well as surface oxide, which saturates the pump anytime it is exposed to atmospheric pressure. The activation thus "resets" the getter, but this reset can only be done a limited amount of times (100 times according to the manufacturer). Since lots of particles are released during activation, this process is typically carried out shortly after the bakeout, since the warm temperature of the chamber minimizes adsorption of the released species. Finally, once the activation has been completed, the sputter ion pump is turned on and the base pressure slowly reached as the chamber cools down to room temperature.

3.3.3 Sample Annealing Procedure

Essential for the investigation shown in Chapter 5 is the ability to anneal samples in an ultrahigh vacuum since this should clean the sample surface completely [82]. A description of the annealing procedure employed in this thesis is given here. As mentioned in Section 3.3.1, samples can be heated up to temperatures of 1000 °C based on resistive heating of the PTS sample holder. A dedicated heating power supply (Heat3 from PREVAC sp. z o.o.) with a built-in PID controller is used to manage the sample holder temperature. The PID controller is used both to set and ramp up the applied current, which it actively regulates by measuring

the sample holder temperature using a dedicated thermocouple. For the sample holder used here, the current ramp is set to 1 A/min, while the maximum current is fixed at 8.6 A, both of which are values provided by the manufacturer.

Before annealing begins, the sample holder is moved as far away from the optical viewport by means of the z-axis manipulator. This is necessary in order to protect the viewport from exposure to the very high temperatures of the sample holder. In addition, the pneumatic valve is set to heating mode, after which heating can be commenced. Given the rather low current ramp-up, ramping of the temperature to the setpoint can take as long as 1 hour depending on the desired final temperature. Nonetheless, any annealing time specified in Chapter 5 is counted from the moment the setpoint has been reached. After samples have been annealed for the desired duration, the heating power supply is switched off and the pneumatic valve moved to cooling mode. Cooling to room temperature typically takes 30 minutes, with the cooling accelerated by applying compressed air to the cooling inlet of the sample receiving station. After having been cooled to room temperature, the sample holder is moved back up to the viewport, allowing measurements to be performed.

3.3.4 Optical Transduction Integration

The aforementioned optical viewport located on top of the UHV chamber (see Figure 3.9(a)) allows integration with an optical transduction scheme. While the electrical feedthrough of the chamber also allows additional transduction schemes, optical methods are employed for all the results presented here due to their flexibility and ease of use. In the simplest implementation scheme, the entire UHV setup is placed on the same optical table as the laser-Doppler vibrometer and aligned with its objectives. A photograph of such a scheme is given in Figure 3.10(a). The photo also highlights various components not included in Figure 3.9. High-voltage cables used for resistive heating of the sample holder can be observed, in-addition to the thermocouple used for temperature monitoring. Hoses used for the pneumatic connection and the sample holder cooling are shown connected to the chamber as well. Heating tape and aluminium foil used for the bakeout of the UHV system can be observed as well and are left on to avoid having to re-wrap the system every time a bakeout needs to be performed. The inset of Figure 3.10(a) shows a sample inside the UHV during annealing, as indicated by the glow of the sample holder. Figure 3.10(b) shows a second perspective of the setup shown in Figure 3.10(b), more clearly displaying certain components of the setup, such as the hose used for water cooling of the turbopump.

While the scheme presented in Figures 3.10(a) and 3.10(b) provides easy alignment with the vibrometer optics and therefore the largest signal-to-noise ratio for the measurements, the

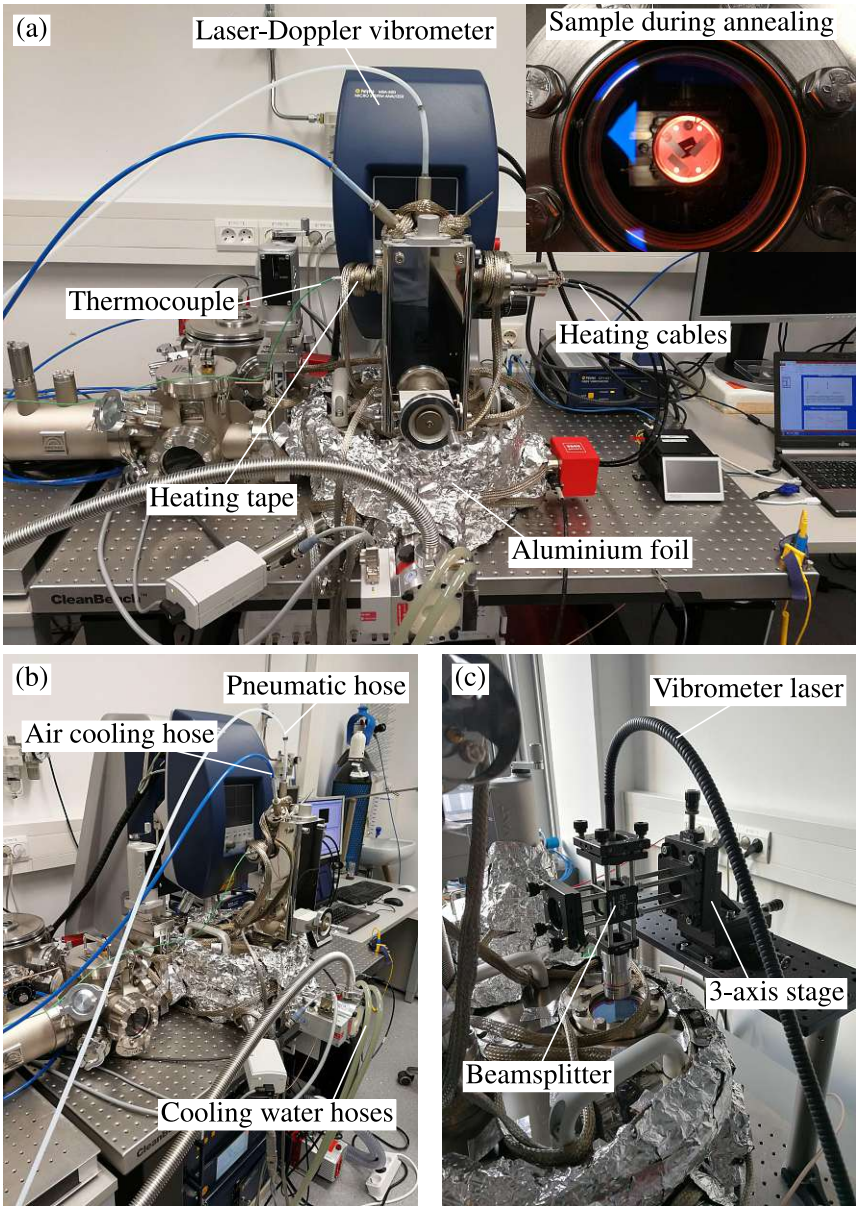

Figure 3.10: Implementation of an optical transduction scheme with the ultrahigh vacuum setup. (a) Photograph of the UHV system placed on an optical table and aligned with the laser-Doppler vibrometer. Various components of the setup have been highlighted for clarity. The inset shows the sample holder in vacuum during an annealing process. (b) A second perspective of the setup shown in (a), more clearly displaying certain components. (c) Custom-build optical microscope head to which both the vibrometer laser and the actuation laser can be attached and thus enabling sample measurement without the need to move the entire system.

downside is the need to move the entire UHV system, including the load lock chamber, for every required measurement. For this reason, another method of optical transduction was developed for the later parts of the project. The solution was to build a custom microscope head, to which the lasers of the vibrometer could be attached. An early version of such a microscope is shown in Figure 3.10(c), consisting of two optical pathways, one being for the vibrometer laser and the second for the actuation laser. The two lasers are recombined using a beamsplitter (CCM1-PBS252/M from Thorlabs GmbH) and sent to an objective lens (the same ones used for the Polytec vibrometer). Control of the laser positions on the sample is achieved using a manual 3-axis translation stage (PT3A/M from Thorlabs GmbH), which is secured to an optical breadboard elevated using four pillar posts to the height of the UHV chamber. Visualization of the samples was done by means of a second beamsplitter, to which a complementary metal oxide semiconductor (CMOS) camera (UI-5220SE from Integrated Dynamic Solutions, Inc.) is attached (not shown in Figure 3.10(c)). To avoid including a third beamsplitter and therefore additional loss of laser power along the optical pathway, no white light source is used, instead using the laser light reflected off the samples for visualization.

3.4 Finite Element Analysis

Despite analytical models existing for many of the mechanical properties studied here, these are often incomplete or limited to standard resonator geometries such as strings and membranes [16]. As such, simulations of the mechanical properties accompany many of the measured results shown in this thesis. These simulations are exclusively performed using COMSOL Multiphysics, which is a commercially available simulation software based on the finite element method. Various properties are simulated, with three main categories emerging: Quality factor, phononic bandgap, and thermal responsivity. Each of these three types of simulations will be discussed separately.

3.4.1 Structural Mechanics Simulations

Before explaining how the different physical quantities are simulated, a general introduction to the mechanical simulation configuration is given, which applies to all simulations performed in this thesis. In order to simulate mechanical properties of resonators, the *Structural Mechanics Module* of COMSOL is employed [184]. This module is specifically designed for handling the simulation of, among others, static, eigenfrequency, transient, and frequency response problems related to structural mechanics. Both 2D and 3D models can be built and studied, depending on the problem at hand.

For the resonators studied here, with typical thicknesses on the order of tens of nanometers, but lateral dimensions of several millimeters, a shell interface is employed. Using this interface, it suffices to draw a two-dimensional projection of the geometry of interest in the xy-plane, while the thickness is given as a parameter in the shell interface. A linear elastic material model is used, with most material properties of the SiN based on values found in the literature [101]. For all structural mechanics simulations, it is necessary to define the Young's modulus E, Poisson's ratio ν, and mass density ρ. The tensile stress of the resonators investigated here is accounted for by assuming a bidirectional homogeneous stress $\sigma_{xx} = \sigma_{yy} = \sigma_{\text{film}}$, where σ_{film} is the stress of the SiN film taken from experiments. A fixed constraint is applied to the anchors of the resonators, which translates into zero motion allowed on the chosen edges.

Having set up the simulation geometry and associated physics, the next step is to mesh the geometry, i.e. divide the geometry into smaller regions in which the physical equations are solved. Given that multiple non-uniform resonator geometries are studied here, a triangular mesh is chosen to mesh corners and round edges more densely. In general, making the mesh finer corresponds to more accurate results, but also increases the memory requirements significantly. As such, mesh refinement studies are performed for each type of simulation, where the mesh is made increasingly fine until the simulated quantities change by minimal amounts when making the mesh even finer, i.e. the values have converged. The exact mesh size at which convergence is reached depends on how complicated the geometry is, but a general rule of $< 10\%$ change can be applied to all the simulations shown in this thesis. An example of an as-built clamp-widened string geometry can be observed in Figure 3.11(a), with the inset highlighting the mesh in the narrowest region of the string. For increased accuracy, it is essential to have multiple mesh elements along the narrowest regions of the geometries.

The final step is to choose which type of study, or analysis, one wishes to perform on the geometry. Since the focus is on mechanical resonators, where the properties of specific mechanical modes are of interest, an eigenfrequency study needs to be performed. While this of course means that mechanical eigenfrequencies are simulated as opposed to the resonance frequency measured in the experiments, one has to keep in mind that for slight damping the two frequencies are nearly equal (see Equation (2.12)) [16]. Given that only high-Q resonators are investigated here, the slight damping assumption holds and the eigenfrequency study can be applied.

For the non-uniform geometries studied here, such as clamp-widened strings and phononic crystal membranes, the stress will not be uniform throughout the resonator. If a pure eigenfrequency study is employed, the stress is assumed to be uniform throughout the resonator and the simulated eigenfrequencies typically overestimated. Therefore, a stationary study step has to be included prior to the eigenfrequency study, which serves to simulate the stress redistri-

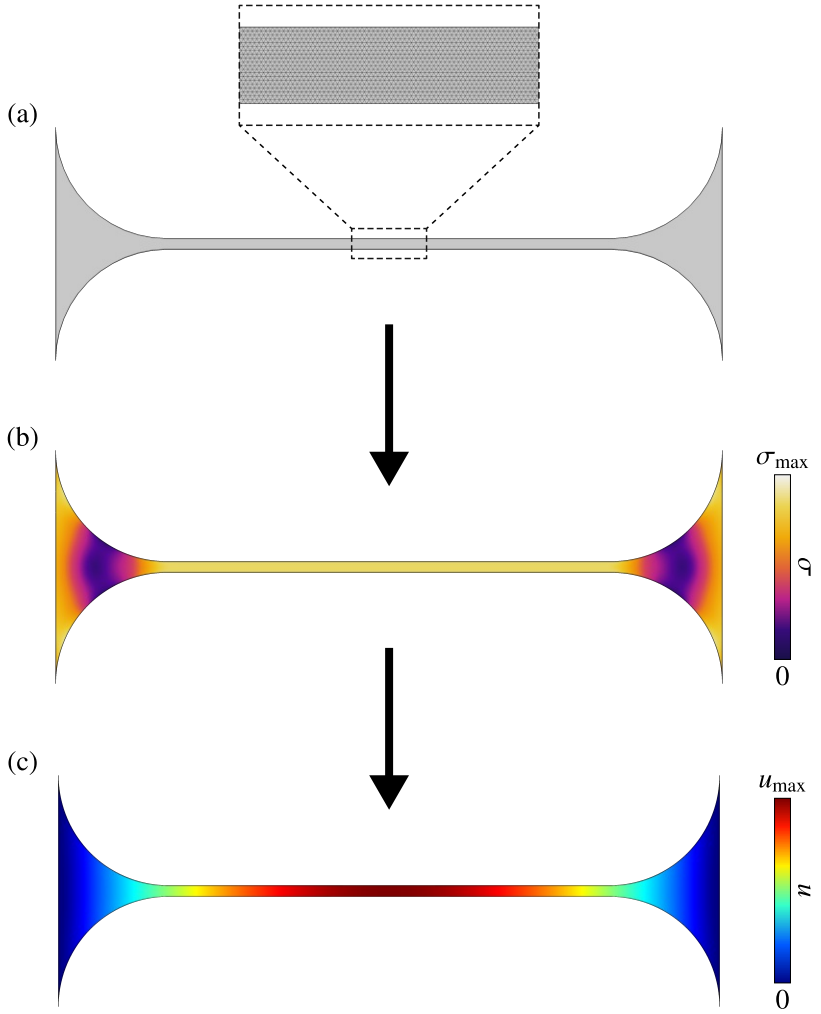

Figure 3.11: Different steps required to simulate the properties of strained mechanical resonators. (a) An as-built geometry of a clamp-widened string resonator. The inset shows the triangular mesh in the narrowest region of the string. (b) Simulated stress distribution in the string acquired through a stationary study step. (c) Displacement field of the string, resulting from performing an eigenfrequency study using the simulated stress distribution in (b).

bution in the resonator. A simulation of the von Mises stress σ_v of a clamp-widened string is given in Figure 3.11(b), clearly showing the non-uniformity of the stress [185]. Given the assumption of a bidirectional plane stress and no shear stress, the von Mises stress can be shown to be equivalent to the tensile stress $\sigma_v = \sigma$ [147].

The eigenfrequency simulation will then use the simulated stress distribution in order to accurately simulate the mechanical eigenmodes of the resonator, with the fundamental out-of-plane mode of a clamp-widened string shown in Figure 3.11(c). Mechanical properties of

higher-order modes can be obtained as well. The validity of this approach will be made even clearer in the following section.

3.4.2 Quality Factor

Simulations of the mechanical quality factor are central to the results given in Chapter 4 and will also be employed for the analysis of certain results in Chapter 5. The necessity to simulate Qs stems from the lack of analytical models of dissipation dilution for geometries other than uniform strings and membranes [16]. For nontrivial geometries, a numerical approach is currently the most effective way to predict Qs. More specifically, the parameter that is simulated is the dissipation dilution factor, meaning that this approach is only valid for strained resonators. The method works by evaluating the energies of the system, as was first shown analytically by Unterreithmeier *et al.* [37]. Recalling the discussion in Section 2.2.4, the dissipation dilution factor α_{dd} in the linear regime, i.e. for small vibrational amplitudes, is given by the ratio of the energy stored in the tension W_{ten} to the energy stored in the bending W_{bend}. Given that $W_{\mathrm{ten}} \gg W_{\mathrm{bend}}$, it means that W_{ten} can be equivalently defined as the total stored energy W. Employing Rayleigh's method, which states that the energy commutes completely between its kinetic and potential state, the total stored energy can be assumed to also be equal to the maximal kinetic energy W_{kin} of the system, $W = W_{\mathrm{kin}}$. Both W_{bend} and W_{kin} can be calculated directly using the simulated mode shape of the resonance of interest, and the dissipation dilution factor is then given as $\alpha_{\mathrm{dd}} = W_{\mathrm{kin}}/W_{\mathrm{bend}}$.

Once α_{dd} is known, the Q can be estimated using Equation (2.74), which states that $Q \approx \alpha_{\mathrm{dd}} Q_{\mathrm{int}}$, with Q_{int} being the intrinsic quality factor. Q_{int} can then be made as a fit parameter, which can account for variations in Q from sample to sample, with this variation possibly resulting from fabrication related issues. Alternatively, a guess of Q_{int} can be made by using Equation (2.72), $Q_{\mathrm{int}} = \left(Q_{\mathrm{mat}}^{-1} + Q_{\mathrm{surf}}^{-1}\right)^{-1}$, using the parameters of bulk losses Q_{vol} and thickness-dependent surface losses Q_{surf} for SiN [48]

In order to show the rationale behind this approach, a comparison between FEM simulations and analytical calculations of Q for uniform resonators is plotted versus frequency in Figure 3.12. The case of a string resonator with dimensional parameters $L = 1$ mm, $w = 5$ µm, and $h = 50$ nm is displayed in Figure 3.12(a), where the Q of the first 10 out-of-plane modes have been simulated and compared with Equation (2.81). Evidently, the simulated results agree with the analytical values to within 3%. The small discrepancy could be a result of the mesh not being dense enough at the anchors of the string, which is the region of largest curvature and therefore has the biggest influence on the Q (see Figure 2.6(b)).

Simulated Qs for the first 10 harmonic ($n = j$) modes of a square membrane with $L =$

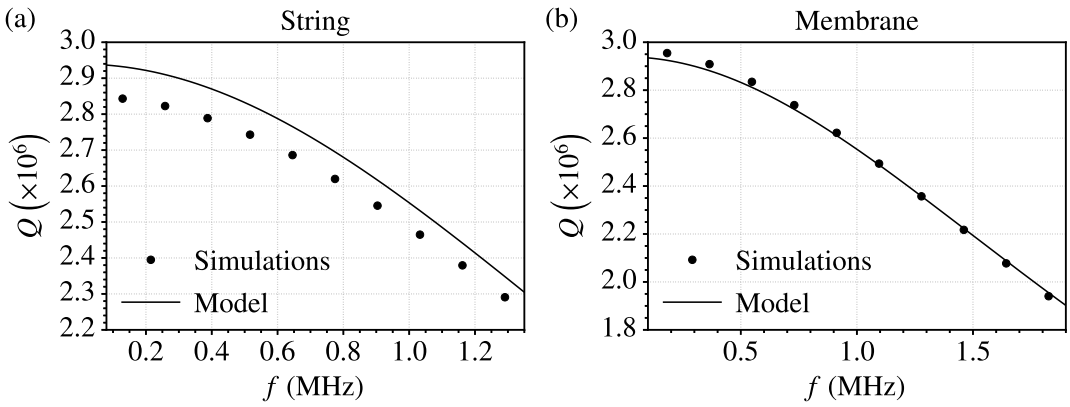

Figure 3.12: Finite element method simulations of the quality factors of strained resonators. (a) Simulated Qs for the first 10 out-of-plane modes of a string resonator with dimensional parameters $L = 1$ mm, $w = 5$ µm, and $h = 50$ nm. Calculations using the analytical model for dissipation dilution of a string are shown as well [16]. (b) Simulations of Q for the first 10 harmonic ($n = j$) modes of a square membrane with $L = 1$ mm and $h = 50$ nm, along with a comparison to the dissipation dilution model for a membrane. Assumed material parameters for the SiN are $E = 250$ GPa, $\nu = 0.23$, $\rho = 3000$ kg/m^3, and $\sigma_{\text{film}} = 200$ MPa.

1 mm and $h = 50$ nm can be seen in Figure 3.12(b). The simulations are compared with analytical calculations of Q using the α_{dd} given in Equation (2.84). Good agreement is observed between the two sets of data, which shows the accuracy and flexibility of this approach. Application of the method to nontrivial geometries is discussed in Chapter 4.

3.4.3 Phononic Bandgap

Phononic crystal membranes are employed for part of the investigation shown in Chapter 5 and central to the results in Chapter 7. All PnC samples employed in this thesis were fabricated in-house using the methods discussed in Section 3.1. FEM simulations are essential to the proper design and control of the frequencies of PnC membranes and the simulation setup will therefore be discussed in this section. At the same time, this section provides a detailed description of the PnC membrane design used here.

The chosen phononic crystal design employed in this thesis is taken from the work of Tsaturyan *et al.*, since this is the first and most well-studied soft-clamped phononic crystal system [39]. For this design, the rectangular unit cell resulting in the honeycomb lattice of the PnC membranes is shown in Figure 3.13(a). Evidently, the PnC is defined by its lattice constant a, the size of the unit cell in the x-direction, and hole radius r, which has a fixed relation to the lattice constant given as $r \sim 0.26a$. The unit cell size in the y-direction is

1.54a, while the tether width size is set to 0.04a.

A template for the simulation of the phononic band structure of a given unit cell has in fact been provided by COMSOL themselves [186]. The simulations performed here were based on this template as well. To simulate phononic bandgaps, an eigenfrequency study is required. However, as shown by Tsaturyan *et al.*, the redistribution of the stress, as a result of the narrow tethers in the unit cell, has to be simulated as well. If the stress is assumed to be homogeneous throughout the resonator, the size of the bandgap is significantly overestimated [147]. As such, a stationary study step is included prior to the eigenfrequency step. For the stationary analysis, the displacement at the unit cell edges is set to zero, i.e. fixed constraint is applied. In the eigenfrequency study, which now contains the correct stress distribution, the fixed constraint is replaced by a Floquet-Bloch periodicity in both the x- and y-directions. The wavevector is then swept across the first Brillouin zone, which can also be seen in Figure 3.13(a). An exemplary simulation of the phononic band diagram for the first four bands can be seen in Figure 3.13(b). For this simulation, a lattice constant $a = 140$ µm was chosen. The phononic bandgap can be observed in the frequency region $f \sim 0.68 - 0.82$ MHz. A complete bandgap is not achieved, which is a consequence of the extreme ratio of membrane thickness to lattice constant [187], as has been reported in previous investigations [39, 77, 188]. Only stiff in-plane modes persist in the bandgap, which should not influence the properties of the out-of-plane modes of interest. As result, the term quasi-bandgap is often used to describe the band structure of such resonators.

In order to built a finite-sized PnC membrane, the rectangular unit cell is repeated over an area $A \sim (20.5 \times a)^2$, with an as-built PnC membrane geometry shown in Figure 3.13(c). At the membrane center, some holes are displaced and removed to form a central defect in the PnC. A number of mechanical modes are then localized to the defect, and therefore given the term defect modes. These modes will display the soft clamping effect, which was introduced in Section 2.2.4.3, and are therefore of interest for high-Q applications [39, 40, 77]. The chosen amount of unit cells in a membrane is similar to that of Tsaturyan *et al.* [39], ensuring that the displacement completely decays at the edges of the membrane.

Defect modes are simulated in a similar dual-step manner to the phononic bandgap, i.e. first employing a stationary step to obtain the stress redistribution, followed by an eigenfrequency analysis. In this case, fixed constraints are applied to the edges of the PnC membrane for both the stationary and eigenfrequency study steps. Given that defect modes are higher-order modes of the PnC membrane, one has to search for eigenfrequencies around the bandgap region. As will be made more clear in Chapter 7, the frequencies of both bandgaps and defect modes follow a behavior similar to that of uniform membranes [16]. Based on fits to simulated bandgap and defect mode frequencies, an effective frequency can be defined, allowing the simulation of defect modes without the need of first simulating the phononic bandgap.

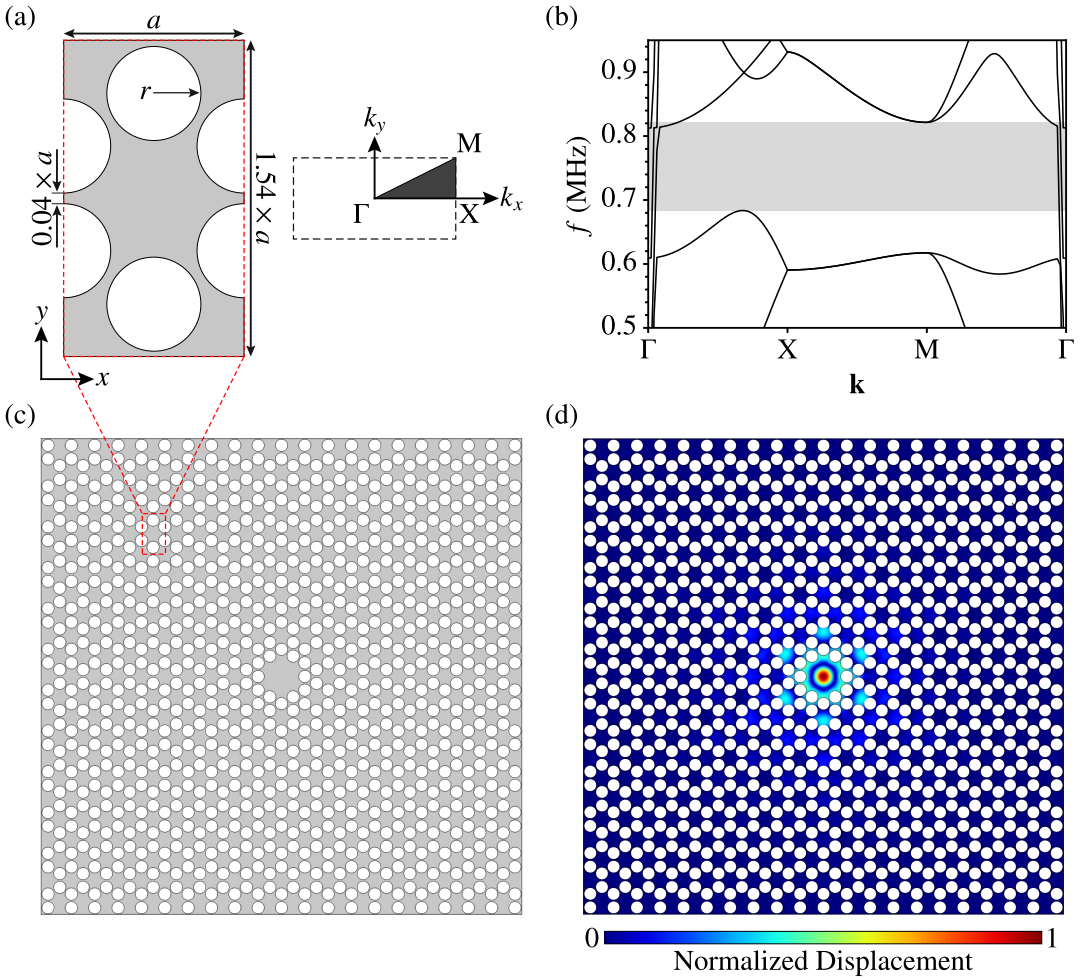

Figure 3.13: Finite element method simulations of phononic bandgaps and defect modes. (a) Rectangular unit cell of the PnC design used here along with the corresponding first Brillouin zone, similar to the design of Tsaturyan *et al.* [39]. (b) Simulated band diagram for a unit cell of lattice constant $a = 140$ µm. (c) Sketch of a phononic crystal membrane built by repeating the unit cell over an area $A \sim (20.5 \times a)^2$, surrounding an engineered defect at the membrane center. (d) Simulation of the displacement field for the fundamental defect mode of a PnC membrane with $a = 140$ µm. Material parameters for the simulations shown in (b) and (d) are $E = 250$ GPa, $\nu = 0.23$, $\rho = 3000$ kg/m^3, and $\sigma_{\text{film}} = 200$ MPa.

A simulated displacement field for the fundamental defect mode of a PnC membrane with $a = 140$ µm is shown in Figure 3.13(d). The displacement can be observed to be largest at the defect center, while exponentially decaying in the PnC, thus validating the FEM simulation approach to studying soft clamped membranes.

3.4.4 Thermal Responsivity

The last type of FEM simulation performed in this thesis is of the thermomechanical properties of nanomechanical resonators. More specifically, the main property to simulate is the relative responsivity $\delta\mathscr{R}$, since maximizing this quantity is essential to thermal sensor performance. Furthermore, since this parameter is measured directly (see Section 3.2.5), it can be used to assess the credibility of the simulations. These simulations are of significant relevance to the results shown in Chapter 7.

For thermal response simulations, the shell interface can be used again to simulate the mechanical properties. The thermomechanical properties are simulated by adding a secondary physics interface, namely the *Heat Transfer in Shells Interface*, which is a part of the *Heat Transfer Module* of COMSOL [105]. As the name would suggest, this interface is specifically designed to simulate heat transfer in layered materials, enabling the modeling of heat transfer through conduction, convection, and radiation. In order to perform these simulations, the following material parameters need to set as well: Coefficient of thermal expansion α, thermal conductivity κ, and specific heat capacity c_p.

Given that most experiments are performed in a high vacuum, heat transfer through convection is not included in the simulations. Emission of thermal radiation has been shown to potentially dominate the heat transfer in large SiN membranes and therefore needs to be accounted for [103]. This is achieved by adding a Surface-to-Ambient Radiation node to the Heat Transfer interface. For this reason, one has to define the surface emissivity ϵ_λ as an additional material parameter in the simulations.

It is crucial to set the correct boundary conditions for these simulations since these have to match those of the experiments in order to get accurate results. For all heat transfer simulations, the rim of the resonators is assumed to be at a fixed temperature, similar to the case for the analytical models discussed in Section 2.3. Given that sample heating is mainly performed using lasers focused on the resonator center, this should be a reasonable assumption. It could be argued that one should simulate the entire sample chip and not the resonator alone, to account for heat transfer from the resonator into the chip. However, in the case of SiN resonators on Si substrates, previous investigations have shown a negligible change in simulated thermal properties when including the sample chip in the simulations [106]. As such, only heat transfer in the resonator alone is simulated, with the resonator rims being fixed at room temperature.

The last step is to define a suitable heat source. Specifically for the case of laser heating, COMSOL has designed a Deposited Beam Power node in the Heat Transfer interface, which has a number of built-in beam profiles, as well as allowing one to define custom profiles. For the simulations performed here, the built-in Gaussian profile of the node is employed, which

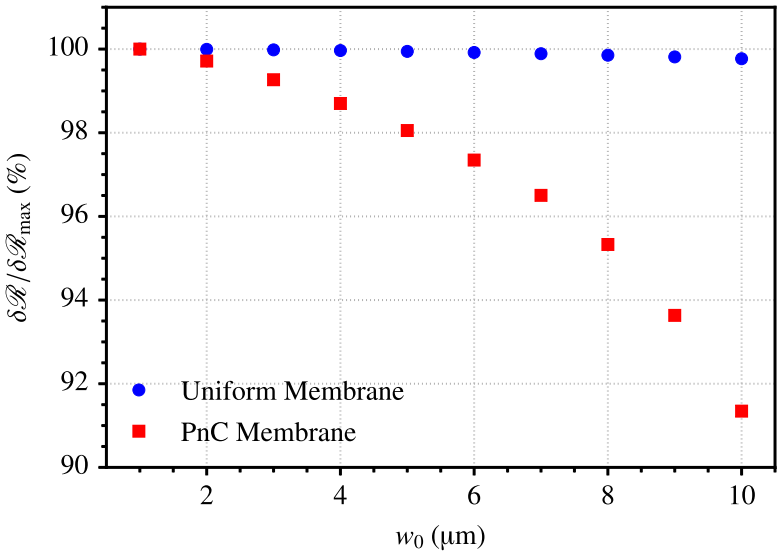

Figure 3.14: Finite element method simulations of the ratio of the relative thermal responsivity to its maximum value $\delta\mathscr{R}/\delta\mathscr{R}_{\max}$ versus the size w_0 of the pointlike Gaussian source, shown both for a uniform membrane and a PnC membrane of size $L \approx 0.6$ mm and $h = 50$ nm. Material parameters for the simulations are $E = 250$ GPa, $\nu = 0.23$, $\rho = 3000$ kg/m^3, $\sigma_{\text{film}} = 200$ MPa, $\alpha = 2.2 \times 10^{-6}$ K^{-1}, $\kappa = 3$ W/(m·K), $c_{\text{p}} = 700$ J/(kg·K), and $\epsilon_\lambda = 0.05$.

should provide an accurate description of the experimental laser beam profiles. Using the built-in Gaussian profile, one has to set the deposited beam power, beam origin and orientation, and the radius of the beam w_0. The beam radius has not been accurately determined in the experiments and therefore needs to be given additional consideration in the simulations. As such, a sweep of the beam radius was performed within experimentally reasonable values and its influence on the simulated relative thermal responsivity $\delta\mathscr{R}$ given in Figure 3.14. The plot shows the percentage change of $\delta\mathscr{R}$ to its maximum value $\delta\mathscr{R}_{\max}$ acquired for a $w_0 = 1$ μm, both for the case of a uniform square membrane and a PnC membrane. Dimensional parameters of the membranes were $L \approx 0.6$ mm and $h = 50$ nm, which represents the smallest lateral membrane size investigated in Chapter 7 and therefore the most sensitive to beam size [102]. Evidently, relative changes smaller than 1% and 10% can be observed for the uniform and PnC membrane, respectively. Given that this represents a lower extreme in membrane size, the beam size can be seen to have a negligible influence on $\delta\mathscr{R}$. A beam size $w_0 = 1$ μm is therefore chosen for all FEM simulations of the thermomechanical properties.

4

Influence of Clamp-Widening on Q

This chapter presents an investigation into the effect of clamp-widening on the quality factor of nanomechanical string resonators. The introduction presents the motivation behind the shown string geometry, while the following sections present both measurements and simulations of the mechanical properties. Results presented in this chapter are based on Paper **II** [189].

4.1 Introduction

Despite great promise and ultrahigh achievable quality factors employing phononic crystal membranes and strain engineering, as highlighted in Section 2.2.4.3, a number of drawbacks present themselves. Given the typical resonance frequencies of nanomechanical resonators based on silicon nitride (100 kHz - 1 MHz), unit cell sizes on the order of at least tens of micrometers are required. This size requirement typically results in devices with lateral dimensions of several millimeters, meaning one would have to work with higher-order mechanical modes, despite a preference for the fundamental mode in cavity optomechanics due to having lower background noise [190, 191]. Combining the large size with a thickness on the order of tens of nanometres, such samples are highly fragile and the fabrication yield mostly very small. Additionally, due to the complexity of the geometries, studies thus far have been limited to only optical transduction, as the addition of electrodes can possibly tamper with the phononic bandgap.

An alternative method of achieving ultrahigh Qs was presented by Norte *et al.* for high-stress nanomechanical trampoline resonators [46]. For the fundamental out-of-plane mode of a trampoline of diagonal length $L_d \sim 1$ mm, Qs as large as $\sim 10^8$ were observed, an order of magnitude larger than what is expected from the dissipation dilution formalism [37, 38, 93]. The enhancement was attributed to the curved widening of the clamping region of the

trampolines to widths larger than the tether width, resulting in a reduction of the stress at the clamp, while enhancing it in the narrow tethers. Other studies employing a similar clamp-widening technique on nanomechanical trampolines have similarly achieved large Qs, but the values were all explainable within the framework of dissipation dilution [192, 193].

Investigations into the effect of engineering the clamping region of nanomechanical string resonators have been done prior by Bereyhi *et al.* [194]. The results turned out to be in the negative, i.e. clamp-widening was found to only have a deteriorating effect on the Q. On the other hand, clamp-tapering was shown to enhance the Qs by more than a factor of two. A theoretical model employing dissipation dilution displayed good agreement with both clamping configurations. As a result, the origin of the ultrahigh Qs observed for trampoline resonators was put into question.

An important difference between the investigations by Norte *et al.* and Bereyhi *et al.* is the orientation of the resonators relative to the supporting silicon frame. In the work by Norte *et al.*, the tethers of the trampolines were oriented diagonally relative to the frame, while the strings used by Bereyhi *et al.* had a perpendicular orientation. The results presented here further investigates the effect of widened clamps on the Q of nanomechanical resonators by comparing the widened geometry for strings oriented both diagonally and perpendicularly with respect to the Si frame. Focus will be on the influence of clamp-widening on both the resonance frequency and Q of the fundamental out-of-plane mode of the strings. In addition, results for higher-order mechanical modes are shown as well. All measured results are compared to finite-element method simulations.

4.2 Material Parameters for Simulations

The simulated data shown here were acquired using the procedure presented in Sections 3.4.1 and 3.4.2. A list of all chosen dimensional and material parameters are given in Table 4.1. Since the strings for the two clamping configurations come from two different fabrication batches, their thickness and initial tensile stress differ. In particular, the initial tensile stress, or film stress, σ_{film}, which represents the stress of the deposited SiN film before release, is of crucial importance to the simulated results. In fact, this is the value given as a parameter for the simulation of the stress redistribution in the strings. The σ_{film}-values given in Table 4.1 were extracted from measurements of the resonance frequencies of the strings without clamp-widening in either configuration, which are analytically described according to Equation (2.32). From this frequency, the string stress σ can be extracted, which in turn can be

used to calculate the film stress according to

$$\sigma_{\text{film}} = \frac{\sigma}{1-\nu}, \tag{4.1}$$

with ν being Poisson's ratio. Despite high-stress samples being of greater interest to the optomechanics field as a result of enhanced dissipation dilution for higher stress values, previous investigations have shown an increase in acoustic radiation losses for high-stress resonators [48, 72, 74]. The effect typically manifests itself as a decrease of the Qs of lower frequency mechanical modes. Given that the focus here is mainly on the fundamental mode, it is necessary to minimize the radiation losses. Since the acoustic mismatch between the resonator and substrate is inversely proportional to the tensile stress, as shown in Equation (2.55), all samples presented here are made from low-stress silicon-rich SiN.

	Clamping configuration	
Assumed material parameters	Diagonal	Perpendicular
Young's modulus (E)	250 GPa	
Mass density (ρ)	3000 kg/m^3	
Poisson's ratio (ν)	0.23	
String central width (w)	5 µm	
String thickness (h)	50 nm	56 nm
Film stress (σ_{film})	0.14 GPa	0.47 GPa

Table 4.1: Material parameters used in the finite element method simulations for both clamp-widened string configurations. Geometric dimensions and tensile stress are extracted from measurements of string samples, while the rest are assumptions based on previous literature on the properties of silicon nitride [101]. Table adapted from [189], with the permission of AIP Publishing.

As already discussed in Section 3.4.2, Qs are not simulated directly, but instead the dissipation dilution factors are simulated. This is achieved by simulating the maximum kinetic energy W_{kin}, which, according to Rayleigh's method, can be assumed to be equal to the total stored energy in the string, and the energy stored in the bending W_{bend}. With this approach, the dissipation dilution factor can be calculated as $\alpha_{\text{dd}} = W_{\text{kin}}/W_{\text{bend}}$. In order to account for the intrinsic losses, Equation (2.72) is used to calculate the intrinsic quality factor Q_{int}. For SiN, the bulk losses are given as $Q_{\text{vol}} = 28000 \pm 2000$, while the surface losses are calculated using $Q_{\text{surf}} = \beta h$, with the factor $\beta = (6 \pm 4) \times 10^{10}$ m^{-1} [48]. For a sample of 50 nm thickness, one can estimate $Q_{\text{surf}} = 3000$. As such, for the samples studied here, bulk material losses can be neglected and $Q_{\text{int}} \approx Q_{\text{surf}}$.

4.3 Clamp-Widened String Geometries

The two string geometries investigated here are presented in Figure 4.1. Strings are anchored in either a diagonal or perpendicular configuration, as can be seen on the optical micrographs in Figures 4.1(a) and 4.1(d), respectively. The diagonal orientation is inspired by the trampoline research of Norte *et al.*, while the perpendicular is similar to Bereyhi *et al.* Zoom-ins of the clamping region are also provided for each configuration, which highlights how the width of the clamp is defined through a clamping radius R. FEM simulations of the tensile stress profile show a strong localization of the stress to the central, uniform-width part of the string, while the clamping region just outside the uniform region displays a much lower stress.

Figures 4.1(b) and 4.1(e) show line profiles of the stress along the length of the strings for the diagonal and perpendicular configuration, respectively, for $R = 0$ µm (uniform string) and $R = 50$ µm. It can be observed how the stress outside the central region reduces to $\sim 16\%$ and $\sim 20\%$ the value in the string center for the diagonal and perpendicular configuration, respectively. In comparison, the uniform strings display no notable change in stress along the length of the string. Such stress engineering techniques combined with phononic crystals have already been successfully employed to achieve ultracoherent nanomechanical resonators [40].

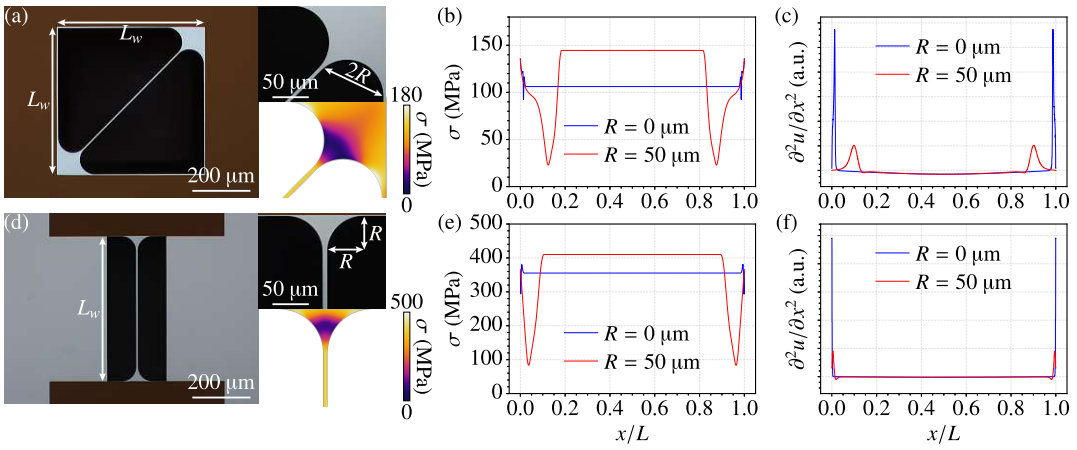

Figure 4.1: Clamp-widened string geometries investigated here. (a) Optical micrograph of a diagonally-oriented string resonator with an opening window size $L_w = 500$ µm. A close-up of the clamping region is given along with a finite element method simulation of the tensile stress for the same region. (b) Stress profile along the length of a diagonal string. (c) Curvature along the length of a diagonal string. (d) Optical micrograph of a perpendicularly-oriented string geometry with $L_w = 500$ µm, along with close-ups of the clamping region. (e) Stress profile along the length of a perpendicular string. (f) Curvature along the length of a perpendicular string. Figure adapted from [189], with the permission of AIP Publishing.

As discussed in Section 2.2.4.1, the energy stored in the bending of the string can analytically be shown to be divided into a sinusoidal bending term and a term arising from the exponential edge shape [16]. Given that the edge shape term of W_{bend} is proportional to $\sqrt{\sigma}$ (see Equation (2.77)), one would expect a reduction of this term with reduced stress at the clamping, translating into reduced bending at the clamping. Indeed, this is what is observed through FEM simulations of the curvature along the string length, as can be observed in Figure 4.1(c) for the diagonal case and in Figure 4.1(f) for the perpendicular case. Again, for both configurations, results with and without clamp-widening are shown. Similar to the case of the stress, the maximum curvature in the clamp-widened case reduces to $< 20\%$ the maximum of the case without widening.

Overall, the clamp-widened string geometry appears to present two advantages compared to the case of a uniform string, namely enhanced stress in the string center and reduced bending at the clamping. Both effects directly result in enhanced dissipation dilution [16]. While it would appear that clamp-widening only presents benefits to dissipation dilution, the widening also means that more material is bending. Thus, more energy is required to bend the string, which counteracts the previously mentioned effects. Therefore, a combination of experiment and theory is required in order to determine which effects dominate the dissipation in the strings.

4.4 Resonance Frequency of the Fundamental Mode

As mentioned earlier, the SiN film stress was determined through measurements of the resonance frequency of uniform strings. Using the extracted σ_{film} value, FEM simulations of the mechanical properties of the clamp-widened strings could be performed. Measured and simulated resonance frequencies f_r of the clamp-widened string geometries are presented in Figure 4.2. Results for diagonally and perpendicularly configured strings are shown in Figure 4.2(a) and 4.2(b), respectively, for increasing clamp radii R. Both sets of data are for strings with an opening window $L_w = 500$ µm.

For both configurations, increasing R can be observed to initially result in an increase of f_r, until the frequency starts to drop at larger values of R. This trend can be understood through a closer look at the evolution of the string geometry with increasing R. Initially, the widening results mainly in stress enhancement, while the overall mode shape remains similar to that of a uniform string, thus the frequency increases. At larger R, however, the low-stress clamping region accounts for a larger percentage of the geometry and, since the string-like mode extends through the clamping region, the frequency decreases. The FEM simulations display good agreement with the measured values, serving as validation of the approach in

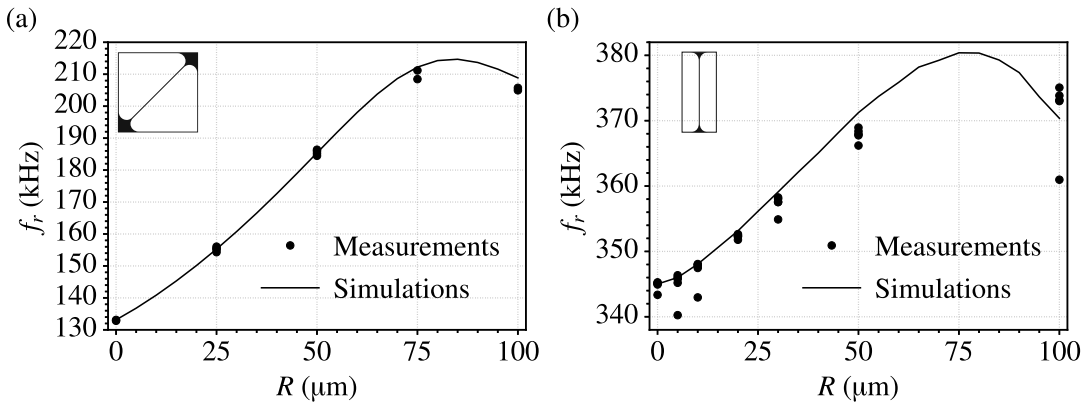

Figure 4.2: Resonance frequencies f_r versus clamp radius R of the fundamental out-of-plane mode for string resonators oriented diagonally (a) and perpendicularly (b) with respect to the supporting silicon frame. Each data point corresponds to a measurement of an individual string sample, while the solid lines are finite element method simulations. Schematics of the respective configuration are given on each plot for clarity. Figure adapted from [189], with the permission of AIP Publishing.

describing the mechanical properties of the clamp-widened strings. For the perpendicular configuration, strings with $R = 100$ μm displayed compressive stress locally in the clamping region. As a result, Qs plummeted, rendering comparison with FEM simulations difficult. In the following section, results for Q are only shown up to $R = 50$ μm for the perpendicular geometry.

4.5 Influence on Q

Having confirmed that the FEM simulations accurately reproduce the measured resonance frequencies, the next step is to investigate the effect of clamp-widening on the Q. These results are divided into two cases: Fundamental out-of-plane mode and higher-order modes. Both cases are discussed separately.

4.5.1 Fundamental Mode

Figure 4.3 shows Qs of the fundamental out-of-plane mode of the clamp-widened string geometries versus clamp radius R. The data are for the same samples presented in Figure 4.2. Each measured data point is an average of 5 measurements of the Q of one string in order to account for fluctuations in the vibrational amplitude. For diagonally-oriented strings, as shown in Figure 4.3(a), an increase in Q is observed for smaller R-values with a maximum

enhancement of ~ 23% for $R = 25$ µm compared to the case of a uniform string. At larger R, the Q starts to roll-off until a minimum is reached at $R = 100$ µm. FEM simulations are presented on the graph as well for a nominal $Q_{\text{int}} = Q_{\text{surf}} = 3000$ for a string of 50 nm thickness. In addition, the uncertainty of Q_{int} is shown as well as a grey-shaded region in order to account for the dispersion in Q-values from sample to sample. The simulations appear to describe the measured trends very well, including predicting a slight Q-enhancement at lower R-values.

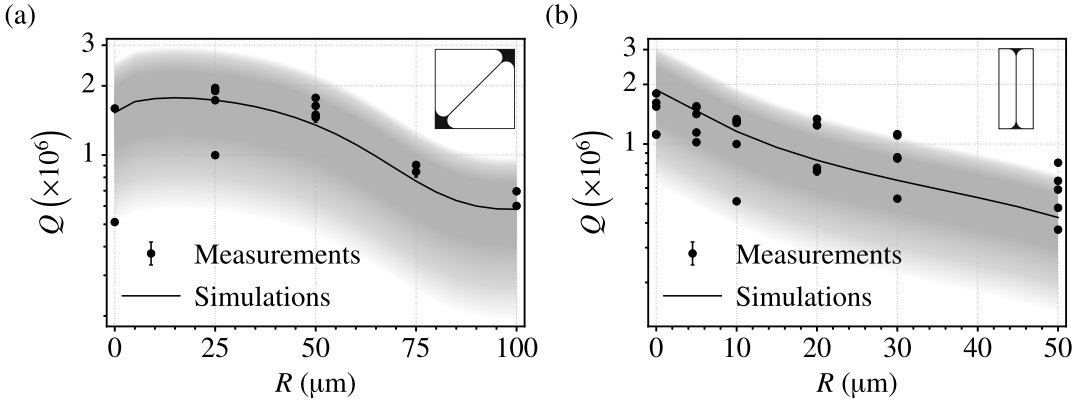

Figure 4.3: Quality factors Q of the fundamental out-of-plane mode of clamp-widened string resonators in a diagonal (a) and perpendicular (b) configuration. Both sets of data are presented as a function of increasing clamp radius R and for a window size $L_w = 500$ µm. Each individual data point is an average of 5 measurements of the same Q. The solid lines represent FEM simulations and the grey-shaded regions indicate the uncertainty of $Q_{\text{int}} = h \cdot \left[(6 \pm 4) \times 10^{10}\ \text{m}^{-1}\right]$ [48]. Schematics of the respective clamping configuration are given on each plot for clarity. Figure adapted from [189], with the permission of AIP Publishing.

Measured and simulated data for the perpendicular configuration are given in Figure 4.3(b). In contrast to the diagonal strings, Q only deteriorates for increasing R in the perpendicular case. FEM simulations qualitatively agree with the measurements. The uncertainty in Q_{int} additionally appears to explain the spread in Qs from string to string very well.

As evident from the data presented above, the orientation of the string has a non-negligible influence on the Q for clamp-widened strings. The results from the perpendicular configuration are in agreement with the findings of Bereyhi *et al.*, i.e. a steady decrease in Q with increasing clamp radius [194]. On the other hand, diagonally-oriented strings display a slight increase in Q for lower values of R. A possible interpretation of the underlying mechanism can be made through a closer inspection of the energies in the system.

As mentioned earlier, the simulated dissipation dilution factor is defined through the kinetic energy W_{kin} and the bending energy W_{bend}. Plotting of the individual energies can there-

fore shed some more light on the observed trends in Q, as can be seen in Figure 4.4. These plots correspond to the energies used to generate the simulations presented in Figure 4.3. In the diagonal case, which is plotted in Figure 4.4(a), W_{kin} can be observed to increase by as much as $\sim 45\%$ for smaller R, while W_{bend} displays an initially slow rise. This in turn translates into an initial rise in α_{dd} for the diagonally-oriented strings. For 40 µm $\leq R \leq$ 85 µm, W_{kin} begins to drop and W_{bend} has a steeper rise, which explains why Q begins to deteriorate compared to the uniform string case. Finally, since W_{kin} appears to increase again for $R >$ 85 µm, this can explain the flattening of Q for the largest R-values.

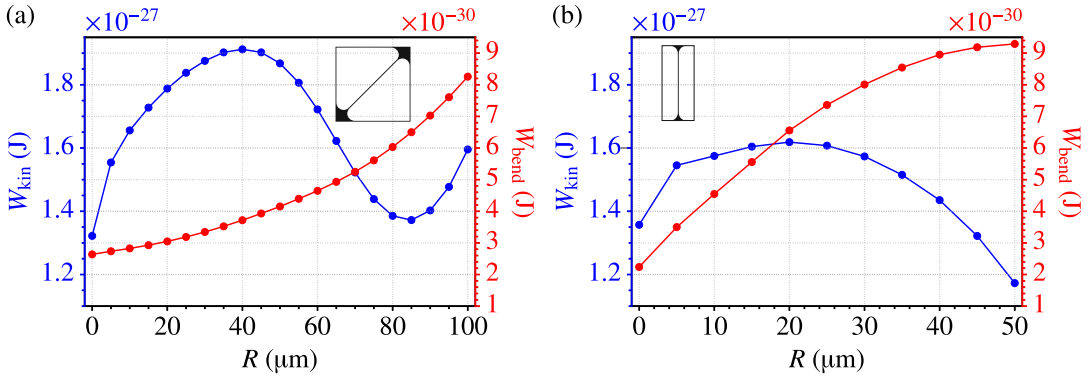

Figure 4.4: Simulated kinetic (W_{kin}) and bending (W_{bend}) energies of clamp-widened strings. (a) Energies of diagonally-oriented string versus clamp radius R for strings with an opening window size L_w = 500 µm. (b) Same as (a) for perpendicularly-oriented strings. Schematics of the respective configuration are given on each plot for clarity.

A distinct difference is observed for the energies of perpendicular strings, as shown in Figure 4.4(b). For this configuration, W_{kin} displays a smaller maximum increase of $\sim 19\%$ compared to the uniform string case. In addition, W_{bend} steeply increases at lower R and thus leads to an immediate drop in α_{dd} with increasing R.

The exact reason behind this discrepancy in the two configurations is not entirely understood. An increase in W_{kin} in both cases is a result of increased stored tensile energy due to the stress enhancement resulting from the clamp-widening. An explanation for the smaller increase in the perpendicular case can be shown to be a result of reduced stress enhancement compared to the diagonal case. On the other hand, simulations of W_{bend} reveal that the clamp-widening method only increases the bending energy, as opposed to what was initially expected. This increase in W_{bend} shows how the increased material bending resulting from the clamp-widening dominates the bending energy. Interestingly, W_{bend} displays different trends for increasing R depending on the clamping configuration, which might be a result of how the strain is distributed in the two cases. Additionally, for equal tensile stress and clamp radius, simulations indicate that perpendicular strings always exhibit a significantly higher curva-

ture compared to the diagonal case. It would appear that the diagonal configuration is more energetically favorable.

In any case, the results presented here cannot explain the observations made by Norte *et al.*, namely a significant Q-enhancement resulting from clamp-widening of trampoline anchors [46]. Furthermore, the authors observed a steady increase of Q with increasing R, which goes against the rolling off of Q at larger R observed here. It should, however, be mentioned that the range of R-values studied by Norte *et al.* were relatively small compared to the range presented here, meaning that a similar trend might have been observed, if larger Rs were studied as well.

4.5.2 Higher-Order Modes

Thus far, the focus of dissipation dilution engineering, in general, has mainly been on the fundamental mode due to the lower background noise, as mentioned in Section 4.1. Nonetheless, to further investigate the influence of clamp-widening and in order to further support the FEM simulation of α_{dd} approach, Qs of higher-order string modes were investigated as well, as shown in Figure 4.5. Data for the first 5 string-like out-of-plane modes is given for both configurations with a $L_w = 500$ μm.

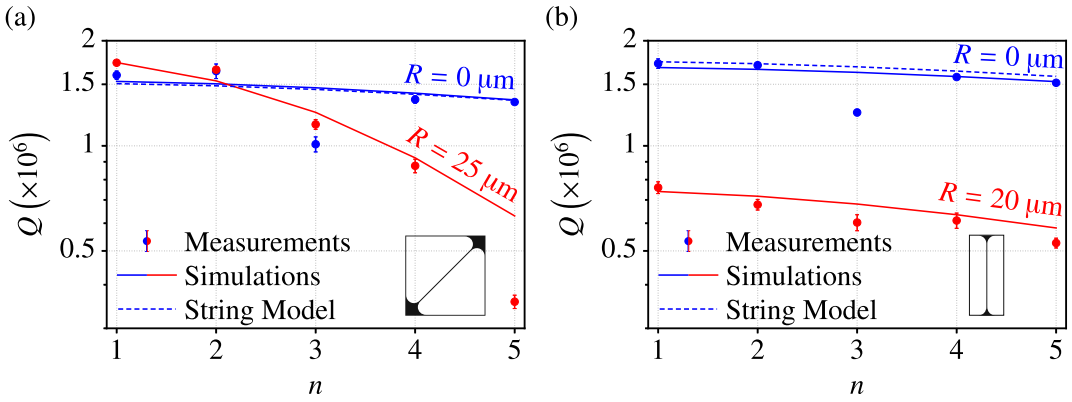

Figure 4.5: Quality factors of higher-order out-of-plane modes of clamp-widened string resonators. (a) Data for strings in a diagonal configuration without ($R = 0$ μm) and with ($R = 25$ μm) a widened clamp for strings with an opening window size $L_w = 500$ μm. Each data point is an average of 5 measurements of the same resonance. Solid lines are FEM simulations, while dashed lines are calculations based on the dissipation dilution equation for uniform strings. (b) Same as (a) for perpendicularly-oriented strings, but with the clamp-widened string having a $R = 20$ μm. For both configurations, $Q_{int} = 3000$ in the theoretical calculations. Schematics of the respective configuration are given on each plot for clarity. Figure adapted from [189], with the permission of AIP Publishing.

Figure 4.5(a) presents measured and simulated Q data for diagonal strings without (R = 0 μm) and with (R = 25 μm) clamp-widening. Each measured data point corresponds to an average of 5 measurements of the same resonance. In addition, a calculation of Q based on the analytical model of dissipation dilution (Equation (2.81)) for uniform strings is given as well. A Q_{int} = 3000 is chosen both for the simulations and the analytical calculations. Evidently, only the fundamental mode is enhanced as a result of clamp-widening, while the Q deteriorates for higher-order modes at a rate significantly faster than for a uniform string. In the case of perpendicular strings, as shown in Figure 4.5(b), Qs of clamp-widened strings are smaller for all modes compared to uniform strings, as expected from the data shown in Figure 4.3(b). Additionally, it appears that Q decreases more gradually compared to diagonally-oriented strings. For this configuration, a nominal Q_{int} = 3000 was chosen for the simulations and calculations as well.

It would seem that clamp-widening presents no advantage to higher-order modes regardless of the configuration. Decreasing Q with mode number is to be expected from dissipation dilution in general as a result of the increased amount of antinodes [37]. Still, it appears clamp-widened strings display a steeper decrease in Q with mode number. Larger R-values were not investigated, due to the difficulty in finding string-like higher-order modes, i.e. where the clamping region only bends out-of-plane synchronously with the central region. Local vibrations at the clamping start to occur in parallel with the central string vibrations and these two sets of vibrations can couple in multiple ways, thus rendering a comparison with uniform strings difficult.

FEM simulations display good agreement with measurements in both configurations. Furthermore, the analytical string model fits well with the simulations for uniform strings. These findings highlight the practicality of FEM simulations in predicting the Qs of resonators subject to dissipation dilution. The method is flexible and can be employed to more complicated geometries as well as to other materials. Only the intrinsic losses have to be set as a fit parameter. One can either use the surface loss limit employed here or possibly estimate Q_{int} through measurements of unstrained resonators implemented in the same fabrication batch.

4.5.3 Interpretation

From all the results presented above, clamp-widening only leads to marginal Q-enhancement and only for diagonally-oriented strings. As such, these results, in conjunction with those of Bereyhi *et al.* calls for a reinterpretation of previous results on trampoline resonators [46, 194]. One important observation of the measurements made by Norte *et al.* is an increase in Q for narrower trampolines. While dissipation dilution indeed enhances for thinner res-

onators, this benefit is cancelled out by increased surface friction [48]. As such, this would indicate that the observed large Qs of trampolines are a result of reduced surface friction, which might be a result of certain steps made during the fabrication process. In particular, the importance of sample cleanliness throughout the fabrication was highlighted by J. P. Moura in his dissertation [148]. The addition of various cleaning steps between each process might lead to reduced surface friction and thus a larger intrinsic Q than that expected from $Q_{\text{surf}} = \beta h$. Alternative means of reducing surface friction are the main focus of the following chapter.

4.6 Summary and Outlook

In conclusion, the influence of the clamp-widening approach on the quality factors of nanomechanical silicon nitride string resonators has been investigated. Emphasis was made on the difference between the orientation of the strings relative to the supporting silicon frame. For clamp-widened strings in a diagonal configuration, the Q of the fundamental out-of-plane mode was found to be slightly enhanced compared to the uniform string case for smaller values of the clamp radius. In contrast, Q only deteriorated for perpendicularly-oriented strings, an observation in agreement with previous investigations into the topic [194]. Higher-order out-of-plane modes were investigated as well in both configurations, in which no visible enhancement of Q could be observed for both configurations. Finite element method simulations of the dissipation dilution factor qualitatively predicted the measured trends in Q, while quantitative prediction of Q was made by assuming surface friction as the main intrinsic loss source. The minimal enhancement observed from clamp-widening can thus not explain the large Qs observed in previous investigations of trampoline resonators [46].

Certain advantages do present themselves for clamp-widened strings in a diagonal configuration compared to normal ones. As evident from the clamp radius dependence observed in Figures 4.2(a) and 4.3(a), Q remains relatively unchanged up to a $R = 50$ μm, but the resonance frequency is increased for the same span of R. As such, the $Q \times f_r$ product is increased, which is beneficial for cavity optomechanics applications [23]. For force sensing applications, increasing Q and f reduces force noise (see Equation (2.113)), in addition to an enhancement of the force responsivity resulting from larger Q [16]. Further increase of the properties mentioned above can possibly be achieved through additional optimization of R and σ_{film} combinations.

5

Reduced Surface Losses

The focus of this chapter will be on Q-enhancement of nanomechanical resonators through elimination of surface friction. An introduction to the current state-of-the-art methods for enlarging Q, and how these results can be further improved by reducing surface losses, is given first. Then, results from high-temperature annealing of various types of nanomechanical resonators, including uniform strings, membranes, and soft-clamped membranes, at ultrahigh vacuum pressures are presented. Finally, a summary of the current state of this investigation is given and steps to move the research forward suggested.

5.1 Introduction

5.1.1 State-of-the-Art Qs at Room Temperature

The results discussed in the previous chapter presented one way of enhancing the quality factor of stressed silicon nitride resonators through optimization of the dissipation dilution effect. Nonetheless, the clamp-engineering techniques, be it tapering or widening, do not present the level of Q-enhancement required for room temperature quantum optomechanics. In order to significantly enhance dissipation dilution, one would need to look to more complicated engineering of resonators, such as the patterning of phononic crystals into the resonators, as already demonstrated for membrane and string resonators [39, 77]. Not only does this approach shield against radiation losses, the evanescent decay of the localized modes into the phononic crystal practically removes the large curvature at the clamping of the resonator (see Figure 2.8(b)), which is the main limitation in the dissipation dilution formula. The term *soft clamping* was coined for this approach, leading to Qs around two orders of magnitude greater than uniform resonators of similar frequency. Combining soft clamping with strain engineering, Qs approaching 1 billion at room temperature as well as $Q \times f_r$ products greater than

10^{15} Hz have been achieved [40].

It would seem that the current state-of-the-art is a full optimization of dissipation dilution in silicon nitride. The edge shape term has been removed using soft clamping and the stress enhanced, through tapering of the localized modes, to values close to the yield strength of the material. Therefore, as was already touched upon in Section 4.5.3, the next logical step for enhancing Q would be to minimize intrinsic loss mechanisms [32]. The thickness of the resonators employed in ultrahigh Q applications is normally in the submicron regime. For such samples, as a result of their large surface-to-volume ratio, surface friction has been shown to be the dominant intrinsic loss mechanism [48].

A number of investigations into the surface losses of mechanical resonators have already been performed. Early investigations showed how Qs of both silicon beams [31] and silicon nitride cantilevers [81] were reduced as the surface-to-volume ratio was increased. This size-dependence of intrinsic losses was inferred to be universal based on thorough literature studies by both Mohanty *et al.* [32] and Villanueva *et al.* [48]. In particular, a linear dependence of Q_{int} on the resonator thickness characterizes surface losses (see Section 2.2.3.2). For stressed resonators, the decrease in Q_{int} counteracts the increased dissipation dilution for reduced thickness [16]. Despite surface losses being universally accepted as the limiting loss mechanism for nanomechanical resonators, few investigations into reducing said losses exist. Yang *et al.* investigated loss mechanisms of submicron Si cantilevers and showed how these losses could be reduced through annealing of resonators in an ultrahigh vacuum, achieving Q-enhancements greater than an order of magnitude [82]. Tao *et al.* showed how to permanently increase Q_{int} by means of chemically passivating the surface of Si cantilevers [85]. If these surface loss reduction techniques can be applied to state-of-the-art stressed resonators, this could potentially present the final step towards performing quantum optomechanics experiments at room temperature.

5.1.2 Mechanisms of Q-enhancement

The limiting sources of dissipation in the strained nanomechanical resonators studied here, along with the procedure through which the Q is enhanced, will be outlined in this section. Various types of SiN resonators are measured, but the mechanisms responsible for the increase in Q are assumed to be the same. Current state-of-the-art Qs are measured in a high vacuum ($p \sim 10^{-6}$ mbar), as shown on the left side of Figure 5.1. At such pressures, the two main sources of dissipation are intrinsic losses and gas damping.

Intrinsic losses are dominated by surface friction, which manifests itself through a linear dependence of Q_{int} on resonator thickness. The exact sources of this surface loss are not

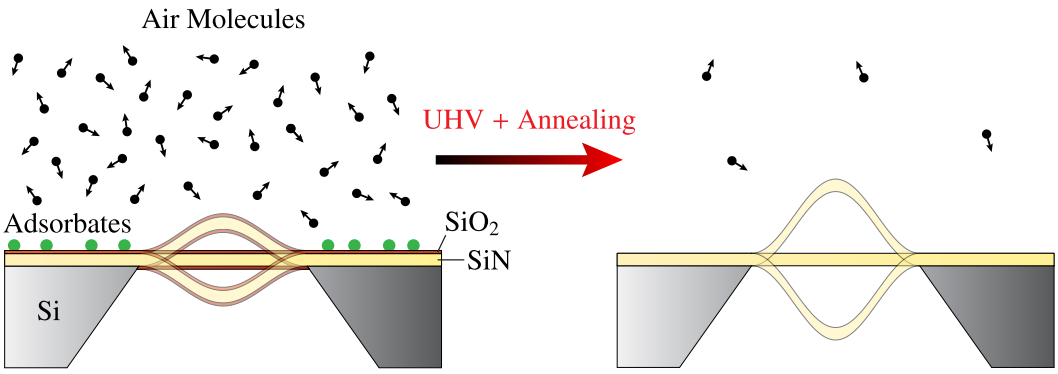

Figure 5.1: Principle of Q-enhancement through performing experiments in an ultrahigh vacuum. At a moderate to high vacuum ($p \geq 10^{-6}$ mbar), a native oxide layer along with adsorbates are present on the resonator surface. In addition, gas damping resulting from air molecules persisting in the vacuum further limits the Q. By reducing the pressure to the ultrahigh vacuum regime ($p \sim 10^{-10}$ mbar) and annealing the sample, both surface losses and gas damping can be negated and the Q enhanced as a result.

entirely understood, but some assumptions can be made. One source of this loss could be the presence of a native oxide layer on top of the SiN, as has been experimentally measured in different studies [86, 195, 196]. This surface layer has been shown to be compressive, which counteracts the tensile nature of the SiN. Defects in this surface layer could be an explanation for the large surface loss observed in thin resonators. Furthermore, material interaction losses can also occur at the interface between the oxide and the resonator. In addition to the native oxide layer, adsorbates on the resonator surface are another possible source of dissipation [82]. Adsorbates are assumed to be present both beneath and on top of the native oxide. These can occur during various fabrication steps, such as KOH residues during wet etching of the Si substrate. Adsorbates can also deposit on the surface during unavoidable exposure to air. Additional sources of surface loss include surface roughness [32] and defects/impurities [81].

Gas damping occurs as a result of the interaction of the resonator with air molecules in the vacuum. This type of loss is highly dependent on the dimensions and frequency of the resonator [16]. While some models have been developed in order to describe gas damping, in particular for squeeze-film damping, these become increasingly inaccurate as the resonator geometry is made complicated [68, 197]. Experimental investigations into gas damping of nanomechanical resonators have been performed for the case of doubly-clamped beams [198], including strings [62, 199], and membranes [200, 201]. Interestingly, for highly strained nanomechanical resonators, a consequence of the intrinsic losses being diluted, is that the

transition between the fluidic and ballistic regimes (see Section 2.2.1) occurs at much lower pressures [33]. As such, gas damping can possibly be the dominant loss mechanism for soft-clamped resonators due to having Qs on the order of 10^8 [39, 40].

How the loss mechanisms can be negated is illustrated on the right side of Figure 5.1. Similar to Yang *et al.*, high-temperature annealing of the samples is performed [82]. Depending on the chosen annealing temperature, both surface adsorbates, as well as native oxide, can be removed from the SiN surface. Furthermore, surface defects might also be minimized resulting from the heat treatment, due to a rearrangement of atoms in the SiN. Annealing samples should therefore eliminate surface friction, reducing intrinsic losses to the limit set by bulk material losses [48]. Crucial to this approach is to anneal samples in an ultrahigh vacuum environment. As previous investigations have shown, native oxide begins to form almost immediately upon air exposure for both Si [202] and SiN [203]. According to Langmuir adsorption theory, a monolayer of gas would adsorb on a surface within 1 second at a pressure $p \sim 10^{-6}$ mbar [204]. While this theory cannot be applied to exactly calculate the adsorption time, it serves to tell that in order to keep the sample surface clean long enough to perform experiments, one requires pressures on the order of $p \sim 10^{-10}$ mbar. In terms of gas damping, this loss mechanism will naturally also be minimized due to the reduced pressure of the vacuum.

5.1.3 Chapter Outline

This chapter presents measured mechanical properties of strained SiN resonators with reduced surface losses. Different geometries are investigated, starting with uniformly stressed strings and membranes, and then moving into soft-clamped membranes. Focus will be on how the intrinsic losses are reduced due to annealing in an ultrahigh vacuum. For each type of geometry, the annealing temperature is varied and its influence on the mechanical properties presented. Besides intrinsic losses, the influence of gas damping on the Q is also discussed. At the end of the chapter, an overview of the results is given, highlighting the current state of research and what the next steps should be.

5.2 Strings

The first part of the investigation will be on nanomechanical string resonators. Narrow strings in general suffer little from radiation losses and are therefore a good platform for fundamental studies [38]. The methods, with which the measurements are performed and the data extracted, are presented in this section and will apply to the remainder of the chapter as well.

5.2.1 Intrinsic Quality Factor Determination

Essential to the interpretation of the results presented here is to extract the intrinsic quality factor. A general approach to measuring Q_{int} of strained resonators is therefore outlined in this section. Figure 5.2(a) shows a scanning electron micrograph of the type of string resonators measured here. These are similar to those used by Schmid *et al.* for various investigations on the mechanical properties of strings [38]. Each chip contains 25 strings of fixed length and thickness, but 5 different widths varying from 3 µm to 50 µm, with 5 strings for each width.

The Q of resonators subjected to dissipation dilution can be expressed in the general form:

$$Q^{-1} = (\alpha_{\text{dd}} Q_{\text{int}})^{-1} + Q_{\text{gas}}^{-1} + Q_{\text{rad}}^{-1}, \tag{5.1}$$

with Q_{rad} being radiation loss. Other sources of dissipation, such as those coming from the transduction technique used, are assumed to be negligible [55, 56]. From Equation (5.1), it is clear that one has to be intrinsically limited in order to accurately determine Q_{int}. As such, resonators have to be chosen which maximize both Q_{gas} and Q_{rad}. For doubly-clamped beams, analytical models have been derived, which predict a general trend $Q_{\text{rad}} \propto L/w$ [70]. As such, only the narrowest strings will be employed in order to minimize radiation losses. Furthermore, low-stress samples are employed to further reduce radiation losses, similar to what was done for the clamp-widening results (see Chapter 4). Minimizing Q_{gas} is expected to occur resulting from the ultrahigh vacuum pressures. However, the role of Q_{gas} is not as clear as expected, as will be discussed further below. Nonetheless, for the extraction of Q_{int}, it is assumed to be negligible.

Assuming both radiation losses and gas damping to be minimized, Equation (5.1) reduces to the dissipation dilution formula, which, in the case of strings, corresponds to Equation (2.81). Material parameters assumed for the silicon-rich SiN are $E = 250$ GPa, $\rho = 3000$ kg/m^3, and $\nu = 0.23$. The tensile stress is determined from measurements of the resonance frequency for various mode numbers. Fitting Equation (2.32) to the measured frequency data allows one to determine σ by setting it as a fit parameter. An example of such a measurement is given in the top part of Figure 5.2(b) for the first 15 modes of a string with $L = 510$ µm, $w = 3$ µm, and $h = 340$ nm. This measurement was performed at a pressure $p = 1 \times 10^{-5}$ mbar in the regular vacuum chamber used for the vibrometer setup (see Figure 3.3), prior to moving the sample into the UHV chamber. Equation (2.32) accurately describes the frequency data, with a $\sigma = 209$ MPa extracted from the fit. The intrinsic quality factor is then determined by fitting measured Qs to the dissipation dilution formula, employing the assumed material parameters and the measured σ, while setting Q_{int} as a fit parameter. Figure 5.2(b) shows such a Q_{int} measurement for the same string discussed above. From the

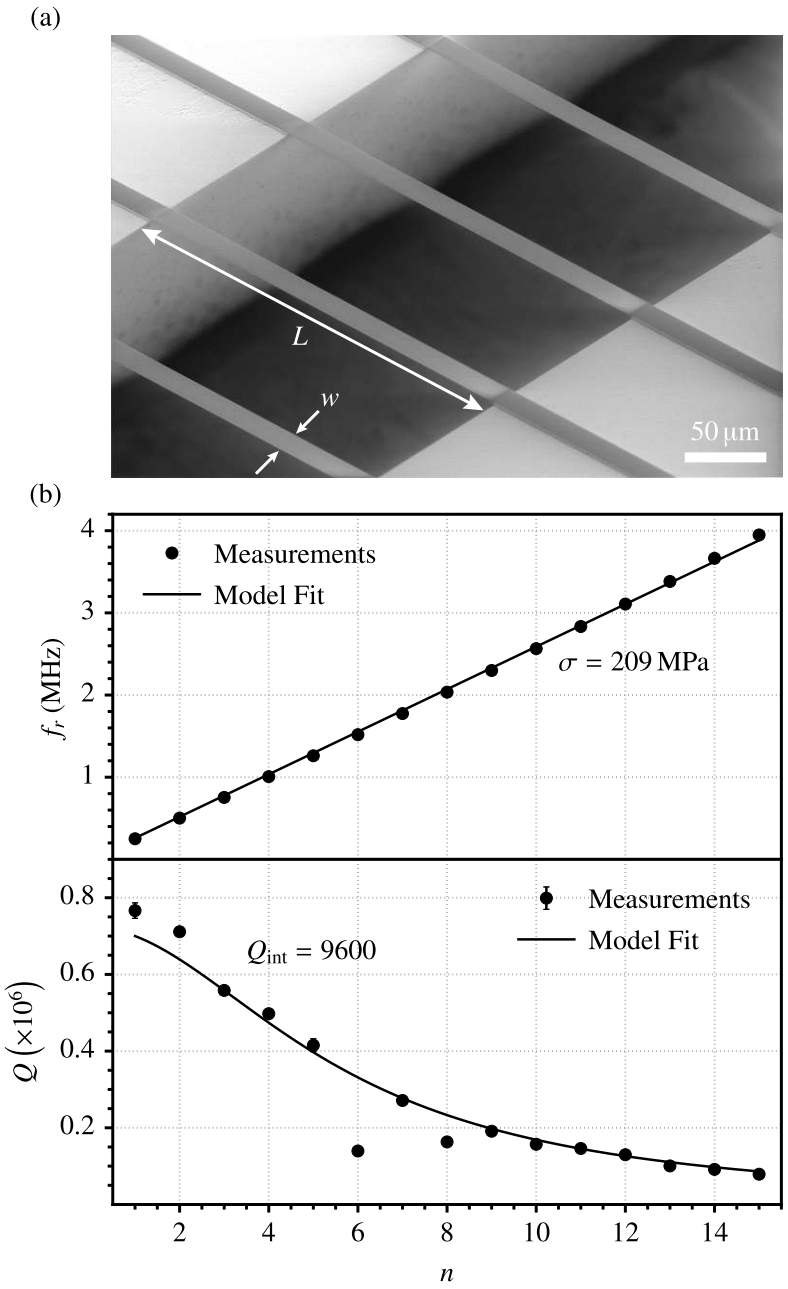

Figure 5.2: Extraction of the tensile stress and intrinsic quality factor of strings. (a) Scanning electron micrograph of the type of strings investigated here. (b) Measurements of the resonance frequency and quality factor versus mode number for a string of $L = 510$ µm, $w = 3$ µm, and $h = 340$ nm, along with model fits used for the extraction of σ and Q_{int}.

fit, a $Q_{\text{int}} = 9600$ can be extracted. Some Qs can be observed to be much lower than the fit, which is most likely due to radiation losses resulting from coupling to mechanical modes of

the sample mounting structure. Such outliers are omitted from the model fits. For all results shown in this chapter, where the above approach can be applied, a minimum of 5 mechanical modes are measured for the determination of Q_{int}.

5.2.2 Influence of Pressure

The first part of this investigation is to discuss the influence of reducing the vacuum pressure. As already discussed, gas damping can potentially be the dominant loss mechanism depending on the size and frequency of the resonator [62]. Therefore, a comparison between Qs measured in high and ultrahigh vacuum is made. A comment on the ultrahigh vacuum pressures used in this chapter should be made. The presented results were acquired over a span of three years and more vacuum equipment was added over time. Furthermore, the UHV chamber bakeout process was also optimized in this time frame. As such, the pressures at which the measurements are performed will vary throughout the chapter.

Figure 5.3 shows a comparison of the Qs of the first 5 out-of-plane modes for the same string resonator discussed in Figure 5.2(b), upon reducing the pressure from $p = 1 \times 10^{-5}$ mbar to $p = 3 \times 10^{-9}$ mbar. Fits to the dissipation dilution equation are also given in both cases. A $\sim 60\%$ enhancement of Q_{int} can be observed, increasing from $Q_{\text{int}} = 9600$ to $Q_{\text{int}} = 15800$. In order to ensure that this increase is of intrinsic nature and not due to reduced interaction with air molecules, calculations using the gas damping formalism was performed as well.

Gas damping in the ballistic regime, where the Knudsen number $Kn > 1$, has been analytically described prior [67–69, 205]. These models are generally not entirely accurate, since gas damping is highly geometry-dependent [62]. Nonetheless, they can be used to roughly estimate the pressure at which gas damping dominates over intrinsic losses. For this purpose, Q_{gas} is calculated using the squeeze-film damping model provided in Equation (2.49) [68]. An estimate of the intrinsic losses can be made using Equation (2.72) [48]. Setting $Q_{\text{vol}} = 28000$ and $Q_{\text{surf}} = \beta h = 20400$ for a thickness $h = 340$ nm, one arrives at $Q_{\text{int}} = \left(Q_{\text{vol}}^{-1} + Q_{\text{surf}}^{-1}\right)^{-1} = 11800$. One can then calculate the pressure-dependence of the quality factor using $Q = \left[(\alpha_{\text{dd}} Q_{\text{int}})^{-1} + Q_{\text{gas}}^{-1}\right]^{-1}$, with such a calculation shown for the fundamental mode in the inset of Figure 5.3. From this calculation, the pressure at which the Q transitions between the two damping regimes appears to be $p \sim 10^{-2}$ mbar, significantly larger than either of the pressures at which measurements were made. As such, the Q-enhancement observed upon reducing pressure in this case cannot be attributed to reduced gas damping and should therefore be of intrinsic nature.

A possible explanation could be the constant adsorption/desorption of adsorbates on the resonator surface, which occurs regardless of the pressure. At lower pressures, however, the

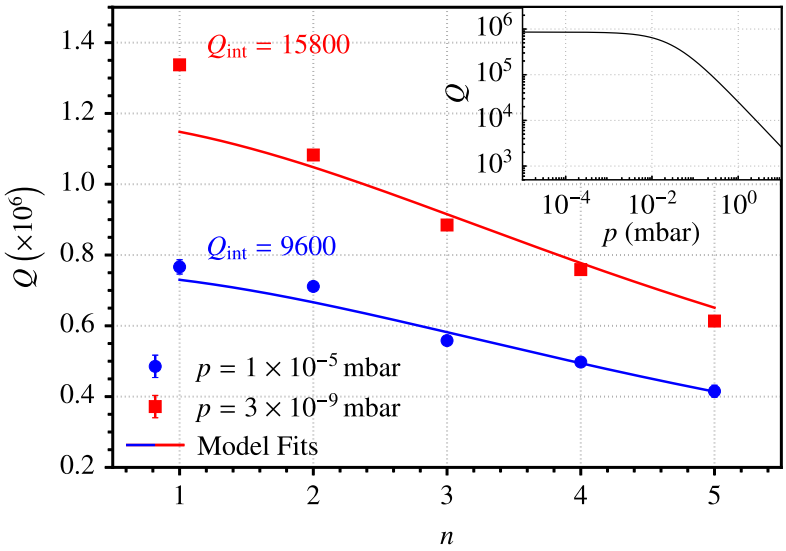

Figure 5.3: Measurements of quality factors for the first five out-of-plane modes of a string resonator with $L = 510$ µm, $w = 3$ µm, $h = 340$ nm, and $\sigma = 209$ MPa, acquired at a pressure of $p = 1 \times 10^{-5}$ mbar and $p = 3 \times 10^{-9}$ mbar. Fits to the dissipation dilution equation are shown as well for each pressure. The inset shows the calculated pressure-dependence of the quality factor using $Q = \left[(\alpha_{dd} Q_{int})^{-1} + Q_{gas}^{-1}\right]^{-1}$, where Q_{int} was estimated using a surface-loss formalism [48] and Q_{gas} calculated assuming squeeze-film damping [68].

chance of a particle landing on the resonator decreases, and thus surface losses will be decreased. For this particular measurement, the sample was kept inside the ultrahigh vacuum chamber during the bakeout process, meaning it was heated for a couple of days at temperatures on the order of 100 °C. This could result in an annealing effect, leading to the slow desorption of surface adsorbates, which slightly enhances Q_{int} [206, 207].

5.2.3 Annealing at 1000 °C

The next step of this investigation is to anneal samples at high temperatures in a UHV in order to minimize surface losses. As a first try, a string sample is annealed to the maximum temperature of 1000 °C for 2 hours. Such temperatures should ideally remove both adsorbates and native oxide from the SiN [82]. For these experiments, strings with $L = 340$ µm, $w = 6$ µm, $h = 177$ nm, and $\sigma \approx 179$ MPa were employed. Measurements of Q for an annealing temperature $T_{anneal} = 1000$ °C can be observed in Figure 5.4. The first 6 out-of-plane modes of two identical strings on the same chip are measured in order to ensure that the effect is

reproducible for multiple samples. The strings are here labeled string 1 and string 2, with their respective data sets shown in Figures 5.4(a) and 5.4(b). In Figure 5.4(a), the temperature label of 25 °C refers to the measurements before annealing.

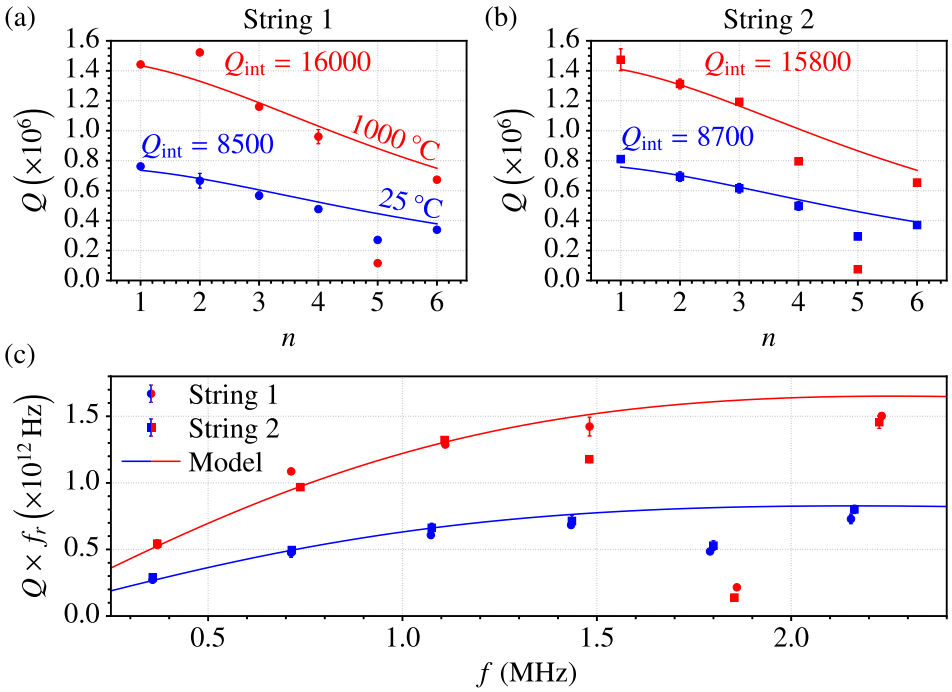

Figure 5.4: Annealing nanomechanical string resonators at $T_{\mathrm{anneal}} = 1000$ °C for 2 hours at a pressure $p = 1 \times 10^{-9}$ mbar. (a) A comparison between the Qs of the first six out-of-plane modes of a string resonator with $L = 340$ µm, $w = 6$ µm, $h = 177$ nm, and $\sigma \approx 179$ MPa, before and after annealing. (b) Same as (a) for an identical string on the same chip. (c) $Q \times f_r$ products versus frequency for the strings measured in (a) and (b) before and after annealing. Calculations using the dissipation dilution equation are shown as well, with the Q_{int}-values calculated from the average of the two strings before and after annealing.

For both strings, an overall enhancement of most Qs can be observed after the annealing process. From fits to the dissipation dilution equation, Q_{int} increases by nearly a factor of 2 for both strings. The exact source of this enhancement cannot be deduced from this experiment, i.e. it can be both a result of the removal of adsorbates as well as native oxide. Since the frequencies of both strings increased slightly after annealing, characterized by a tensile stress increase to $\sigma \approx 191$ MPa, this could indicate that a compressive layer on top has been removed [86]. However, despite the enhancement of Q_{int}, this value is still far below the limit set by bulk material losses in SiN, $Q_{\mathrm{vol}} = 28000$ [48]. As such, this indicates that surface losses have not been eliminated entirely. One explanation for this could be the pressure at which this annealing and subsequent measurement was performed, which was around

$p = 1 \times 10^{-9}$ mbar. At such pressures, one can expect a monolayer to redeposit within a quarter of an hour according to Langmuir adsorption theory [204]. Since the string frequencies continuously shift during changing temperatures, post-annealing measurements of Q can only be done once the sample temperature has stabilized to a value near room temperature. For this reason, the duration from the end of the annealing to starting the measurements was around half an hour, which might have been enough time for a monolayer to form on the surface.

Besides studying the effect on the intrinsic losses, a more important quantity for quantum optomechanics experiments is the product of the quality factor and the frequency [23]. Therefore, the effect of annealing on the $Q \times f_r$ product for both string resonators is shown in Figure 5.4(c). The results are plotted versus frequency in order to show the slight increase in f_r for each mode resulting from the annealing. Besides the measurements, calculations using the dissipation dilution formalism are given as well, calculating Q_{int} before and after annealing from the average of the two strings. Since the string frequencies only marginally increase, the $Q \times f_r$ product overall gets doubled after annealing resulting from the doubling in Q_{int}. For higher-order resonances, the $Q \times f_r$ product begins to decrease again, indicating an optimum for the 6th out-of-plane mode. Despite the observed Q-enhancement, these types of strings are far below the theoretical limit for performing room temperature quantum experiments, $Q \times f_r = k_B T_{\text{room}}/h \approx 6 \times 10^{12}$ Hz with k_B the Boltzmann constant, $T_{\text{room}} = 300$ K, and h the Planck constant [30].

A pronounced decrease in Q can be observed for the 5th mode before and after annealing. Given that this decrease occurs for both strings, it is most likely the result of radiation losses. This loss source possibly comes from interference effects resulting from coupling to resonances in the setup. Support for this argument comes from the fact that the 5th mode Q reduces further after annealing, where the frequency has slightly increased, indicating that the mode frequency lies closer to the resonance in the setup. A reason for this strong coupling could be that the samples are tightly clamped to the sample holder to ensure good thermal contact, which has previously shown to result in significant radiation losses for string resonators [38].

5.2.4 Annealing at Various Temperatures

Having established that UHV annealing can result in enhanced Qs for string resonators, the next step is to investigate the influence of the annealing temperature on the mechanical properties. This can possibly shed more light on what happens to the SiN film during the annealing process. Measurements of both the intrinsic quality factor and the tensile stress for increasing values of T_{anneal} are given in Figure 5.5. A low-stress string was employed with the dimen-

sional parameters $L = 440$ µm, $w = 6$ µm, and $h = 177$ nm. The presented results are based on measurements of first 10 out-of-plane modes of the string resonator, with the data extracted using the method shown in Figure 5.2(b). For further clarity, the theoretical limit of intrinsic losses estimated using $Q_{\text{int}} = \left(Q_{\text{vol}}^{-1} + Q_{\text{surf}}^{-1}\right)^{-1}$ is shown alongside the measured Q_{int}-data in the top panel of Figure 5.5 as well [48]. Annealing was performed for 1 hour at each temperature and the measurements done after the sample had cooled down to room temperature. The pressure during the annealing process was $p = 2 \times 10^{-9}$ mbar. Data points for $T_{\text{anneal}} = 25$ °C refer to measurements done prior to annealing.

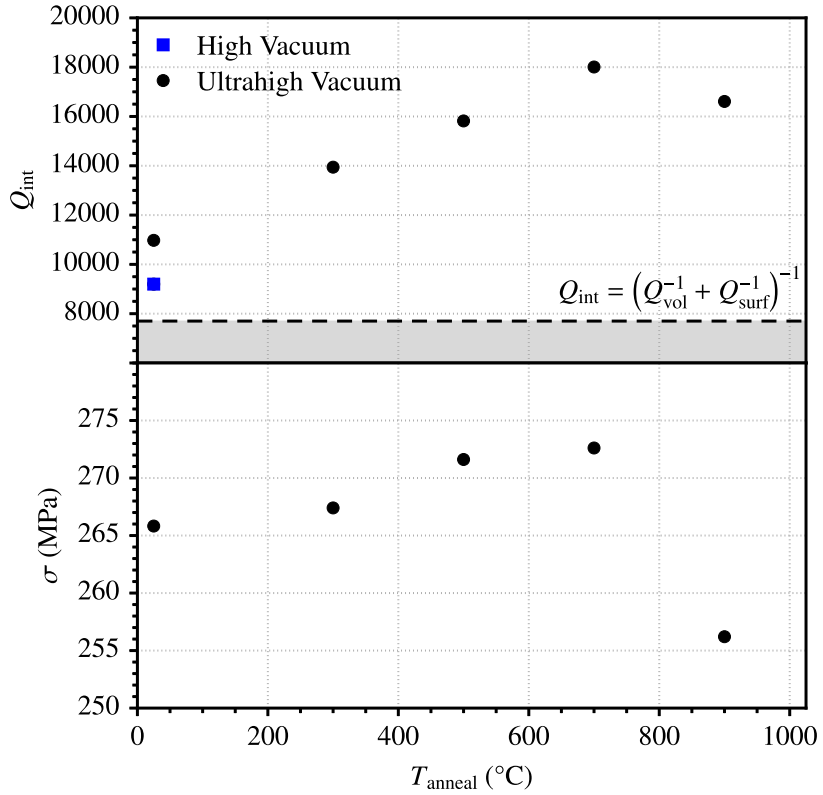

Figure 5.5: Annealing a nanomechanical string resonator for 1 hour at various temperatures. Measurements of both Q_{int} (top panel) and σ (bottom panel) for increasing T_{anneal} are shown. Both sets of data are based on the measurement of the 10 first out-of-plane modes of the string. High vacuum and ultrahigh vacuum indicate measurements performed at pressures of $p = 1 \times 10^{-5}$ mbar and $p = 2 \times 10^{-9}$ mbar, respectively. $T_{\text{anneal}} = 25$ °C refers to measurements performed before annealing. The theoretical limit of Q_{int} is shown in the top panel as well. Dimensions of the string are $L = 440$ µm, $w = 6$ µm, and $h = 177$ nm.

As a starting point, a measured $Q_{\text{int}} = 9200$ acquired at a high vacuum pressure $p = 1 \times 10^{-5}$ mbar is used as a baseline measurement in order to estimate the degree of Q-enhancement achieved from annealing in an ultrahigh vacuum. The effect of placing the

sample in a UHV is a $\sim$ 19% increase in Q_{int}, which is similar to the observation made in Figure 5.3. Upon annealing the sample, Q_{int} gradually increases for increasing T_{anneal}, with a maximum $Q_{\text{int}} = 18000$ reached for $T_{\text{anneal}} = 700$ °C. This is nearly a factor of two enhancement compared to the initial value, which is attributed to reduced surface friction. Interestingly, further increasing the temperature to $T_{\text{anneal}} = 900$ °C leads to a slight reduction of the intrinsic Q to a value $Q_{\text{int}} = 16600$.

In order to understand the observed decrease, the focus is shifted towards the tensile stress measurements shown in the bottom panel of Figure 5.5. The high vacuum measurement of stress is omitted since the value was significantly larger ($\sigma = 289$ MPa) than for the ultrahigh vacuum data, possibly a result of different actuation laser powers used for both sets of measurements. For $T_{\text{anneal}} \leq 700$ °C, a slight increase in σ is observed for increasing T_{anneal}. This increase can arise for multiple different reasons. One explanation is that the high temperatures slowly remove compressively stressed surface adsorbates and possibly parts of the native oxide, though the latter is not expected at these temperatures. However, one can also attribute the effect to film densification, which has been argued to increase the tensile stress due to rapid thermal annealing of LPCVD SiN films [208]. Finally, given the different thermal expansion coefficients of Si [209] and SiN [210], and the fact that the Si substrate is in direct contact with the sample holder and therefore at a higher temperature than the SiN resonator, the Si expands more than the SiN, which increases the tensile stress. If the Si substrate permanently expands after the annealing even after the sample has cooled down, one can imagine a larger stress in the SiN film.

For the largest $T_{\text{anneal}} = 900$ °C employed here, a stark decrease in the tensile stress from $\sigma = 273$ MPa to $\sigma = 256$ MPa is observed. This is the largest relative change in stress for a single annealing temperature observed here, indicating that a new effect comes into play at these temperatures. The decrease in stress also goes against the expectation from removal of compressive surface layers. An investigation into annealing of Si-rich SiN films by Andersen *et al.* have shown significant Si out-diffusion from the substrate into the resonator for annealing temperatures greater than 1100 °C [211]. Since the final value of the stress has an inverse relation to the Si content in the SiN, this could explain the observed stress reduction [136]. Furthermore, Si diffusion might increase bulk material losses due to creating impurity defects in the SiN films, which can explain the reduction of Q_{int} observed. Nonetheless, the maximum annealing temperature used for these results were $T_{\text{anneal}} = 900$ °C, which is still much lower than the 1100 °C used in the study of Andersen *et al.* One should also keep in mind that the SiN resonator is only in contact with the Si substrate through the anchors of the resonator, which would mean significantly less Si contamination in comparison to the case, where the SiN is in direct contact with the substrate uniformly. The exact origin of the reduced Q_{int} for the largest T_{anneal} remains unknown but is most likely a result of changes to

the material properties of the SiN film.

5.3 Uniform Membranes

This section focuses on measurements of the Qs of uniform square membranes in an ultrahigh vacuum. Important here is to show the effect of the annealing temperature on the intrinsic quality factor for membranes, an experiment which is repeated for all types of resonators studied in this chapter.

5.3.1 Radiation Loss

Before showing annealing data for the uniform membranes, a comment on radiation losses should be given. Results in support of radiation losses have already been shown in Figure 5.4, where some mechanical modes plummeted to values far below that expected from dissipation dilution, despite the fact that narrow and low-stress strings were chosen for the experiments. In order to determine the origin of this loss mechanism, the effect of clamping the sample to the ultrahigh vacuum sample holder is investigated. Low-stress uniform square membrane resonators are employed for this investigation, with an optical micrograph of a fabricated sample given in Figure 5.6(a). The membranes employed in this section are of dimensional parameters $L = 810$ μm and $h = 50$ nm.

Figure 5.6(b) shows measured Qs for the first 10 harmonic ($n = j$) out-of-plane modes of a membrane with $\sigma = 161$ MPa. For clarity, this membrane is given the label membrane 1. The membrane chip was placed unclamped on the regular sample holder of the MSA vacuum chamber and the Qs measured at a pressure $p \sim 10^{-5}$ mbar. Harmonic modes are chosen, since radiation loss has been shown to be suppressed for such modes (see Equation (2.54)) [48]. A similar observation is made here, given that the unclamped sample Qs appears to be well-described by fitting to the dissipation dilution equation. Only the fundamental mode seems to be limited by radiation loss, in agreement with previous investigations, which have shown that lower-order modes typically suffer more from radiation losses [42, 48].

Upon clamping the membrane chip to the sample holder, all the Qs of membrane 1 plummeted and could not be measured, which might itself be a result of radiation losses. Despite the chip containing 12 identical membranes, no other membranes were measured unclamped, meaning a different membrane had to be used for the comparison. Measurements of Q for a secondary membrane (labeled membrane 2) clamped to the UHV sample holder can be seen in Figure 5.6(c). A $\sigma = 197$ MPa was extracted for this membrane and the measured data was acquired at a similar pressure to the unclamped case. The discrepancy in stress between

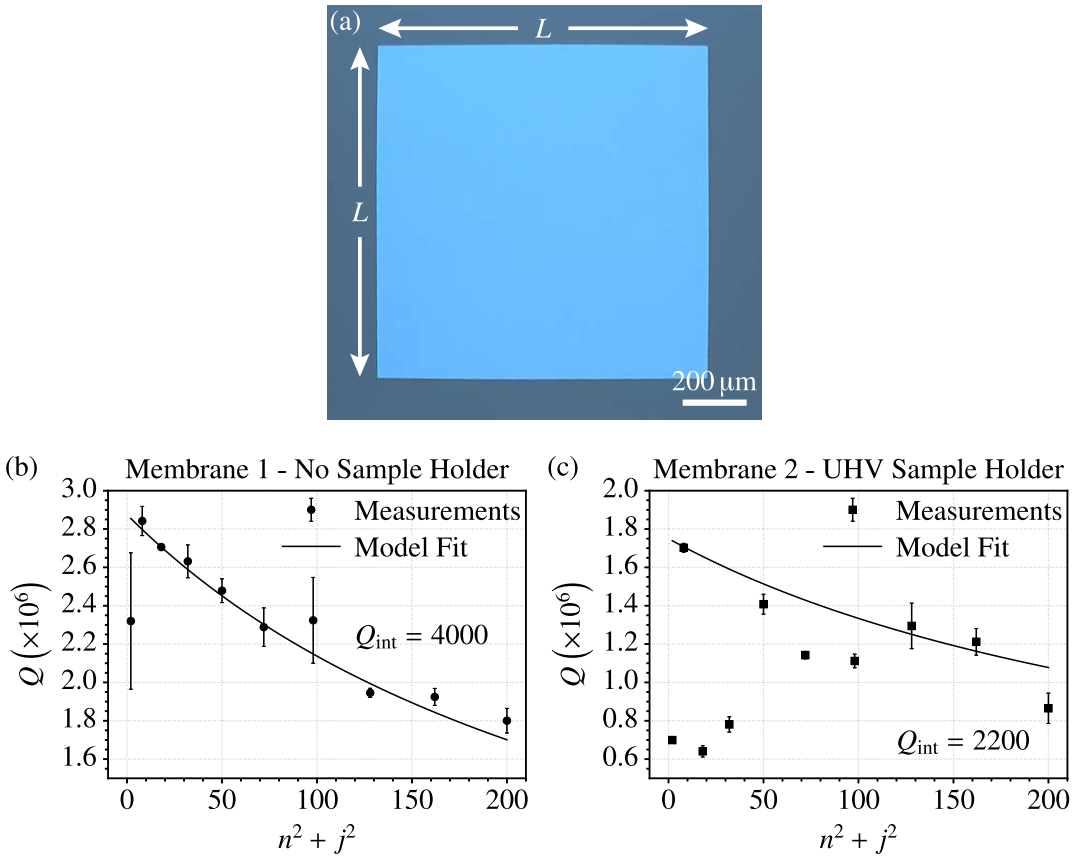

Figure 5.6: Radiation losses in uniform square membrane resonators. (a) Optical micrograph of a uniform membrane similar to the ones studied here. (b) Qs of the first 10 harmonic ($n = j$) out-of-plane modes of a uniform membrane not attached to any sample holder, along with a fit to the dissipation dilution equation. (c) Same as (b) for a membrane clamped on the ultrahigh vacuum sample holder. The measured membranes were located on the same chip, with the dimensional parameters $L = 810$ µm and $h = 50$ nm, and tensile stress values of $\sigma = 161$ MPa and $\sigma = 197$ MPa for (b) and (c), respectively.

the two membranes is most likely a result of the LPCVD growth of the SiN, resulting in a non-uniform stress across the chip, which was confirmed through measurements of many membranes on the chip.

Evidently, the Qs of several modes for the clamped membrane seem to be radiation loss-limited. The effect appears to be more pronounced for lower-order modes, as would be expected [48]. As such, the radiation losses observed both for strings and membranes can be attributed to a strong mechanical coupling between the resonators and the sample mounting structure, which is enhanced due to clamping the membrane to the sample holder. This was confirmed by measuring the Qs of multiple membranes on the clamped chip, all of which

displayed similar trends to membrane 2. Since clamping is necessary to maximize thermal contact between the sample and the sample holder, this loss mechanism could not be avoided here. Measuring much higher-order ($n, m > 10$) modes can suppress radiation losses. However, the limited laser power available for the optical actuation rendered measurements of higher-order modes difficult. Intrinsic quality factors are therefore extracted by fitting the envelope of maximal Qs, as is done in Figure 5.6(c).

5.3.2 Annealing at Various Temperatures

The next step is to anneal uniform membranes in an ultrahigh vacuum, in order to see if the enhancement observed for strings is universal for all types of resonators. For these measurements, membrane 2, which was discussed above, will be employed. The sample was annealed at temperatures ranging from 100 °C to 1000 °C in steps of 100 °C. For each temperature, the annealing time was set to 1 hour, and the mechanical properties measured after the sample had cooled down to around room temperature. The pressure in the chamber at the time of these measurements was $p < 1 \times 10^{-10}$ mbar, but an exact value could not be determined due to being beyond the range of the available pressure measurement equipment, which was listed in Section 3.3.1.

Measurements of both Q_{int} and σ for increasing values of T_{anneal} are plotted in Figure 5.7. Both sets of data are extracted from measuring the first 10 harmonic modes of the membrane. Data acquired at a high vacuum pressure $p = 1 \times 10^{-5}$ mbar are given as well. The label $T_{\text{anneal}} = 25$ °C indicates measurements made before annealing the sample. Given the thickness of this membrane being $h = 50$ nm, one can assume that surface losses will dominate the intrinsic losses and therefore $Q_{\text{int}} \approx Q_{\text{surf}}$ [48]. The theoretical limit of Q_{surf} is shown in the plot containing the Q_{int} data as well.

Similar to the case for strings, the high vacuum measurement of $Q_{\text{int}} = 2200$ will be used as the baseline to establish the degree of Q-enhancement. Placing the sample inside the UHV environment increases the intrinsic quality factor from $Q_{\text{int}} = 2200$ to $Q_{\text{int}} = 3450$, which is a larger increase than what was observed for the string in Figure 5.5. Calculations based on gas damping can once again not explain this observation, meaning its origin must be intrinsic. Since surface losses are larger for thinner membranes, this could explain why the corresponding enhancement is greater for this membrane compared to the strings. Annealing the sample at increasingly high temperatures initially leads to a gradual increase of Q_{int}. A maximum enhancement greater than a factor of 5 is achieved for a temperature $T_{\text{anneal}} = 800$ °C. For $T_{\text{anneal}} > 800$ °C, Q_{int} begins to deteriorate for each increasing temperature step.

The observed behavior of the intrinsic quality factor is in agreement with the experiments

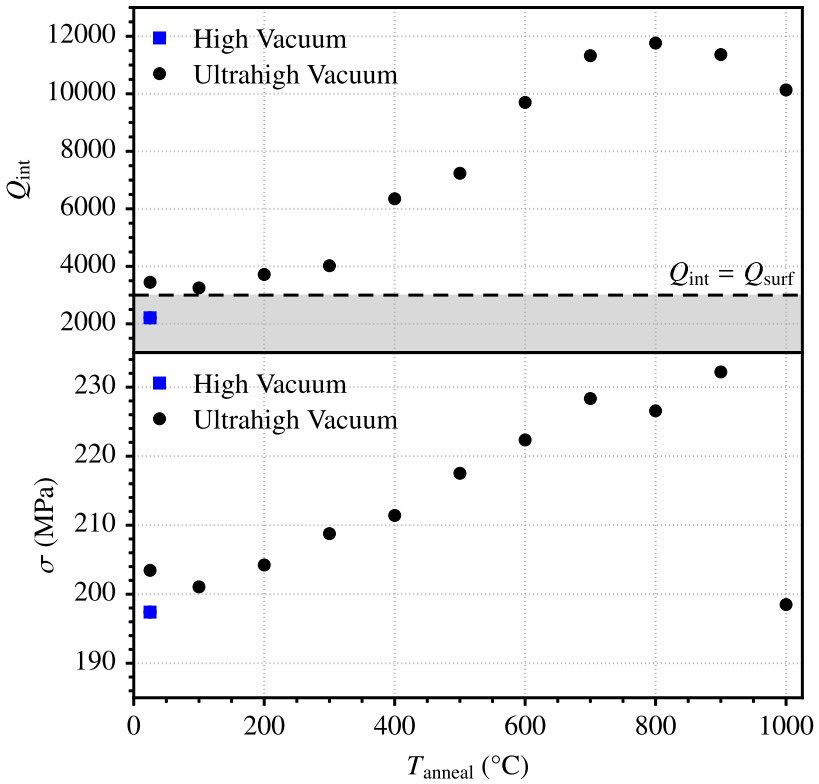

Figure 5.7: Annealing a uniform membrane resonator for 1 hour at various temperatures. Measurements of both Q_{int} (top panel) and σ (bottom panel) are given and plotted as a function of T_{anneal}. Both sets of data are based on measurements of the first 10 harmonic out-of-plane modes of the membrane. The labels high vacuum and ultrahigh vacuum refer to data acquired at pressures $p = 1 \times 10^{-5}$ mbar and $p < 1 \times 10^{-10}$ mbar, respectively. $T_{anneal} = 25$ °C indicate measurements performed before annealing. The theoretical limit for surface losses has been indicated in the top panel as well. Dimensional parameters of the membrane are $L = 810$ µm and $h = 50$ nm.

conducted on string resonators (see Figure 5.5), in which case a maximum Q_{int} was achieved for $T_{anneal} = 700$ °C, while decreasing for $T_{anneal} = 900$ °C. However, the enhancement factor achieved for the uniform membrane is greater than that achieved using strings, which can be attributed to the thickness of the membrane. Since Q_{surf} is proportional to h, while the limit set by bulk losses is fixed at $Q_{vol} = 28000$, one can obviously expect greater enhancements for thinner samples. Another cause of the larger enhancement factor could be that the membrane had more annealing steps, thus leading to the sample being heated for a longer time. The exact influence of time and temperature requires further investigation, i.e. whether a similar increase in Q_{int} could be achieved by annealing the sample at 800 °C for a longer time and skipping the lower temperature steps is currently not known.

Investigating the tensile stress for increasing annealing temperatures, as shown in the bottom panel of Figure 5.7, again provides valuable information for the interpretation of the Q-data. A steady increase in σ for $T_{\text{anneal}} \leq 900$ °C is observed, while a sharp drop is observed for $T_{\text{anneal}} = 1000$ °C, indicating a change in the properties of the SiN resonator. While these observations are in agreement with those made for string resonators, the addition of more heating steps shows what appears to be a transition between two mechanisms. For $T_{\text{anneal}} \leq 700$ °C, the tensile stress gradually increases for each annealing step, which can possibly be attributed to the aforementioned film densification [208]. At larger temperatures, σ appears to saturate, before dropping significantly at 1000 °C, which indicates another process comes into play, such as Si out-diffusion into the SiN [211].

Another point to discuss for uniform membranes is the influence of annealing on the $Q \times f_r$ product. Measurements of Q versus T_{anneal} for the (4,4) and (9,9) modes of the membrane discussed in Figure 5.7 are shown in Figure 5.8. These two modes were among the few mostly unaffected by radiation losses throughout the measurements and can therefore clearly show the effect of reduced intrinsic losses. The baseline data points at $T_{\text{anneal}} = 25$ °C are the ultrahigh vacuum measurements prior to annealing. As a result of the annealing, the $Q \times f_r$ product increases by maximum factors of approximately 6 for both mechanical modes. The UHV annealing in fact enhances the $Q \times f_r$ product to values beyond the limit for quantum coherency at room temperature, as has been highlighted in the figure as well. An overall larger $Q \times f_r$ product is achieved for the (9,9) mode, which can be expected for uniform square membranes [48]. These results show that even low-stress SiN samples can overcome the quantum limit at room temperature by reducing surface friction.

5.4 Phononic Crystal Membranes

Having established reproducible quality factor enhancement as a result of ultrahigh vacuum annealing, it is time to combine this method with resonator designs exhibiting optimal dissipation dilution. For this purpose, phononic crystal membranes of the type invented by Tsaturyan *et al.* are employed, since this is the first and most well-studied soft-clamped resonator system [39]. The different defect modes available for this PnC design are first presented, before moving into measurements of the mechanical properties in an ultrahigh vacuum.

5.4.1 Defect Modes

The unit cell of the chosen phononic crystal design was already introduced in Section 3.4.3, including how the FEM simulations of both the phononic bandgap and defect modes are

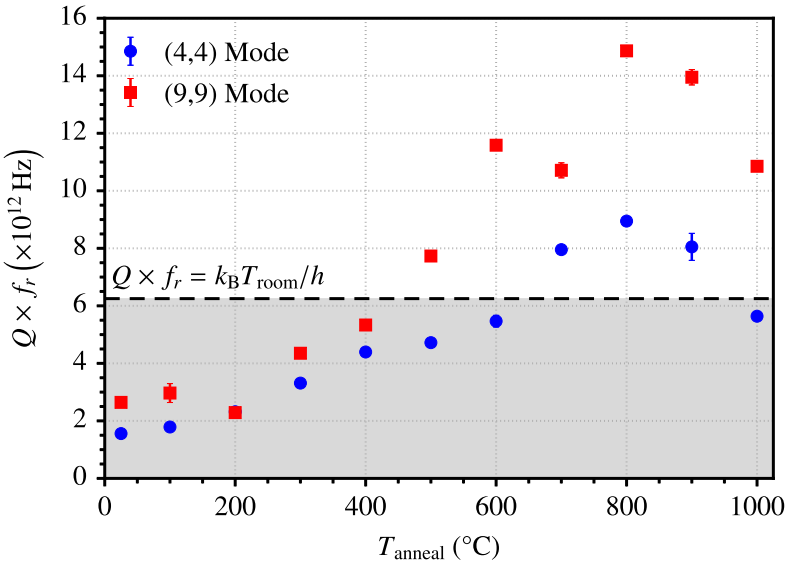

Figure 5.8: $Q \times f_r$ product versus annealing temperature for the (4,4) and (9,9) modes of the uniform membrane investigated in Figure 5.7. The room temperature quantum coherency limit has been indicated as well.

performed. Here, measurements of fabricated samples are shown, which reveals the presence of multiple defect modes in the bandgap. An optical micrograph of a successfully fabricated sample is shown in Figure 5.9(a). The PnC membranes are characterized by their lattice constant a. Though the rectangular unit cell of this design translates into a slightly rectangular PnC membrane, one can assume the membrane to be square to a good approximation. In this way, the lateral size L of the membrane scales with the lattice constant at the fixed ratio $L \sim 20.5 \times a$. For the membrane shown in Figure 5.9(a), with a lattice constant $a = 340$ µm, a lateral size $L \approx 7$ mm can be calculated.

The mechanical properties of the PnC membranes are measured by focusing the probe laser of the vibrometer on the central defect. Measured Brownian motion spectra are displayed in Figure 5.9(b) for a PnC membrane with $a = 140$ µm ($L \approx 2.9$ mm) and $\sigma_{film} = 150$ MPa. The phononic bandgap region is characterized by a significantly lower density of mechanical modes when compared with the surrounding forest of modes. Depending on the location of the probe laser, different defect modes can be measured, with a total of 5 different defect modes identified for this PnC membrane design. FEM simulations of the corresponding defect mode shapes are shown in Figure 5.9(c). Mode 1 is also called the fundamental defect mode due to resembling the fundamental mode of a uniform membrane, while the modes labeled 2-5 are higher-order resonances. The defect modes are actuated using radiation pressure,

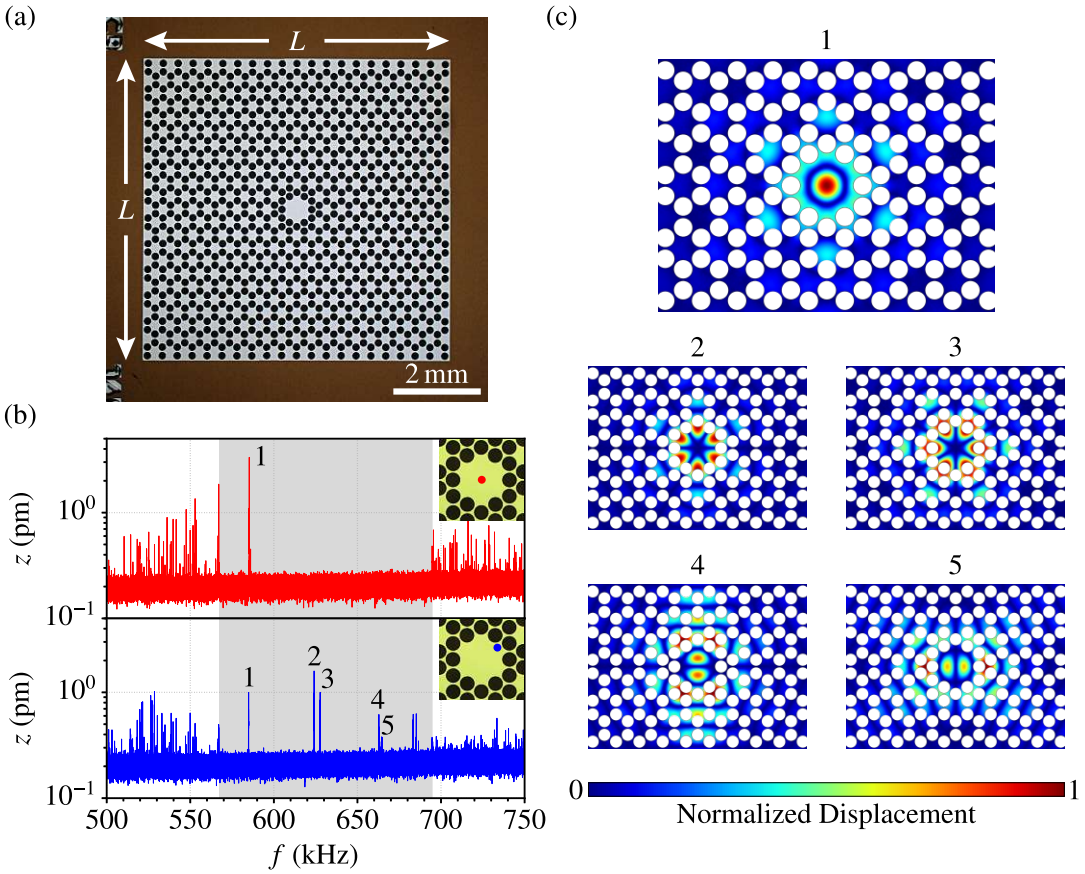

Figure 5.9: Defect modes of the phononic crystal membrane design employed here, taken from the work of Tsaturyan *et al.* [39]. (a) An optical micrograph of a fabricated PnC membrane sample with $a = 340$ µm, corresponding to a membrane side length $L \sim 20.5 \times a \approx 7$ mm. (b) Brownian motion spectra of a PnC membrane with $a = 140$ µm ($L \approx 2.9$ mm) for different locations of the probe laser, as outlined on the optical micrographs in the inset. The phononic bandgap is indicated by the grey-shading, while the labels 1-5 designate the different defect modes. (c) Finite element method simulations of the mode shapes for the five defect modes highlighted in (b).

which is achieved by focusing the actuation laser on an antinode of a given resonance (see Section 3.2.2.1), similar to the probe laser.

Thus far, the focus of this chapter has been on low-stress SiN samples, due to the reduced influence of radiation losses for lower stress values [72, 74]. However, besides soft-clamping, the phononic crystal serves to shield the defect modes from phonon tunneling out of the resonator and into the surrounding substrate. Therefore, this section will focus on high-stress SiN samples, with initial tensile stress values $\sigma_{\text{film}} = 1.1$ GPa. In this way, dissipation dilution is maximized and the results achieved can be compared to state-of-the-art Qs of nanomechanical

resonators.

5.4.2 Different Loss Mechanisms

PnC membranes have previously been shown to be susceptible to gas damping to pressures beyond the high vacuum regime ($p < 10^{-6}$ mbar) [147]. As such, the effect of reducing the vacuum pressure will be emphasized in this section as well. For this purpose, a PnC membrane of $a = 260$ µm ($L \approx 5.3$ mm) is employed. Both the fundamental mode and mode 2 were initially measured at a pressure $p = 1 \times 10^{-6}$ mbar, with Qs of $\sim (16 \pm 1) \times 10^6$ and $\sim (19 \pm 2) \times 10^6$ extracted for the two modes, respectively. These values are already significantly larger than any Qs measured for strings and uniform membranes, directly showing the effect of soft-clamping [39]. This membrane is then placed inside the UHV chamber and measured at various pressures.

Upon measuring the sample inside the UHV, the Q of the fundamental mode plummeted to such low values that any further characterization is rendered meaningless. This behavior was observed for the fundamental defect mode of many samples and can perhaps be traced back to the clamping of the samples to the sample holder. Any such clamping might change the stress of the membrane, which shifts the mode outside the bandgap and the Q therefore significantly reduced. Such behavior was rarely seen for the higher-order modes, which are located much deeper inside the bandgap. For this reason, all Q-measurements shown in this section are for higher-order modes.

Measured Q-values for mode 2 of the PnC membrane discussed above for various pressures are shown in Figure 5.10(a). A clear enhancement in Q can be observed, with a factor of ~ 8 increase when reducing the pressure from 1×10^{-6} mbar to 1×10^{-10} mbar, resulting in a $Q = (145 \pm 6) \times 10^6$. This enhancement is much larger than what was observed for strings and uniform membranes, indicating it cannot simply be a result of reduced surface losses and is therefore attributed to reduced gas damping. The lack of pressure control in the UHV chamber means that Q could not be measured in the regime from 1×10^{-6} mbar to 1×10^{-9} mbar. However, the apparent saturation of Q for $p \leq 1 \times 10^{-9}$ mbar indicates a transition from a gas damping limited to an intrinsically limited regime. From FEM simulations of the dissipation dilution factor, a $Q_{\text{int}} \approx 3250$ can be extracted for the data point at $p = 1 \times 10^{-10}$ mbar, which fits within the uncertainty of theoretical calculations using $Q_{\text{surf}} = \beta h$ [48]. These results show that for PnC membranes, it is crucial to measure in a UHV in order to fully maximize the Q regardless of surface friction.

Assuming the sample to be limited exclusively by surface friction at $p = 1 \times 10^{-10}$ mbar, the next step would be to anneal the sample in the UHV. Therefore, the membrane was an-

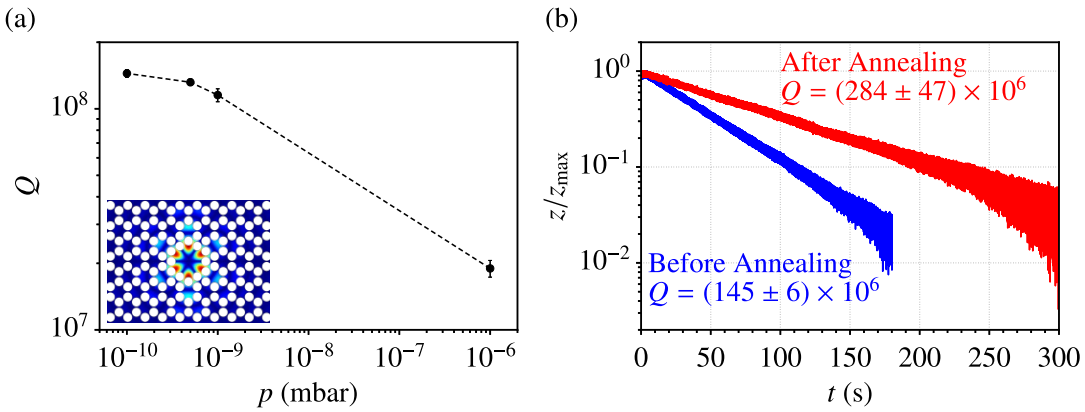

Figure 5.10: Quality factor enhancement of defect modes. (a) Pressure-dependence of Q for mode 2 of a PnC membrane with $a = 260$ µm ($L \approx 5.3$ mm) and $\sigma_{\text{film}} = 1.1$ GPa. The dashed line is a guide to the eye. A simulation of the displacement field for the measured mode is given in the inset for clarity. (b) Ringdown measurements of mode 2 before and after annealing the sample for 2 hours at 800 °C.

nealed at the optimal temperature $T_{\text{anneal}} = 800$ °C, as deduced from the measurements in Figure 5.7, for 2 hours. The annealing results are shown in Figure 5.10(b) in the form of ringdown measurements of the vibrational amplitude z, normalized to the maximum amplitude z_{max}. Annealing the sample enhances the Q by approximately a factor of 2 to value of $Q = (284 \pm 47) \times 10^6$. This corresponds to a total increase of a factor of ~ 15 compared to the initial value measured at $p = 1 \times 10^{-6}$ mbar. The $Q \times f_r$ product for the largest measured Q is $(2.79 \pm 0.46) \times 10^{14}$ Hz, which is comparable to the results achieved by both Tsaturyan *et al.* [39] and Ghadimi *et al.* [40]. In order to further enhance the Q through reduced surface losses, another annealing step was performed at $T_{\text{anneal}} = 1000$ °C. Unfortunately, the Q decreased significantly after this second heating step for unknown reasons and no further investigation of this sample was performed.

5.4.3 Annealing at Various Temperatures

Since ultrahigh Qs have been shown to be attainable for PnCs measured in a UHV, the annealing procedure needs to be optimized. The results for uniform membranes shown in Figure 5.7 indicate enhancements greater than a factor of 5 possible under the right conditions. Therefore, a PnC membrane was annealed for 1 hour at various temperatures, in a similar manner to what was already done for both strings and uniform membranes. The measured results are shown in Figure 5.11. A PnC membrane of $a = 280$ µm ($L \approx 5.7$ mm) is employed and measurements are shown for defect modes 2 and 3. For these measurements, the base

pressure inside the UHV chamber slowly increased due to a possible leak or contamination. As such, the pressures at which annealing was performed rose from $p = 6 \times 10^{-10}$ mbar to $p = 2 \times 10^{-9}$ mbar between the initial and final measurement.

Measured Q-data, as shown in Figure 5.11(a), show a gradual increase for annealing temperatures $T_{\text{anneal}} < 1000$ °C, in reasonable agreement with the data shown for strings and membranes earlier in the chapter. However, upon annealing at $T_{\text{anneal}} = 1000$ °C, the Q of mode 2 deteriorates, while that of mode 3 is enhanced. The behavior of mode 3 is unlike previous temperature variation experiments, prompting a secondary annealing step at 1000 °C, but this time for 2 hours. This secondary annealing step results in another $\sim 25\%$ enhancement in the Q of mode 3, while mode 2, which initially decreased upon annealing at 1000 °C, now gets enhanced by a factor of 2 as well. The final measured quality factors for modes 2 and 3 were $Q = (168 \pm 14) \times 10^6$ and $Q = (210 \pm 14) \times 10^6$, respectively, resulting in overall enhancements of factors ~ 6 and ~ 7 compared to the initial values at $T_{\text{anneal}} = 25$ °C. These are the largest Q-enhancements achieved using annealing in this investigation, approaching an order of magnitude enhancement.

The underlying mechanism responsible for the additional enhancement resulting from the secondary annealing step is currently not understood. For strings and uniform membranes, Qs began to deteriorate already at $T_{\text{anneal}} = 900$ °C, while no such limiting temperature is observed for PnC membranes. Observing the resonance frequency data for the two defect modes, as given in Figure 5.11(b), the behaviour is similar to that observed for strings and uniform membranes, namely a steady increase for temperatures $T_{\text{anneal}} < 900$ °C, while decreasing for $T_{\text{anneal}} = 1000$ °C. This observation could support the Si out-diffusion hypothesis since more and more Si would diffuse with time, which explains the frequency decreasing further down for the second annealing step at 1000 °C. However, the fact that the Q increases at 1000 °C would indicate a secondary mechanism coming into play, which influences the Q regardless of the resonance frequency. This could be a result of the oxide layer slowly desorbing from the SiN surface, which increases Q_{int}. Support for this contribution from two separate mechanisms would be the fact that the Q of mode 2 initially decreases for $T_{\text{anneal}} = 1000$ °C. Following the second annealing step at 1000 °C, the enhancement achieved through increasing Q_{int} must be greater than the reduction resulting from reduced dissipation dilution due to the reduced stress, thus leading to an overall Q-enhancement. A decrease in Q_{int} resulting from Si diffusion could also be expected, but appears also to be outweighed by the reduced surface losses.

In Figure 5.11(c), the $Q \times f_r$ product for modes 2 and 3 are shown, displaying a similar enhancement to the Q-data, despite the reduction in frequency for $T_{\text{anneal}} = 1000$ °C. Therefore, the annealing approach shown can directly improve previously published results and thus potentially allow room temperature quantum experiments. If this enhancement was applied to

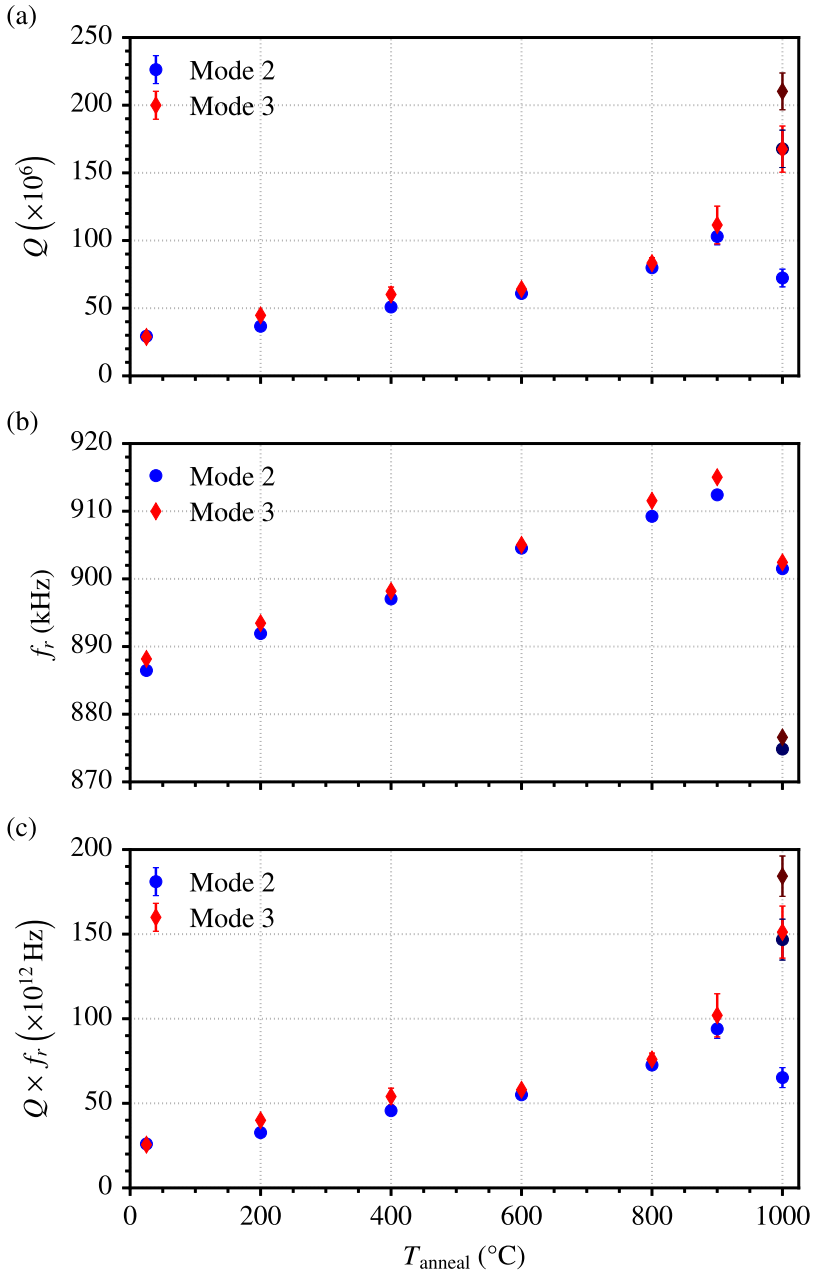

Figure 5.11: Annealing a phononic crystal membrane at various temperatures. Measurements of quality factor (a), resonance frequency (b), and $Q \times f_r$ product (c) for the higher-order defect modes 2 and 3 are shown as a function of T_{anneal} with each annealing step being of 1 hour duration. Darker-shaded data points indicate a secondary 2 hour annealing step at T_{anneal} = 1000 °C. T_{anneal} = 25 °C refers to measurements performed before annealing. The parameters of the measured PnC membrane are a = 280 µm ($L \approx 5.7$ mm) and σ_{film} = 1.1 GPa.

the sample studied in Section 5.4.2, with an initial $Q = (145 \pm 6) \times 10^6$, the final Q would potentially be greater than 1 billion and thus set a new record at room temperature. Unfortunately, the sample investigated in Figure 5.11 had an initial $Q_{\text{int}} \approx 550$, as deduced from FEM simulations, which is far below that expected from Q_{surf} [48]. While this low Q can be attributed to fabrication induced defects, it could also be a result of a slight contribution from gas damping, since the base pressure here was larger than for the measurements discussed in Section 5.4.2.

5.4.4 Effect of Air Exposure

Throughout this chapter, focus has been on enhancing the Q of nanomechanical resonators through UHV annealing. While results in support of reduced intrinsic losses have been shown, the origin of this reduction has only been proposed to be a result of reduced surface friction, but no solid evidence has been provided. At this point, the observed enhancements might simply be the result of an annealing effect, unrelated to the surface friction. Therefore, this section will display measurements aiming to explain the origin of said Q-enhancements.

For the following investigation, the PnC membrane sample displayed in Figure 5.11 will be employed. After the secondary annealing step at 1000 °C, the sample was taken out of the UHV chamber and placed inside the load lock chamber of the UHV system. Then, the UHV gate valve was closed and the load lock vented until reaching atmospheric pressure. The sample was then left at this pressure overnight. Upon reloading the sample into the UHV chamber, the Qs of modes 2 and 3 had decreased significantly, with mode 3 being immeasurable due to the very low Q. However, mode 2 could be measured and results for both Q and f_r are given in Figures 5.12(a) and 5.12(b), respectively.

Evidently, the Q of mode 2 reduces from $Q = (168 \pm 14) \times 10^6$ to $Q = (44 \pm 2) \times 10^6$ after having been exposed to air overnight, strongly supporting that adsorbates have readsorbed on the resonator surface, in addition to regrowth of native oxide. Reannealing the sample at $T_{\text{anneal}} = 900$ °C for 1 hour results in an enhancement to $Q = (79 \pm 2) \times 10^6$. This suggests that the deterioration resulting from air exposure is a reversible effect, further supporting reduced surface friction as being the origin of the observed Q-enhancement. Inspecting the frequency data, a decrease in f_r is also observed after air exposure, which suggests growth of compressive layers on the surface of the SiN [86]. Annealing the sample in a UHV again increases f_r, which would imply desorption of adsorbates and possibly a native oxide layer on the surface. Running the annealing process for a longer time could potentially allow the sample to reach its frequency prior to air exposure, provided the temperature $T_{\text{anneal}} < 1000$ °C.

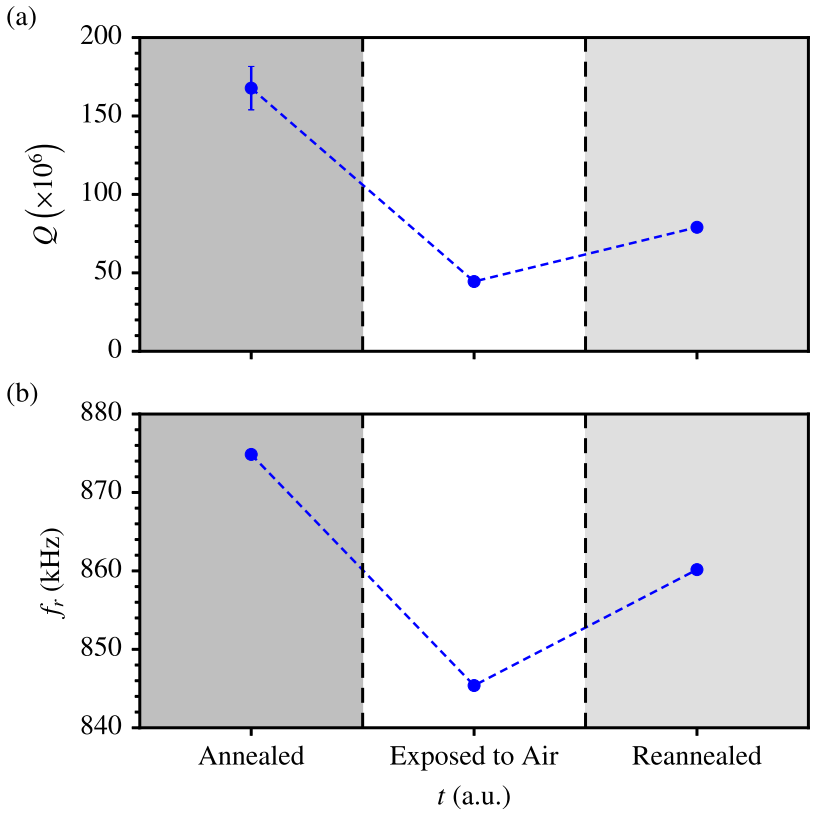

Figure 5.12: Effect of air exposure on the quality factor (a) and the resonance frequency (b) of mode 2 for the PnC membrane investigated in Figure 5.11. The x-axis is labeled "time", highlighting the various steps taken in the experiment. "Annealed" corresponds to measurements conducted prior to air exposure. Dashed blue lines are a guide to the eye.

5.5 Summary and Outlook

In conclusion, this chapter has shown a detailed investigation into reducing intrinsic losses of nanomechanical resonators. The method used to reduce intrinsic losses was to anneal samples up to temperatures of 1000 °C in an ultrahigh vacuum environment. Various resonator geometries were investigated, including strings, uniform membranes, and softly-clamped phononic crystal membranes. It was shown how placing samples inside an ultrahigh vacuum alone could result in a slight intrinsic quality factor enhancement for strings and uniform membranes, assumed to be a result of various adsorbates desorbing from the resonator surface. The enhancement resulting from reducing the vacuum pressure was significantly larger for PnC membranes, which was attributed to reduced gas damping. Upon annealing the samples in the UHV, the intrinsic quality factors were enhanced for all resonator designs, with the enhancement being ascribed to reduced surface friction. This was confirmed by exposing

a sample to air overnight and remeasuring it in the UHV, in which case the Q had reduced significantly.

Figure 5.13 shows the current state of the investigation by repeating Figure 2.5 initially used for the theoretical discussion of surface friction in Section 2.2.3.2. The plot shows the theoretical intrinsic quality factor based on Equation (2.72) as a function of resonator thickness, including the expected limits from surface losses and bulk losses. For the theoretically calculated Q_{int}-values, the uncertainty resulting from Q_{surf} is given as well (grey-shaded area). Overlaid on the theoretical curves are measured intrinsic Qs before and after UHV annealing for the samples shown in Figures 5.5, 5.7, and 5.11. In all cases, Q_{int} can be observed to be enhanced beyond the surface loss limit, highlighting the reduction in surface losses. The enhancement factor can also be observed to increase for thinner resonators, which makes sense, given that surface losses affect thinner resonators greater. However, in none of the cases presented does the final Q_{int} approach the theoretical limit set by $Q_{\text{vol}} = 28000$, indicating that surface losses have not been completely negated in any case [48].

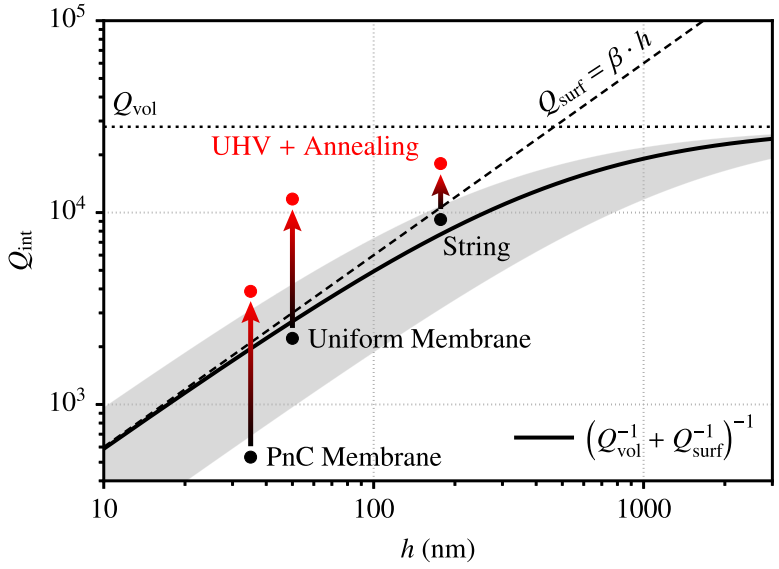

Figure 5.13: Enhancement of the intrinsic quality factor achieved in this investigation. The figure is fundamentally the same as Figure 2.5, but with measured values of Q_{int} acquired in this chapter given as well for all investigated resonator geometries, both before (black points) and after (red points) annealing in an ultrahigh vacuum.

No conclusion can currently be made for why surface losses could not be removed entirely. In order to explain what happens, measurements of the resonance frequency/tensile stress were given throughout the chapter as well. For the largest available annealing temperature

of 1000 °C, the resonance frequency of all resonators decreased, indicating a change of the material properties. Considering that removal of compressive native oxide should increase the frequency, this suggests changes to the bulk properties of the SiN. One possible explanation would be the out-diffusion of Si atoms from the substrate and into the SiN resulting from the annealing [211]. Increasing the Si content in the SiN could explain the reduced frequencies since the tensile stress reduces for increasing amounts of Si [136]. Furthermore, this diffusion could potentially create defects in the SiN resonator and thus decrease Q_{int}, which would explain why the theoretical limit of Q_{vol} could not be reached.

The next step would be to determine the origin of the reduced surface losses shown here. For that purpose, surface characterization techniques would have to be performed in conjunction with the Q-measurements, such as energy-dispersive X-ray spectroscopy (EDX) or X-ray photoelectron spectroscopy (XPS). These techniques could highlight the content of Si, SiN, and SiO_2 both in the bulk as well as the surface of the resonator, thus showing both the potential removal of native oxide in addition to any Si contamination occurring resulting from the annealing. Removing any sample from the UHV and transporting it to suitable characterization equipment would almost immediately contaminate the surface. Therefore, a secondary annealing chamber would be needed, one which is directly connected to suitable measurement equipment. Techniques such as atomic force microscopy (AFM) could also be used to check the surface roughness before and after annealing.

Besides characterizing the resonator surface, the annealing procedure needs to be optimized. The problem of time versus temperature requires further investigation, i.e. if similar enhancements to that observed for $T_{\text{anneal}} = 1000$ °C could be achieved by annealing at $T_{\text{anneal}} = 800 - 900$ °C for a longer duration. However, annealing temperatures on the order of 1000 °C are needed to remove native oxide, which is required in order to completely negate surface losses. Therefore, one could perhaps place a protective layer between the SiN and Si substrate, which would accept all Si atoms diffusing out of the Si substrate. Finally, the annealing temperatures reported here are measured at the sample holder surface. It is very likely that the resonator is at a lower temperature than the sample holder, which has to be accounted for in order to properly anneal samples.

Despite the questions left unanswered, the largest enhancements in Q_{int} reported here would be enough to potentially achieve Qs greater than 1 billion at room temperature if applied to resonators which maximize dissipation dilution [39, 40]. The reduction in the resonance frequency upon annealing at 1000 °C had negligible influence on the $Q \times f_r$ product, which was enhanced similarly to the Q. As such, the results presented here could pave the way towards performing room temperature quantum experiments.

6

Frequency Fluctuations in High-Q Resonators

In this chapter, an investigation into the frequency stability of high quality factor nanomechanical string resonators is presented. Firstly, an introduction into how the frequency stability is measured, both in open- and closed-loop configuration, is given, including a definition of the noise sources and how these manifest themselves in the frequency fluctuations. Then, the influence of various experimental parameters on the frequency stability in open-loop configuration is shown and compared to theory-based calculations. Finally, closed-loop measurements and calculations are presented as well and weighted against the open-loop case. The results and associated discussions presented in this chapter are based on Paper **VII** [170].

6.1 Introduction

Until now, the focus of the thesis has been to enhance the quality factor for fundamental research applications. However, one of the main reasons behind the huge amount of research into nanomechanical resonators has been their potential application as sensors. The reduction in resonator dimensions leads to increased responsivity towards a number of physical quantities, including mass [17, 172, 173, 212–214], force [18, 215–218], and temperature [95, 151, 219–222]. For most nanomechanical sensors, the main principle of detection has been through a shift of the resonance frequency f_r. The minimum detectable frequency shift δf is determined by the precision of the resonance frequency measurement. A simple expression quantifying the average relative frequency stability in the white noise limited regime is the so-called Robins' formula [108, 223]:

$$\left\langle \frac{\delta f}{f_r} \right\rangle = \frac{1}{2Q} \frac{1}{\mathrm{SNR}}, \tag{6.1}$$

where SNR is the signal-to-noise ratio, i.e. the ratio of the maximum driven signal to the noise floor. From Equation (6.1), it is apparent that minimizing the system noise results in optimized frequency stability. Various intrinsic noise sources can result in frequency fluctuations, with prominent examples provided in Section 2.4. Given that most of these noise sources are predictions based on theory with only few experimental observations [112], the most fundamental limit turns out to be thermomechanical noise [113–115, 125, 126]. A theoretical description of this noise source was provided in Section 2.4.1.

For frequency precision measurements, an important factor is the relation between the measurement bandwidth BW of the readout electronics and the resonance linewidth Γ of the resonator. Most studies and theoretical models thus far have assumed a regime where $\mathrm{BW} \ll \Gamma$, which is the white noise limited regime [112, 223]. However, as a result of Equation (6.1), a lot of attention has been placed on maximizing Q for optimum sensor performance. With the recent demonstrations of optimal dissipation dilution using soft clamping and strain engineering, resonators routinely achieve $\Gamma \ll 1$ Hz [39, 40, 77]. Operation of such resonant sensors would therefore require BW's as small as a few mHz in order to remain within the $\mathrm{BW} \ll \Gamma$ regime. Such slow detection speeds are impractical for many sensor applications, which require high-speed detection of minute amounts of a quantity.

A number of investigations into the frequency stability of high-Q resonators have been previously published, yielding different conclusions in terms of the effects of raising Q. Fong *et al.* studied the frequency and phase noise of high-Q SiN resonators, arguing that observed frequency fluctuations were a result of defect motion with a broad distribution of relaxation times [224]. Furthermore, it was concluded that increasing Q results in an increased susceptibility towards the intrinsic frequency noise of the resonator. On the other hand, Roy *et al.* reported enhanced frequency stability of silicon resonators as Q was lowered, when driving the resonator at the onset of Duffing nonlinearity in the thermomechanically limited regime [225, 226], where $Q \propto 1/\mathrm{SNR}$ [227]. This observation was attributed to a flattening of the phase noise spectrum at low frequencies. The same scenario was thoroughly investigated theoretically by Demir *et al.*, who found no Q-dependence of the frequency stability [125].

This chapter presents a detailed investigation into the frequency fluctuations of high-Q nanomechanical SiN string resonators [170]. All presented measurements are performed in the thermomechanically resolved regime and the focus will be on the case where $\mathrm{BW} \gg \Gamma$. Measurements are given in both open-loop and closed-loop tracking configurations, showing how these compare with one another in terms of noise level and speed. Influence of various experimentally controllable parameters on the frequency fluctuations is presented and discussed. Measured data are corroborated by computations based on a theoretical model throughout the chapter.

6.2 Fundamental Definitions

In order to better explain the measured results, certain fundamental definitions have to be given, as shown in Figure 6.1. The samples studied here are high-stress nanomechanical string resonators made from SiN. A false-colored scanning electron microscopy image of the strings is given in Figure 6.1(a), including a zoom-in on one such string for clarity. The dimensional parameters of the strings are length $L = 1$ mm, width $w = 6$ µm, and thickness $h = 312$ nm. Only the fundamental out-of-plane string mode is investigated, which has a frequency $f_r = 264$ kHz, from which a tensile stress $\sigma = 0.85$ GPa can be extracted. Quality factors Q of this mode typically lie in the 10^5 regime at high vacuum.

Frequency stability measurements are performed in either an open-loop or closed-loop configuration, the principle behind both already described in Section 3.2.3.1, using a lock-in amplifier. For either type of measurement, the driven response is first measured in order to determine the nominal f_r, with illustrations given in Figure 6.1(b). A piezo is here used to drive the resonance, the strength of the drive being quantified through the piezo driving voltage U. The maximum driven signal is the vibrational amplitude at resonance $z_{\max}$. In addition, Figure 6.1(b) comparatively shows the resolution bandwidth BW of the low-pass filter and resonance linewidth Γ, emphasizing the fact that BW $\gg \Gamma$. For all the measurements presented here, a BW $= 3598$ Hz is chosen, while the sampling rate is set to 28784 Sa/s, which is a factor of 8 greater than the BW.

A typical phase response around the resonance frequency is shown in Figure 6.1(c). Open loop measurements are performed by actuating the sample at resonance and then recording the phase $\phi(t)$ over time. In order for this approach to work, thermal drifts have to be small enough that the phase stays within the linear phase regime. If this criteria is met, conversion from a phase shift $\Delta\phi$ to a frequency shift Δf can be made using the slope of the phase response at resonance (see Section 2.1.1):

$$\Delta\phi = \frac{2Q}{f_r}\Delta f. \tag{6.2}$$

For the closed-loop case, both the resonance frequency and the phase at resonance are given as parameters in the phase-locked-loop control of the lock-in amplifier and used to track the frequency $f(t)$ directly.

For the analysis of the frequency fluctuations data, it is essential to identify the noise sources of the system [126]. These noise sources can also be measured through the lock-in amplifier by measuring the square root of the power spectral density $\mathrm{PSD}^{1/2}$ around f_r with the piezo drive turned off. A sketch of the $\mathrm{PSD}^{1/2}$ is given in Figure 6.1(d), allowing the identification of the two main noise sources present in the system, namely the thermomechan-

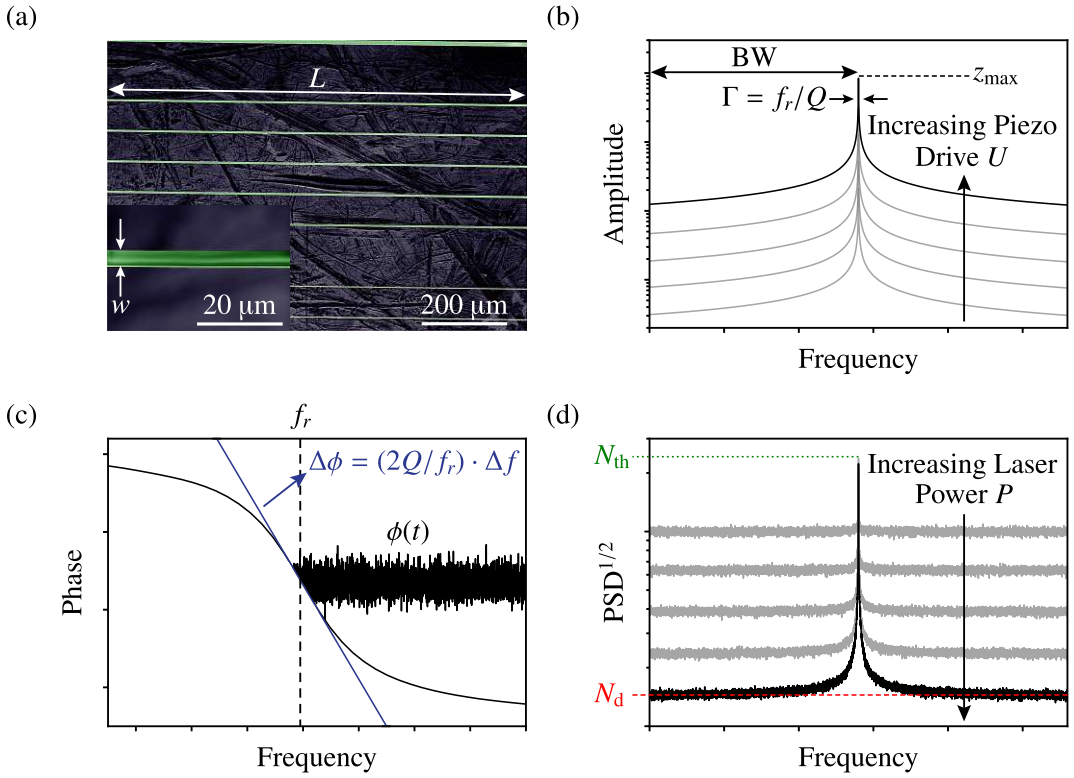

Figure 6.1: Data acquisition and fundamental definitions. (a) False-colored scanning electron micrograph of the nanomechanical string resonators studied here, which have a length L = 1 mm, width w = 6 µm, and thickness h = 312 nm. Inset shows a close-up of one of the string resonators. (b) Definition of the driven vibrational amplitude z_{max}, resonance linewidth Γ, and resolution bandwidth BW. (c) Open-loop measurement of frequency fluctuations by driving the sample at resonance and tracking the phase over time. The phase can then be converted to frequency through the slope of the phase response at resonance. (d) Illustration of the square root of the power spectral density $PSD^{1/2}$ around resonance, highlighting the two sources of noise: Thermomechanical noise N_{th} and detection noise N_d. The plots in (b) and (d) are only sketches made for clarity and do not display actual measurements.

ical noise of the resonator N_{th} and the detection noise of the optical transduction scheme N_d. Figure 6.1(d) also demonstrates how the detection noise limit can be reduced by increasing the vibrometer laser power P.

The frequency stability is here quantified using the Allan deviation σ_A, the definition of which is given in Section 2.4.2. As a consequence of BW $\gg \Gamma$, in the case where thermomechanical noise can be clearly resolved above the detection noise, two separate white noises are present in the system. How the noise sources manifest themselves in the open-loop Allan deviation is shown through an exemplary measurement plot in Figure 6.2. The closed-loop case is slightly different and will be discussed in Section 6.6. Evidently, σ_A is separated into

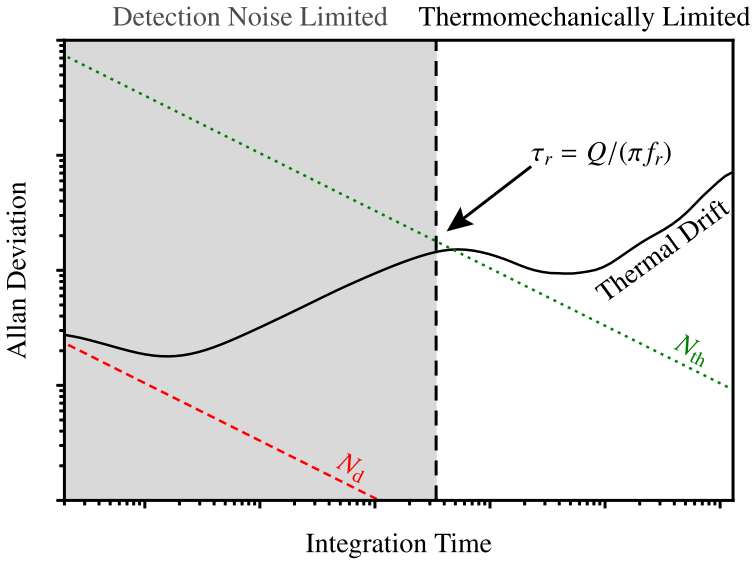

Figure 6.2: Manifestation of the noise sources in the Allan deviation, with the different noise regimes being separated by the resonator time constant $\tau_r = 1/(\pi\Gamma) = Q/(\pi f_r)$. For $\tau > \tau_r$, the resonator is predominantly thermomechanically limited, except for the largest τ-values, in which case thermal drift becomes the dominant limitation, while for $\tau < \tau_r$, the resonator is mainly limited by detection noise. Figure adapted from [170].

a detection noise and a thermomechanical noise regime. The integration time at which the noise transitions between the two regimes is the intrinsic resonator time constant τ_r defined as:

$$\tau_r = \frac{1}{\pi\Gamma} = \frac{Q}{\pi f_r}. \tag{6.3}$$

This relation was already shown during the discussion of ringdown measurements in Section 3.2.4 (see Equation (3.5)). For $\tau > \tau_r$, the resonator is mainly limited by thermomechanical noise, indicated by the white-shaded region in Figure 6.2. The resonance frequency typically also drifts over time, either through variations of the temperature in the laboratory, or due to drifts in the laser power, as will be discussed further below. As such, for very large τ-values, thermal drift typically increases σ_A. The detection noise limited regime (grey-shaded region in Figure 6.2) is then defined as the region where $\tau < \tau_r$. At even smaller τ-values, a secondary drop in σ_A occurs, which is due to the limit of the low-pass filter bandwidth. This part is intentionally left out of Figure 6.2 and all other σ_A plots in this chapter to make the data visualisation clearer, as already discussed in Section 3.2.3.2.

Theory-based Allan deviation curves are shown alongside measurements throughout the chapter. Such curves are generated using the integral given in Equation (2.121), which require

experimental knowledge of f_r, Q, $z_{\max}$, N_{th}, and N_{d} [125]. In the regime where additive white noise dominates the frequency stability, the Allan deviation is given as:

$$\sigma_{\text{A}} = \frac{1}{2Q}\frac{N_{\text{l}}}{z_{\max}}\sqrt{\frac{1}{\tau}}, \tag{6.4}$$

where N_{l} is the (white) noise level of the system, defined as the square root of the one-sided noise spectral density, which in this case can be thermomechanical noise ($N_{\text{l}} = N_{\text{th}}$) or detection noise ($N_{\text{l}} = N_{\text{d}}$). The term $N_{\text{l}}/z_{\max}$ is the signal-to-noise ratio, with the noise being in units of X/Hz and that of the driven amplitude in X, with X representing units of voltage, displacement, etc.

6.3 Laser Power Fluctuations

Before diving into the frequency fluctuations of the string resonators, the noise of the vibrometer laser is characterized. Since all the frequencies are optically transduced, unavoidable fluctuations of the laser power present an additional limitation to the frequency stability. For this purpose, the vibrometer laser power is measured using a silicon photodiode (S120C from Thorlabs GmbH) connected to a digital power meter console (PM100D from Thorlabs GmbH). The analog output of the power meter is then connected to the auxiliary input of the lock-in amplifier so that the power can be tracked over time with similar settings as the rest of the measurements. This in turn is made possible due to the fast response time of the photodiode (< 1 µs, provided by the manufacturer).

The lock-in amplifier provides a measured voltage, which is initially converted into a photodiode current, and afterward to a power using the responsivity of the photodiode at the laser wavelength ($\lambda = 633$ nm). A 5 minute recording of the largest available vibrometer laser power is given in Figure 6.3(a). Important here is to note that the power drifts over time, an unavoidable consequence of using the vibrometer laser. For very thermally responsive samples, this drift can dominate the entire Allan deviation. The problem can be minimized by turning the laser on for some hours before performing measurements.

In order to convert the laser noise into frequency noise of the resonator, knowledge of the relative thermal responsivity $\delta\mathscr{R}$ is required. While an analytical model exists, the wavelength- and thickness-dependent optical absorption coefficient $\mathcal{A}$ for this batch of SiN strings is unknown, rendering a meaningful calculation of $\delta\mathscr{R}$ difficult. As such, $\delta\mathscr{R}$ is instead determined experimentally by measuring the resonance frequency versus laser power. Measurements of f_r for each of the vibrometer power steps is given Figure 6.3(b). A nonlinear shift is observed, which is in contrast to the linear dependence expected from theory (see Equation (2.94)). As

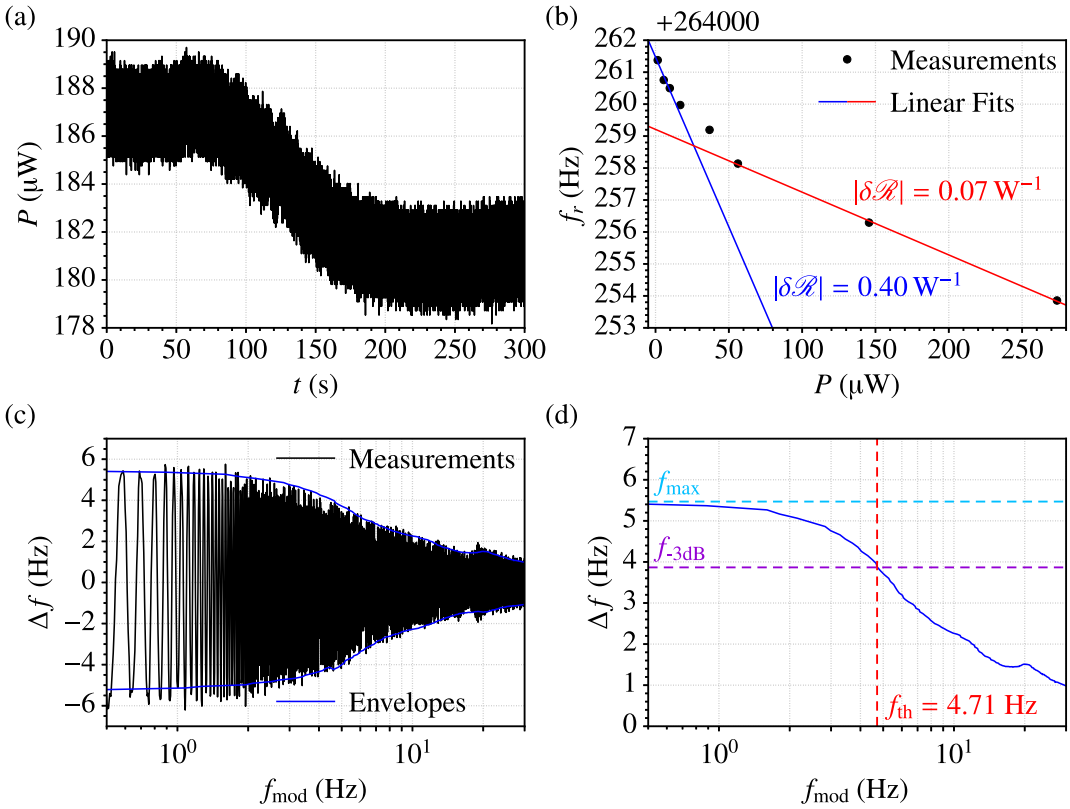

Figure 6.3: Measurement of the power fluctuations of the vibrometer laser. (a) A recording of the laser power for a 5 minute measurement duration. (b) Measured resonance frequencies of a string sample for each power step of the vibrometer laser. Two slopes can be identified as a result of emission of thermal radiation. (c) Measured resonance frequency response versus modulation frequency of a secondary diode laser along with the envelopes of the measurement. (d) Upper envelope from (c), showing how the thermal response frequency f_{th} is extracted.

discussed in Section 2.3.1.2, this is a result of emission of thermal radiation, which, in the case of pure SiN strings, results in a nonlinear frequency detuning, even at very low powers. An approximation can be made by defining two slopes and then, depending on the chosen vibrometer power step, calculating laser power fluctuations according to one of the two slopes.

With the knowledge of the laser power fluctuations δP and the relative thermal responsivity $\delta\mathscr{R}$, frequency fluctuations of the string can be calculated using [16, 170]:

$$\left\langle \frac{\delta f}{f_r} \right\rangle = \delta\mathscr{R} \cdot \delta P. \tag{6.5}$$

One can then take the Allan deviation of the curve generated using Equation (6.5). The frequency response of the resonator to the laser power fluctuations comes from photothermal

heating. As such, knowledge of the time it takes the strings to reach thermal steady state, defined as the thermal time constant τ_{th}, is required. With the recent discoveries of radiative heat transfer in SiN membranes, an up-to-date analytical model for the thermal time constant of strings currently lacks. Therefore, τ_{th} has to be experimentally determined.

The procedure with which τ_{th} is measured is similar to that reported by Piller *et al.* [103]. Firstly, the resonance frequency of the string has to be locked using the PLL of the lock-in amplifier, and then the response to a temperature modulation recorded. For this purpose, a secondary diode laser is amplitude modulated, and the detuning of the string resonance frequency Δf recorded as function of the modulation frequency f_{mod}. Important here is to measure at a high vacuum, in order to minimize heat transfer to surrounding air molecules [62]. A plot of the measured frequency response is given in Figure 6.3(c) along with the envelopes of the measurement. The detuning can be observed to initially be constant for $f_{\text{mod}} \lesssim 2$ Hz, but then starting to decay at higher frequencies. Evaluation of τ_{th} can be made with either of the envelopes, with the upper envelope given in Figure 6.3(d). If the maximum detuning is named f_{max}, then the thermal time constant is evaluated at the modulation frequency f_{th} where the detuning has decreased by 3 dB, $f_{\text{-3dB}} = f_{\text{max}}/\sqrt{2}$. The thermal time constant can be calculated from the thermal response frequency: $\tau_{\text{th}} = 1/(2\pi f_{\text{th}}) \approx 33.8$ ms. The raw frequency fluctuations data generated using Equation (6.5) is then low-pass filtered with a pass frequency $f_{\text{pass}} = f_{\text{th}}$ before the Allan deviation is evaluated. Such an Allan deviation curve will be shown in the following section.

6.4 Influence of Signal-to-Noise Ratio in Open-Loop

The effect of the signal-to-noise ratio of the open-loop Allan deviation is investigated first. As explained in Figure 6.1, one can control the SNR either by increasing the vibrometer laser power, which reduces the detection noise, or through increasing the piezo drive, which increases the vibrational amplitude, i.e. the driven signal. Measured and theory-based σ_{A} curves for various SNRs are given in Figure 6.4. Each measured plot is for a fixed drive U, while P is increased from 1.5 µW to 270 µW. Measurements of the vibrational amplitudes and noise levels in the electrical domain are converted from volts to meters using the decoders of the vibrometer and then used to generate the theoretical σ_{A} curves. Calculations based on Equation (6.4) are given as well in the case of thermomechanical noise (green dotted lines) and detection noise (red-shaded dashed lines). Vertical dashed lines on each plot correspond to the resonator time constant $\tau_r = 0.34$ s. All these measurements were performed in a high vacuum $p \sim 1 \times 10^{-5}$ mbar.

Figure 6.4(a) presents curves for the lowest employed $U = 5$ µV, which represents a case

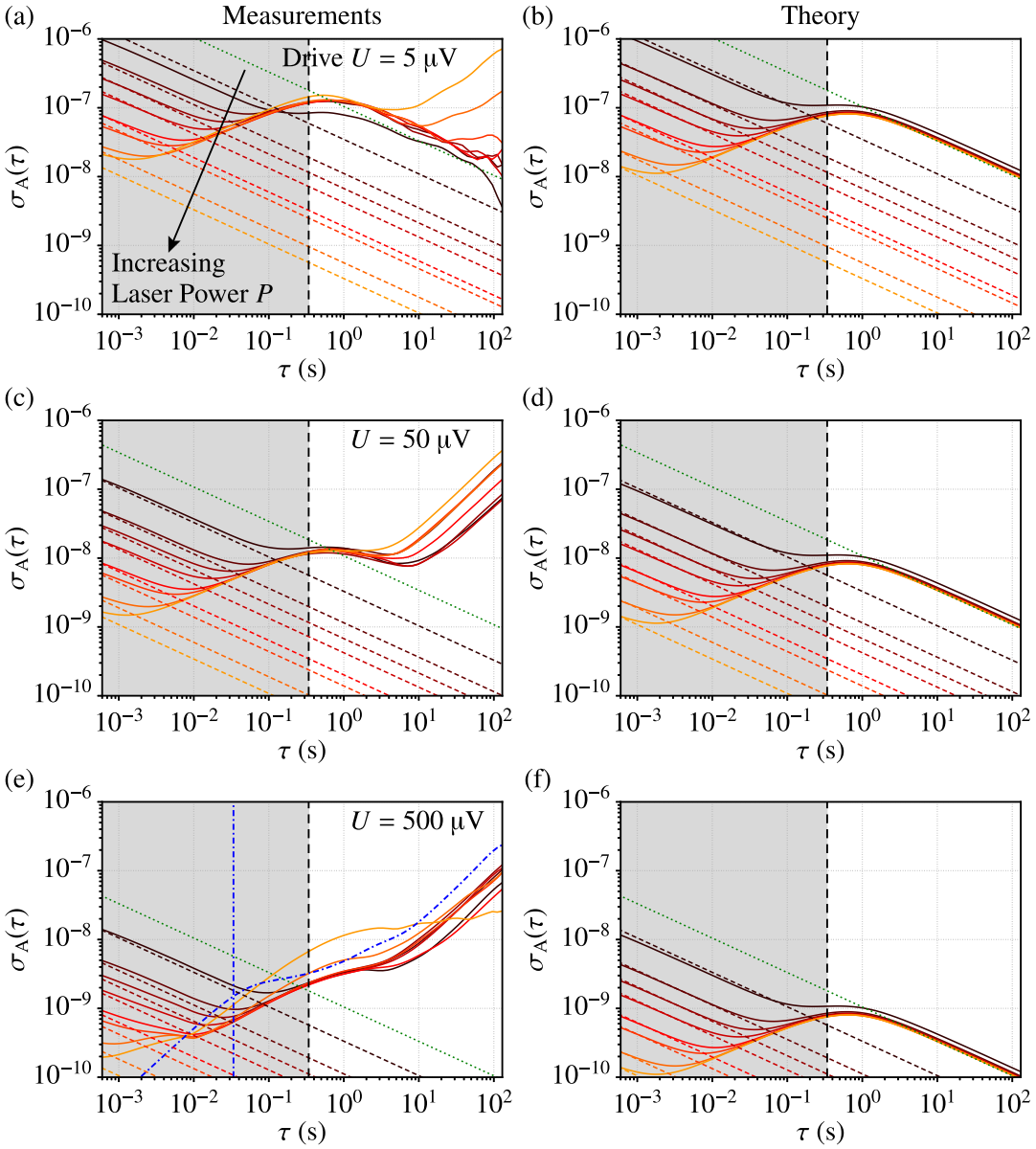

Figure 6.4: Effect of varying detection noise on the Allan deviation in open-loop configuration. Measured Allan deviations were recorded by varying the vibrometer laser power P from 1.5 µW to 270 µW, for a fixed piezo driving voltage U = 5 µV (a), U = 50 µV (c), and U = 500 µV (e). Corresponding theory-based calculations are given in (b), (d), and (f), respectively. Calculations using Equation (6.4) are given as well for $N_\mathrm{I} = N_\mathrm{th}$ (green dotted lines) and $N_\mathrm{I} = N_\mathrm{d}$ (red-shaded dashed lines). The black vertical dashed lines indicate $\tau = \tau_r$. In (e), a curve generated from laser power fluctuations corresponding to P = 270 µW is shown as well (blue dashdotted curve), which has been low-pass filtered at a frequency corresponding to the thermal time constant τ_th (blue vertical dashdotted line). Figure adapted from [170].

where the resonator is driven well within the linear regime. The thermomechanical and detection noise regimes can be clearly distinguished with the transition occurring around $\tau = \tau_r$, as expected. In addition, the decrease in N_d correctly explains the decrease in σ_A at lower τ-values, which is confirmed through the white noise asymptote calculations. The thermomechanically limited regime is unaffected by the increase in P, which makes sense since only the detection noise is altered by P. Thermal drift appears to increase with increasing laser power, which can be attributed to the laser power fluctuations discussed in the previous section, with additional support of this argument given below.

Upon increasing the drive to $U = 50\ \mu\mathrm{V}$, σ_A can be observed to be improved by an order of magnitude, indicating that the sample is still driven in the linear regime. Further increase to $U = 500\ \mu\mathrm{V}$ results in behavior that cannot simply be explained as an increase in SNR. The thermomechanical asymptote is far below the measured σ_A, meaning that the resonator is limited by an additional noise source. Since the string was still behaving linearly, as confirmed through frequency sweeps of the vibrational amplitude around resonance, Duffing nonlinearity can be ruled out as the origin of the observed limit. The observation that only the thermomechanical regime is affected, i.e. the detection noise regime continuously decreases with increasing P, supports that this is a noise source affecting the resonator intrinsically.

In fact, it turns out that the limit is a result of the aforementioned frequency fluctuations arising from fluctuations in the laser power. Besides the Allan deviation curves coming from tracking the string resonance frequency, an additional curve generated using Equation (6.5) is given in Figure 6.4(e) as well (blue dashdotted curve). This particular measurement corresponds to the data presented in Figure 6.3(a), i.e. for the largest available vibrometer laser power. A blue vertical dashdotted line is shown as well and indicates $\tau = \tau_\mathrm{th}$. Laser power fluctuations appear to decently describe the observed limit, both quantitatively and in terms of reproducing the measured trends. The slope of the blue σ_A curve at large τ fits with that of the other curves, which suggests that the thermal drifts observed here come from the laser as well. A slight offset in σ_A can be seen and is most likely due to laser aging since the laser noise was measured two years after the string measurements were performed. Back then, a $P = 270\ \mu\mathrm{W}$ was measured, which is much larger than the average value seen in Figure 6.3(a). These findings strongly support laser power fluctuations as the origin of the observed frequency stability limit observed here.

Theory-based computations are shown in Figures 6.4(b), 6.4(d), and 6.4(f) [125]. The effect of reducing detection noise appears to be accurately reproduced by the theory. Laser power fluctuations have not been incorporated into the theoretical model, hence why the Allan deviation remains thermomechanically limited for $\tau > \tau_r$. For the same reason, thermal drifts at large τ are not observed in the theoretical curves.

Returning the focus to the SNR, the next step is to observe the behavior of σ_A for a

fixed laser power, but varying piezo drive. Both measured and theory-based σ_A's of this sort are given in Figure 6.5. For the measurements, which are shown in Figure 6.5(a), the piezo drive was increased from $U = 5$ µV to $U = 1.5$ mV, while the laser power was kept at $P = 17$ µW. Increasing U can be observed to initially result in a linear reduction of σ_A for all τ, until a limit is reached in the thermomechanical regime for larger U-values. Given that this hard limit occurs at similar σ_A's and with a similar thermal drift slope to the measurements in Figure 6.4(e), this can also be attributed to laser power fluctuations. The theoretical curves given in Figure 6.5(b) display good agreement with measurements at lower vibrational amplitudes, but start to diverge for larger amplitudes, since laser power fluctuations have not been incorporated into the model.

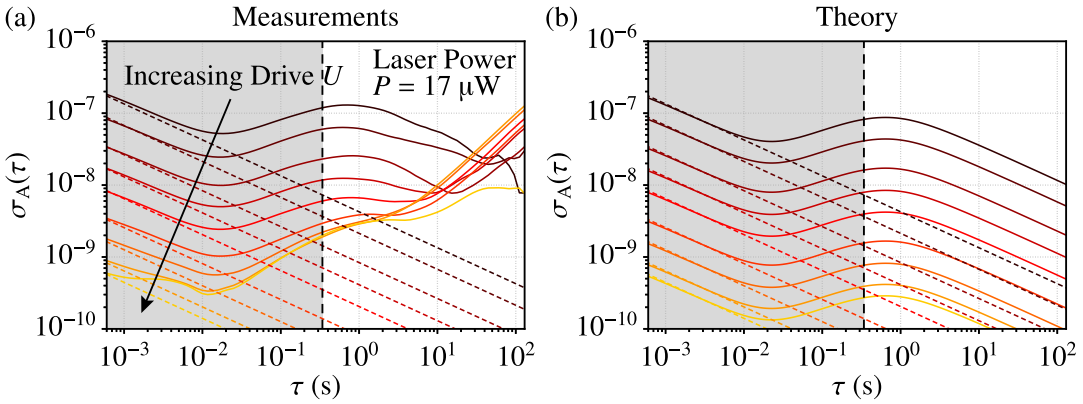

Figure 6.5: Influence of piezo drive voltage on the Allan deviation in open-loop configuration. (a) Measured Allan deviations for drive voltages ranging from $U = 5$ µV to $U = 1.5$ mV. (b) Theory-based Allan deviations for driven amplitudes corresponding to the measurements in (a). Red-shaded dashed lines indicate calculations based on Equation (6.4) for $N_l = N_d$. Black vertical dashed lines indicate the resonator time constant τ_r. Figure adapted from [170].

6.5 Influence of Q in Open-Loop

Having investigated the effect of SNR on the frequency stability in open-loop configuration, the next step is to study the effect of changing the quality factor. For this purpose a needle valve attached to the vacuum chamber is employed to slowly increase the pressure from $p = 3 \times 10^{-6}$ mbar up to $p = 20$ mbar, which in turn deteriorates the Q due to gas damping [62]. Measured and theory-based Allan deviation curves for decreasing values of Q can be found in the left and right column of Figure 6.6, respectively. All measurements were recorded for a fixed laser power, but increasing piezo drives. Due to high levels of laser-induced thermal drifts on the day of the measurements, the measured σ_A-curves for $p = 3 \times 10^{-6}$ mbar were

acquired at a $P = 17$ μW. For the rest of the measurements, a maximum value of $P = 270$ μW was employed, ensuring that the thermomechanical noise could be resolved. Each measured plot states both the pressure at which the measurement was made in addition to the resonance linewidth.

As the Q is reduced, a clear shift in the transition region between the detection and thermomechanical noise regimes to lower integration times can be discerned. The point of transition between the two regimes consistently lies around $\tau = \tau_r$, and a linear dependence of said region on Q can be extracted, as expected from the analytical definition of the response time given in Equation (6.3). As Γ starts to approach the BW of the measurement, σ_A becomes thermomechanically limited for all τ in the span of the measurements. The laser power fluctuations remains a hard limit in the thermomechanical regime for all Qs, most evident through the limits for $\Gamma = 3.59$ Hz and $\Gamma = 36.3$ Hz being of similar magnitude, in addition to the thermal drift appearing at large τ for all Γ-values. However, a quantitative estimate of the limit for each Γ would require measuring the thermal responsivity at each pressure. Since the thermal conductivity of air begins to increase significantly for $p \geq 10^{-1}$ mbar [158], convection starts to play a more dominant role in the heat transfer and therefore $\delta\mathscr{R}$ reduces. Since $\delta\mathscr{R}$ was only measured at a high vacuum, a quantitative estimate of the laser fluctuations limit cannot be given for the data in Figure 6.6.

Theoretical Allan deviations once again capture most of the experimental dynamics except for the limit set by laser power fluctuations. For larger linewidths, the asymptotes apparently start to deviate from the theoretical curves. The reason for this behavior is that the asymptotes, as defined in Equation (6.4), assume only one source of white noise alone. In cases where the ratio between N_th and N_d is small, or when Γ approaches BW, both of which is the case for the lowest Qs in Figure 6.6, the two noise regimes cannot be cleanly separated. In these cases, N_th (N_d) has a non-negligible contribution for small (large) τ.

The Q-dependence of τ_r observed in Figure 6.6, which can be indirectly inferred from σ_A, can also be directly measured through the response of the phase to external stimuli, be it mass, force, or temperature. An apparent misconception in the nanomechanical sensors field is that the phase/frequency should respond instantaneous to stimuli, while the amplitude displays a transient response. In fact, both the amplitude and phase exhibit a transient response, with a response time in open-loop determined by the intrinsic resonator time constant τ_r [126, 170, 174]. Measurements of the transient phase response for different Qs are given in Figure 6.7. By varying the piezo drive frequency within the linear phase regime, a step response of the phase can be acquired, with an example of a measurement given in Figure 6.7(a). An exponential decay of the type $\phi(t) = \phi_0 e^{-t/\tau_r} + c$ is fitted to the step response of the phase in order to extract τ_r. As shown in the inset of Figure 6.7(a), five measurements of the step response is made for each Q, with the final value of τ_r being an average of the measurements. A plot of

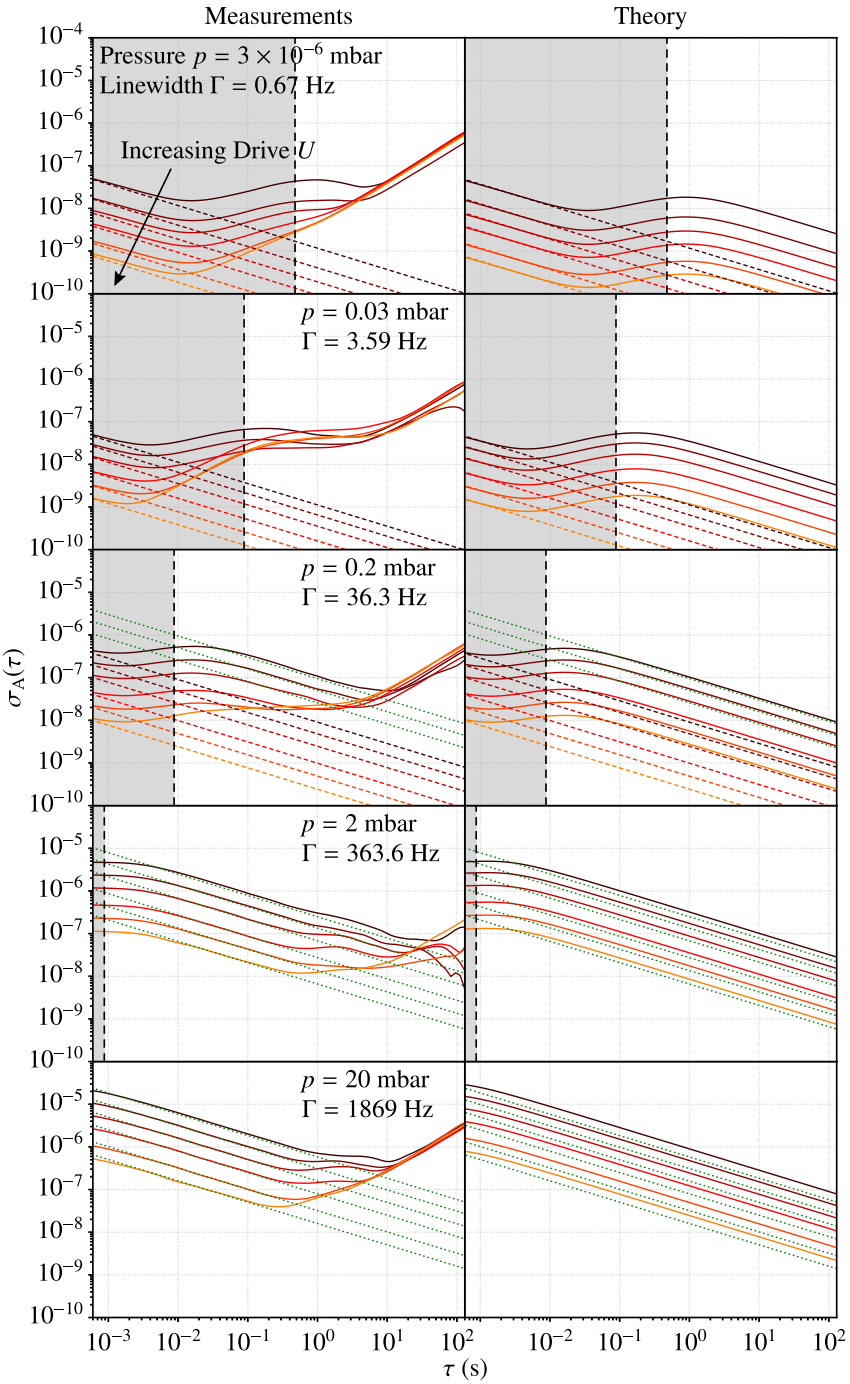

Figure 6.6: Q-dependence of the frequency stability in open-loop configuration. Measured (left column) and theory-based (right column) Allan deviations for resonance linewidths of 0.67 Hz (a), 3.59 Hz (b), 36.3 Hz (c), 363.6 Hz (d), and 1869 Hz (e). Green dotted and red-shaded dashed lines are calculations using Equation (6.4) for thermomechanical and detection noise limits, respectively. Black vertical dashed lines mark $\tau = \tau_r$. Figure adapted from [170].

τ_r-values extracted using the fitting procedure for various values of Q is given in Figure 6.7(b) and compared to values calculated using Equation (6.3). Good agreement can be observed, showing that the phase has a transient step response with a time constant given by τ_r. In addition, this method provides an alternative method for extracting the Q of mechanical resonators (see Section 3.2.4).

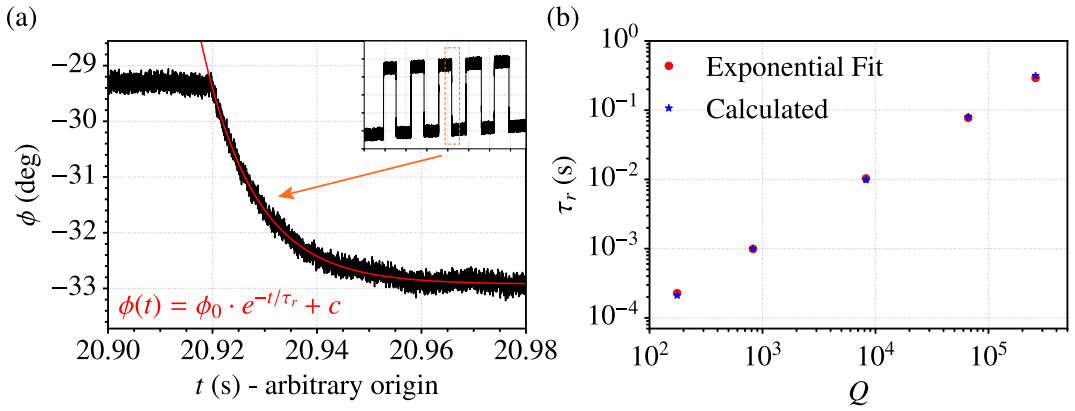

Figure 6.7: Transient response of the phase in open-loop configuration. (a) Extraction of the response time from an exponential fit to the step response of the phase. Inset shows that the response is recorded from an average of five measurements of the phase step. (b) Comparison of response times acquired through the procedure shown in (a) and that calculated using Equation (6.3). Figure adapted from [170].

Some general comments on the open-loop tracking of the resonance frequency can be made based on the measurements presented in this and the previous section. For high-Q resonators, the Allan deviation becomes separated into two regimes depending on the ratio of BW to Γ. Since the regime where $\tau < \tau_r$ is limited by detection noise, σ_A at times becomes even smaller than the thermomechanical limit. Nonetheless, this does not represent the actual performance limit of the resonator. In reality, the resonator itself filters the phase response in addition to the filtering done by the low-pass filter of the demodulator, which reduces σ_A in the detection noise regime. However, the resonator phase is unable to respond to any stimuli occurring at time scales faster than τ_r. As such, the frequency stability remains fundamentally limited by thermomechanical noise, in agreement with theoretical investigations on the subject [125, 126].

From the measurements shown in Figure 6.6, it would appear that the main effect of Q on σ_A is to shift τ_r. As a matter of fact, lowering Q increases the measurement bandwidth by increasing Γ, enabling high-speed applications. Since the curves at different pressures were recorded with similar SNRs, no apparent dependence of the frequency stability on Q can be observed. However, these results cannot be used as a counter-argument to the findings of Roy

et al., since the measurements presented here were not acquired in the Duffing-limited regime [227]. Evidently, laser power fluctuations arising from the optical readout present a limit to the stability in the thermomechanical regime measured here.

6.6 Closed-Loop Measurements

The final focus of this chapter will be on the closed-loop tracking of the resonance frequency. While open-loop configuration can help provide an understanding of fundamental limits to frequency stability, the method is limited by intrinsic properties of the resonator. The main drawback is the measurement range, which is limited to the linear phase regime. Any event that causes resonance frequency shifts beyond Γ will immediately render the measurement meaningless, be it thermal drifts or stimuli (mass, force, temperature, etc.). For this purpose, closed-loop schemes exist, in which a feedback constantly changes the drive frequency to always be near f_r, as already discussed in Section 3.2.3.1. Closed-loop Allan deviations of the nanomechanical strings will therefore be presented and discussed below. It should be mentioned that a method has been proposed to infer the closed-loop frequency stability limit from open-loop measurements, however, this methodology is not pursued further here [228].

For the closed-loop experiments presented here, the PLL of the lock-in amplifier is used to lock on to the phase and in this way track the resonance frequency directly. In addition to the filter bandwidth, an additional bandwidth for the closed-loop system has to be set, which will be named the target bandwidth (TBW) here. This bandwidth should be set larger than the expected shifts in the resonance frequency, but typically smaller than the BW of the filter in the demodulator. A desired value of TBW can be chosen by adjusting the feedback gain parameters of the controller accordingly, which in this study is a proportional-integral (PI) controller [125].

The effect of varying TBW from 0.25 Hz to 719.6 Hz on σ_A is shown both in the experimental and theory-based cases in Figures 6.8(a) and 6.8(b), respectively. A filter BW of 3598 Hz was chosen, while the sampling rate was set to 28784 Sa/s, in order to keep the settings similar to the open-loop configuration. An additional recording of σ_A in open-loop configuration is shown for comparison. Calculations based on Equation (6.4) for thermomechanical and detection noise limits are given as well. Evidently, the closed-loop response time is determined by the TBW of the system, in contrast to the open-loop case, in which the intrinsic resonator properties set the response time. As the TBW is increased, the point of transition between the two noise regimes shifts towards lower integration times. Another observation is that σ_A reduces in the detection noise regime with decreasing TBW, despite the noise remaining unchanged throughout the measurements. For the smallest TBW = 0.25 Hz,

satisfying the condition TBW < Γ, the detection noise limit is even lower than in the open-loop measurement.

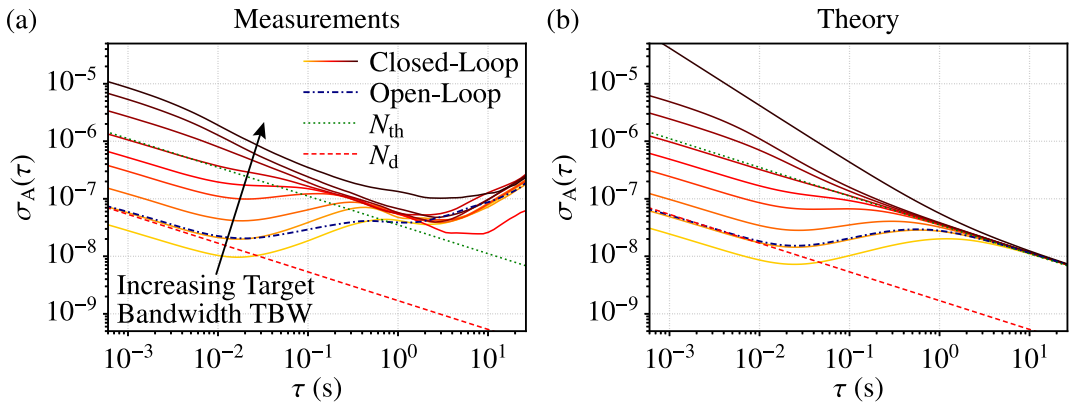

Figure 6.8: Closed-loop measurements of the frequency fluctuations of nanomechanical string resonators. Measured (a) and theory-based (b) Allan deviations for target bandwidths of (from bottom to top): 0.25 Hz, 0.5 Hz, 1 Hz, 2.5 Hz, 5 Hz, 10 Hz, 25 Hz, 50 Hz, and 719.6 Hz. Blue dashdotted line is an open-loop measurement. Calculations using Equation (6.4) are given as well in the case of thermomechanical (green dotted line) and detection (red dashed line) noise limits. Figure adapted from [170].

If the condition TBW < Γ is met, the detection noise gets filtered by the loop in addition to the filtering provided by the intrinsic response of the resonator and the demodulator, which reduces the detection noise σ_A as a result. Nonetheless, similar to the open-loop case, the perceived improvement of frequency stability in the detection noise regime is merely resulting from the choice of BW relative to Γ. Regardless of the TBW chosen, σ_A remains thermomechanically limited for τ greater than the response time. Any frequency shift occurring at time scales in the detection noise regime would not be detected as the loop will be unable to respond. In the case of TBW = 0.25 Hz, where the detection noise is at its lowest, the response of the loop would be even slower than the intrinsic τ_r. As such, closed-loop tracking offers flexibility in terms of measurement speed at the expense of increased noise. It should be noted that for the largest TBWs in Figure 6.8, the noise at smaller τ, but above the response time, appears to exhibit a τ^{-1} slope in addition to the $\tau^{-1/2}$ slope expected for pure white noise. This secondary slope is possibly a result of the smoother cut-off of the TBW compared to the filter BW, which results in the detection noise being mixed with the thermomechanical noise for large TBWs [228].

6.7 Summary and Outlook

A thorough investigation of the frequency fluctuations of high-Q string resonators has been presented here. Emphasis was placed on the regime where the resonance linewidth is significantly smaller than the resolution bandwidth, a condition often satisfied for resonators subjected to dissipation dilution [37, 38]. The frequency stability was here characterized using the Allan deviation, which was calculated from recordings of the phase in open-loop or the resonance frequency in closed-loop tracking configurations. Based on open-loop measurements, it was shown how the Allan deviation gets separated into two regimes, one limited by thermomechanical noise of the resonator and the other by detection noise of the optical transduction scheme. Quantification of these regimes was made through experimental variation of the signal-to-noise ratio, either by reducing the detection noise floor or increasing the driven vibrational amplitude, and comparing with white noise asymptotes of the Allan deviation. The regimes were found to be separated at an integration time corresponding to the intrinsic response time of the resonator in the open-loop case. Controlled reduction of the resonator Q showed a linear dependence of τ_r on Q. While thermomechanical noise was the fundamental noise source at lower driven amplitudes, laser power fluctuations arising from the optical readout set a hard limit on the frequency stability at larger amplitudes. Finally, in the closed-loop configuration, τ_r was found to no longer be intrinsically limited but instead given by the measurement bandwidth of the loop itself. Computed Allan deviations based on theory were shown throughout and found to agree well with measurements for both tracking configurations.

The results presented here are not limited to SiN strings, but apply to all kinds of high-Q resonant sensors. While the detection noise regime of the Allan deviation would hint at stabilities beyond the thermomechanical limit, this was argued to be an artifact of the relation between resolution bandwidth and resonance linewidth. The response time always sets the lower limit for speed of detection regardless of tracking configuration, meaning that thermomechanical noise remains the most fundamental limit of detection [125]. Since the theoretical Allan deviations accurately predict the thermomechanical and detection noise limits, this can be used for the design and optimization of future nanomechanical resonant sensors with unprecedented sensitivity.

An original goal of this investigation was to experimentally characterize the ultimate frequency stability limits of high-Q resonant sensors and how these would depend on the Q. This would require the ability to operate at the onset of Duffing nonlinearity in the thermomechanically resolved regime for all Qs. The Duffing limit could not be reached here, due to the lower stability limit set by the laser power fluctuations. While this issue can possibly be circumvented by employing lower laser powers, this in turn can increase the detection

noise level to the point that the thermomechanical noise becomes buried within the detection noise. Future studies could try to recreate the measurements employing a more power-stable readout laser. Additionally, samples with even lower relative responsivities would be beneficial for minimizing the laser-induced noise. Finally, alternative means of transduction can be implemented, such as capacitive [150] or inductive [151].

7

Thermal Response of Phononic Crystal Membranes

This chapter focuses on the thermomechanical properties of localized defect modes embedded in phononic crystal membranes. Firstly, a description of the thermal response of phononic crystal membranes based on simulations is given, showing how these fare compared with uniform membranes. Measurements of the relative thermal responsivity of defect modes are then given for various membrane sizes. Subsequently, a special case of a phononic crystal engineered into a trampoline resonator is shown, which further enhances the thermal response. Finally, defect mode and bandgap tuning measurements are presented, demonstrating a defect mode exiting the bandgap completely resulting from photothermal heating. The results and associated discussions presented in this chapter are based on Paper **VI** [102].

7.1 Introduction

Having established methods of minimizing the mechanical dissipation and characterized the frequency fluctuations in strained silicon nitride resonators, the next logical step would be the demonstration of their sensing performance. As mentioned in Section 6.1, nanomechanical resonators can be employed to detect a number of physical quantities [16]. In the case of SiN resonators, one of the most promising applications is as temperature sensors [95]. The principle of detection is a change of the tensile stress in response to a changing temperature, which translates into a thermal detuning of the resonance frequency. An emerging subfield of thermal sensors based on SiN resonators is photothermal sensing, where the source of heat is the absorption of electromagnetic radiation by the resonator. This effect allows such resonators to be employed as radiation detectors [151, 229]. Any sample placed on the resonator will absorb additional light, causing a larger detuning of the frequency. Sensors based on this

detection principle have been successfully employed to detect complex chemical compounds [97, 99, 100, 230], single nanoparticles [96, 98, 152, 231], and single molecules [101], highlighting the flexibility of the technique.

The current state-of-the-art resonator design is that of uniform membranes, due to being more robust, easier to align with and larger coupling to optical sources, and allowing implementation of multiple transduction schemes when compared to string resonators [100, 101, 151]. These advantages come at the expense of a significantly reduced thermal responsivity compared to strings due to the larger number of pathways for heat to flow off the membrane [16]. Nonetheless, a number of paths to enhance the thermal responsivity present themselves. Firstly, the thermal response is limited by material parameters, such as the thermal conductivity κ and the tensile stress σ (see Section 2.3.2). Possible solutions to these issues have already been demonstrated in the literature, such as perforating the resonator to reduce the effective κ [100] and oxygen plasma treatment as a method of reducing σ [86]. Secondly, given that many of the aforementioned applications rely on coherent sources with beam diameters significantly smaller than the resonator, essentially acting as a point source, the temperature profile is highly localized to the center of the membrane [232]. A finite element method simulation of the temperature profile of a uniform membrane heated centrally by a Gaussian source of 1 μm radius, essentially a pointlike source, is shown in Figure 7.1(a). When comparing this profile with the displacement field of the fundamental out-of-plane mode of a uniform membrane, as shown in Figure 7.1(b), minimum overlap between the two fields can be observed.

In this chapter, a solution to the minimum overlap problem is presented using soft-clamped phononic crystal membranes [39, 102]. While the main focus of such resonators has been to enhance the Q for optomechanical purposes [22], the displacement field of localized defect modes of PnC membranes, given in Figure 7.1(c), displays an obviously larger overlap with the temperature field given in Figure 7.1(a). Furthermore, the addition of holes to the membrane reduces the effective κ, which localizes the temperature to the central defect. As a result of these two benefits, one can expect a localized higher average temperature in the PnC defect, which results in an enhanced thermal response. It should, however, be mentioned that the localized temperature is not a result of phonon localization resulting from the PnC itself, as has been previously reported using PnCs engineered into various materials, in particular for the case of Si [233–238]. Since the wavelength of heat transporting phonons (on the order of nanometers) is significantly smaller than the lattice constants used here (≥ 30 μm), the PnC cannot control the heat flow coherently. Thermal isolation from the PnC is only a result of the reduced thermal conductivity due to the perforation [239–241].

Various properties of localized modes in low-stress PnC membranes will be presented. First, numerical simulations of the phononic band structure of the PnC are shown and how the

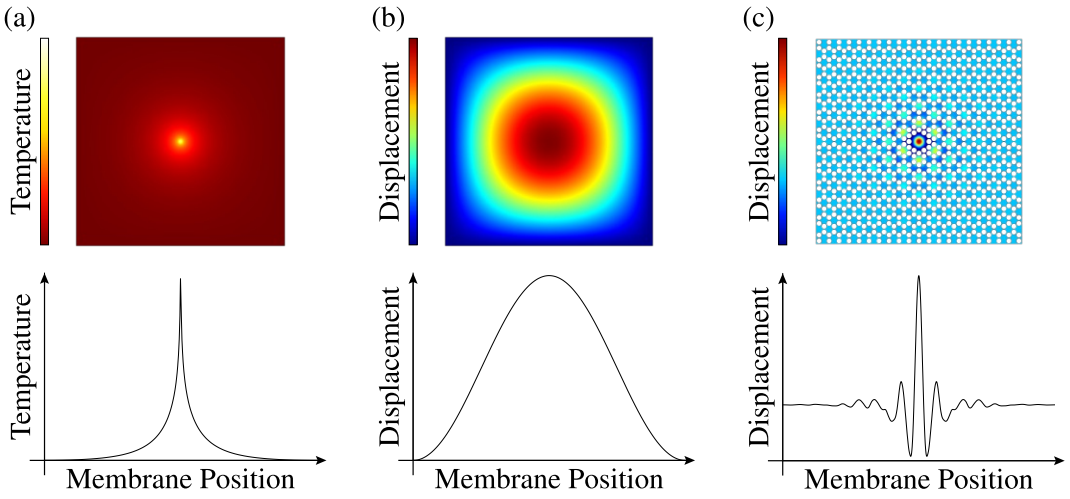

Figure 7.1: Finite element method simulations of the overlap between the temperature and displacement fields of uniform and phononic crystal membranes. A temperature profile of a uniform membrane heated with a central pointlike source (a) is compared with the displacement field of the fundamental mode of a uniform membrane (b) and the fundamental defect mode of a PnC membrane (c). The line profiles are made along the diagonal of the membranes. Note that the line plot of the PnC displacement is a polynomial fit through the simulated values for clarity. Figure adapted from [102].

frequency and width of the bandgap is affected by lowering the tensile stress. Attention is then shifted towards the thermal properties of PnC membranes and how these compare with uniform membranes without any PnCs. Both measured and simulated thermal responsivities are shown for increasing lateral membrane dimensions. A PnC engineered into a nanomechanical trampoline resonator is then presented and the effect on the thermal response discussed. Finally, photothermal detuning of the defect mode to frequencies outside the phononic bandgap is experimentally demonstrated.

7.2 Phononic Bandgap of Low-Stress PnC Membranes

All samples employed here are made from 50 nm thick silicon-rich SiN. The chosen phononic crystal design employed is the one from Tsaturyan *et al.*, which was given a detailed introduction in Section 3.4.3. As evident from the theoretical discussion provided in Section 2.3, minimizing the tensile stress is essential for maximizing the thermal response of stressed resonators, since the thermal responsivity is inversely proportional to the stress [16]. Therefore, in order to employ soft-clamped PnC membranes for thermal sensing, it is essential that a phononic bandgap remains even at very low stress values. For this purpose, FEM simulations

of the phononic band structure were performed for increasingly low values of the initial tensile stress σ_{film}. A list of material parameters employed for the bandgap simulations can be found in Table 7.1. An exemplary band diagram for the case of $\sigma_{\text{film}} = 30$ MPa is given in Figure 7.2(a) for a unit cell with $a = 140$ µm. Evidently, a quasi phononic bandgap remains, as evidenced by the lack of out-of-plane modes in the frequency region $f \sim 0.27 - 0.32$ MHz.

Assumed material parameters	
Membrane thickness (h)	50 nm
Young's modulus (E)	250 GPa
Mass density (ρ)	3000 kg/m^3
Poisson's ratio (ν)	0.23
Coefficient of thermal expansion (α)	2.2×10^{-6} K^{-1}
Thermal conductivity (κ)	3 W/(m·K)
Specific heat capacity (c_p)	700 J/(kg·K)
Surface emissivity (ϵ_λ)	0.05

Table 7.1: Fixed material parameters used for the finite element method simulations of low-stress phononic crystal membranes. For the bandgap simulations, only the membrane thickness, Young's modulus, mass density, and Poisson ratio are needed, while for simulations of the thermal response, all parameters are used. Membrane thickness and surface emissivity are extracted from measurements, while the rest are assumptions based on previous literature on the properties of silicon nitride [101].

While the simulations predict that a bandgap persists even at very low stress values, it is of course necessary to confirm this observation experimentally. For this reason, Figure 7.2(b) shows a measurement of the Brownian motion spectrum for a PnC membrane with similar parameters to the one simulated in Figure 7.2(a). The simulated phononic bandgap is highlighted by the grey region on the plot. A visibly low density of mechanical modes can be observed in the predicted bandgap region, highlighting that a phononic bandgap persists even at very low stress and that the simulations accurately predict the phononic bandgaps.

Figure 7.2(c) shows simulated phononic bandgaps versus σ_{film} for a PnC with $a = 140$ µm. Simulations were performed for σ_{film}-values from 30 MPa to 990 MPa in steps of 30 MPa. The grey-shaded region highlighting the bandgap is generated by fitting the simulated bandgap edges with a function proportional to $\sqrt{\sigma_{\text{film}}}$. Evidently, both the width and center frequency of the bandgap scales with $\sqrt{\sigma_{\text{film}}}$, which is the expected behavior of the eigenfrequency of resonators under tensile stress [16]. The measured bandgap edges extracted from the Brownian motion spectrum shown in Figure 7.2(b), along with a similar measurement for a membrane with $\sigma_{\text{film}} = 150$ MPa, are overlaid on the simulations. For both stress values, good agreement is observed both in terms of bandgap width and center frequency. Additionally, simulated fundamental defect mode frequencies are given, in order to highlight a similar rela-

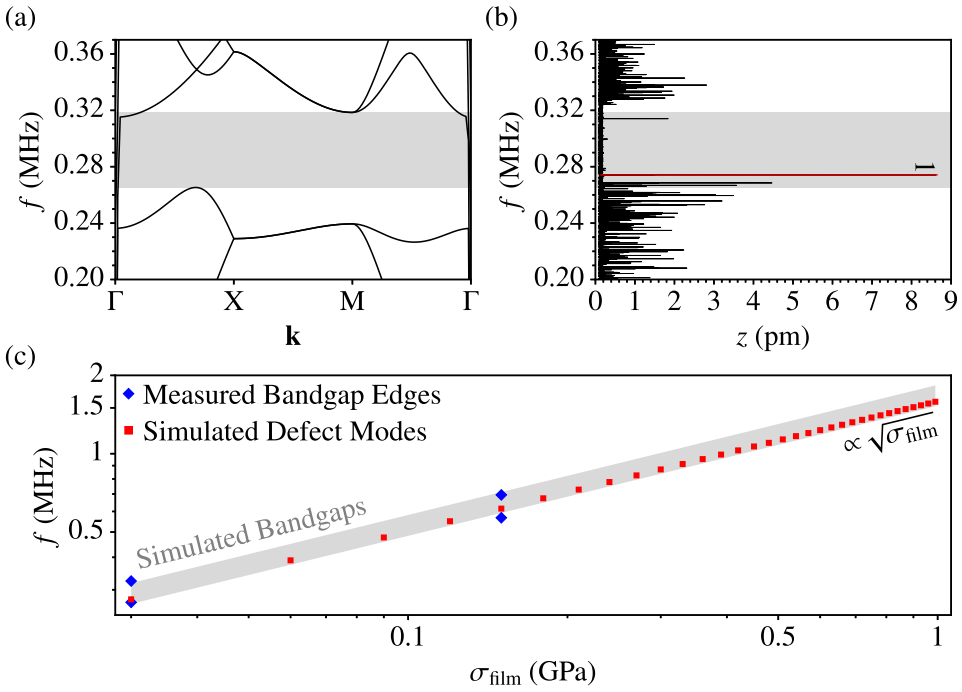

Figure 7.2: Phononic bandgaps in low-stress SiN membranes. (a) Finite element method simulation of the band diagram for a unit cell of lattice constant a = 140 µm and initial stress σ_{film} = 30 MPa. (b) Measured Brownian motion spectrum of a PnC membrane with the same mechanical properties as the one simulated in (a). The red-colored peak with the label 1 corresponds to the fundamental defect mode of the membrane. (c) Influence of σ_{film} on the width and center frequency of the phononic bandgap for a fixed a = 140 µm. The simulated bandgap edges are marked by the grey-shaded region, underlining the proportionality with $\sqrt{\sigma_{\text{film}}}$. Blue diamonds are measured bandgap edges, while red squares correspond to simulated fundamental defect mode frequencies. Figures (a) and (c) adapted from [102].

tion to σ_{film} and that the mode remains within the bandgap for all stress values. These results show that PnC membranes maintain a quasi-bandgap even at very low initial stresses and should therefore be readily applicable for thermal sensing applications.

7.3 Thermal Properties of Defect Modes

Based on the simulated band structures, it is clear localized modes can persist in the phononic bandgap despite increasingly low tensile stress values. The next step is to investigate the thermal response of PnC membranes and how these compare with uniform membranes without any perforation. This section will present both measured and simulated results of the thermal properties of square PnC membranes. Parameters used for the numerical simulations are

shown in Table 7.1. For the remainder of the chapter, focus will only be on membranes of film stress $\sigma_{\text{film}} = 30$ MPa. Given that comparisons are made to uniform square membranes, it should be repeated that the lateral size of the PnC membranes is approximately given by $L \sim 20.5 \times a$.

7.3.1 Temperature Localization

Figure 7.3 presents FEM simulations of the thermal properties of PnC membranes. All of the simulated results were acquired by heating the membranes at the center with a Gaussian source of 1 μm radius, comparable in size to the laser beams employed for the measurements. A temperature distribution plot for a PnC membrane with $a = 140$ μm ($L \approx 2.9$ mm) for an absorbed power $P_{\text{abs}} = 0.6$ μW can be seen in Figure 7.3(a). The temperature can be observed to be highly localized to the central defect with a maximum temperature T_{max}, while quickly approaching room temperature T_{room} in the surrounding PnC. A line profile of the temperature along the diagonal length L_d of the membrane is shown in Figure 7.3(b), which is compared to the case of a uniform membrane of equal size. Clearly, the PnC membranes result in increased temperatures at the center, with T_{max} of the PnC membrane being ~ 3 K larger than for the uniform membrane. The localization in the defect is also apparent from the line profile in that the temperature rises more rapidly in the center compared to in the PnC.

Simulations of T_{max} for increasing values of P_{abs} are shown in Figure 7.3(c), both for a PnC membrane and an equally sized uniform membrane. A linear dependence on P_{abs} is observed in both cases, which is the expected behavior for membrane resonators [100]. However, a steeper rise is observed for PnC membranes, underlining their larger thermal response compared to uniform membranes. These results are not limited to PnC membranes, but are rather consequences of the perforation reducing the effective κ.

A FEM simulation of the resonance frequency detuning for increasing P_{abs} can be seen in Figure 7.3(d) for the fundamental defect mode of a PnC membrane with the same parameters as the one displayed in Figure 7.3(a). The frequency initially shifts linearly for $P_{\text{abs}} < 1$ μW, which is indicated by the linear fit, but starts to deviate from linearity for larger P_{abs}. Similar simulations performed for the fundamental mode of uniform membranes in the same power range remain linear [103]. As such, this is a property exclusive to defect modes, resulting from the mode shifting out of the bandgap due to the heating. Support for this hypothesis is given in Figure 7.3(d), where the region of the plot encompassing the bandgap has been given a grey-shading.

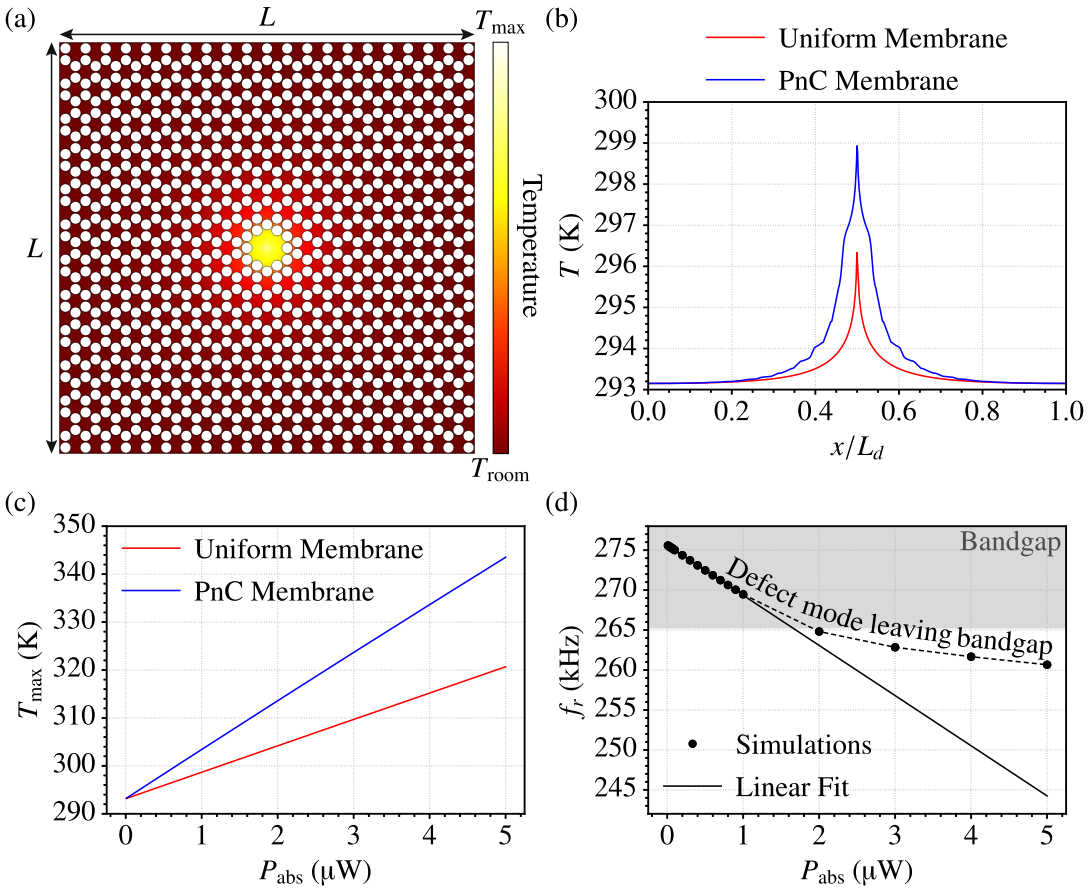

Figure 7.3: Thermal properties of phononic crystal membranes. (a) Finite element method simulation of the temperature distribution of a PnC membrane with $a = 140$ μm ($L \approx 2.9$ mm) and $\sigma_{film} = 30$ MPa, for an absorbed power $P_{abs} = 0.6$ μW. The maximum temperature at the defect center is T_{max}, while the membrane boundary temperature is set to $T_{room} = 293.15$ K. (b) Line profile of the temperature along the diagonal length L_d for the PnC membrane shown in (a) compared with a uniform membrane of similar size. For the PnC membrane profile, full lines have been drawn through the holes of the membrane for clarity. (c) Comparison of T_{max} versus P_{abs} for a PnC membrane and a uniform membrane. (d) Simulated absorbed power-dependence of the resonance frequency f_r for the fundamental defect mode of the membrane shown in (a) along with a linear fit to the data for $P_{abs} < 1$ μW. The dashed line serves as a guide to the eye, while the grey-shaded region highlights the phononic bandgap. Figures (a) and (d) adapted from [102].

7.3.2 Mode Delocalization

How the fundamental defect mode shape changes resulting from detuning out of the phononic bandgap can be seen in Figure 7.4. The shown simulations correspond to the last five power steps given in Figure 7.3(d). As a result of the defect mode slowly exiting the bandgap, the

displacement field starts to penetrate further into the PnC with each increasing power step. For the largest absorbed power $P_{\text{abs}} = 5$ µW, the mode has completely delocalized and extends throughout the membrane. The lack of an abrupt delocalization from one power to another is probably a result of the bandgap also detuning due to the increased heating. Both defect mode and bandgap detuning will be experimentally demonstrated in Section 7.5.

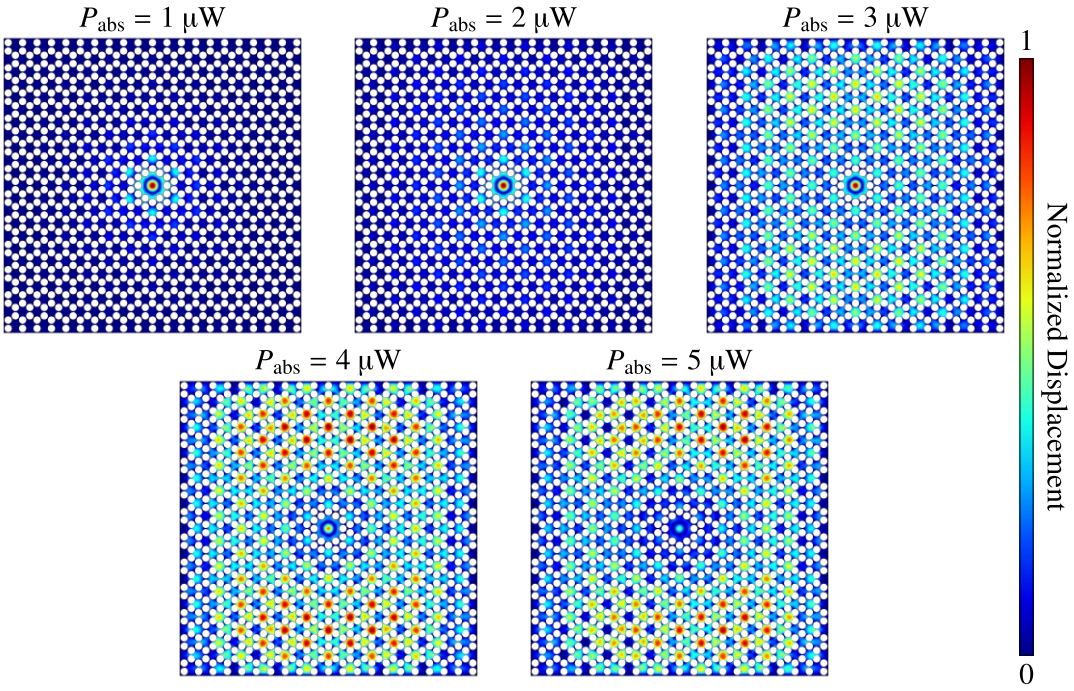

Figure 7.4: Finite element method simulations of the fundamental defect mode shape for increasing absorbed power values. These mode shapes correspond to the last five power steps in Figure 7.3(d). Figure adapted from [102].

7.3.3 Enhanced Thermal Responsivity

Having numerically established enhanced thermal response of localized modes on phononic crystal membranes, the next step is to characterize samples experimentally. The key parameter characterizing the performance of thermal sensors is the relative thermal responsivity $\delta\mathscr{R}$, which was shown in Section 2.3 to be the relative frequency shift $\delta f = \Delta f / f_r$, caused by a detuning Δf of the resonance frequency f_r, per absorbed power P_{abs} [16]. If heat transfer is assumed to be dominated by thermal conduction, $\delta\mathscr{R}$ of membranes can be predicted analytically using Equation (2.108) [100]. In the case of PnC membranes, where the stress is nonuniform resulting from the perforation, an effective stress would have to be used in place

of the relaxed resonator stress in order to properly use the equation.

Even though the analytical model predicts a lack of dependence of $\delta\mathscr{R}$ on the lateral size L, recent investigations into the thermal transport of nanomechanical SiN membranes have, however, shown a non-negligible contribution from radiative heat transfer [103, 104]. This effect becomes more pronounced as the size of the membrane is increased and can significantly reduce $\delta\mathscr{R}$ compared to that predicted from Equation (2.108). A numerical demonstration of this reduction in $\delta\mathscr{R}$ was provided in Section 2.3.2.2 for a uniform square membrane. Given the lateral size of the PnC membranes studied here, which can be on the order of several millimeters, emission of thermal radiation needs to be taken into account. Therefore, all heat transfer simulations presented in this chapter include surface emissivity ϵ_λ as a property of the material. A nominal $\epsilon_\lambda = 0.05$ is chosen, taken from the work of Piller *et al.* [103], which was based on measured optical data of 50 nm thick SiN membranes [242]. Both the analytical model given in Equation (2.108) as well as the FEM simulations are only valid in the high vacuum regime, where convective heat transfer can be neglected. Convection plays a more dominant role at larger pressures, which results in a deterioration of $\delta\mathscr{R}$ [102].

The thermal response of low-stress PnC membranes can be observed in Figure 7.5. Relative responsivities are measured by varying the power of a secondary diode laser focused on the membrane center and fitting a linear function to the detuning of the resonance frequency. This approach is valid at low powers since the frequency response remains linear for small temperature changes [103]. Simulated responsivities are similarly acquired from the linear detuning regime shown in Figure 7.3(d). Measured and simulated values of $\delta\mathscr{R}$ for the fundamental defect mode as a function of L can be seen in Figure 7.5(a). In addition, simulated $\delta\mathscr{R}$s of the fundamental out-of-plane mode of uniform membranes are shown for comparison. An enhanced thermal response can be observed for defect modes, with a minimum enhancement factor of 5 compared to uniform membranes of equal size. The observed size dependence is a result of the aforementioned radiative heat transfer, which reduces $\delta\mathscr{R}$ for larger membranes. Interestingly, the decrease in $\delta\mathscr{R}$ appears less prominent for defect modes, which is possibly a result of the smaller effective size of the defect mode compared to the fundamental mode of uniform membranes. FEM simulations agree well with measurements, including reproducing measured trends, which strongly support emission of thermal radiation being the cause of the observed size dependence of $\delta\mathscr{R}$.

To ensure that the observed enhancement of $\delta\mathscr{R}$ is caused by an increased overlap between the temperature and displacement fields for defect modes and not simply a result of a reduced κ due to the perforation, a comparison between $\delta\mathscr{R}$ of the fundamental defect mode and the fundamental out-of-plane mode of the entire PnC membrane is made, as shown in Figure 7.5(b). Both measured and simulated $\delta\mathscr{R}$s can be observed for both sets of data. Regardless of the membrane size, $\delta\mathscr{R}$ of the defect mode remains larger than the fundamental

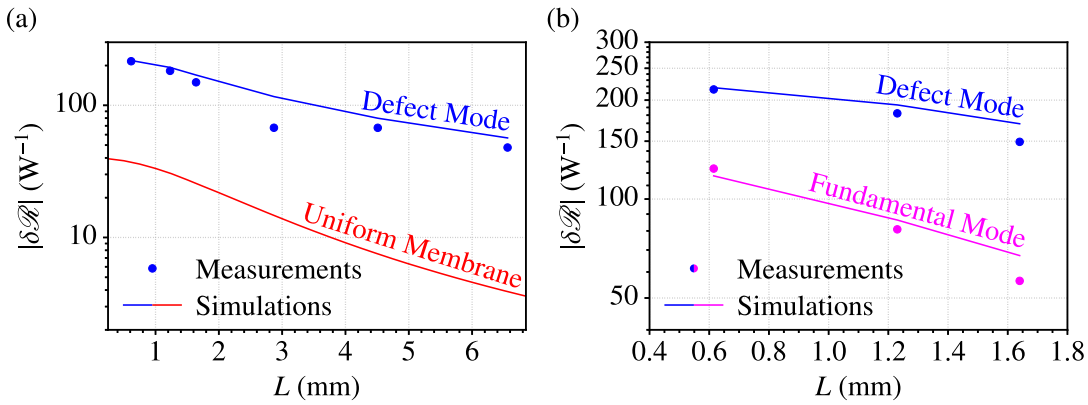

Figure 7.5: Thermal response of 30 MPa phononic crystal membranes. (a) Measured (blue dots) and simulated (blue solid line) relative thermal responsivities of the fundamental defect mode of PnC membranes versus lateral size L, compared to simulated responsivities (red solid line) of equally sized uniform membranes. (b) Comparison between $\delta\mathscr{R}$ of fundamental defect modes (blue data) and the fundamental out-of-plane mode of the entire PnC membrane (magenta data) for increasing L. Figure adapted from [102].

PnC membrane mode. Furthermore, the fundamental PnC mode appears to roll off faster with increasing L, which is most likely a result of the reduced overlap with the temperature field. It should be noted that $\delta\mathscr{R}$ of the fundamental PnC membrane mode is still larger than that of uniform membranes, which can be attributed to a reduced effective κ resulting from the perforation [239–241]. The presented results show that localized modes of PnC membranes display enhanced thermal response compared to equally sized uniform membranes, owing to the combined effect of reduced thermal conductivity and increased overlap of the displacement field to the temperature field.

7.4 Geometrical Stress Reduction

As discussed in Section 7.1 and evident from Equation (2.108), minimizing the tensile stress presents another way of enhancing the thermal responsivity. Since a quasi bandgap remains regardless of the tensile stress, reduction of σ_{film} presents the next step of increasing $\delta\mathscr{R}$. Given the difficulty in accurately controlling the tensile stress of SiN during the LPCVD process, alternative means of stress reduction have to be used. One possibility would be to reduce the stress using an oxygen plasma [86], which has successfully enhanced the response of uniform square membranes [101]. However, given the fragility of PnC membranes and a lack of precise control of the final stress, this method was not employed here.

An alternative method to reduce the tensile stress is geometric strain engineering. By

carefully engineering regions of narrow width into a resonator, one can localize the stress in certain regions, while minimizing it in others. Such an approach was employed to increase the stress in soft-clamped string resonators, which enhanced the dissipation dilution effect and thus unprecedentedly large Qs at room temperature were achieved [40]. Geometric strain engineering has also demonstrated two orders of magnitude enhancement of the fundamental mode Q of fractal-like resonators [243, 244].

The goal of this study, however, is to geometrically reduce the stress of the resonator in order to enhance $\delta\mathscr{R}$. One possible solution is to employ nanomechanical trampoline resonators. The four narrow tethers of a trampoline ensure high stress localization to the tethers while minimizing the stress in the central pad [46]. Increased thermal isolation is also achieved as a result of the narrow tethers. Owing to these key features, trampoline resonators have previously been employed for thermal sensing applications, using silicon [245], graphene [246], and silicon nitride [247] as the resonator material. Trampolines made from silicon nitride have additionally been demonstrated to work as position-sensitive detectors [152].

Here, the reduced stress and increased thermal isolation of trampoline resonators are combined with the benefits of localized modes on PnC membranes, by engineering a PnC directly into the central pad of a trampoline. An optical micrograph of a successfully fabricated trampoline PnC is shown in Figure 7.6(a). The opening window size of the trampoline is $L_w \approx 1.5$ mm and a tether width $w = 20$ μm at the corners of the window. A lattice constant $a = 30$ μm is chosen for this trampoline size. The rounding of the central pad edges is not randomly chosen, but optimized to achieve an even stress distribution [152]. A FEM simulation of the tensile stress along the diagonal length of a uniform trampoline without any PnC of equal dimensions to that in Figure 7.6(a) can be seen in Figure 7.6(b). The PnC region of the trampoline has been marked on the plot for clarity. As expected, the stress is significantly lower in the central pad compared to the tethers, with an average stress $\sigma = 2.7$ MPa calculated in the region of the pad covering the PnC. This is approximately an order of magnitude lower than the initial stress of the SiN, meaning an enhanced thermal response is to be expected.

Figure 7.6(c) shows a measurement of the Brownian motion of the trampoline PnC in a frequency region around the bandgap. A narrow and badly developed bandgap can be deduced in the frequency range $f \sim 600 - 700$ kHz, with the fundamental defect mode resonance located at a frequency $f \approx 603$ kHz. Unlike the bandgaps observed for PnCs engineered into square membranes, a lot of small peaks can be observed inside the bandgap, as well as a lack of clear bandgap edges. The most likely reason behind this observation is the stress distribution in the trampoline central pad, which is not perfectly uniform, as evident from Figure 7.6(b). Since the properties of the quasi bandgap are determined by the tensile stress, one can imagine nonuniform average stress in the PnC having deteriorating effects on the

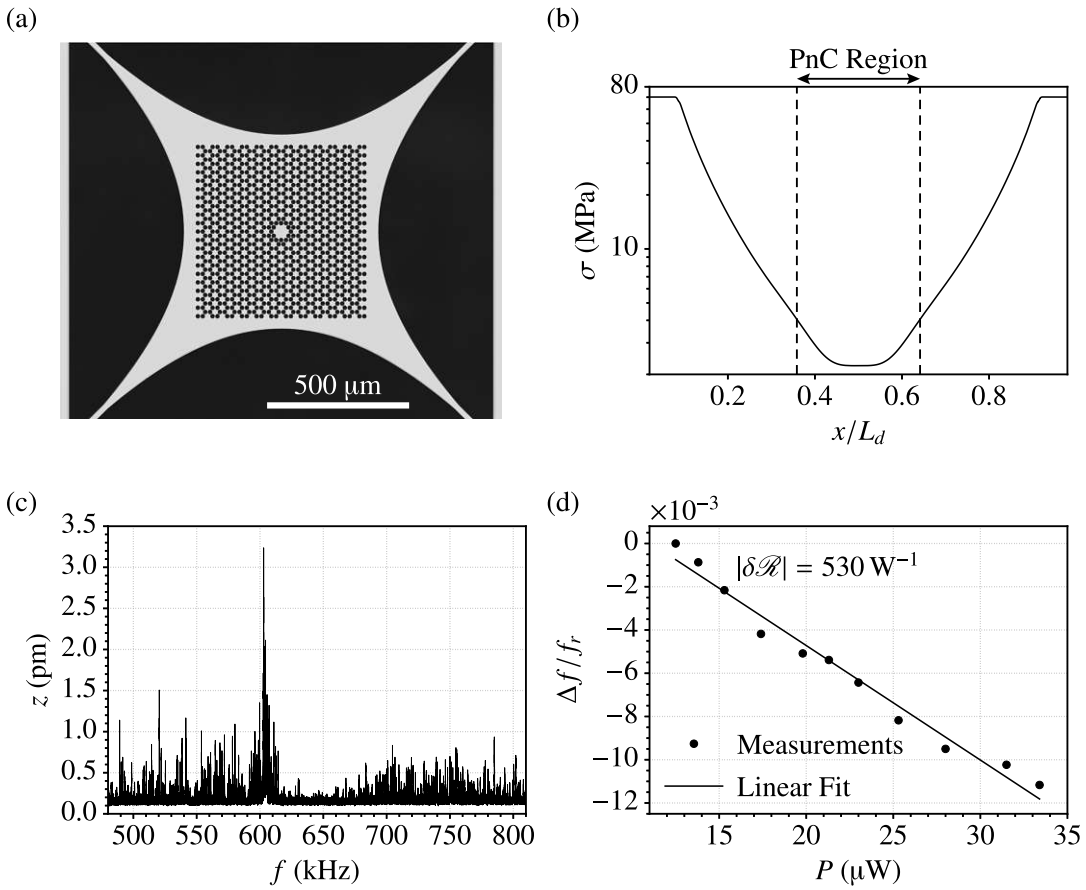

Figure 7.6: Phononic crystal engineered into a nanomechanical trampoline. (a) Optical micrograph of a trampoline PnC with $a = 30$ μm and $\sigma_{\text{film}} = 30$ MPa. (b) Line profile of the tensile stress along the diagonal length of the trampoline. The region of the trampoline containing the PnC is indicated in the plot. (c) Measured Brownian motion around the fundamental defect mode. (d) Relative frequency shift of the fundamental defect mode of the trampoline PnC. A linear fit to the data is given as well, with a $|\delta\mathscr{R}| = 530\ \text{W}^{-1}$ extracted from the fit. Figure adapted from [102].

bandgap [39]. Furthermore, at such low stress values, the bandgap width will be minimal, which might also explain the lack of a well-defined bandgap. An additional observation is that a forest of modes appears to surround the fundamental defect mode. Since this measurement was recorded with a larger vibrometer laser power, in order to properly resolve the bandgap, it could be that the mode is beginning to shift out of the bandgap, as will be discussed further in the next section. As such, measured thermal responsivities are acquired at lower vibrometer laser powers to ensure that the defect mode is located within the bandgap.

A measurement of the relative frequency shift for the fundamental defect mode of the trampoline PnC for increasing laser powers focused on the defect center is given in Figure 7.6(d).

From the linear fit to the recorded relative frequencies, a $|\delta\mathscr{R}| = 530\ \mathrm{W}^{-1}$ can be extracted. This is the largest measured $\delta\mathscr{R}$ reported here, being approximately a factor of 2.5 greater than the $\delta\mathscr{R}$ of a square PnC membrane of equal lattice constant. One can qualitatively attribute the enhancement to the reduced tensile stress of the trampoline pad, which is an order of magnitude lower than σ_{film} of the as-deposited SiN film. Nonetheless, a FEM simulation of the relative thermal responsivity for a square PnC membrane with $\sigma_{\mathrm{film}} = 2.7$ MPa resulted in a $|\delta\mathscr{R}| \approx 1400\ \mathrm{W}^{-1}$, significantly larger than what was measured for the trampoline PnC. This discrepancy is most likely a result of the uneven stress in the PnC of the trampoline. However, this could also be a sample-specific issue, with the very low fabrication yield for trampoline PnCs rendering a statistical average difficult.

7.5 Thermal Defect Mode and Bandgap Tuning

The final part of this chapter will focus on defect mode and bandgap tuning of PnC membranes. When heating with a central point source, the temperature of the PnC membrane is localized to the defect, as was shown through FEM simulations in Figure 7.3(a). As such, the local thermal expansion of the defect mode causes a local reduction in the stress, which is much larger than the overall stress reduction of the entire PnC membrane. One would therefore expect the defect mode frequency to detune faster than the bandgap, to the point where the mode would completely exit the bandgap. This property has already been observed through simulations given in Figure 7.3(d) and Figure 7.4.

Here, an experimental demonstration of temperature localization is given using a square PnC membrane with $a = 60\ \mu\mathrm{m}$ ($L \approx 1.2$ mm), with the results presented in Figure 7.7. Two cases are compared: Locally heating the defect center using a laser and heating the entire PnC membrane using a white light source. In either case, the detuning of the fundamental defect mode frequency and the bandgap center frequency is measured. The case of laser heating is shown in Figure 7.7(a). Measurements of the displacement in a frequency span covering the phononic bandgap are shown for increasing laser powers focused on the defect center. Logarithmic values of displacement are given in order to more clearly discern the bandgap region, and measurements recorded at higher powers are shifted vertically for clarity. The defect mode can be seen to detune faster than the bandgap with increasing P, appearing to have completely exited the bandgap for the largest value of P. This can be deduced not only from the fact that the defect mode shifts beyond the lower edge of the bandgap, but also because the resonance peak decreases in amplitude and becomes comparable to the surrounding forest of modes. Additionally, a nonlinear P-dependence of the defect mode detuning can be deduced. This nonlinearity is more pronounced in Figure 7.7(b), which shows the relative frequency

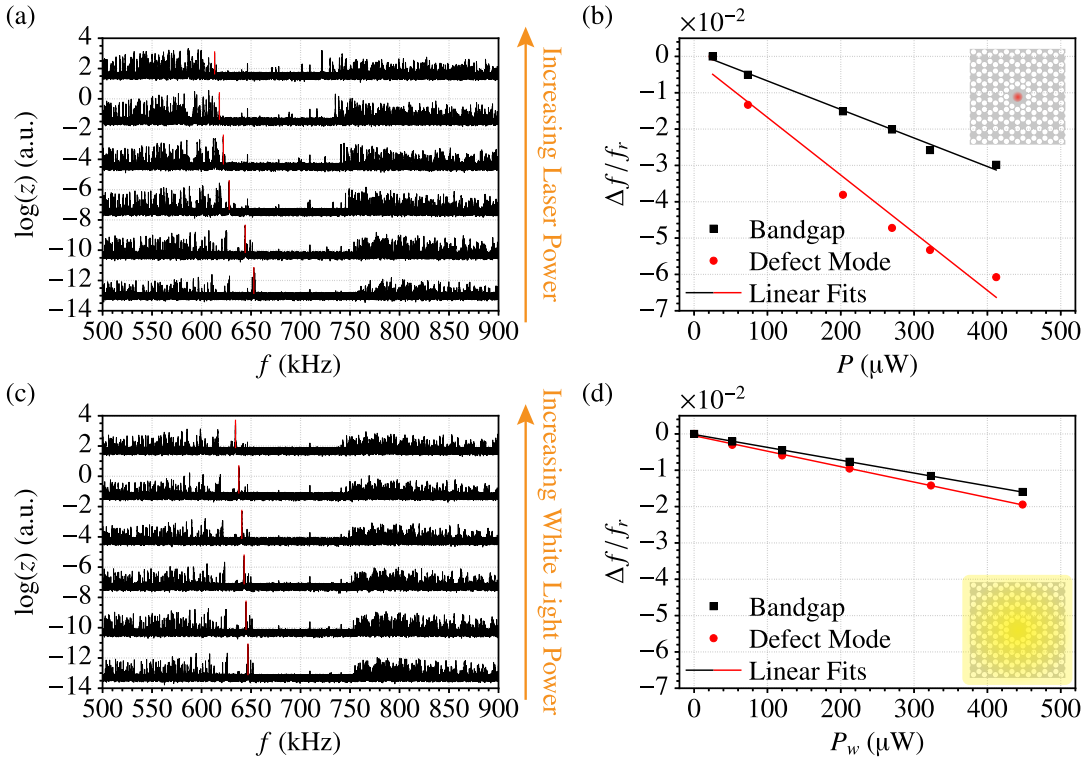

Figure 7.7: Photothermal detuning of the fundamental defect mode and bandgap frequencies. (a) Logarithmic displacement versus frequency for a PnC membrane with $a = 60$ μm ($L \approx 1.2$ mm) and $\sigma_{\text{film}} = 30$ MPa for increasing laser powers. Measurements recorded at increasing laser powers have been shifted vertically for clarity, while the fundamental defect mode is highlighted in red. (b) Relative frequency shift versus laser power for the defect mode and the bandgap center frequency, along with linear fits to both sets of data. (c) Same as (a) for increasing powers of the vibrometer white light source. (d) Relative frequency shifts for increasing white light powers. Drawings in (b) and (d) illustrate laser and white light heating, respectively, for clarity. Figure adapted from [102].

shift of both the defect mode and bandgap center frequency as a function of laser power. The source of this nonlinearity is the detuning of the defect mode to frequencies outside of the bandgap, similar to what was observed through simulations in Figure 7.3(d). In comparison, the bandgap center frequency appears to detune linearly with power. Linear fits to both sets of data are given, which describes the bandgap data well but deviates for the defect mode at larger P due to the mode exiting the bandgap.

An alternative to heating with a point source would be to heat the entire PnC membrane uniformly. In such a scenario, one would expect the defect mode and bandgap frequencies to detune equally since the temperature localization associated with a point source would not come into play. Here, uniform heating is achieved using the white light source of the

vibrometer, which, for the chosen microscope objective, covers the entire $L \approx 1.2$ mm membrane. Such uniform heating measurements are shown in Figure 7.7(c) for increasing white light powers P_w. A slight detuning to lower frequencies is observed for both the defect mode and the bandgap center, but the location of the defect mode relative to the lower edge of the bandgap remains nearly unchanged. Plots of the relative frequency shift can further support this argument, as shown in Figure 7.7(d). Both sets of data display a linear shift for increasing P_w, with only a marginally faster detuning for the defect mode. This difference could be resulting from the fact that the frequencies are still being recorded with the vibrometer, meaning a constant laser heating of the defect center remains in addition to the white light heating.

7.6 Summary and Outlook

To conclude, this chapter demonstrated how localized modes on phononic crystal membranes can be employed for photothermal sensing applications. Finite element method simulations of the phononic band structure showed that a quasi-bandgap remains even for a very low initial tensile stress, which was confirmed through measurements of the Brownian motion spectra of PnC membranes. Simulated temperature profiles of PnC membranes heated at the center defect showed a strong temperature localization to the defect, resulting from a reduction of the effective thermal conductivity of the membrane due to the perforation. This localization translates into a larger maximum membrane temperature for a given absorbed power when compared to uniform membranes of equal size. An additional consequence of temperature localization is a larger overlap of the temperature field and the displacement field for defect modes, which should further increase their thermal response.

Measurements of the relative thermal responsivity of the fundamental defect mode for various defect sizes confirmed an enhanced thermal response of defect modes compared to the fundamental out-of-plane mode of uniform membranes, with the potential of more than an order of magnitude enhancement. Furthermore, it was shown that smaller PnC membranes result in larger relative responsivities as a result of reduced cooling due to radiative heat transfer. FEM simulations corroborated the experimental results very well. Geometric strain engineering was employed to reduce the initial tensile stress even further, which was achieved by embedding a PnC membrane inside a nanomechanical trampoline. A relative responsivity of $|\delta\mathscr{R}| = 530\ \mathrm{W}^{-1}$ was extracted for the fundamental defect mode of a trampoline PnC, which is a factor of 2.5 greater than the largest value reported for square PnC membranes.

Finally, defect mode and bandgap tuning of PnC membranes was experimentally demonstrated through laser heating of the center defect. It was shown how the defect mode responds much stronger to laser heating compared to the bandgap center frequency, to the point where

the mode completely exited the bandgap. This was attributed to a much larger temperature in the defect compared to the surrounding PnC, serving as experimental confirmation of temperature localization in PnC membranes. FEM simulations could reproduce the observed exiting of the defect mode from the bandgap, where it was observed that the displacement field of the defect mode slowly delocalizes until extending throughout the PnC. Further confirmation of temperature localization was achieved by uniformly heating the entire PnC membrane using the white light source of the vibrometer. In this case, the defect mode and bandgap center frequency shifted almost equally as a response to the heating.

While the results presented in this chapter show the great promise of defect modes on PnC membranes as thermal sensors, there is still plenty of room for improvement. Strain engineering using nanomechanical trampolines could enhance the thermal response, but the nonuniform stress distribution appeared to deteriorate the isolation of the bandgap, which resulted in a smaller enhancement than theoretically expected. A straightforward solution would be to increase the size of the central pad relative to the PnC, so that the PnC is located completely within the uniform stress region of the trampoline center. The tethers of the trampoline can also be made narrower, which increases thermal isolation.

A general problem associated with stress reduction is a significant narrowing of the PnC bandgap width. As the bandgap gets narrower, combined with enhanced thermal responsivity due to reduced tensile stress, less power is required to detune the defect mode to frequencies outside the bandgap, limiting the range of powers in which the PnC membranes can be employed. While higher-order defect modes can be used [39], the fundamental defect mode displays the largest overlap between temperature and displacement fields and is therefore preferred. A more promising solution would be to change the PnC design. As shown by Reetz *et al.*, increasing the mass contrast of the PnC widens the phononic bandgap and therefore improves defect mode localization [248]. The main consequence of this approach is a reduction of soft clamping and therefore reduced quality factors, which should not influence the thermal responsivity [16].

Finally, a drawback of using pure SiN resonators for photothermal sensing is the low optical absorption coefficient of $\mathcal{A} \approx 0.5\%$ [101]. Increasing the absorption would allow more light to be converted to heat and thus a larger frequency detuning for a given incident power. A possible solution would be to deposit a suitable absorbing layer on top of the SiN, which not only enhances the thermal response but also increases the spectral range of the sensor [151, 242]. Combining the mentioned suggestions for improving the thermal response of PnC membranes, this could pave the way for a new generation of broad range thermal sensors with unprecedented sensitivities.

References

[1] V. Smil, *Transforming the Twentieth Century: Technical Innovations and Their Consequences* (Oxford University Press, Apr. 2006).

[2] R. P. Feynman, "There's plenty of room at the bottom," Resonance **16**, 890–905 (2011).

[3] R. P. Feynman, R. B. Leighton, and M. Sands, *The Feynman Lectures on Physics, Vol. III: The New Millennium Edition: Quantum Mechanics* (Basic Books, 2011).

[4] Y. H. Choi and H.-K. Han, "Nanomedicines: current status and future perspectives in aspect of drug delivery and pharmacokinetics," Journal of Pharmaceutical Investigation **48**, 43–60 (2017).

[5] T. Ihn, *Semiconductor Nanostructures* (Oxford University Press, Nov. 2009).

[6] A. McGurn, *Nanophotonics* (Springer International Publishing, 2018).

[7] A. N. Cleland, *Foundations of Nanomechanics* (Springer Berlin Heidelberg, 2003).

[8] S. D. Senturia, *Microsystem Design* (Kluwer Academic Publishers, 2002).

[9] M. Bao, *Analysis and Design Principles of MEMS Devices* (Elsevier Science, 2005).

[10] S. Beeby, G. Ensel, M. Kraft, and N. M. White, *MEMS Mechanical Sensors* (Artech House, 2004).

[11] A. N. Cleland and M. L. Roukes, "Fabrication of high frequency nanometer scale mechanical resonators from bulk Si crystals," Applied Physics Letters **69**, 2653–2655 (1996).

[12] A. Boisen, S. Dohn, S. S. Keller, S. Schmid, and M. Tenje, "Cantilever-like micromechanical sensors," Reports on Progress in Physics **74**, 036101 (2011).

[13] K. L. Ekinci and M. L. Roukes, "Nanoelectromechanical systems," Review of Scientific Instruments **76**, 061101 (2005).

[14] E. H. Horak and R. H. Goldsmith, "Drumming up single-molecule beats," Proceedings of the National Academy of Sciences **115**, 11115–11117 (2018).

[15] K. Eom, H. S. Park, D. S. Yoon, and T. Kwon, "Nanomechanical resonators and their applications in biological/chemical detection: nanomechanics principles," Physics Reports **503**, 115–163 (2011).

[16] S. Schmid, L. G. Villanueva, and M. L. Roukes, *Fundamentals of Nanomechanical Resonators*, 1st edition (Springer, 2016).

[17] J. Chaste, A. Eichler, J. Moser, G. Ceballos, R. Rurali, and A. Bachtold, "A nanomechanical mass sensor with yoctogram resolution," Nature Nanotechnology **7**, 301–304 (2012).

[18] J. L. Arlett, J. R. Maloney, B. Gudlewski, M. Muluneh, and M. L. Roukes, "Self-sensing micro- and nanocantilevers with attonewton-scale force resolution," Nano Letters **6**, 1000–1006 (2006).

[19] J. M. L. Miller, A. Ansari, D. B. Heinz, Y. Chen, I. B. Flader, D. D. Shin, L. G. Villanueva, and T. W. Kenny, "Effective quality factor tuning mechanisms in micromechanical resonators," Applied Physics Reviews **5**, 041307 (2018).

[20] D. Leeson, "A simple model of feedback oscillator noise spectrum," Proceedings of the IEEE **54**, 329–330 (1966).

[21] A. N. Cleland and M. L. Roukes, "Noise processes in nanomechanical resonators," Journal of Applied Physics **92**, 2758–2769 (2002).

[22] A. Cleland, "Photons refrigerating phonons," Nature Physics **5**, 458–460 (2009).

[23] M. Aspelmeyer, T. J. Kippenberg, and F. Marquardt, "Cavity optomechanics," Reviews of Modern Physics **86**, 1391–1452 (2014).

[24] J. Chan, T. P. M. Alegre, A. H. Safavi-Naeini, J. T. Hill, A. Krause, S. Gröblacher, M. Aspelmeyer, and O. Painter, "Laser cooling of a nanomechanical oscillator into its quantum ground state," Nature **478**, 89–92 (2011).

[25] J. D. Teufel, T. Donner, D. Li, J. W. Harlow, M. S. Allman, K. Cicak, A. J. Sirois, J. D. Whittaker, K. W. Lehnert, and R. W. Simmonds, "Sideband cooling of micromechanical motion to the quantum ground state," Nature **475**, 359–363 (2011).

[26] T. A. Palomaki, J. D. Teufel, R. W. Simmonds, and K. W. Lehnert, "Entangling mechanical motion with microwave fields," Science **342**, 710–713 (2013).

[27] R. Riedinger, A. Wallucks, I. Marinković, C. Löschnauer, M. Aspelmeyer, S. Hong, and S. Gröblacher, "Remote quantum entanglement between two micromechanical oscillators," Nature **556**, 473–477 (2018).

[28] E. E. Wollman, C. U. Lei, A. J. Weinstein, J. Suh, A. Kronwald, F. Marquardt, A. A. Clerk, and K. C. Schwab, "Quantum squeezing of motion in a mechanical resonator," Science **349**, 952–955 (2015).

[29] J.-M. Pirkkalainen, E. Damskägg, M. Brandt, F. Massel, and M. A. Sillanpää, "Squeezing of quantum noise of motion in a micromechanical resonator," Physical Review Letters **115**, 243601 (2015).

[30] F. Marquardt, J. P. Chen, A. A. Clerk, and S. M. Girvin, "Quantum theory of cavity-assisted sideband cooling of mechanical motion," Physical Review Letters **99**, 093902 (2007).

[31] D. W. Carr, S. Evoy, L. Sekaric, H. G. Craighead, and J. M. Parpia, "Measurement of mechanical resonance and losses in nanometer scale silicon wires," Applied Physics Letters **75**, 920–922 (1999).

[32] P. Mohanty, D. A. Harrington, K. L. Ekinci, Y. T. Yang, M. J. Murphy, and M. L. Roukes, "Intrinsic dissipation in high-frequency micromechanical resonators," Physical Review B **66**, 085416 (2002).

[33] M. Imboden and P. Mohanty, "Dissipation in nanoelectromechanical systems," Physics Reports **534**, 89–146 (2014).

[34] S. S. Verbridge, J. M. Parpia, R. B. Reichenbach, L. M. Bellan, and H. G. Craighead, "High quality factor resonance at room temperature with nanostrings under high tensile stress," Journal of Applied Physics **99**, 124304 (2006).

[35] S. S. Verbridge, D. F. Shapiro, H. G. Craighead, and J. M. Parpia, "Macroscopic tuning of nanomechanics: substrate bending for reversible control of frequency and quality factor of nanostring resonators," Nano Letters **7**, 1728–1735 (2007).

[36] S. S. Verbridge, H. G. Craighead, and J. M. Parpia, "A megahertz nanomechanical resonator with room temperature quality factor over a million," Applied Physics Letters **92**, 013112 (2008).

[37] Q. P. Unterreithmeier, T. Faust, and J. P. Kotthaus, "Damping of nanomechanical resonators," Physical Review Letters **105**, 027205 (2010).

[38] S. Schmid, K. D. Jensen, K. H. Nielsen, and A. Boisen, "Damping mechanisms in high-Q micro and nanomechanical string resonators," Physical Review B **84**, 165307 (2011).

[39] Y. Tsaturyan, A. Barg, E. S. Polzik, and A. Schliesser, "Ultracoherent nanomechanical resonators via soft clamping and dissipation dilution," Nature Nanotechnology **12**, 776–783 (2017).

[40] A. H. Ghadimi, S. A. Fedorov, N. J. Engelsen, M. J. Bereyhi, R. Schilling, D. J. Wilson, and T. J. Kippenberg, "Elastic strain engineering for ultralow mechanical dissipation," Science **360**, 764–768 (2018).

[41] B. M. Zwickl, W. E. Shanks, A. M. Jayich, C. Yang, A. C. B. Jayich, J. D. Thompson, and J. G. E. Harris, "High quality mechanical and optical properties of commercial silicon nitride membranes," Applied Physics Letters **92**, 103125 (2008).

[42] D. J. Wilson, C. A. Regal, S. B. Papp, and H. J. Kimble, "Cavity optomechanics with stoichiometric SiN films," Phys. Rev. Lett. **103**, 207204 (2009).

[43] P.-L. Yu, T. P. Purdy, and C. A. Regal, "Control of material damping in high-Q membrane microresonators," Physical Review Letters **108**, 083603 (2012).

[44] S. Chakram, Y. S. Patil, L. Chang, and M. Vengalattore, "Dissipation in ultrahigh quality factor sin membrane resonators," Physical Review Letters **112**, 127201 (2014).

[45] G. D. Cole, P.-L. Yu, C. Gärtner, K. Siquans, R. M. Nia, J. Schmöle, J. Hoelscher-Obermaier, T. P. Purdy, W. Wieczorek, C. A. Regal, and M. Aspelmeyer, "Tensile-strained $In_xGa_{1-x}P$ membranes for cavity optomechanics," Applied Physics Letters **104**, 201908 (2014).

[46] R. A. Norte, J. P. Moura, and S. Gröblacher, "Mechanical resonators for quantum optomechanics experiments at room temperature," Physical Review Letters **116**, 147202 (2016).

[47] A. H. Ghadimi, "Ultra-coherent nano-mechanical resonators for quantum optomechanics at room temperature," PhD thesis (École polytechnique fédérale de Lausanne, 2018).

[48] L. G. Villanueva and S. Schmid, "Evidence of surface loss as ubiquitous limiting damping mechanism in sin micro- and nanomechanical resonators," Physical Review Letters **113**, 227201 (2014).

[49] S. G. Kelly, *Fundamentals of Mechanical Vibrations*, 2nd edition (McGraw-Hill, 2000).

[50] S. M. Heinrich and I. Dufour, "Fundamental Theory of Resonant MEMS Devices," in *Resonant MEMS*, 2nd edition (John Wiley & Sons, Ltd, 2015) Chap. 1, pages 1–28.

[51] R. E. Blake, "Basic Vibration Theory," in *Harris' Shock and Vibration Handbook*, 5th edition (McGraw-Hill, 2002) Chap. 2.

[52] S. Timoshenko and S. Woinowsky-Krieger, *Theory of Plates and Shells*, 2nd edition (McGraw-Hill, 1959).

[53] A. Leissa, *Vibration of Plates* (NASA SP-160, 1969).

[54] B. C. Stipe, H. J. Mamin, T. D. Stowe, T. W. Kenny, and D. Rugar, "Noncontact friction and force fluctuations between closely spaced bodies," Physical Review Letters **87**, 096801 (2001).

[55] A. Cleland and M. Roukes, "External control of dissipation in a nanometer-scale radiofrequency mechanical resonator," Sensors and Actuators A: Physical **72**, 256–261 (1999).

[56] K. Schwab, "Spring constant and damping constant tuning of nanomechanical resonators using a single-electron transistor," Applied Physics Letters **80**, 1276–1278 (2002).

[57] J. E. Sader, "Frequency response of cantilever beams immersed in viscous fluids with applications to the atomic force microscope," Journal of Applied Physics **84**, 64–76 (1998).

[58] J. W. M. Chon, P. Mulvaney, and J. E. Sader, "Experimental validation of theoretical models for the frequency response of atomic force microscope cantilever beams immersed in fluids," Journal of Applied Physics **87**, 3978–3988 (2000).

[59] C. P. Green and J. E. Sader, "Frequency response of cantilever beams immersed in viscous fluids near a solid surface with applications to the atomic force microscope," Journal of Applied Physics **98**, 114913 (2005).

[60] C. A. V. Eysden and J. E. Sader, "Frequency response of cantilever beams immersed in viscous fluids with applications to the atomic force microscope: arbitrary mode order," Journal of Applied Physics **101**, 044908 (2007).

[61] F. R. Blom, "Dependence of the quality factor of micromachined silicon beam resonators on pressure and geometry," Journal of Vacuum Science & Technology B: Microelectronics and Nanometer Structures **10**, 19 (1992).

[62] S. S. Verbridge, R. Ilic, H. G. Craighead, and J. M. Parpia, "Size and frequency dependent gas damping of nanomechanical resonators," Applied Physics Letters **93**, 013101 (2008).

[63] S. Schmid and C. Hierold, "Damping mechanisms of single-clamped and prestressed double-clamped resonant polymer microbeams," Journal of Applied Physics **104**, 093516 (2008).

[64] O. Ergincan, G. Palasantzas, and B. J. Kooi, "Viscous damping of microcantilevers with modified surfaces and geometries," Applied Physics Letters **101**, 061908 (2012).

[65] R. B. Bhiladvala and Z. J. Wang, "Effect of fluids on the Q factor and resonance frequency of oscillating micrometer and nanometer scale beams," Physical Review E **69**, 036307 (2004).

[66] S. Bianco, M. Cocuzza, S. Ferrero, E. Giuri, G. Piacenza, C. F. Pirri, A. Ricci, L. Scaltrito, D. Bich, A. Merialdo, P. Schina, and R. Correale, "Silicon resonant microcantilevers for absolute pressure measurement," Journal of Vacuum Science & Technology B: Microelectronics and Nanometer Structures **24**, 1803 (2006).

[67] R. Christian, "The theory of oscillating-vane vacuum gauges," Vacuum **16**, 175–178 (1966).

[68] M. Bao, H. Yang, H. Yin, and Y. Sun, "Energy transfer model for squeeze-film air damping in low vacuum," Journal of Micromechanics and Microengineering **12**, 341–346 (2002).

[69] P. Li and R. Hu, "On the air damping of flexible microbeam in free space at the free-molecule regime," Microfluidics and Nanofluidics **3**, 715–721 (2007).

[70] M. C. Cross and R. Lifshitz, "Elastic wave transmission at an abrupt junction in a thin plate with application to heat transport and vibrations in mesoscopic systems," Physical Review B **64**, 085324 (2001).

[71] D. M. Photiadis and J. A. Judge, "Attachment losses of high Q oscillators," Applied Physics Letters **85**, 482–484 (2004).

[72] I. Wilson-Rae, "Intrinsic dissipation in nanomechanical resonators due to phonon tunneling," Phys. Rev. B **77**, 245418 (2008).

[73] Z. Hao, A. Erbil, and F. Ayazi, "An analytical model for support loss in micromachined beam resonators with in-plane flexural vibrations," Sensors and Actuators A: Physical **109**, 156–164 (2003).

[74] I. Wilson-Rae, R. A. Barton, S. S. Verbridge, D. R. Southworth, B. Ilic, H. G. Craighead, and J. M. Parpia, "High-Q nanomechanics via destructive interference of elastic waves," Physical Review Letters **106**, 047205 (2011).

[75] P.-L. Yu, K. Cicak, N. S. Kampel, Y. Tsaturyan, T. P. Purdy, R. W. Simmonds, and C. A. Regal, "A phononic bandgap shield for high-Q membrane microresonators," Applied Physics Letters **104**, 023510 (2014).

[76] Y. Tsaturyan, A. Barg, A. Simonsen, L. G. Villanueva, S. Schmid, A. Schliesser, and E. S. Polzik, "Demonstration of suppressed phonon tunneling losses in phononic bandgap shielded membrane resonators for high-Q optomechanics," Optics Express **22**, 6810 (2014).

[77] A. H. Ghadimi, D. J. Wilson, and T. J. Kippenberg, "Radiation and internal loss engineering of high-stress silicon nitride nanobeams," Nano Letters **17**, 3501–3505 (2017).

[78] C. Zener, "Internal friction in solids. I. theory of internal friction in reeds," Physical Review **52**, 230–235 (1937).

[79] C. Zener, "Internal friction in solids II. general theory of thermoelastic internal friction," Physical Review **53**, 90–99 (1938).

[80] R. Lifshitz and M. L. Roukes, "Thermoelastic damping in micro- and nanomechanical systems," Physical Review B **61**, 5600–5609 (2000).

[81] K. Y. Yasumura, T. D. Stowe, E. M. Chow, T. Pfafman, T. W. Kenny, B. C. Stipe, and D. Rugar, "Quality factors in micron- and submicron-thick cantilevers," Journal of Microelectromechanical Systems **9**, 117–125 (2000).

[82] J. Yang, T. Ono, and M. Esashi, "Energy dissipation in submicrometer thick single-crystal silicon cantilevers," Journal of Microelectromechanical Systems **11**, 775–783 (2002).

[83] X. Feng, C. Zorman, M. Mehregany, and M. Roukes, "Dissipation in single-crystal 3C-SiC ultra-high frequency nanomechanical resonators," in 2006 Solid-State, Actuators, and Microsystems Workshop Technical Digest (June 2006).

[84] X. M. H. Huang, X. L. Feng, C. A. Zorman, M. Mehregany, and M. L. Roukes, "VHF, UHF and microwave frequency nanomechanical resonators," New Journal of Physics **7**, 247–247 (2005).

[85] Y. Tao, P. Navaretti, R. Hauert, U. Grob, M. Poggio, and C. L. Degen, "Permanent reduction of dissipation in nanomechanical Si resonators by chemical surface protection," Nanotechnology **26**, 465501 (2015).

[86] N. Luhmann, A. Jachimowicz, J. Schalko, P. Sadeghi, M. Sauer, A. Foelske-Schmitz, and S. Schmid, "Effect of oxygen plasma on nanomechanical silicon nitride resonators," Applied Physics Letters **111**, 063103 (2017).

[87] P. R. Saulson, "Thermal noise in mechanical experiments," Physical Review D **42**, 2437–2445 (1990).

[88] G. I. González and P. R. Saulson, "Brownian motion of a mass suspended by an anelastic wire," The Journal of the Acoustical Society of America **96**, 207–212 (1994).

[89] Y. L. Huang and P. R. Saulson, "Dissipation mechanisms in pendulums and their implications for gravitational wave interferometers," Review of Scientific Instruments **69**, 544–553 (1998).

[90] B. S. Berry, "Dynamical method for the thermomechanical study of thin membranes," Journal of Vacuum Science & Technology B: Microelectronics and Nanometer Structures **7**, 1565 (1989).

[91] B. Berry and W. Pritchet, "New developments in the dynamic mechanical analysis of thin-layer materials," MRS Proceedings **226**, 179 (1991).

[92] B. Berry, "Damping mechanisms in thin-layer materials," in *M3D: Mechanics and Mechanisms of Material Damping* (ASTM International, 1992), pages 28–28–17.

[93] S. A. Fedorov, N. J. Engelsen, A. H. Ghadimi, M. J. Bereyhi, R. Schilling, D. J. Wilson, and T. J. Kippenberg, "Generalized dissipation dilution in strained mechanical resonators," Physical Review B **99**, 054107 (2019).

[94] W.-H. Chuang, T. Luger, R. Fettig, and R. Ghodssi, "Mechanical property characterization of LPCVD silicon nitride thin films at cryogenic temperatures," Journal of Microelectromechanical Systems **13**, 870–879 (2004).

[95] T. Larsen, S. Schmid, L. Grönberg, A. O. Niskanen, J. Hassel, S. Dohn, and A. Boisen, "Ultrasensitive string-based temperature sensors," Applied Physics Letters **98**, 121901 (2011).

[96] T. Larsen, S. Schmid, L. G. Villanueva, and A. Boisen, "Photothermal analysis of individual nanoparticulate samples using micromechanical resonators," ACS Nano **7**, 6188–6193 (2013).

[97] S. Yamada, S. Schmid, T. Larsen, O. Hansen, and A. Boisen, "Photothermal infrared spectroscopy of airborne samples with mechanical string resonators," Analytical Chemistry **85**, 10531–10535 (2013).

[98] S. Schmid, K. Wu, P. E. Larsen, T. Rindzevicius, and A. Boisen, "Low-power photothermal probing of single plasmonic nanostructures with nanomechanical string resonators," Nano Letters **14**, 2318–2321 (2014).

[99] T. S. Biswas, N. Miriyala, C. Doolin, X. Liu, T. Thundat, and J. P. Davis, "Femtogram-scale photothermal spectroscopy of explosive molecules on nanostrings," Analytical Chemistry **86**, 11368–11372 (2014).

[100] M. Kurek, M. Carnoy, P. E. Larsen, L. H. Nielsen, O. Hansen, T. Rades, S. Schmid, and A. Boisen, "Nanomechanical infrared spectroscopy with vibrating filters for pharmaceutical analysis," Angewandte Chemie International Edition **56**, 3901–3905 (2017).

[101] M.-H. Chien, M. Brameshuber, B. K. Rossboth, G. J. Schütz, and S. Schmid, "Single-molecule optical absorption imaging by nanomechanical photothermal sensing," Proceedings of the National Academy of Sciences **115**, 11150–11155 (2018).

[102] P. Sadeghi, M. Tanzer, N. Luhmann, M. Piller, M.-H. Chien, and S. Schmid, "Thermal transport and frequency response of localized modes on low-stress nanomechanical silicon nitride drums featuring a phononic-band-gap structure," Physical Review Applied **14**, 024068 (2020).

[103] M. Piller, P. Sadeghi, R. G. West, N. Luhmann, P. Martini, O. Hansen, and S. Schmid, "Thermal radiation dominated heat transfer in nanomechanical silicon nitride drum resonators," Applied Physics Letters **117**, 034101 (2020).

[104] C. Zhang, M. Giroux, T. A. Nour, and R. St-Gelais, "Radiative heat transfer in free-standing silicon nitride membranes," Physical Review Applied **14**, 024072 (2020).

[105] COMSOL, Inc., *Heat Transfer Module User's Guide, Version 5.5*, Accessed: 2021-02-05, (2019)

[106] A. C. Ceccacci, "Mechanical resonators for material characterization: sensor development and applications," PhD thesis (Technical University of Denmark, 2017).

[107] W. Weaver, S. P. Timoshenko, and D. H. Young, *Vibration Problems in Engineering*, 5th edition (Wiley Interscience, 1990).

[108] K. L. Ekinci, Y. T. Yang, and M. L. Roukes, "Ultimate limits to inertial mass sensing based upon nanoelectromechanical systems," Journal of Applied Physics **95**, 2682–2689 (2004).

[109] J. R. Vig and Yoonkee Kim, "Noise in microelectromechanical system resonators," IEEE Transactions on Ultrasonics, Ferroelectrics, and Frequency Control **46**, 1558–1565 (1999).

[110] J. Atalaya, A. Isacsson, and M. I. Dykman, "Diffusion-induced dephasing in nanomechanical resonators," Physical Review B **83**, 045419 (2011).

[111] O. Maillet, X. Zhou, R. R. Gazizulin, R. Ilic, J. M. Parpia, O. Bourgeois, A. D. Fefferman, and E. Collin, "Measuring frequency fluctuations in nonlinear nanomechanical resonators," ACS Nano **12**, 5753–5760 (2018).

[112] M. Sansa, E. Sage, E. C. Bullard, M. Gély, T. Alava, E. Colinet, A. K. Naik, L. G. Villanueva, L. Duraffourg, M. L. Roukes, G. Jourdan, and S. Hentz, "Frequency fluctuations in silicon nanoresonators," Nature Nanotechnology **11**, 552–558 (2016).

[113] T. R. Albrecht, P. Grütter, D. Horne, and D. Rugar, "Frequency modulation detection using high-Q cantilevers for enhanced force microscope sensitivity," Journal of Applied Physics **69**, 668–673 (1991).

[114] A. N. Cleland, "Thermomechanical noise limits on parametric sensing with nanomechanical resonators," New Journal of Physics **7**, 235–235 (2005).

[115] E. Gavartin, P. Verlot, and T. J. Kippenberg, "Stabilization of a linear nanomechanical oscillator to its thermodynamic limit," Nature Communications **4**, 2860 (2013).

[116] B. Hauer, C. Doolin, K. Beach, and J. Davis, "A general procedure for thermomechanical calibration of nano/micro-mechanical resonators," Annals of Physics **339**, 181–207 (2013).

[117] R. Bowley and M. Sánchez, *Introductory Stastical Mechanics* (Oxford University Press, 1999).

[118] R. J. Barlow, *Statistics: A Guide to the Use of Statistical Methods in the Physical Sciences* (Wiley, 1993).

[119] D. Allan, "Statistics of atomic frequency standards," Proceedings of the IEEE **54**, 221–230 (1966).

[120] D. W. Allan, N. Ashby, and C. C. Hodge, *The science of timekeeping*, Hewlett Packard Application Note 1289, 2000.

[121] E. Rubiola, *Phase Noise and Frequency Stability in Oscillators* (Cambridge University Press, 2008).

[122] D. Howe, D. Allan, and J. Barnes, "Properties of signal sources and measurement methods," in Thirty Fifth Annual Frequency Control Symposium (1981).

[123] W. J. Riley, *Handbook of Frequency Stability Analysis* (NIST Special Publication 1065, 2008).

[124] A. Makdissi, F. Vernotte, and E. Clercq, "Stability variances: a filter approach," IEEE Transactions on Ultrasonics, Ferroelectrics and Frequency Control **57**, 1011–1028 (2010).

[125] A. Demir and M. S. Hanay, "Fundamental sensitivity limitations of nanomechanical resonant sensors due to thermomechanical noise," IEEE Sensors Journal **20**, 1947–1961 (2020).

[126] A. Demir, "Understanding fundamental trade-offs in nanomechanical resonant sensors," Journal of Applied Physics **129**, 044503 (2021).

[127] M. Ohring, "Chapter 6 - Chemical Vapor Deposition," in *Materials Science of Thin Films*, edited by M. Ohring, 2nd edition (Academic Press, San Diego, 2002), pages 277–355.

[128] E. A. Irene, "Residual stress in silicon nitride films," Journal of Electronic Materials **5**, 287–298 (1976).

[129] J. A. Thornton and D. Hoffman, "Stress-related effects in thin films," Thin Solid Films **171**, 5–31 (1989).

[130] M. Stadtmüeller, "Mechanical stress of CVD-dielectrics," Journal of The Electrochemical Society **139**, 3669–3674 (1992).

[131] A. Kaushik, H. Kahn, and A. Heuer, "Wafer-level mechanical characterization of silicon nitride MEMS," Journal of Microelectromechanical Systems **14**, 359–367 (2005).

[132] W. D. Nix and B. M. Clemens, "Crystallite coalescence: a mechanism for intrinsic tensile stresses in thin films," Journal of Materials Research **14**, 3467–3473 (1999).

[133] E. Chason and P. R. Guduru, "Tutorial: understanding residual stress in polycrystalline thin films through real-time measurements and physical models," Journal of Applied Physics **119**, 191101 (2016).

[134] T. Makino, "Composition and structure control by source gas ratio in LPCVD SiN_x," Journal of The Electrochemical Society **130**, 450–455 (1983).

[135] P. Pan and W. Berry, "The composition and physical properties of LPCVD silicon nitride deposited with different NH_2/SiH_2Cl_2 gas ratios," Journal of The Electrochemical Society **132**, 3001–3005 (1985).

[136] P. French, P. Sarro, R. Mallée, E. Fakkeldij, and R. Wolffenbuttel, "Optimization of a low-stress silicon nitride process for surface-micromachining applications," Sensors and Actuators A: Physical **58**, 149–157 (1997).

[137] H.-S.-G. für angewandte Forschung e.V., `https://www.hahn-schickard.de` (visited on 02/08/2021).

[138] W. Software, `https://wieweb.com/site` (visited on 02/08/2021).

[139] D. M. B.V., `https://www.deltamask.nl/frames.html` (visited on 02/08/2021).

[140] R. Fotomasken, `https://www.rose-fotomasken.de` (visited on 02/08/2021).

[141] J. L. Lindström, G. S. Oehrlein, and W. A. Lanford, "Reactive ion etching of silicon nitride deposited by different methods in CF_4/H_2 plasmas," Journal of The Electrochemical Society **139**, 317–320 (1992).

[142] B. E. E. Kastenmeier, P. J. Matsuo, J. J. Beulens, and G. S. Oehrlein, "Chemical dry etching of silicon nitride and silicon dioxide using $CF_4/O_2/N_2$ gas mixtures," Journal of Vacuum Science & Technology A: Vacuum, Surfaces, and Films **14**, 2802–2813 (1996).

[143] H. Seidel, L. Csepregi, A. Heuberger, and H. Baumgärtel, "Anisotropic etching of crystalline silicon in alkaline solutions: I. orientation dependence and behavior of passivation layers," Journal of The Electrochemical Society **137**, 3612–3626 (1990).

[144] K. Williams, K. Gupta, and M. Wasilik, "Etch rates for micromachining processing-part II," Journal of Microelectromechanical Systems **12**, 761–778 (2003).

[145] S. Wolf and R. N. Tauber, *Silicon Processing for the VLSI Era: Process Technology* (Lattice Press, 1986).

[146] S. Schmid, S. Dohn, and A. Boisen, "Real-time particle mass spectrometry based on resonant micro strings," Sensors **10**, 8092–8100 (2010).

[147] Y. Tsaturyan, "Ultracoherent soft-clamped mechanical resonators for quantum cavity optomechanics," PhD thesis (University of Copenhagen, 2019).

[148] J. P. Moura, "Making light jump," PhD thesis (Delft University of Technology, 2019).

[149] A. Barg, Y. Tsaturyan, E. Belhage, W. H. P. Nielsen, C. B. Møller, and A. Schliesser, "Measuring and imaging nanomechanical motion with laser light," Applied Physics B **123**, 8 (2016).

[150] P. A. Truitt, J. B. Hertzberg, C. C. Huang, K. L. Ekinci, and K. C. Schwab, "Efficient and sensitive capacitive readout of nanomechanical resonator arrays," Nano Letters **7**, 120–126 (2007).

[151] M. Piller, N. Luhmann, M.-H. Chien, and S. Schmid, "Nanoelectromechanical infrared detector," in Optical sensing, imaging, and photon counting: from X-rays to THz 2019, Vol. 11088, edited by O. Mitrofanov (International Society for Optics and Photonics, 2019), pages 9–15.

[152] M.-H. Chien, J. Steurer, P. Sadeghi, N. Cazier, and S. Schmid, "Nanoelectromechanical position-sensitive detector with picometer resolution," ACS Photonics **7**, 2197–2203 (2020).

[153] S. Schmid, M. Wendlandt, D. Junker, and C. Hierold, "Nonconductive polymer microresonators actuated by the kelvin polarization force," Applied Physics Letters **89**, 163506 (2006).

[154] Q. P. Unterreithmeier, E. M. Weig, and J. P. Kotthaus, "Universal transduction scheme for nanomechanical systems based on dielectric forces," Nature **458**, 1001–1004 (2009).

[155] R. B. Karabalin, M. H. Matheny, X. L. Feng, E. Defaÿ, G. L. Rhun, C. Marcoux, S. Hentz, P. Andreucci, and M. L. Roukes, "Piezoelectric nanoelectromechanical resonators based on aluminum nitride thin films," Applied Physics Letters **95**, 103111 (2009).

[156] A. D. O'Connell, M. Hofheinz, M. Ansmann, R. C. Bialczak, M. Lenander, E. Lucero, M. Neeley, D. Sank, H. Wang, M. Weides, J. Wenner, J. M. Martinis, and A. N. Cleland, "Quantum ground state and single-phonon control of a mechanical resonator," Nature **464**, 697–703 (2010).

[157] L. E. Drain, *The Laser Doppler Technique* (John Wiley & Sons Ltd., 1980).

[158] H. Wu, S. Grabarnik, A. Emadi, G. de Graaf, and R. F. Wolffenbuttel, "Characterization of thermal cross-talk in a MEMS-based thermopile detector array," Journal of Micromechanics and Microengineering **19**, 074022 (2009).

[159] J. C. Maxwell, *A Treatise on Electricity and Magnetism*, 1st edition (Oxford: Clarendon Press, 1873).

[160] D. R. Evans, P. Tayati, H. An, P. K. Lam, V. S. J. Craig, and T. J. Senden, "Laser actuation of cantilevers for picometre amplitude dynamic force microscopy," Scientific Reports **4**, 5567 (2014).

[161] D. Ma, J. L. Garrett, and J. N. Munday, "Quantitative measurement of radiation pressure on a microcantilever in ambient environment," Applied Physics Letters **106**, 091107 (2015).

[162] B. Ilic, S. Krylov, K. Aubin, R. Reichenbach, and H. G. Craighead, "Optical excitation of nanoelectromechanical oscillators," Applied Physics Letters **86**, 193114 (2005).

[163] I. Bargatin, I. Kozinsky, and M. L. Roukes, "Efficient electrothermal actuation of multiple modes of high-frequency nanoelectromechanical resonators," Applied Physics Letters **90**, 093116 (2007).

[164] M. Vassalli, V. Pini, and B. Tiribilli, "Role of the driving laser position on atomic force microscopy cantilevers excited by photothermal and radiation pressure effects," Applied Physics Letters **97**, 143105 (2010).

[165] A. C. Hillier and A. J. Bard, "ac-mode atomic force microscope imaging in air and solutions with a thermally driven bimetallic cantilever probe," Review of Scientific Instruments **68**, 2082–2090 (1997).

[166] T. Larsen, S. Schmid, S. Dohn, J. E. Sader, A. Boisen, and L. G. Villanueva, "Position and mode dependent optical detection back-action in cantilever beam resonators," Journal of Micromechanics and Microengineering **27**, 035006 (2017).

[167] S. Schmid, P. Senn, and C. Hierold, "Electrostatically actuated nonconductive polymer microresonators in gaseous and aqueous environment," Sensors and Actuators A: Physical **145-146**, 442–448 (2008).

[168] X. L. Feng, C. J. White, A. Hajimiri, and M. L. Roukes, "A self-sustaining ultrahigh-frequency nanoelectromechanical oscillator," Nature Nanotechnology **3**, 342–346 (2008).

[169] L. G. Villanueva, R. B. Karabalin, M. H. Matheny, E. Kenig, M. C. Cross, and M. L. Roukes, "A nanoscale parametric feedback oscillator," Nano Letters **11**, 5054–5059 (2011).

[170] P. Sadeghi, A. Demir, L. G. Villanueva, H. Kähler, and S. Schmid, "Frequency fluctuations in nanomechanical silicon nitride string resonators," Physical Review B **102**, 214106 (2020).

[171] Y. T. Yang, C. Callegari, X. L. Feng, K. L. Ekinci, and M. L. Roukes, "Zeptogram-scale nanomechanical mass sensing," Nano Letters **6**, 583–586 (2006).

[172] A. K. Naik, M. S. Hanay, W. K. Hiebert, X. L. Feng, and M. L. Roukes, "Towards single-molecule nanomechanical mass spectrometry," Nature Nanotechnology **4**, 445–450 (2009).

[173] M. S. Hanay, S. Kelber, A. K. Naik, D. Chi, S. Hentz, E. C. Bullard, E. Colinet, L. Duraffourg, and M. L. Roukes, "Single-protein nanomechanical mass spectrometry in real time," Nature Nanotechnology **7**, 602–608 (2012).

[174] S. Olcum, N. Cermak, S. C. Wasserman, and S. R. Manalis, "High-speed multiple-mode mass-sensing resolves dynamic nanoscale mass distributions," Nature Communications **6**, 7070 (2015).

[175] E. Ogier, *AVAR*, (2021) `https://www.mathworks.com/matlabcentral/fileexchange/55765-avar` (visited on 02/11/2021).

[176] D. M. Pozar, *Microwave Engineering*, 4th edition (Wiley, 2011).

[177] G. F. Weston, *Ultrahigh Vacuum Practice* (Butterworth & Co. (Publishers) Ltd., 1985).

[178] P. Hofmann, *Surface Physics: An Introduction* (Self-published, 2013).

[179] J. H. Moore, C. C. Davis, and M. A. Coplan, *Building Scientific Apparatus*, 4th edition (Cambridge University Press, 2009).

[180] J. T. Y. Jr., *Experimental Innovations in Surface Science - A Guide to Practical Laboratory Methods and Instruments*, 2nd edition (Springer International Publishing, 2015).

[181] L. Marton and C. Marton, *Vacuum Physics and Technology* (Academic Press, 1980).

[182] E. Rizzi, L. Mauri, M. Moraja, A. Conte, A. Bonucci, G. Longoni, and M. Amiotti, "Outgassing and gettering," in *Handbook of Silicon Based MEMS Materials and Technologies* (Elsevier, 2015), pages 713–733.

[183] M. H. Asadian, S. Askari, and A. M. Shkel, "An ultrahigh vacuum packaging process demonstrating over 2 million Q-factor in MEMS vibratory gyroscopes," IEEE Sensors Letters **1**, 1–4 (2017).

[184] COMSOL, Inc., *Structural Mechanics Module User's Guide, Version 5.5*, Accessed: 2021-02-05, (2019)

[185] R. v. Mises, "Mechanik der festen körper im plastisch-deformablen zustand," Nachrichten von der Gesellschaft der Wissenschaften zu Göttingen, Mathematisch-Physikalische Klasse **1913**, 582–592 (1913).

[186] N. Elabbasi, *Modeling Phononic Band Gap Materials and Structures*, (2016) `https://www.comsol.com/blogs/modeling-phononic-band-gap-materials-and-structures` (visited on 02/05/2021).

[187] S. Mohammadi, A. A. Eftekhar, A. Khelif, H. Moubchir, R. Westafer, W. D. Hunt, and A. Adibi, "Complete phononic bandgaps and bandgap maps in two-dimensional silicon phononic crystal plates," Electronics Letters **43**, 898–899 (2007).

[188] A. Z. Barasheed, T. Müller, and J. C. Sankey, "Optically defined mechanical geometry," Physical Review A **93**, 053811 (2016).

[189] P. Sadeghi, M. Tanzer, S. L. Christensen, and S. Schmid, "Influence of clamp-widening on the quality factor of nanomechanical silicon nitride resonators," Journal of Applied Physics **126**, 165108 (2019).

[190] T. D. Stowe, K. Yasumura, T. W. Kenny, D. Botkin, K. Wago, and D. Rugar, "Attonewton force detection using ultrathin silicon cantilevers," Applied Physics Letters **71**, 288–290 (1997).

[191] Y. Tao, J. M. Boss, B. A. Moores, and C. L. Degen, "Single-crystal diamond nanomechanical resonators with quality factors exceeding one million," Nature Communications **5**, 3638 (2014).

[192] C. Reinhardt, T. Müller, A. Bourassa, and J. C. Sankey, "Ultralow-noise SiN trampoline resonators for sensing and optomechanics," Physical Review X **6**, 021001 (2016).

[193] R. Fischer, D. P. McNally, C. Reetz, G. G. T. Assumpção, T. Knief, Y. Lin, and C. A. Regal, "Spin detection with a micromechanical trampoline: towards magnetic resonance microscopy harnessing cavity optomechanics," New Journal of Physics **21**, 043049 (2019).

[194] M. J. Bereyhi, A. Beccari, S. A. Fedorov, A. H. Ghadimi, R. Schilling, D. J. Wilson, N. J. Engelsen, and T. J. Kippenberg, "Clamp-tapering increases the quality factor of stressed nanobeams," Nano Letters **19**, 2329–2333 (2019).

[195] G.-R. Yang, Y.-P. Zhao, Y. Hu, T. P. Chow, and R. J. Gutmann, "XPS and AFM study of chemical mechanical polishing of silicon nitride," Thin Solid Films **333**, 219–223 (1998).

[196] M. Brunet, D. Aureau, P. Chantraine, F. Guillemot, A. Etcheberry, A. C. Gouget-Laemmel, and F. Ozanam, "Etching and chemical control of the silicon nitride surface," ACS Applied Materials & Interfaces **9**, 3075–3084 (2017).

[197] M. Bao and H. Yang, "Squeeze film air damping in MEMS," Sensors and Actuators A: Physical **136**, 3–27 (2007).

[198] D. M. Karabacak, V. Yakhot, and K. L. Ekinci, "High-frequency nanofluidics: an experimental study using nanomechanical resonators," Physical Review Letters **98**, 254505 (2007).

[199] S. Schmid, B. Malm, and A. Boisen, "Quality factor improvement of silicon nitride micro string resonators," in 2011 IEEE 24th international conference on micro electro mechanical systems (Jan. 2011).

[200] D. R. Southworth, H. G. Craighead, and J. M. Parpia, "Pressure dependent resonant frequency of micromechanical drumhead resonators," Applied Physics Letters **94**, 213506 (2009).

[201] J. Lee, Z. Wang, K. He, J. Shan, and P. X.-L. Feng, "Air damping of atomically thin MoS_2 nanomechanical resonators," Applied Physics Letters **105**, 023104 (2014).

[202] M. Morita, T. Ohmi, E. Hasegawa, M. Kawakami, and M. Ohwada, "Growth of native oxide on a silicon surface," Journal of Applied Physics **68**, 1272–1281 (1990).

[203] S. I. Raider, R. Flitsch, J. A. Aboaf, and W. A. Pliskin, "Surface oxidation of silicon nitride films," Journal of The Electrochemical Society **123**, 560–565 (1976).

[204] M. Kralj and K. Wandelt, "Experimental basics," in *Surface and Interface Science* (John Wiley & Sons, Ltd, 2013) Chap. 3.1, pages 74–80.

[205] W. E. Newell, "Miniaturization of tuning forks," Science **161**, 1320–1326 (1968).

[206] H. Haucke, X. Liu, J. F. Vignola, B. H. Houston, M. H. Marcus, and J. W. Baldwin, "Effects of annealing and temperature on acoustic dissipation in a micromechanical silicon oscillator," Applied Physics Letters **86**, 181903 (2005).

[207] T. H. Metcalf, X. Liu, and M. R. Abernathy, "Improving the mechanical quality factor of ultra-low-loss silicon resonators," Journal of Applied Physics **123**, 235105 (2018).

[208] W. Jiang, D. Xu, B. Xiong, and Y. Wang, "Effects of rapid thermal annealing on LPCVD silicon nitride," Ceramics International **42**, 1217–1224 (2016).

[209] Y. Okada and Y. Tokumaru, "Precise determination of lattice parameter and thermal expansion coefficient of silicon between 300 and 1500 K," Journal of Applied Physics **56**, 314–320 (1984).

[210] A. K. Sinha, H. J. Levinstein, and T. E. Smith, "Thermal stresses and cracking resistance of dielectric films (SiN, Si_3N_4, and SiO_2) on Si substrates," Journal of Applied Physics **49**, 2423 (1978).

[211] K. Andersen, W. Svendsen, T. Stimpel-Lindner, T. Sulima, and H. Baumgärtner, "Annealing and deposition effects of the chemical composition of silicon-rich nitride," Applied Surface Science **243**, 401–408 (2005).

[212] K. L. Ekinci, X. M. H. Huang, and M. L. Roukes, "Ultrasensitive nanoelectromechanical mass detection," Applied Physics Letters **84**, 4469–4471 (2004).

[213] S. Dominguez-Medina, S. Fostner, M. Defoort, M. Sansa, A.-K. Stark, M. A. Halim, E. Vernhes, M. Gely, G. Jourdan, T. Alava, P. Boulanger, C. Masselon, and S. Hentz, "Neutral mass spectrometry of virus capsids above 100 megadaltons with nanomechanical resonators," Science **362**, 918–922 (2018).

[214] M. Yuksel, E. Orhan, C. Yanik, A. B. Ari, A. Demir, and M. S. Hanay, "Nonlinear nanomechanical mass spectrometry at the single-nanoparticle level," Nano Letters **19**, 3583–3589 (2019).

[215] D. Rugar, R. Budakian, H. J. Mamin, and B. W. Chui, "Single spin detection by magnetic resonance force microscopy," Nature **430**, 329–332 (2004).

[216] I. Kozinsky, H. W. C. Postma, I. Bargatin, and M. L. Roukes, "Tuning nonlinearity, dynamic range, and frequency of nanomechanical resonators," Applied Physics Letters **88**, 253101 (2006).

[217] J. Moser, J. Güttinger, A. Eichler, M. J. Esplandiu, D. E. Liu, M. I. Dykman, and A. Bachtold, "Ultrasensitive force detection with a nanotube mechanical resonator," Nature Nanotechnology **8**, 493–496 (2013).

[218] T. Bagci, A. Simonsen, S. Schmid, L. G. Villanueva, E. Zeuthen, J. Appel, J. M. Taylor, A. Sørensen, K. Usami, A. Schliesser, and E. S. Polzik, "Optical detection of radio waves through a nanomechanical transducer," Nature **507**, 81–85 (2014).

[219] A. K. Pandey, O. Gottlieb, O. Shtempluck, and E. Buks, "Performance of an AuPd micromechanical resonator as a temperature sensor," Applied Physics Letters **96**, 203105 (2010).

[220] X. C. Zhang, E. B. Myers, J. E. Sader, and M. L. Roukes, "Nanomechanical torsional resonators for frequency-shift infrared thermal sensing," Nano Letters **13**, 1528–1534 (2013).

[221] Y. Zhang, Y. Watanabe, S. Hosono, N. Nagai, and K. Hirakawa, "Room temperature, very sensitive thermometer using a doubly clamped microelectromechanical beam resonator for bolometer applications," Applied Physics Letters **108**, 163503 (2016).

[222] U. Adiyan, T. Larsen, J. J. Zárate, L. G. Villanueva, and H. Shea, "Shape memory polymer resonators as highly sensitive uncooled infrared detectors," Nature Communications **10**, 4518 (2019).

[223] W. Robins, *Phase Noise in Signal Sources: Theory and Applications*, Vol. 9 (IET, 1984).

[224] K. Y. Fong, W. H. P. Pernice, and H. X. Tang, "Frequency and phase noise of ultra-high Q silicon nitride nanomechanical resonators," Physical Review B **85**, 161410(R) (2012).

[225] N. Kacem, S. Hentz, D. Pinto, B. Reig, and V. Nguyen, "Nonlinear dynamics of nanomechanical beam resonators: improving the performance of NEMS-based sensors," Nanotechnology **20**, 275501 (2009).

[226] N. Kacem, J. Arcamone, F. Perez-Murano, and S. Hentz, "Dynamic range enhancement of nonlinear nanomechanical resonant cantilevers for highly sensitive NEMS gas/mass sensor applications," Journal of Micromechanics and Microengineering **20**, 045023 (2010).

[227] S. K. Roy, V. T. K. Sauer, J. N. Westwood-Bachman, A. Venkatasubramanian, and W. K. Hiebert, "Improving mechanical sensor performance through larger damping," Science **360**, eaar5220 (2018).

[228] T. Manzaneque, P. G. Steeneken, F. Alijani, and M. K. Ghatkesar, "Method to determine the closed-loop precision of resonant sensors from open-loop measurements," IEEE Sensors Journal **20**, 14262–14272 (2020).

[229] C. Zhang, M. Giroux, T. A. Nour, and R. St-Gelais, "Thermal radiation sensing using high mechanical Q-factor silicon nitride membranes," in 2019 IEEE sensors (2019), pages 1–4.

[230] A. J. Andersen, S. Yamada, E. Pramodkumar, T. L. Andresen, A. Boisen, and S. Schmid, "Nanomechanical IR spectroscopy for fast analysis of liquid-dispersed engineered nanomaterials," Sensors and Actuators B: Chemical **233**, 667–673 (2016).

[231] V. P. Rangacharya, K. Wu, P. E. Larsen, L. H. E. Thamdrup, O. Ilchenko, E.-T. Hwu, T. Rindzevicius, and A. Boisen, "Quantifying optical absorption of single plasmonic nanoparticles and nanoparticle dimers using microstring resonators," ACS Sensors **5**, 2067–2075 (2020).

[232] A. Jöckel, M. T. Rakher, M. Korppi, S. Camerer, D. Hunger, M. Mader, and P. Treutlein, "Spectroscopy of mechanical dissipation in micro-mechanical membranes," Applied Physics Letters **99**, 143109 (2011).

[233] P. E. Hopkins, C. M. Reinke, M. F. Su, R. H. Olsson, E. A. Shaner, Z. C. Leseman, J. R. Serrano, L. M. Phinney, and I. El-Kady, "Reduction in the thermal conductivity of single crystalline silicon by phononic crystal patterning," Nano Letters **11**, 107–112 (2011).

[234] J. Nakagawa, Y. Kage, T. Hori, J. Shiomi, and M. Nomura, "Crystal structure dependent thermal conductivity in two-dimensional phononic crystal nanostructures," Applied Physics Letters **107**, 023104 (2015).

[235] M. R. Wagner, B. Graczykowski, J. S. Reparaz, A. E. Sachat, M. Sledzinska, F. Alzina, and C. M. S. Torres, "Two-dimensional phononic crystals: disorder matters," Nano Letters **16**, 5661–5668 (2016).

[236] K. Takahashi, M. Fujikane, Y. Liao, M. Kashiwagi, T. Kawasaki, N. Tambo, S. Ju, Y. Naito, and J. Shiomi, "Elastic inhomogeneity and anomalous thermal transport in ultrafine Si phononic crystals," Nano Energy **71**, 104581 (2020).

[237] N. Zen, T. A. Puurtinen, T. J. Isotalo, S. Chaudhuri, and I. J. Maasilta, "Engineering thermal conductance using a two-dimensional phononic crystal," Nature Communications **5**, 3435 (2014).

[238] L. Yang, J. Chen, N. Yang, and B. Li, "Significant reduction of graphene thermal conductivity by phononic crystal structure," International Journal of Heat and Mass Transfer **91**, 428–432 (2015).

[239] D. Song and G. Chen, "Thermal conductivity of periodic microporous silicon films," Applied Physics Letters **84**, 687–689 (2004).

[240] J. Tang, H.-T. Wang, D. H. Lee, M. Fardy, Z. Huo, T. P. Russell, and P. Yang, "Holey silicon as an efficient thermoelectric material," Nano Letters **10**, 4279–4283 (2010).

[241] Y. Zhang, B. Qiu, N. Nagai, M. Nomura, S. Volz, and K. Hirakawa, "Enhanced thermal sensitivity of MEMS bolometers integrated with nanometer-scale hole array structures," AIP Advances **9**, 085102 (2019).

[242] N. Luhmann, D. Høj, M. Piller, H. Kähler, M.-H. Chien, R. G. West, U. L. Andersen, and S. Schmid, "Ultrathin 2 nm gold as impedance-matched absorber for infrared light," Nature Communications **11**, 2161 (2020).

[243] S. A. Fedorov, A. Beccari, N. J. Engelsen, and T. J. Kippenberg, "Fractal-like mechanical resonators with a soft-clamped fundamental mode," Physical Review Letters **124**, 025502 (2020).

[244] A. Beccari, M. J. Bereyhi, R. Groth, S. A. Fedorov, A. Arabmoheghi, N. J. Engelsen, and T. J. Kippenberg, "Hierarchical tensile structures with ultralow mechanical dissipation," arXiv:2103.09785 (2021).

[245] A. Varpula, A. V. Timofeev, A. Shchepetov, K. Grigoras, J. Hassel, J. Ahopelto, M. Ylilammi, and M. Prunnila, "Thermoelectric thermal detectors based on ultrathin heavily doped single-crystal silicon membranes," Applied Physics Letters **110**, 262101 (2017).

[246] A. Blaikie, D. Miller, and B. J. Alemán, "A fast and sensitive room-temperature graphene nanomechanical bolometer," Nature Communications **10**, 4726 (2019).

[247] M.-H. Chien and S. Schmid, "Nanoelectromechanical photothermal polarization microscopy with 3 Å localization precision," Journal of Applied Physics **128**, 134501 (2020).

[248] C. Reetz, R. Fischer, G. Assumpção, D. McNally, P. Burns, J. Sankey, and C. Regal, "Analysis of membrane phononic crystals with wide band gaps and low-mass defects," Physical Review Applied **12**, 044027 (2019).